FINAL REPORT

CATHODIC PROTECTION OF COASTAL PRESTRESSED CONCRETE PILES: PREVENTION OF HYDROGEN EMBRITTLEMENT

JOHN R. SCULLY
Associate Professor
Center for Electrochemical Science and Engineering
Department of Materials Science and Engineering
University of Virginia

DAVID G. ENOS
Graduate Research Assistant
Center for Electrochemical Science and Engineering
Department of Materials Science and Engineering
University of Virginia

ALBERT J. WILLIAMS, JR.
Graduate Research Assistant
Center for Electrochemical Science and Engineering
Department of Materials Science and Engineering
University of Virginia

GERARDO G. CLEMEÑA, Ph.D.
Principal Research Scientist
Virginia Transportation Research Council

V · I · R · G · I · N · I · A
VTRC

TRANSPORTATION RESEARCH COUNCIL

VIRGINIA TRANSPORTATION RESEARCH COUNCIL

Standard Title Page - Report on Federally Funded Project

1. Report No. FHWA/VA-98-R26	2. Government Accession No.	3. Recipient's Catalog No.
4. Title and Subtitle Final Report: Cathodic Protection of Coastal Prestressed Concrete Piles: Prevention of Hydrogen Embrittlement		5. Report Date June 1998
		6. Performing Organization Code
7. Author(s) John R. Scully, David G. Enos, Albert J. Williams, Jr., and Gerardo G. Clemeña		8. Performing Organization Report No. VTRC 98-R26
9. Performing Organization and Address Virginia Transportation Research Council 530 Edgemont Road Charlottesville, VA 22903		10. Work Unit No. (TRAIS) 1457-010-940
		11. Contract or Grant No.
12. Sponsoring Agencies' Name and Address Virginia Department of Transportation FHWA 1401 E. Broad Street 1504 Santa Rosa Road Richmond, VA 23219 Richmond, VA 23239		13. Type of Report and Period Covered
		14. Sponsoring Agency Code

15. Supplementary Notes

16. Abstract

Assessing the effect of cathodic protection (CP) on a chloride-contaminated bridge pile involved defining the hydrogen embrittlement behavior of the pearlitic reinforcement and quantifying the local (i.e., at the steel/concrete interface) chemical and electrochemical conditions, both prior to and throughout the application of CP. The hydrogen embrittlement behavior of the reinforcement was assessed through a combination of Devanathan/Stachurski permeation experiments to quantify subsurface hydrogen concentrations, C_H, as a function of the applied hydrogen overpotential, O, and crack initiation tests for bluntly notched and fatigue precracked tensile specimens employing elastic-plastic finite element analysis and linear elastic fracture mechanics, respectively. A series of laboratory scale piles was constructed to determine relevant environmental and electrochemical conditions at the steel/concrete interface.

Laboratory-scale piles were partially immersed in ASTM artificial ocean water and allowed to stabilize. With time, localized corrosion (crevicing) was initiated along the reinforcement and was accompanied by a shift in the pH of the occluded environment from an alkaline pH 12.6 to 5.5 and below due to ferrous ion hydrolysis. CP current densities from 0.1 to 2.5 $\mu A/cm^2$ (per unit area reinforcement) were applied via a skirt anode located at the waterline.

By combining the effect of local CP level as a function of position along the reinforcement on hydrogen absorption with the information on the hydrogen embrittlement characteristics of the reinforcement as a function of hydrogen concentration, safe windows for the application of CP may be identified. With the exception of 100 mV depolarization/decay criteria, it was not possible to sufficiently protect the splash zone of the pile with its high corrosion rate without exceeding the threshold hydrogen concentration for embrittlement at some zone within the reinforcement.

17. Key Words impressed current cathodic protection, prestressed concrete, prestressing steel, hydrogen embrittlement, ferrous ion hydrolysis	18. Distribution Statement No restrictions. This document is available to the public through NTIS, Springfield, VA 22161.

19. Security Classif. (of this report) Unclassified	20. Security Classif. (of this page) Unclassified	21. No. of Pages 224	22. Price

Form DOT F 1700.7 (8-72)   Reproduction of completed page authorized

FINAL REPORT

CATHODIC PROTECTION OF COASTAL PRESTRESSED CONCRETE PILES: PREVENTION OF HYDROGEN EMBRITTLEMENT

John R. Scully
Associate Professor
Center for Electrochemical Science and Engineering
Department of Materials Science and Engineering
University of Virginia

David G. Enos
Graduate Research Assistant
Center for Electrochemical Science and Engineering
Department of Materials Science and Engineering
University of Virginia

Albert J. Williams, Jr.
Graduate Research Assistant
Center for Electrochemical Science and Engineering
Department of Materials Science and Engineering
University of Virginia

Gerardo G. Clemeña, Ph.D.
Principal Research Scientist
Virginia Transportation Research Council

(The opinions, findings, and conclusions expressed in this report
are those of the authors and not necessarily those of the sponsoring agencies.)

ABSTRACT

Assessing the effect of cathodic protection (CP) on a chloride-contaminated bridge pile involves defining the hydrogen embrittlement behavior of the pearlitic reinforcement combined with quantifying the local (i.e., at the steel/concrete interface) chemical and electrochemical conditions both before and during the application of CP. We assessed the hydrogen embrittlement behavior of the reinforcement through a combination of Devanathan/Stachurski permeation experiments to quantify subsurface hydrogen concentrations, C_H, as a function of the applied hydrogen overpotential, η, and crack initiation tests for bluntly notched and fatigue pre-cracked tensile specimens employing elastic-plastic finite element analysis and linear elastic fracture mechanics, respectively. We constructed a series of laboratory-scale piles to determine relevant environmental and electrochemical conditions at the steel/concrete interface.

Laboratory-scale piles were partially immersed in ASTM artificial ocean water and allowed to stabilize. With time, localized corrosion (crevicing) was initiated along the reinforcement and was accompanied by a shift in the pH of the occluded environment from an alkaline pH 12.6 to 5.5 and below because of ferrous ion hydrolysis. CP current densities from 0.1 to 3.0 $\mu A/cm^2$ (per unit area reinforcement) were applied via a skirt anode located at the waterline.

By combining the effect of local CP level as a function of position along the reinforcement on hydrogen absorption with the information on the hydrogen embrittlement characteristics of the reinforcement as a function of hydrogen concentration, safe windows for applying CP may be identified. With the exception of the 100 mV depolarization/decay criterion, it was not possible to sufficiently protect the splash zone of the piles with its high corrosion rate without exceeding the threshold hydrogen concentration for embrittlement at some zone within the reinforcement.

FINAL REPORT

CATHODIC PROTECTION OF COASTAL PRESTRESSED CONCRETE PILES: PREVENTION OF HYDROGEN EMBRITTLEMENT

John R. Scully
Associate Professor
Center for Electrochemical Science and Engineering
Department of Materials Science and Engineering
University of Virginia

David G. Enos
Graduate Research Assistant
Center for Electrochemical Science and Engineering
Department of Materials Science and Engineering
University of Virginia

Albert J. Williams, Jr.
Graduate Research Assistant
Center for Electrochemical Science and Engineering
Department of Materials Science and Engineering
University of Virginia

Gerardo G. Clemeña, Ph.D.
Principal Research Scientist
Virginia Transportation Research Council

INTRODUCTION

Overview of Problem

The environmental degradation of aging steel-reinforced concrete structures is a problem that is today receiving much attention by the corrosion protection community. The prestressed structures of concern are those exposed to high-chloride environments such as bridge decks exposed to deicing salts or coastal marine bridge piles that, by their nature, are partially immersed in ocean water. Although concrete pore water solutions are alkaline and promote steel passivity, chloride ingress can lead to depassivation and active corrosion of the steel. Understanding the issues involved with the avoidance of hydrogen embrittlement while applying cathodic protection (CP) as a corrosion abatement technique in the latter of the two is the focus of this work.

A prestressed concrete coastal marine bridge pile consists of a concrete pile containing an arrangement of high-strength steel prestressing tendons. The orientation of the tendons is such

that they run from the top to the bottom of the pile and that a minimum of 5 cm of concrete separates each tendon from the external environment (in this case, air or ocean water). The tendons themselves are fabricated from isothermally transformed, ultrafine pearlitic steel that has been cold drawn to achieve the very high yield strengths to maintain elastic loading during this application. Each tendon is under a tensile load of approximately 70% of its yield strength, allowing the imposition of a compressive load on the concrete pile, permitting the use of the prestressed concrete under mildly tensile loads (a condition that is typically unavailable for unreinforced concrete, which has very poor tensile properties). If a tendon were to fail because of the reduction in cross-sectional area resulting from corrosion, it would no longer be capable of placing the compressive load on the concrete structure. Corrosion-induced spalling of the concrete is also an issue.

Currently, CP is being pursued as a viable corrosion control method to address this environmental degradation problem, based on its successful application in the corrosion abatement within black steel-reinforced bridge decks. The black steel reinforcement used in such bridge decks, however, has a relatively low yield strength and thus is not as susceptible to overprotection-induced hydrogen embrittlement as the high-strength, eutectoid steels used for prestressing applications. In addition, the rebar is not placed under the large tensile loads to which prestressing tendon is exposed, further reducing the significance of hydrogen embrittlement. As a result, the successful CP of a prestressed structure requires that significant overprotection be avoided. Unfortunately, because of a fundamental lack of understanding of the local environment at the steel/concrete interface, and consequently the effect of various levels of CP on hydrogen production and entry into the reinforcement, selecting the appropriate CP procedures and criteria is not easy.

A number of issues must be addressed to assess the effects of CP on chloride-contaminated, prestressed concrete structures, such as marine bridge piles containing high-strength steel reinforcement. These issues may be broadly grouped into two categories: (1) understanding the environment, and (2) understanding the mechanical behavior of the steel. First, the chemical environment must be understood, in terms of both the bulk environment within the concrete itself and the environment that will develop at the steel/concrete interface as a function of both time and position within a marine bridge pile. The combination of CP practices, pile geometry, polarization behavior, and concrete conductivity determines the position-dependent, cathodic reactions and their associated rates at the steel/concrete interface. The applied cathodic reaction rates along with the local chemistry at the steel surface will then define the hydrogen activity produced at the steel/concrete interface and thus determine the observed steady state steel lattice hydrogen concentration. Finally, the effects of mobile and trapped hydrogen on fracture initiation within the high-strength eutectoid steels commonly used for prestressing tendons must also be determined. This requires an understanding of the relationship between the steady state steel lattice hydrogen concentration and the fracture initiation stress (for a blunt notch), or threshold stress intensity (for a precracked specimen), for the isothermally transformed, drawn pearlitic steel typically used for prestressing tendon. Although such relationships exist for quench and tempered steels, little information is available for the

2

isothermally transformed, ultrafine pearlite that is the subject of this study. Second, the local steady state steel lattice hydrogen concentrations as a function of the applied CP level and vertical position within a marine bridge pile must be defined. This information is also lacking in the literature. The combination of this information will enable the establishment of safe CP procedures for atmospherically exposed, reinforced concrete structures.

Bulk vs. Local Concrete Pore Solutions and Corrosion of Prestressing Steel

The composition of the bulk pore solution within a concrete structure is a function of the type of cement and aggregate used, as well as any additives used to enhance physical or chemical properties (e.g., air entrainment, fumed silica) or to promote more rapid curing of the structure (e.g., $CaCl_2$) (Gratten-Bellew, 1994; Christensen, 1992). Many factors that will cause alteration of the bulk pore solution and, consequently, the local pore solution as well, resulting in deviations from the commonly accepted bulk composition. As a result, the local environment at the steel/concrete interface may not be accurately simulated by any single bulk pore solution.

Exposure to marine environments, such as would be the case with coastal bridge piles, or exposure to deicing salts will result in chloride ingress into the concrete structure. As a result, the portions of a concrete structure exposed to such an environment will have elevated chloride levels, although other regions may not. For example, in a marine bridge pile, the splash (i.e., regions at or near the waterline) and submerged regions (i.e., regions below the waterline) will have an elevated chloride concentration (two or more times greater) than regions far above the waterline, as is illustrated in Figure 1.1 (Hartt, 1994). Chloride may also be introduced through flaws in the concrete (e.g., cracks, large pores/air pockets), by the aggregate, or through addition as a hardening accelerator (i.e., $CaCl_2$) during pouring (Gratten-Bellew, 1994; Christensen, 1992). Although the concentrations of chloride typically present at the steel/concrete interface are not of sufficient magnitude to cause general corrosion or pitting, they are sufficient to result in the initiation of crevice corrosion[1] by a dissolution, local acidification (by ferrous ion hydrolysis) and Cl^- accumulation mechanism (Vrable, 1980; Gonzalez, 1993). In addition to variations in the chloride concentration as a function of vertical position, the degree to which the pore structure within the concrete is saturated will vary. At positions near or below the waterline, the pore structure will be saturated with water, although above the waterline it may not be (Hartt, 1994). As a result, the availability of the oxygen at the steel/concrete interface (i.e., the rate with which oxygen may diffuse through the pore structure) will also vary with position. At positions near or above the waterline (i.e., splash and atmospheric zones) where oxygen transport is controlled by gas phase diffusion, dissolved oxygen concentrations will be higher than below the waterline (i.e., submerged zone) where oxygen transport is dominated by diffusion through the aqueous, saturated pore structure, resulting in lower concentrations that may be readily depleted (Hartt, 1994). As a result of the combination of varying chloride and oxygen

---

[1] Crevice sites include not only the occluded geometries intrinsic in the braided strand but also concrete aggregate in contact with the steel reinforcement.

concentrations as a function of vertical position within the marine bridge pile, the degree of corrosion in the reinforcement will also vary with vertical position, as illustrated in Figure 1.2 (Hartt, 1994).

Experiments conducted by Gonzalez et al. (1993) illustrated that crevice corrosion was readily initiated and accompanied by acidification of the local environment for a steel sample containing an occluded cell geometry and immersed in aerated, chloride-contaminated pore solutions. In these experiments, steel artificial crevice assemblies were immersed in both aerated and deaerated saturated calcium hydroxide solutions to which chloride concentrations from 0.001 to 0.1 M were added. Crevice corrosion was readily initiated within aerated solutions and accompanied by an acidification of the solution within the occluded geometry to a pH of approximately 6. Crevice corrosion was not observed in the deaerated case.

In addition to the crevice corrosion experiments, a series of experiments was performed to assess the pitting potential for the steel samples as a function of chloride concentration in the same $Ca(OH)_2$ + NaCl solutions. As illustrated in Figure 1.3, the pitting potential became increasingly negative with increased chloride concentration. These pitting potential experiments (performed on metal samples without the presence of a crevice former) were augmented by exposures performed at the open circuit potential (OCP), much as the crevice corrosion experiments were conducted. In these OCP experiments, no pitting was observed for either the aerated or deaerated experiments at chloride concentrations as high as 1 M. The results of Gonzalez were similar to those of Bergsma (1977) where an artificial pit was formed in steel immersed in saturated calcium hydroxide solution containing 2% $CaCl_2$. Local pHs as low as 6 were observed.

Otero et al. (1990) conducted experiments identical with those performed by Gonzalez. In addition, they performed a series of experiments on rebar embedded within chloride-contaminated mortar. The rebar was polarized anodically at a current density of 10 $\mu A/cm^2$ in an effort to simulate an actively corroding segment of reinforcement. The simulated steel/concrete interfaces resulted in the observance of local acidification within the crevices to a pH of 4.9 to 5. For the mortar-covered samples, the initiation of corrosion was accompanied by the cracking of the concrete. The pH of the solution that emerged from these cracks was monitored and found to be as low as 2.6. Similarly, upon exposure of the simulated crevices to air, the local pH decreased to 2.6. This second reduction in pH was attributed to the oxidation of ferrous ions (Fe^{2+}) to ferric ions (Fe^{3+}) in an oxidizing environment and may not be relevant to events occurring at the steel/concrete interface if the local oxygen concentration has been depleted by CP.

Once corrosion has been initiated on the steel reinforcement, the local environment will be significantly different from that within the bulk concrete. As metal dissolution takes place, ferrous ions are introduced into the local environment. These ions may then hydrolyze, reducing the local pH to as low as 4.8 (based on the 0.8 M solubility of $FeCl_2$ in H_2O). Table 1.1 presents the local pH that may result because of ferrous and ferric ion hydrolysis for concentrations up to

4

the solubility limit of Fe^{2+} in water. Note that considerably lower pH levels may be achieved if ferrous (Fe^{2+}) ions have oxidized to ferric (Fe^{3+}) ions, which has been suggested to occur. Thus, following the initiation of corrosion of the steel reinforcement, although the bulk pore solution pH will be 12.5 or greater, the local pH may be much lower (Gonzalez, 1993; Bergsma, 1977). Combining this information with the fact that the degree of corrosion, and hence the ferrous ion concentration, will vary as a function of vertical position along the bridge pile, it is reasonable to expect that the local pH will also vary as a function of vertical position.

In addition to chloride-induced corrosion of the prestressing steel, a number of other chemical species must be considered. With time, the constituents within the concrete will react with atmospheric CO_2. This process, known as carbonation, results in a decrease of the pH within the concrete from a highly alkaline >12.5 to 9 or below (Papadakis, 1989). The carbonation process involves the reaction of the calcium hydroxide within the concrete with atmospheric carbon dioxide to form calcite through the reaction

$$Ca(OH)_2(s) + CO_2(g) \rightarrow CaCO_3 (s) + H_2O \tag{1}$$
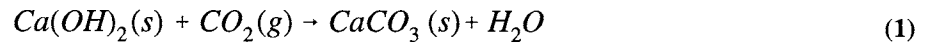
In addition to the calcium hydroxide within the concrete, the original components of the portland cement including calcium silicate hydrate (CSH)

$$3\,CaO{\cdot}2\,SiO_2{\cdot}3\,H_2O + 3\,CO_2 \rightarrow (3\,CaCO_3{\cdot}2\,SiO_2{\cdot}3\,H_2O) \tag{2}$$

tricalcium silicate (C_3S)

$$(3\,CaO{\cdot}SiO_2) + 3\,CO_2 + v\,H_2O \rightarrow 3\,SiO_2{\cdot}v\,H_2O + 3\,CaCO_3 \tag{3}$$
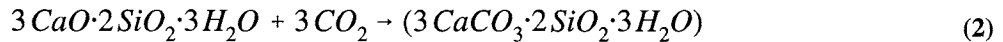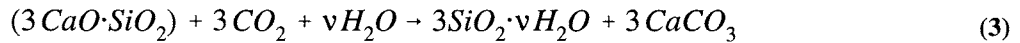
and dicalcium silicate (C_2S)

$$(2\,CaO{\cdot}SiO_2) + 2\,CO_2 + v\,H_2O \rightarrow 2\,SiO_2{\cdot}v\,H_2O + 2\,CaCO_3 \tag{4}$$
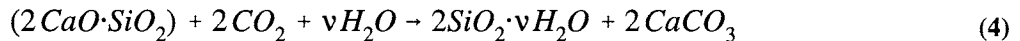
will also react with atmospheric CO_2 to form a combination of silica gel and calcite. These three reactions have been only qualitatively studied; thus, there is some uncertainty as to the degree of hydration in each reaction. The rate of carbonation is a function of the availability of CO_2, the relative humidity level of the environment, the water-to-cement ratio of the concrete, and the time required for diffusional ingress (determined by the CO_2 level within the atmosphere combined with the nature of the pore structure within the concrete). Thus, for a structure such as a marine bridge pile, the rate of carbonation will largely be a function of vertical position along the pile, as the environmental parameters will vary when progressing from the submerged zone to the splash and then atmospherically exposed regions. Under normal atmospheric exposure conditions, the rate of advancement of the carbonation front is very slow, on the order of 1 cm every 3.5 years. Thus, for reinforcement within the atmospherically exposed regions with a typical concrete coverage of 5 cm, the carbonation front would not reach the plane of the reinforcement for nearly 17.5 years. For regions near or below the waterline (i.e., the splash and

submerged zones), where CO_2 diffusion is hindered by the water saturated pore structure, the rate of advancement would be considerably slower. Once the carbonation front reaches the steel reinforcement, the lower pH will result in the depassivation and corrosion of the steel reinforcement (Hansson, 1995).

At issue, then, in defining safe CP limits is whether adequate CP can be achieved throughout a structure without inducing hydrogen production, absorption, and embrittlement somewhere along the vertically placed reinforcement, given the likelihood of the chemical variations in the local environment with vertical position in addition to the presence of prior corrosion and the resulting stress concentrating defects in the reinforcement. To address this issue, we must review the corrosion morphologies likely to be present along the reinforcement in addition to existing CP practices.

Corrosion Morphology for Steel Reinforcement in Concrete

In terms of understanding the implications of corrosion on the structural integrity of a prestressed concrete marine bridge pile subjected to CP, the nature of any stress-concentrating flaws, such as corrosion pits, must be understood in addition to quantification of the local environment at the steel/concrete interface. Numerous researchers have reported corrosion induced (i.e., reduction of cross sectional area) failures of prestressed concrete structures because of corrosion induced cracking of the steel reinforcement. Such corrosion induced failure was typically accompanied by significant longitudinal splitting (Monfore, 1960). Typically, this corrosion is localized in nature, consisting of pitting or crevice corrosion (Gonzalez, 1990, 1993; Monfore, 1960), though some researchers have suggested that failure of the prestressing tendons occurs at fatigue cracks that have formed because of cyclic loading of the reinforcement (Athanassiadis, 1981). Unfortunately, though the presence of localized corrosion is frequently reported within the literature, these same studies are generally remiss in reporting the actual morphology of the flaws, in terms of their depth and aspect ratio.

Efforts to determine localized corrosion morphology of iron in neutral and alkaline chloride containing environments has been conducted. However, few, if any, such studies have been conducted within actual chloride-contaminated concrete. For example, Marshet et al. (1988) performed a study on the pitting morphology of steel in high temperature (90°C) chloride-contaminated sodium bicarbonate (0.1 M $NaHCO_3$ + 1,000 ppm Cl) by polarizing samples to -400, -200, and 0 mV_{SCE} for 10,000 hours. A wide distribution of pit depths was reported, and an expression was derived to calculate the probability of a pit with a particular depth forming as a function of exposure time. Pit depths ranging from 0.2 to 2.5 mm were reported after 10,000 hours, though their aspect ratios were not quantified. However, other researchers have found that localized corrosion in carbon steels is typically hemispherical in nature (Szklarska-Smialowska, 1986). Although this information is within an environment that differs from concrete, it does illustrate the important point that a range of flaw geometries (from shallow, sharp pits to large

blunt ones) may be present on a corroding structure. These geometries will range in acuity from blunt, notchlike pits (Marsh, 1988) to fatigue cracks (Athanassiadis, 1981).

Criteria for Ensuring Sufficient CP and Preventing Overprotection

When cathodically protected, a metal is polarized such that corrosion is either thermodynamically unfavorable (i.e., $E_{applied} < E_{rev}^{Fe/Fe^{2+}}$) or kinetically very slow. Several techniques have been used successfully to apply CP to reinforced concrete structures. These techniques include impressed current CP systems and sacrificial anode systems (Hong, 1993; Kessler, 1995). An important issue for either type of CP system is establishing criteria for adequate protection. In order to achieve an adequate degree of protection, the corrosion rate of the reinforcement must be reduced to an acceptable level without causing other types of damage to the system (e.g., hydrogen embrittlement of the steel reinforcement or degradation of the steel/concrete interface through chemical alteration and/or cathodic polarization). Unfortunately, the irregular geometry and nonuniform resistivity of most concrete structures (i.e., concrete resistivity varies with position relative to the waterline, being lowest below the waterline, and highest above it) (Hartt, 1994) results in significant IR ohmic voltages. This nonuniformity subsequently leads to applied cathodic current and electrochemical potential distributions. These positional variations in cathodic current density make it difficult to maintain the same level of protection throughout the structure (Hartt, 1992, 1994; Pangrazzi, 1994; Chaix, 1995). Thus, although some regions may receive the desired degree of protection, others may be over- or underprotected.

There have been a number of guidelines or proposed criteria for cathodically protecting atmospherically exposed, reinforced concrete structures. Initially, criteria designed for cathodically protecting underground structures were applied. One such technique is the absolute potential-based criterion, where the level of polarization of the reinforcement was maintained such that the potential of the metal surface was equal to or lower than -850 $mV_{Cu/CuSO4}$ (-790mV_{SCE}) (Funahashi, 1991). The basis for this criterion was simply that the steel be polarized to a potential equal to or more negative than the reversible potential for iron oxidation.[2]

Another criterion that was used to protect underground structures was the E-log I criterion (NACE, 1990). From an experimentally determined E-Log I plot for the steel reinforcement within the concrete structure (constructed by gradually polarizing the structure to increasingly cathodic [negative] potentials), the current corresponding to the onset of the linear (i.e., Tafel) region of the oxygen reduction mixed charge transfer-concentration polarization controlled portion of the plot (see Figure 1.4) was selected as the required protection level. This approach was completely empirical in nature (i.e., not based upon the electrochemical theory of corrosion) and as such did not attempt to address the condition of the structure beyond the establishment of

---

[2] The selected potential is intended to equal, but may or may not equal, the true reversible potential since lack of knowledge of the Fe^{2+} concentration precludes the ability to exactly determine E_{rev}.

the aforementioned plot. Application of this approach was often problematic as for many combinations of structural geometry and environmental exposure conditions, determination of the linear region of the E-log I plot is often difficult or impossible (Funahashi, 1991). Moreover, the current, I, used to construct the E-Log I plot represents the total current applied to the structure, and as such does not identify regions of locally high or low applied current density.

A third protection criterion initially used for underground structures and later applied to atmospherically exposed concrete structures is the 100 mV polarization shift criterion (NACE, 1990). In this technique, sufficient CP current is applied such that, at all locations within the structure, the potential decay, defined as the difference between the instant-off potential (i.e., the iR corrected applied potential or the true surface potential), and the potential after terminating the CP current and allowing the structure to stabilize at a new open circuit potential, is 100 mV or greater. If the magnitude of this difference is at least 100 mV, then the structure is considered to be adequately protected. However, it has been demonstrated that 100 mV of depolarization is not, in many cases, sufficient to protect the structure, and that values as large as 200 mV or greater may be required (Funahashi, 1991). In other words, the amount of depolarization required will be a direct function of the condition (in terms of degree of corrosion) of the reinforcement. For example, if we consider the case of an actively corroding material, the electrode is more polarizable: a small change in applied potential results in a large change in current, thus a smaller achieved depolarization will be required for corrosion abatement. If, on the other hand, we consider a nearly passive system, the electrode will be more non-polarizable: a small change in applied potential results in a small change in current, thus a larger amount of depolarization may be required for corrosion abatement.

In addition to the magnitude of the achieved polarization or degree of depolarization, a related issue to be considered, for impressed current CP systems in particular, is the cathodic reactions operative at the steel surface as a function of time. Initially, at low impressed cathodic current densities the oxygen reduction reaction will occur

$$\frac{1}{2}O_2 + H_2O + 2e^- \rightarrow 2OH^- \qquad (5)$$

However, it is reasonable to expect that the dissolved oxygen concentration at the steel/concrete interface may be depleted with time at a fixed cathodic current density if the reduction reaction rate at the steel/concrete interface exceeds the flux of oxygen through the concrete from the external environment. This will cause a negative shift in the applied potential for a fixed applied cathodic current density. Eventually, the potential may be reduced sufficiently to allow the water reduction reaction to take place

$$H_2O + e^- \rightarrow OH^- + H_{ads} \quad \textit{Alkaline Conditions} \qquad (6)$$

$$H^+ + e^- \rightarrow H_{ads} \quad \textit{Acidic Conditions} \qquad (7)$$

8
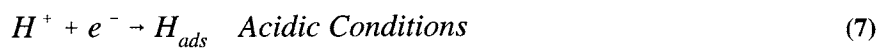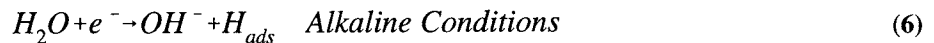
If the potential is shifted such that hydrogen production occurs, a portion of the H_{ads} will become absorbed (i.e., $H_{ads} \rightarrow H_{abs}$), but most will be evolved harmlessly by chemical or electrochemical desorption (i.e., $H_{ads} + H_{ads} \rightarrow H_2$ (gas)). The reinforcement may be embrittled and a hydrogen-induced crack initiated, as a result of the former process, if the combination of the dissolved hydrogen concentration within the steel, applied stress state, and distribution of crack-initiating flaws in the steel meet the conditions for crack initiation.

Recently, the efforts of a number of researchers have been combined to produce an additional qualification to currently practiced CP criteria, addressing the issue of overprotection and, hence, embrittlement of the steel reinforcement (Pangrazzi, 1994; Hartt, 1993; Parkins, 1982). A criterion has been developed based upon constant extension rate tensile (CERT) test results from smooth, notched, and precracked specimens in simulated pore solutions of varying pH over a range of applied potentials. Two different potential regimes were established in which the prestressing tendon was embrittled. The more positive potential regime was a function of pH and attributed to anodic dissolution (i.e., pitting) of the tensile specimens. Focusing on the more negative potential regime, it was found that once the applied potential progressed to values more negative than a threshold value of approximately -950 mV_{SCE}, the load at failure was degraded when compared to a comparable test in air. This threshold was found to be independent of solution pH in saturated (25 mM) $Ca(OH)_2$ as well as 13.5 mM $Ca(OH)_2$ + HCl solutions for pHs between 7 and 12.5. (Hartt, 1993) However, the threshold became more positive than -900 mV_{SCE} for pH levels below 6. This is illustrated in Figure 1.5, which presents the normalized fracture load for applied potentials of -900 mV_{SCE} and -1300 mV_{SCE} as a function of pH. Similar results achieved by Parkins et al. (1982) are presented in Figure 1.6. In the figure, the normalized failure load as a function of applied potential is presented for pH values ranging from 2 to 10.5. As can be seen in the figures, the threshold potential (for cathodic polarization induced embrittlement) is more negative than -900 mV_{SCE} for pH values between 8.5 and that of saturated $Ca(OH)_2$ (12.6). Based upon this result, combined with the assumption that $Ca(OH)_2$ + x HCl pore solution analogs accurately simulate the conditions within a pile, and that the local pH does not decrease below 6, Hartt et al. (1993) have stated that hydrogen embrittlement will be avoided if the applied CP potential is less negative than a threshold value of -900 mV_{SCE}. The reversible potential for the hydrogen evolution reaction (HER) is determined from the relation

$$E_{REV}^{HER} = -0.241 \ V_{SCE} + 0.059 Log[a_{H^+}]$$ (8)

where a_{H^+} is the activity of the H^+ ion in solution, approximately equal to the concentration for dilute solutions. From this expression, the reversible potential is found to be -981 mV_{SCE} in pH 12.5, saturated $Ca(OH)_2$. This is consistent with the -900 mV_{SCE} safe limit deduced, which is based upon this value.

Application of a reversible electrode potential-based criteria to an actual prestressed concrete structure requires reassessment of the universality of the -900 mV_{SCE} threshold discussed. In particular, it must be established whether, in fact, a pH of 6 or below might not be

achieved at the steel/concrete interface in light of the discussion regarding the susceptibility of prestressing steel to crevice corrosion. In addition, the appropriateness of 13.5 mM $Ca(OH)_2$ + HCl as a simulant for the environment present at the steel/concrete interface must also be addressed. If, in fact, the local environment is not accurately simulated by 13.5 mM $Ca(OH)_2$ + HCl, then critical potential thresholds for hydrogen crack initiation in more realistic bulk analogs of the local environment should be defined. Finally, the origins of the observed pH independence (Figures 1.5 and 1.6) of the potential threshold in 13.5 mM $Ca(OH)_2$ + HCl for pH's ranging from 7 to 12.5 should be better understood, given the 59 mV change in hydrogen overpotential that will accompany each unit change in pH. The origins of the relatively constant threshold potential for embrittlement in the aforementioned pH range in $Ca(OH)_2$ + x HCl are addressed.

Applying CP to Actual and Laboratory-scale Piles

A variety of laboratory-scale, steel-reinforced concrete piles have been used by researchers to assess the effects of CP on actual chloride-contaminated concrete structures (Hartt, 1994; Pangrazzi, 1994; Chaix, 1995). These laboratory-scale piles typically consist of a concrete pile with one or more embedded reinforcing steel segments. In addition, chloride is often added to the concrete mix during the production of the piles to accelerate corrosion initiation. These studies have focused on quantifying the variations in the applied current or potential with position for various levels of impressed current or potentiostatic CP.

A series of such experiments was performed by Hartt et al. (1994), Pangrazzi (1994), and Chaix (1995). Piles as described (see Figure 1.7) were constructed using chloride-contaminated concrete containing 0.3 wt% Cl⁻ (via $CaCl_2$). Piles were partially immersed in ocean water prior to, and throughout, the application of CP. Both fixed potential (potentiostatic) (Pangrazzi, 1994) and impressed current (galvanostatic) (Hartt, 1994) CP systems were investigated. CP was implemented via a conductive rubber anode placed at the waterline. The potentiostatic experiments were conducted at applied cathodic potentials of -0.72, -0.77, -0.85, -0.95, and -1.10 V_{SCE}. Potentials were referenced to a saturated calomel electrode ionically connected to the pile at the waterline. During these experiments, the local applied cathodic current densities (for the potentiostatic case) and potentials (for the galvanostatic case) were monitored as a function of vertical position within the pile using a combination of continuous and segmented steel tendons. The resulting current and potential distributions were very nonuniform, as illustrated in Figure 1.8. For the applied potential of -0.95 V_{SCE}, the local current densities ranged from 0.18 $\mu A/cm^2$ in the atmospheric zone above the waterline (approximately 45 cm above the waterline), to 5.64 $\mu A/cm^2$ in the splash zone at the waterline, to 0.46 $\mu A/cm^2$ in the submerged zone beneath the waterline (approximately 45 cm below the waterline). Similarly, the degree of depolarization also varied as a function of vertical position with values of 25, 190, and 87 mV observed for the atmospheric, splash, and submerged zones, respectively. In these experiments, it was also found that only at potentials of -0.95 and -1.10 V_{SCE} was the degree of CP of sufficient magnitude to ensure corrosion abatement.

Experiments performed using an impressed current CP system also resulted in a nonuniform potential distribution, as is illustrated in Figure 1.9 (Hartt, 1994). In these experiments, an applied current density[3] of 1.375 $\mu A/cm^2$ resulted in potentials ranging from -0.975 V_{SCE} in the submerged zone, to -0.700 V_{SCE} in the splash zone, to -0.200 V_{SCE} in the atmospheric zone 135 cm above the waterline. Additional experiments performed at a current density of 2.2 $\mu A/cm^2$ resulted in potentials ranging from -1.05 V_{SCE} in the submerged zone, to -1.35 V_{SCE} in the splash zone at the skirt anode base, to -0.2 V_{SCE} in the atmospheric zone. The conclusion drawn from these experiments was that an impressed current CP system should be constructed that implemented a potential "cut off" of -900 mV_{SCE} to successfully protect a marine bridge pile without introducing the danger of hydrogen embrittlement. However, this assumes a bulk pore solution represented by $Ca(OH)_2$, with a pH approaching 12.5.

Implications of Local Environment Concerning CP

It is reasonable to assume that the pH, oxygen concentration, moisture level, and chemical composition of the steel/concrete interfacial environment may differ significantly from the bulk environment within the concrete as well as vary as a function of vertical position. In addition, the review of the literature revealed that the criteria used to ensure the safe application of CP without introducing the danger of hydrogen embrittlement are based solely upon the magnitude of the achieved polarization. No measurements of hydrogen concentration within steel prestressing wires after or during CP within a concrete pile have been made to the best of our knowledge. In terms of the prevention of overprotection-induced hydrogen embrittlement of the steel reinforcement, the validity of such a purely potential-based approach must be closely scrutinized in light of the expected pH and pore solution chemistry changes as a function of vertical position within a marine bridge pile.

The current criterion proposed for the prevention of hydrogen embrittlement in atmospherically exposed reinforced concrete structures is the -900 mV_{SCE} criterion proposed by Hartt et al. based on CERT experiments described previously (Hartt, 1993; Parkins, 1982). This criterion is apparently based upon the assumption that the local environment at the steel/concrete interface is a solution containing primarily $Ca(OH)_2$. Such environments tend to be alkaline in nature, particularly at the metal/solution interface where hydroxyl production, because of the applied CP current, takes place. Also, the use of the reversible electrode potential criterion assumes that the potential at which hydrogen production becomes appreciable is essentially equivalent to the reversible potential for the hydrogen evolution reaction (HER) within a saturated solution of $Ca(OH)_2$. If corrosion and thus ferrous ion production and subsequent hydrolysis has taken place, the local environment may differ significantly in both composition and pH from that of an alkaline pore solution analog such as $Ca(OH)_2$. The pH within such $Ca(OH)_2$ based pore solution analogs at the metal/solution interface approaches and exceeds 12.6, resulting in a reversible potential for the HER of approximately -981 mV_{SCE}.

---

[3] Average current density for entire strand (i.e., assuming a uniform current distribution).

Moreover, if localized corrosion has taken place within an occluded geometry along the reinforcing tendon, the resulting environment that will exist within that occluded geometry will deviate markedly from the $Ca(OH)_2$ solutions investigated in Hartt's studies. Such an environment will likely be high in chloride and of a pH approaching 4.8 because of ferrous ion hydrolysis. As a result, if steel in such an environment is cathodically polarized to a potential approaching -900 mV_{SCE}, a potential deemed safe by Hartt's criterion, it will actually experience several hundred millivolts of cathodic overpotential with respect to the reversible potential for the HER. The data of Hartt et al. demonstrated that there was a degree of embrittlement even at -900 mV_{SCE} in the saturated $Ca(OH)_2$ + HCl environment below pH 6. Thus, in an instance where embrittlement was not predicted based on the current proposed -900 mV_{SCE} criterion, hydrogen production did take place and embrittlement did result. Apparently, this result was discounted as representing an unlikely scenario.

Fracture Micromechanisms of Fully Pearlitic Steels

It is essential that the fracture initiation behavior of isothermally transformed, drawn, and stress-relieved pearlitic steels be understood as a function of hydrogen concentration. The prestressing strand investigated in this study is compositionally very similar to AISI/SAE 1080 carbon steel with a yield strength of 1696 MPa. Microstructurally, the steel is fully pearlitic, with an average interlamellar spacing of 95 nm. Processing of the prestressing steel involves first isothermally transforming the previously austenitized steel to achieve a nominally fully pearlitic microstructure, after which it is cold drawn to an 85% reduction in area and stress relieved.[4] The microstructure produced by the cold drawing of the prestressing strand is highly anisotropic, as illustrated schematically in Figure 1.10, with pearlite lamellae preferentially aligned parallel with the tensile axis (Embury, 1966; Chandhok, 1966). The wire has been found to have a <110> texture (<110> direction within ferrite lamellae aligned roughly parallel to the drawing axis, as illustrated in Figure 1.10) such that the {100} planes within the ferrite are preferentially oriented 45° to, and rotationally symmetric about, the wire axis. The deformation associated with the drawing process also results in the formation of an elongated dislocation cell structure, with the cell size determined by the combination of the interlamellar spacing of the pearlite coupled with the degree of cold work (Embury, 1966).

Because of the highly anisotropic nature of the drawn wire, it also has a high mode I (i.e., perpendicular to the wire axis) fracture toughness when tested in laboratory air, with values as high as 80 MPa√m reported in the literature (Athanassiadis, 1981). High-strength, low-alloy steels of similar yield strength have been demonstrated to be severely embrittled by hydrogen, with a fracture toughness on the order of 20 MPa√m (Gangloff, 1986). However, cold drawn

---

[4] The actual times and temperatures of the isothermal heat treatment and stress relief treatment used in the production of the prestressing steel are proprietary and as such not revealed by the manufacturer. However, one may speculate that transformation to pearlite would be at a temperature near 550°C (based on the CCT curve for AISI/SAE 1080 steel) and that stress relieving would be done at a temperature sufficiently low such that spheroidization of the steel was unlikely, such as 400°C or below.

pearlitic steels, whether stress relieved or not, are highly resistant to hydrogen degradation when compared to their quench and tempered low-alloy steel counterparts (Marandet, 1977). The increased resistance to hydrogen embrittlement has been postulated to be the result of the highly anisotropic microstructure (i.e., because of the processing of the wire, the pearlite lamellae are preferentially aligned parallel to the tensile axis, perpendicular to the crack front of an advancing mode I crack) that has the effect of diverting a propagating mode I crack parallel with the drawing axis where the applied stress intensity is considerably lower, much like a lamellar composite.

In the uncharged state, fracture of an isotropic pearlitic steel (i.e., pearlite colonies randomly oriented throughout the microstructure) consists predominantly of two modes. The first, known as the shear cracking process first proposed by Miller and Smith, consists of the formation of slip bands within the ferrite lamellae in pearlite colonies oriented such that the lamellae are parallel to the tensile axis (Miller, 1970; Park, 1979; Lewandowski, 1986a, 1986b, 1987). The resulting stress concentration caused by the slip bands results in fracture of the individual cementite lamellae. In coarse pearlitic microstructures, the cementite lamellae fail in a brittle manner. The cementite lamellae may fail in a ductile manner for finer interlamellar spacings, within tensile specimens possessing low stress triaxiality (Lewandowski, 1986). The failed cementite lamellae, subsequently, provide an easy path for further deformation. As a result, more intense shear occurs within the ferrite lamellae, which causes additional cementite lamellae to fail. With increased deformation, the initial voids that resulted from the fractured cementite lamellae become large and link up, resulting in a macroscopic crack as is illustrated schematically in Figure 1.11. This form of cracking will occur along the plane of maximum shear stress, approximately 45 degrees from the tensile axis within an isotropic material, within appropriately aligned pearlite colonies. A second type of fracture mode is transgranular cleavage, occurring on {100} planes within the ferrite with cleavage facets confined to one or more closely oriented pearlite colonies (Park, 1979). Cleavage has been demonstrated to occur across several adjacent pearlite colonies whose ferrite lamellae share a common {100} orientation. Such cleavage occurs at the peak stress location ahead of a notch or sharp crack (Lewandowski, 1987). Nucleation sites are believed to be either MnS inclusions that were previously fractured during processing, or other cracks associated with pearlite colonies, such as the shear cracking discussed. In general, cleavage was found to be more prevalent in notched and precracked specimens with high stress triaxiality, as opposed to the almost exclusively ductile, MVC typically observed in unnotched tensile specimens.

When eutectoid steels with an isotropic pearlitic microstructures as discussed are hydrogen charged, the predominant failure mode has been found to become a locally ductile, tearing-topography-surface (TTS) (Thompson, 1985), as demonstrated by Toribio et al. (Toribio, 1991a, 1991b, 1993.) The TTS is a nonclassical fracture mode observed in a number of alloy systems and appears to be the result of ductile or microplastic tearing on a submicron scale (Thompson, 1979). The location of fracture initiation in this case is unclear. It has been suggested that crack initiation occurs at the location of the maximum stress or strain (Thompson, 1985; Toribio, 1993), some combination of the two (Thompson, 1985), or when a critical stress

13

or strain is exceeded over some microstructurally significant distance (Lewandowski, 1986; Thompson, 1985). Ferrite-pearlite boundaries, nonmetallic inclusions (e.g., MnS), and preexisting cementite microcracks within the pearlite have all been suggested as initiation sites (Alp, 1987).

Unfortunately, although some research has been completed on the mechanisms of crack initiation and growth both with and without hydrogen for isotropic pearlitic microstructures (i.e., randomly oriented pearlite colonies), little has been done on heavily cold worked microstructures such as that present in the prestressing steel.

Work conducted by various researchers on hydrogen-charged, cold worked pearlitic steel wire has revealed several common features. A series of such experiments was conducted by Townsend (1972) on fine pearlitic (interlamellar spacing not specified), cold drawn 1075 bend bars (σ_{YS} = 1461 MPa, σ_{UTS} = 1682 MPa). These bend bars were hydrogen charged in H_2S, which lead to the observance of cracking 45° to the wire axis, attributed to the texture of the wire. Langstaff et al. (1981) conducted experimentation on hydrogen charged AISI 4140 wire bend bars (austenitized, quenched, tempered, and drawn) also found cracking to occur at 45° from the tensile axis. In addition, they found that with increased hydrogen charging (300 to 38,800 $\mu A/cm^2$ in 1 N H_2SO_4 + 1 g/l thiourea), there was an increased amount of longitudinal splitting, parallel to the tensile axis. The longitudinal splitting was assumed to occur along the dislocation cell boundaries discussed. Experimentation conducted on smooth prestressing steel (σ_{YS} = 1590 MPa, σ_{UTS} = 1800 MPa) tensile bars by Price (1984) and Cherry et al. (1980) revealed fracture surfaces dominated by ductile shear and longitudinal splitting. Nucleation was assumed to occur at fractured nonmetallic inclusions, presumably MnS, within the steel (fractographic evidence was not presented in either study), and the crack was assumed to grow slowly through the sample. Based on the fractography from the former studies, it appears that much of the fracture surfaces may be described as TTS. Parkins et al. (1982) performed experimentation on notched and precracked samples of prestressing tendon compositionally similar to AISI/SAE 1085, as mentioned previously. In the fractography from that study, four distinct regions were identified: (1) ductile (MVC) regions perpendicular to the tensile axis, (2) regions of cleavage surrounded by ductile regions, (3) longitudinal splitting, and (4) shear lips along the peripheral regions of the sample. There was no attempt to identify the nucleation site in this study. Moreover, no effort was made to quantify the dissolved hydrogen concentrations obtained in any of the aforementioned studies

.

Experiments on precracked samples of prestressing tendon were also performed by Toribio et al. (1996), both in charged and uncharged conditions. In the case of the uncharged samples, crack propagation progressed at an angle 70 to 90 degrees from the plane of the pre-crack, turning roughly parallel to the tensile axis. This behavior was in stark contrast to hot rolled material of the same composition, where TTS was observed when uncharged, but cleavage was observed upon charging to -1.2 V_{SCE} within a $Ca(OH)_2$ solution. The hot rolled material also exhibited consistently lower failure loads at a given E_{app}. In the transition region for the cold drawn material (i.e., transition from fatigue precrack to hydrogen crack) near the fatigue

14

precrack, the fracture mode was predominantly microvoid coalescence with small cleavage facets and some longitudinal splitting throughout. In the case of the cathodically charged samples, although there was a reduction in the fracture load relative to the fracture load in air, there was no change in the fracture mode. No effort was made to quantify the hydrogen concentrations examined, identify the governing microstructural feature or determine the fracture initiation site and propagation mechanism.

At present, the mechanism of hydrogen assisted fracture initiation of the prestressing strand is unclear. In isotropic pearlitic structures (i.e., randomly oriented pearlite colonies), the fracture mode in the uncharged case is predominantly cleavage in specimen geometries that promote a large degree of stress triaxiality (Toribio, 1991a, 1991b). When such specimens are hydrogen charged, the failure mode becomes predominantly ductile in nature (i.e., TTS failure). Conversely, in the case of drawn pearlitic wire, the failure mode appears to be predominantly ductile shear in both the charged and uncharged case, with no significant change in the microscopic fracture mode as the hydrogen concentration is increased. There is also a large amount of longitudinal splitting (i.e., crack propagation parallel to the tensile axis) in cold drawn pearlitic steels, both when charged and uncharged. The observed degree of longitudinal splitting, however, increases with increased hydrogen concentration, and is best characterized as brittle, cleavage-like cracks propagating parallel to the pearlite lamellae, and consequently the drawing axis of the steel wire. This difference in behavior between the drawn and undrawn material is likely the result of the highly anisotropic nature of the pearlite lamellae within the drawn material, coupled with the existence of a cellular dislocation structure within the ferrite lamellae. Unfortunately, no truly conclusive information has been presented to date within the literature, preventing anything other than speculation as to the origin of this difference in fracture behavior.

Additional research is required to identify the microstructural features that govern the fracture initiation process, and how they are influenced by hydrogen concentration. Given the low fracture toughness of hydrogen charged high-strength steels, the critical flaw size that will result in fast fracture is relatively small. In light of this information, it is unlikely that the fracture process is propagation controlled as has been implied by Cherry and Price but is instead more likely to be nucleation controlled

.

Clearly, there is a critical need to define the relationship between the subsurface hydrogen concentrations achieved within the steel with the fracture initiation stress or stress intensity. Many such relationships, both theoretical and empirical in nature, have been derived for quench and tempered steels, but little can be found for fully pearlitic steels.

Crack Initiation Criteria for Hydrogen-Embrittled Carbon Steels

Many researchers have developed relationships that relate the fracture stress or stress intensity to the hydrogen concentration within various steels. Some of these relationships are empirical in nature, such as that derived by Gerberich and Chen (1975) for AISI 4340, maraging,

and 9Ni-4Co steels. They derived an expression relating the threshold stress intensity for crack initiation with a critical hydrogen concentration achieved at some point, r, within the stress/strain field in front of the advancing crack

$$K_{th} = \ln\left(\frac{C_{cr}}{C_0}\right) \frac{3RT\sqrt{2\pi r}}{2(1+v)V_H} \tag{9}$$

where C_{cr} is the critical hydrogen concentration achieved a microstructurally significant distance, r, in front of the crack tip, C_0 is the equilibrium hydrogen concentration, R is the gas constant, T is temperature, v is Poisson's ratio, and V_H the partial molar volume of hydrogen within the metal lattice.

Another empirical relationship, derived by Akhurst and Baker (1981) for a quench and tempered 3½ NiCrMoV steel was based upon the concept that the fracture stress is reduced by the effect of hydrogen on the cohesive strength of the metal lattice, where

$$\sigma^* = \sigma_0^* - AC_0\exp\left(\frac{V_H\sigma_{ii}}{3RT}\right) \tag{10}$$

where σ^* is the hydrogen reduced cohesive strength of the metal, σ_0^* is the intrinsic lattice cohesive strength, C_0 the lattice hydrogen concentration, $\sigma_{ii}/3$ the hydrostatic stress, V_H the partial molar volume of hydrogen in the metal lattice, R the gas constant, and T temperature.

Other theoretical relationships have been established that relate fracture stress to the hydrogen concentration at a particular microstructurally significant site, such as that applied by Scully et al. (Scully, 1991) for the grain boundary fracture stress of a PH 13-8 Mo stainless steel

$$\sigma_f = \sigma_f^* - \alpha_i X_i^{½} - \alpha_H C_o\exp\left(\frac{\sigma_H V_H}{RT}\right)\exp\left(\frac{-E_b}{RT}\right) \tag{11}$$

where σ_f^* is the intrinsic fracture strength, α_i and α_H are constants, and X_i and the C_o expression are relations expressing the concentration of impurity species and hydrogen, respectively, at the grain boundary.

A series of empirical relationships has also been determined for cracking in various bainitic and martensitic alloy steels. These empirical relations are calculated via regression analyses of K_{th}-C_H data and are of several general forms, such as the following power relationship for the threshold stress intensity for crack initiation (Gangloff, 1986)

16

$$K_{th} \ (\text{MPa}\sqrt{m}) = AC_0^{-B} \tag{12}$$

where C_0 is the lattice hydrogen concentration and A and B are unitless, empirically determined constants. For example, Yamakawa found for AISI/SAE 4135 steel that A = 16.1 and B = 0.102 (1984). As was discussed by Gangloff, the similarity between the various empirical relationships suggests a common mechanism for crack initiation in these steels.

Similar relationships have been suggested relating the hydrogen concentration to the fracture initiation stress of the linear-log form (Hirth, 1980; Klein, 1993)

$$\sigma_f = \sigma_f^* - \alpha \log(C_o)$$

where σ_f is the fracture initiation stress of the embrittled material, σ_f^* is the fracture initiation stress in the uncharged state, C_o is the hydrogen concentration, and α an empirically determined constant.

Unfortunately, there is little information available in the form of relationships similar to those detailed between the fracture initiation stress or stress intensity and the hydrogen concentration for pearlitic steels such as that used for prestressing tendon. In fact, little other than the failure load as a function of the applied potential has been reported in the literature for prestressing steels, with no effort made to quantify the subsurface hydrogen concentrations achieved.

PROBLEM STATEMENT

To date, CP has been used to successfully protect black steel-reinforced bridge decks, and based upon this fact has been targeted for application to chloride-contaminated, prestressed concrete bridge piles. The black steel reinforcement used in such bridge decks, however, possesses a relatively low yield strength and as such is not as susceptible to overprotection induced hydrogen embrittlement as the high-strength, eutectoid steels used for prestressing applications. In addition, the rebar is not placed under the high tensile loads to which prestressing tendon is exposed, further reducing the significance of hydrogen embrittlement. Prestressing steels possess a high yield strength and are placed under large loads within a corrosive environment. As a result, the successful CP of a prestressed structure requires that significant overprotection be avoided. However, as illustrated, the local environmental and electrochemical conditions, and in turn steady state steel lattice hydrogen concentrations present within the steel reinforcement used in such a marine bridge pile will vary as a function of vertical position relative to the waterline. As a result, although CP appears to be a viable corrosion mitigation technique, it is unclear whether a sufficient level of CP can be achieved throughout the structure to afford protection without overprotection and possible hydrogen embrittlement of the high-strength reinforcing tendon at some point within the pile. This uncertainty originates

17

from the development of local environments at the steel/concrete interface that differ from that within the bulk concrete and, in turn, their effect on hydrogen production and absorption in steels, coupled with the high sensitivity of the fracture behavior of high-strength steels to dissolved hydrogen.

The safe application of CP to chloride-contaminated concrete structures requires that several important pieces of information be known. First, it is essential that the local (i.e., at the steel/concrete interface) chemical and electrochemical conditions, including the steady state steel lattice hydrogen concentrations achieved within the prestressing steel, be understood. Secondly, in order to assess the implications of these conditions, the hydrogen embrittlement behavior of the reinforcement itself as a function of the steady state steel lattice hydrogen concentration must be determined.

In particular, the following issues remain unresolved:

1. The actual environment, in terms of its composition (e.g., alkaline $Ca(OH)_2$ containing pore solution, $FeCl_2$ environment resulting from corrosion, Ocean water because of a crack in the concrete) and pH, as a function of position within a chloride-contaminated marine bridge pile is unknown and as such must be determined.

2. The level of CP applied as a function of position within a chloride-contaminated marine bridge pile is unknown. It is critical that the level of protection, in terms of applied potential or local current density, be understood in order to determine if the structure has been sufficiently protected, and if the danger of hydrogen production, absorption, and embrittlement does exist.

3. The implications of the local environment as a function of position within a chloride-contaminated marine bridge pile at a given CP level in terms of the steady state steel lattice hydrogen concentration achieved within the prestressing steel must be assessed.

4. The fracture behavior of the prestressing tendon, both in the hydrogen charged and uncharged state, must be determined in the form of the functional dependance of the fracture initiation stress or stress intensity (σ_i or K_i) on the steady state steel lattice hydrogen concentration (C_H). This information will allow meaningful conclusions to be drawn from characterization of the hydrogen levels produced within prestressing steels in marine bridge piles subjected to various levels of CP.

5. The nature of corrosion induced defects along the reinforcement must be assessed allowing the intrinsic fracture initiation stress can be compared to the local stresses resulting from such stress concentrating flaws.

18

6. The fracture micromechanisms for cold drawn, pearlitic steel must be determined, above and beyond the determination of the critical stress or stress intensity required for hydrogen crack initiation within the prestressing steel as detailed. In other words, the micromechanisms of hydrogen crack initiation in terms of existing critical microstructural features and those created by local plastic deformation, as well as the dependance of this initiation process on both lattice and local trapped hydrogen concentrations must be defined.

PURPOSE AND SCOPE

A number of issues must be addressed to quantify safe windows for, as well as the potentially detrimental effects of, CP on reinforced concrete structures, including understanding the following:

1. The electrochemical conditions in terms of the pH and applied potential at the steel/concrete interface as a function of both position and time during the application of CP, and how these conditions compare to current criteria for the achievement of sufficient CP.

2. The local steady state steel lattice hydrogen concentration achieved, if any, as a function of the applied CP level and vertical position within a laboratory-scale pile

3. The effect of relevant hydrogen concentrations on the fracture initiation stress and threshold stress intensity within the prestressing steel.

By combining 1 and 2, it will be possible to predict, given a set of environmental and electrochemical conditions, the steady state steel lattice hydrogen concentration within the steel reinforcement. This information may then be compared to the relationship between a known steady state steel lattice hydrogen concentration within the steel and the fracture initiation stress established in element 3 to estimate the lattice hydrogen concentration-dependent fracture initiation stress of the prestressing steel. This parameter can be compared to the local stress or stress intensity in the presence of surface flaws or defects ranging from blunt and sharp notches to a fatigue precrack with an applied remote stress of 70% σ_y. Safe CP limits may be determined by defining CP levels that provide adequate CP for suppression of corrosion without inducing hydrogen embrittlement defined by decreases in the threshold stress or stress intensity for crack initiation.

19

METHODS

Material Characterization and Solution Preparation

Mechanical and Microstructural Characterization of the Prestressing Strand

ASTM A416 grade 270 low relaxation prestressing strand for use within simulated piles and for constant extension rate testing was obtained from Florida Wire and Cable, Inc. The prestressing tendon was similar in composition to AISI/SAE 1080 steel (see Table 4.1) with a nominally fully pearlitic microstructure (95 nm interlamellar spacing) as illustrated from a point of view parallel to the drawing axis in Figures 4.1a and 4.1b (low and high magnification views, respectively). As can be seen in the figure, the microstructure was composed of a distribution of small pearlite colonies, ranging in size from 2 to 10 μm. These colonies are likely the result of the drawing process, which has been demonstrated to transform initially uniform grains into elongated, ribbon like grains that curl about the drawing axis in cold drawn, BCC (011) textured materials (Hosford, 1964). There was no evidence of the existence of prior austenite grain boundaries nor the presence of proeutectoid phases (ferrite or cementite) or other large scale microstructural features. As is typical with steels of this composition, there were a large number of inclusions throughout the microstructure. Figure 4.2 illustrated a MnS stringer, of which there were many, aligned parallel to the drawing axis of the wire. Also present within the steel were Ca rich precipitates, illustrated in Figure 4.3. The latter differed from the former in that they were fewer in number, and not elongated by the drawing process. The average spacing between MnS inclusions was found to be approximately 20 μm. These inclusions were elongated parallel to the drawing axis because of the drawing process, with the aforementioned spacing being measured in a plane perpendicular to the drawing axis. The drawing process has a rather dramatic effect on the microstructure of the strand. The microstructure produced by the cold drawing of the prestressing strand is highly anisotropic, with pearlite lamellae preferentially aligned parallel to the tensile axis (Embury, 1966; Chandhok, 1966), as well as the formation of shear bands and microvoids within the microstructure (Porter, 1978). The wire has been found to have a <110> texture (with respect to ferrite lamellae), such that the {100} planes within the ferrite are preferentially oriented 45° to the wire axis. The deformation associated with the drawing process also results in the formation of an elongated dislocation cell structure, with the cell size determined by the interlamellar spacing of the pearlite. (Embury, 1966) Based on these results, a dislocation cell size on the order of 35 nm would likely be present in the prestressing steel investigated in this study.

A summary of typical mechanical properties for similar fine pearlitic steels, both drawn and undrawn, is presented in Table 4.2. Because of the ultra fine pearlitic microstructure coupled with the large amount of cold work experienced by the prestressing strand, it is very high strength ($\sigma_y > 1400$ MPa). Experimental studies performed on prestressing steel can be seen to have a number of gaps in the documentation of basic material property data. For example, the literature may be remiss in reporting prior austenite grain size or colony size in these steels. This is likely because of the fully pearlitic microstructure (i.e., pearlite colonies will either grow through

austenite grain and twin boundaries and be altered (Hillert, 1960; Brooks, 1987; Rathenau, 1954) or be arrested (Brooks, 1987), thereby hindering any attempts to assess the prior austenite grain size from a fully transformed microstructure) and the drawing process (i.e., drawing to large reduction in area results in the alignment of the pearlite lamellae parallel to the drawing axis, resulting in the elimination of discrete pearlite colonies within the microstructure [Embury, 1966]). Mechanical property data for the steel investigated in this study are presented in the form of a true stress-true strain curve in Figure 4.4. As can be seen in the figure, the 0.2% offset yield strength was found to be 1696 MPa, and the Young's modulus 185 GPa, agreeing well with literature values for drawn pearlitic wire reported in Table 4.2. Also illustrated in the figure are the points selected to describe the stress strain curve for FEM analyses.

Sample Preparation for Hydrogen Permeation and Other Electrochemical Experiments

Permeation experiments were conducted using SAE/AISI 1080 carbon steel plate[5] that had been isothermally transformed to achieve a fully pearlitic microstructure. A heat treatment procedure applied by Lewandowski et al. (1986) was used to produce a fully pearlitic microstructure with a prior austenite grain size of 170 µm, a pearlite colony size of 5.5 to 7.5 µm, and average pearlite interlamellar spacing of 0.1 µm (austenitized for 3 hours at 1000°C, followed by 45 minutes at 550°C to isothermally transform the microstructure to pearlite). This accurately simulated the pearlite interlamellar spacing, colony size, and composition (Table 4.1) of the prestressing strand, as illustrated in Figures 4.5a and 4.5b (low and high magnification views of plane perpendicular with rolled surface, respectively). Following heat treatment, the foils were cold rolled to an effective plastic strain of 1.94, equivalent to that of the prestressing steel based upon the knowledge that the strand was drawn to an ~85% reduction in area. Next, the foils were stress relieved at 425° C to achieve a microhardness equivalent to that of the prestressing strand (530 H_{knoop}, 500 g load). The steel foils were wet polished on both sides to an 800 grit finish following the mechanical processing procedure. The steel foils were then cleaned and degreased ultrasonically in 1,1-trichloroethane followed by acetone and finally methanol. The exit side of the foil was then argon etched to remove the surface oxide, then coated with a thin layer of palladium in a high vacuum (10^{-7} torr) sputtering system from a 99.999% palladium target. For mortar-covered samples, a 1-cm-thick layer of mortar (0.49 water/cement ratio, type III portland cement) was placed upon the charging surface of the foils and allowed to cure at room temperature and 100% relative humidity for two weeks prior to use. Once prepared, the sample was fixed into a polytetrafluoroethylene (PTFE) holding clamp and placed in the cell (mortar-covered permeation foils were first placed within the PTFE holding clamp, after which the mortar was applied).

In addition to the 1,080 steel samples, permeation experiments were also performed on 99.5% iron foils that simulated the hydrogen permeation windows on the hydrogen sensors that is

---

[5] It was necessary to use an AISI/SAE 1080 steel foil for permeation experiments as the cold drawn wire could not be rolled into a sheet configuration although still accurately simulating the prestressing strand.

discussed (see Table 4.1 for compositional information). For these foils, palladium was deposited using a solution containing a 25% solution of a commercially available electroless palladium plating bath.[6] Each foil was prepared as detailed previously, after which one surface was coated with a maskant (a toluene soluble peelable maskant was used[7]). The foil was then rinsed in 10% (0.9 M) H_2SO_4 solution, followed by deionized water, after which it was immersed in the plating bath for 45 min, allowing the deposition of a continuous metallic palladium coating. Following plating, the maskant was removed in toluene and the exit surface was repolished to an 800 grit finish.

General Practices for Solution Preparation

All experimental solutions were made using 18 MΩ deionized water and reagent grade chemicals. ASTM artificial ocean water was made in accordance with ASTM D1141. Saturated $Ca(OH)_2$ solutions were made by first adding twice the amount of $Ca(OH)_2$ required to saturate the solution, after which the solution was then deaerated and filtered prior to use. The buffered, low pH environment consisted of 0.1 N H_3BO_4 + 1 mM $Ca(OH)_2$ + 3.3 mM KCl that was pH adjusted to 4 or 6 using HCl and NaOH as needed. A final environment containing 0.1 M HCl + 0.3 M NaCl + 10 ppm H_2S (from Na_2S) was used to obtain high subsurface hydrogen concentrations (Yamakawa, 1984). The HCl environment was prepared with all of the constituents listed, save the Na_2S. The solution was then deaerated and finally the Na_2S was added just prior to transfer to the charging cell. H_2S egress into the surrounding environment was controlled via a $CuSO_4$ trap, for sulphide gettering, located on the nitrogen purge gas outlet. All solutions were either aerated or deaerated with nitrogen prior to and throughout all experimentation as required for each test.

Electrochemical Polarization Characteristics

Establishing Critical Potentials and Cathodic Polarization Kinetics

Establishing basic electrochemical behavior and determining pitting potentials were accomplished via a series of potentiodynamic scans. Samples were prepared by polishing to a wet 600 grit finish after which they were degreased with acetone and placed into the environment. All experiments were conducted using a standard flat cell, as illustrated in Figure 4.6. Open circuit potentials were allowed to stabilize for 10 hours prior to performing the scan. Scans were performed at a scan rate of 0.1667 mV/s unless noted otherwise. Scans were initiated 30 mV anodic to the open circuit potential for cathodic scans, and 30 mV cathodic to the open circuit potential for anodic scans. All experimental solutions were prepared as detailed and

---

[6] Electroless plating of palladium was accomplished using Pallamerse procured from Technic, Inc.

[7] Turco 5145 Peelable Maskant and Stop-Off Coating, Turco Products, Inc., Westminster, California.

deaerated for 24 hours by bubbling nitrogen through a gas dispersion stone within the solution prior to use.

Determining and Correcting the Cathodic Reaction Rate for Local Changes in pH
via Rotating Disk Electrode Experiments

Upon the application of cathodic polarization, the local pH at the metal/solution interface will be increased because of hydroxyl (i.e., OH^-) production, the rate of which is directly proportional to the cathodic reaction rate. In the case of the steel/$Ca(OH)_2$ system, where the hydrogen absorption efficiency and the true applied hydrogen overpotential-current density relationships are both direct functions of the interfacial pH, it is critical that this information be obtained. Therefore, understanding and controlling this local pH are essential if the hydrogen absorption kinetics are to be understood. To accomplish this, rotating disk electrode (RDE) experiments were performed. The RDE technique allows the diffusional boundary layer to be determined, and hence the surface pH, by varying the rotation rate of the electrode.

For the unstirred or stagnant case, the diffusional boundary layer thickness for any mass transfer controlled electrochemical process can be expressed as a function of the diffusivity of the specie of interest and time

$$\delta = (\pi D t)^{\frac{1}{2}} \tag{14}$$

However, all practical electrochemical cells will have some uncharacterized and thus uncontrolled degree of stirring associated with them because of thermal fluctuations, convection because of deaeration of the environment, etc. Although the relationship expressed in Equation 14 is an adequate representation of the diffusional boundary layer thickness for relatively short times, it greatly overestimated the thickness for longer times owing to uncharacterized stirring. In the case of the rotating disk electrode, the thickness of the diffusional boundary layer after initial boundary layer depletion is fixed by the rotation rate of the electrode, and can be expressed by the expression

$$\delta = 1.61 D^{\frac{1}{3}} v^{\frac{1}{6}} \omega^{-\frac{1}{2}} \tag{15}$$

where D the diffusivity of the reacting specie, v the solution's kinematic viscosity (approximately 0.01 cm^2/s for dilute aqueous solutions), and ω the rotation rate in radians/s. Assuming that the concentration gradient in this boundary layer is approximately linear, Fick's first law can be used to calculate the surface concentration of hydroxyl ions, and hence the surface pH, by approximating the concentration gradient as

$$\frac{dC}{dX} = \frac{\left(C^{surface} - C^{bulk}\right)}{\delta} \tag{16}$$

23

Where $C^{surface}$ is the hydroxyl concentration at the metal/solution interface and C^{bulk} is the hydroxyl concentration within the bulk solution (both in moles/liter). We are then able to express the surface concentration of hydroxyl ions as a function of the diffusional boundary layer thickness (and hence RDE rotation rate) and the applied current density (which defines the flux of hydroxyl ions from the metal surface) as

$$C^{surface} = C^{bulk} + \frac{\delta J}{D} = C^{bulk} + \frac{\delta\left(\frac{i}{nF}\right)}{D} \tag{17}$$

that in turn enables us to define the surface pH as

$$pH^{surface} = 14 + \log\left(C^{bulk} + \frac{\delta J}{D}\right) = 14 + \log\left(C^{bulk} + \frac{\delta\left(\frac{i}{nF}\right)}{D}\right) \tag{18}$$

enabling correction of the applied overpotential at a given applied cathodic current density for changes in the surface pH induced by the applied current density.

The cell used to perform the RDE experiments is presented in Figure 4.7. As can be seen in the figure, the cell was designed such that the solution could be continuously deaerated throughout the course of the experiment. RDE experiments were conducted in saturated $Ca(OH)_2$ at pH 12.6 and pH 9.2, as well as within NaOH at pH 12.5. The pH 9.2 $Ca(OH)_2$ environment was prepared by first following the procedures outlined. Once the solution was filtered the pH was adjusted using HCl to the desired level. As a result, the pH 9.2 solution has the same $Ca^{(II)}$ concentration as the pH 12.6 environment. All environments were deaerated for 24 hours prior to performing the experiment. The sample consisted of a 1.8-cm diameter PTFE mandril containing a 5-mm-diameter 99.9% Fe electrode that was wet polished to an 800 grit finish prior to each experiment. Experiments were performed at 500 and 750 rpm by applying a series of cathodic current densities ranging from 5×10^{-6} to 1×10^{-3} A/cm^2, each for a period of two hours (allowing the system to stabilize). The local pH and the true surface hydrogen overpotential were then calculated for each current density, with the absolute value of the hydrogen overpotential, η, defined as

$$\eta = |E_{applied}| - |E_{reversible}| = |E_{applied}| - |-0.241 - 0.059 pH^{surface}| \tag{19}$$

where all potentials are measured with respect to the saturated calomel reference electrode. This correction enabled accurate determination of the kinetics of the hydrogen evolution reaction via the establishment of true η - Log i plots.

24

Determining Subsurface Mobile Hydrogen Concentrations

Devanathan/Stachurski Permeation Technique

The Devanathan/Stachurski permeation technique enables the establishment of the kinetics of hydrogen absorption as well as the effective hydrogen diffusivity and steady state steel lattice hydrogen concentrations within the material being examined (Devanathan, 1962, 1964). The cell design used for laboratory testing is presented in Figure 4.8. Galvanostatic charging was accomplished via a battery powered galvanostat. The exit surface was held potentiostatically at -200 mV$_{SCE}$. For all experiments, the exit side solution was pH 12.5 NaOH. Both the exit and charging side electrolytes were deaerated for 24 hours prior to, and throughout the course of, each experiment using nitrogen. The temperature of both cells was maintained at 27°C (300 K). Throughout each test, the local environment at the steel/solution interface was controlled via an impinging jet system, as detailed, and illustrated in Figure 4.9a. This enabled the local interfacial pH to be approximated, such that any deviations from that of the bulk electrolyte could be accounted for.

As illustrated for RDE experiments, cathodic polarization will result in an increase in the local pH. A typical impinging jet experimental setup is illustrated in Figure 4.9b. As can be seen in the figure, the impinging jet electrode consists of a jet of diameter d, which directs a column of solution, flowing at a velocity v, tangential to the actual electrode that is positioned a distance H away from the jet. The nature of the jet (i.e., turbulent of laminar) is described by the Reynolds number, Re, where

$$Re = \frac{Vd}{\gamma} \tag{20}$$

where V is the solution velocity, d is the diameter of the jet and γ the kinematic viscosity of the solution. A second term used to define the impinging jet electrode system is the Schmidt number, Sc, which represents the ratio of the diffusive boundary layer thickness (which we wish to use to define the surface pH) to the hydrodynamic one (defined by the flow properties of the system), where

$$Sc = \frac{\gamma}{D} \tag{21}$$

where D is the diffusivity of the specie of interest.

Upon impingement of the jet with the electrode, there are three discrete regions or flow regimes along the surface. The first is known as the uniform access, or ua, region. In this region, defined by values of x/d (where x is the radial position along the electrode relative to the centerline of the impinging jet) less than or equal to 0.5 to 1, the rate of mass transfer (and hence the hydrodynamic boundary layer thickness) is assumed to be constant. The second well-defined flow regime is the wall jet region, located at x/d in excess of 3 to 5. In this region, the mass

transfer rate is a function of, and thus varies, with radial position. The third region is the transition region between the uniform access and wall jet regions.

Calculation of the boundary layer thickness requires quantification of the mass transfer rate as a function of position along the electrode. The mass transfer rate is expressed in the form of the Sherwood number, Sh, which is of the general form;

$$Sh = \frac{Kd}{D} \quad \text{or} \quad Sh = [constant]Re^{x}Sc^{y} \tag{22}$$

where K is a constant expressing the ratio of the rate of the reaction to the concentration driving force, d is the nozzle diameter, and D is the diffusivity of the specie of interest.

The actual relationship for the Sherwood number will vary as a function of the geometry of the system in question, as well as with which region (i.e., wall jet or uniform access) that it is being calculated for. In this system, d = 0.5 mm, V = 1237.5 cm/s, γ = 0.01 cm^2/s, D = 5.26 x 10^{-5} cm^2/s, and H = 2 cm. This leads to a Reynolds number of 6187.9 (turbulent jet) and a Schmidt number of 190.1. In typical systems, H is made as small as possible, to optimize flow at the specimen surface, with H/d values of 0.1 typical. Chin and Tsang (Chin, 1978) presented an expression for the Sherwood number for cases where H/d > 10 for the uniform access region. Their expression was

$$Sh = 0.53294Re^{\frac{1}{2}}Sc^{\frac{1}{3}}g(Sc) \tag{23}$$

where

$$g(Sc) = 1 - \frac{0.084593}{Sc^{1/3}} - \frac{0.016368}{Sc^{2/3}} - \frac{0.0057398}{Sc} + \frac{0.0014288}{Sc^{4/3}} + \frac{0.0013088}{Sc^{5/3}} + \dots \tag{24}$$

If we then relate the Sherwood number (using the general form expressed in Equation 22) to the diffusionally limited current density, i_L, we are able to arrive at the expression

$$i_L = (constant)(nFD)(Re^{x}Sc^{y})\left(\frac{\Delta C}{\delta}\right) \tag{25}$$

This allows us to calculate the concentration gradient, $(\Delta C/\delta)$, which would result from a given current density, but does not enable us to independently determine the boundary layer thickness (i.e., we have one equation and two unknowns).

An alternate method to obtain the diffusive boundary layer thickness is by determining the diffusionally limited current density of a reaction for which the concentration gradient of the appropriate species is well known. One such process for which this is readily determined is the oxygen reduction reaction. Figure 4.9c presents a potentiodynamic polarization scan for the impinging jet system discussed in pH 12.6 NaOH. From the figure, the limiting current density of 38.5 μA/cm^2 is readily obtained. Combining this value with an estimate of the bulk solution dissolved oxygen concentration in the deaerated case (assumed to be 60 ppb, 100 times lower

than an ambiently aerated solution), the fact that the surface concentration of oxygen is zero, and using the relationship

$$i_L = \frac{nFDC_b}{\delta} \tag{26}$$

where $D = 1.9 \times 10^{-5}$ cm^2/s for oxygen, the diffusive boundary layer thickness is found to be 3.92 µm. These data agree well with typical values for the diffusional boundary layer thickness for various electrode configurations, presented in Table 4.3 (Gileadi, 1993).

Using this boundary layer thickness, it is possible to calculate the surface pH that would result for current densities applied in the Devanathan/Stachurski permeation experiments, the results of which are presented in Table 4.4 for the environments investigated in this study. As can be seen in the table for the alkaline environments (pH 12.5 NaOH and pH 12.6 Ca(OH)$_2$), even if the combination of the largest current density is combined with the largest possible diffusion layer thickness, there will be a negligible change in the surface pH. This small change results in only a fraction of a millivolt change in overpotential. As a result, for the current densities used in this study, correction of the applied overpotential for small changes in the surface pH is not necessary in the case of highly alkaline (pH 12.5 and 12.6) environments.

Conversely, in the case of the lower pH environments (pH 6 borate buffered environment, pH 8.2 ASTM ocean water, pH 9.2 Ca(OH)$_2$), this correction is essential, as illustrated in the table. In the latter cases, a shift in the local pH on the order of a pH unit was observed, corresponding to a correction of nearly 60 mV in the true applied hydrogen overpotential. These corrections were made to assess the true hydrogen absorption kinetics in each of these environments.

Time dependant permeation flux data were analyzed to obtain hydrogen diffusion data using the technique of McBreen et al. (1966). In this technique, the LaPlace solution to Fick's second law

$$\frac{J_t}{zF} = \frac{DC_H^i}{L} + 2(C_H - C_H^i)\sum_{n=0}^{\infty}(-1)^n \left(\frac{D}{\pi t}\right)^{0.5} e^{-[(2n+1)L]^2/4DT} \tag{27}$$

is manipulated such that the effective diffusivity of hydrogen from either rise or decay transients can be calculated, as illustrated[8]:

---

[8] Because of the exponential nature of the series expansion in Equation 27, only the first term (i.e., n = 0) is significant and, subsequently, used for analysis.

27

$$\log(|(J_{ss}-J_t)|\sqrt{t}) = \log\left[\frac{2F\sqrt{D}|(C_H-C_H^i)|}{\sqrt{\pi}}\right] - \frac{L^2\log(e)}{4D}\left(\frac{1}{t}\right) \qquad (28)$$

Where J_t is the instantaneous permeation flux density, J_{ss} is the steady state permeation flux density prior to the rise or decay transient being analyzed, z is the number of electrons transferred, F is Faraday's constant (96,500 C/mol), D is the effective diffusivity of hydrogen within the steel, C_H^i is the steady state steel lattice hydrogen concentration at the charging surface prior to the rise or decay transient, C_H is the steady state steel lattice hydrogen concentration fixed at the charging surface during the transient, L is the thickness of the foil, t is time, and T is temperature. Thus, a plot of $\log(|(J_{ss}-J_t)|t^{0.5})$ vs. 1/t will be linear with a slope equal to $L^2\log(e)/4D$ as illustrated in Figure 4.10. (It should be noted that the aforementioned solution is only valid for $J_t/J_{ss} < 0.965$, corresponding to relatively long times or small values of 1/t in the figure, where the data can be seen to be nonlinear.)

Figure 4.11 presents the measured steady state permeation flux density (J_{ss}) as a function of inverse foil thickness for the 1080 steel foils used in this study. Since this plot is linear, it may be concluded that the measured permeation transients were bulk diffusion, and not surface controlled. Figure 4.12 presents the calculated hydrogen diffusivities as a function of charging current density, and hence lattice hydrogen concentration, for various foils. As can be seen in the figure, an effect of charging current density (and, thus, lattice hydrogen concentration) was not observed. This fact verifies that the effective diffusivity of hydrogen within the prestressing strand is not a strong function of lattice hydrogen concentration. Consequently, an overall mean effective diffusivity has been calculated for all of the AISI/SAE 1080 steel foils of 6.72 ± 0.70 x 10^{-7} cm^2/s. This diffusivity is compared with literature values in Table 4.5. D_{eff} decreases with decreasing pearlite interlamellar spacing, cold work, quenching to produce a martensitic microstructure, and increasing carbon content in ferritic/pearlitic steels. D_{eff} is increased by both spheroidizing and tempering of martensitic materials. As a result, by making the assumption that D is independent of concentration, coupled with the knowledge that the observed hydrogen permeation is bulk diffusion controlled, it is possible to apply Fick's first law to calculate the steady state steel lattice hydrogen concentration

$$J = -D\frac{dC}{dX} \qquad (29)$$

approximating dC as (C_H - C_0) where C_H is the steady state steel lattice hydrogen concentration fixed within the steel foil at the charging surface for a given hydrogen fugacity, and C_0 the lattice hydrogen concentration fixed at the exit surface of the steel foil that approaches zero for the conditions applied in this study (i.e., E_{app} = -200 mV$_{SCE}$ in pH 12.5 NaOH, yielding 780 mV of anodic hydrogen overpotential at the exit surface). Similarly, dX is equated to the foil thickness, L. The sub-surface mobile or steady state steel lattice hydrogen concentration, C_H, may then be calculated from the expression

28

$$C_H = -\frac{J_{ss}L}{nFD} \qquad (30)$$

Embeddable Hydrogen Permeation Sensors

Embeddable hydrogen permeation sensors were obtained from the Force Institute in Denmark (model IHS-12). These devices function similarly to the Devanathan/Stachurski cell discussed previously, and are illustrated schematically in Figure 4.13. Each cell is a 10-mil (0.0254 cm) mild steel permeation window (compositionally similar to AISI/SAE 1010, as illustrated in Table 4.1) through which hydrogen may be absorbed on the external surface, diffuse through, and be oxidized on the internal surface. Each cell functions identically to the oxidation, or exit side of the Devanathan/Stachurski cell detailed, with the charging solution/cell represented by whatever environment the sensor is placed within. In this study, these sensors were embedded in concrete and the charging surfaced electrically connected to the reinforcing tendon. The hydrogen sensors, therefore, experienced the same level of CP as the prestressing steel. If hydrogen is produced, because of CP or corrosion coupled with cathodic reduction of water on the surface of the permeation membrane, and is, subsequently, absorbed into the membrane, it will diffuse to the exit surface and be oxidized. As a result, a current will be measured that is in turn proportional to the actual hydrogen permeation flux. From the measured flux densities, it is then possible to calculate the resultant steady state lattice hydrogen concentration within the permeation window, as detailed previously.

Of interest is the steady state steel lattice hydrogen concentration within the prestressing steel corresponding to a given flux density measured by the permeation sensors. In the case of the sensors used in this study, the permeation windows were constructed of a 99.6% Fe, mild steel (microstructurally, the sensor window was reported by the manufacturer to be composed of 10-μm, uniaxed ferrite grains; compositionally the sensor window was similar to AISI/SAE 1010, as shown in Table 4.1). Therefore, the observed permeation flux densities for the sensors must be converted into what the corresponding flux densities for a 1080 steel reinforcing strand under the same electrochemical conditions would be. To accomplish this conversion, the kinetics of the hydrogen evolution reaction on the sensor window and the prestressing tendon must be compared.

For iron in alkaline NaOH solutions (Bockris, 1965) and Ca(OH)$_2$ solutions (Lillard, 1996), the cathodic reaction rate (current density) for the HER is described by the coupled discharge-recombination mechanism. As such, the cathodic current density is defined by the expression

$$i_{cath} = i_0 \exp\left(\frac{-\alpha\eta F}{RT} \right) = k_r \theta^2 \qquad (31)$$

29

where i_{cath} is the cathodic current density, i_0 is the exchange current density for the hydrogen evolution reaction on the steel, α is the transfer coefficient, η is the overpotential, F is Faraday's constant, T is the temperature, k_r is the recombination rate constant for adsorbed hydrogen on the metal surface, and θ is the surface coverage of adsorbed hydrogen on the metal surface. The steady state steel lattice hydrogen concentration will also be a function of the adsorbed hydrogen surface coverage, and is defined as

$$C_H = \frac{k_{abs}}{k_{des}}\theta \tag{32}$$

where k_{abs} is the hydrogen absorption rate constant and k_{des} the hydrogen desorption rate constant at the steel surface. The permeation flux, as measured by the mild steel hydrogen sensors, is a direct function of this hydrogen concentration as well as the diffusivity of hydrogen in the sensor's metal foil under investigation, through the relationship

$$J_{ss} = \frac{nFD_{eff}C_H}{L} \tag{33}$$

where J_{ss} is the steady state permeation flux density and L the thickness of the permeation window. An expression that relates the permeation flux density to the cathodic water reduction reaction rate at the surface may be obtained by combining Equations 31, 32, and 33. This expression (Equation 34) predicts that the permeation flux density is a function of $(i_{cath})^{\frac{1}{2}}$ for the coupled discharge-recombination HER mechanism

$$J_{ss} = \frac{nFD_{eff}}{L}\left(\frac{k_{abs}}{k_{des}}\right)\left(\frac{i_0}{k_r}\right)^{\frac{1}{2}}\exp\left(\frac{-\alpha\eta F}{2RT}\right) = \frac{nFD_{eff}}{L}\left(\frac{k_{abs}}{k_{des}}\right)\left(\frac{i_{cath}}{k_r}\right)^{\frac{1}{2}} \tag{34}$$

As can be seen in Figure 4.14, the permeation flux density is indeed a function of the hydrogen reduction rate, i_{cath}, to the $\frac{1}{2}$ power over the range of current densities shown, where i_{cath} is defined in Equation 31. Figure 4.15 presents cathodic polarization scans performed on both 1080 steel and 99.5% iron samples in saturated, deaerated $Ca(OH)_2$. As can be seen in the figure, the cathodic kinetics of the hydrogen evolution reaction are similar for both materials. Relating this fact to the aforementioned expressions, one may conclude that both i_0 and α are similar for the two materials. Thus, if a comparison is made between the permeation fluxes that would be obtained at a given overpotential for each steel, the difference in the steady state permeation flux given by Equation 34 is related solely to differences in one or more of the factors in the following expression

$$\frac{J_{ss}L}{nF(i_{cath})^{\frac{1}{2}}} = D_{eff}\left(\frac{k_{abs}}{k_{des}}\right)\left(\frac{1}{k_r}\right)^{\frac{1}{2}} \tag{35}$$

Note that the left-hand side of the equation is composed of experimentally measurable quantities or constants, although the right-hand side is composed entirely of interfacial or bulk

material properties. As mentioned previously, the permeation window in the hydrogen sensors was constructed of rolled 99.6% Fe, mild steel foil (0.025 cm thick), compositionally (Table 4.1) and microstructurally (Figure 4.16) similar to commercially available cold worked 99.5% iron foils. As such, Devanathan/Stachurski hydrogen permeation measurements were performed on both 99.5% iron foils simulating the sensor windows (Lillard, 1996) and a cold rolled 1080 steel foil with a microstructure and composition equivalent to that of the reinforcing tendon. Figure 4.14 presents the steady state permeation flux as a function of the charging current density for 0.025 cm thick foils of both 99.5% iron and 1080 steel in saturated calcium hydroxide.[9] The two cases differ only in slope as related to the right-hand side of Equation 35. From Figure 4.14, it is possible to derive the following conversion relationship

$$J_{SS}^{1080 Steel} = 0.633 \cdot J_{SS}^{Sensor} \tag{36}$$

where $J_{SS}^{1080\ Steel}$ and J_{SS}^{Sensor} are the steady state permeation fluxes for 1080 steel and the hydrogen sensor (mild steel) and 0.633 is the ratio of the right-hand side of Equation 35 for the 1080 steel to that of the sensor. Comparing the known diffusivity of 1.2×10^{-6} cm^2/s for both the 99.5% iron (Lillard, 1996) and the permeation sensor window (99.6% Fe) to the diffusivity of 6.72×10^{-7} cm^2/s for the 1080 steel, we see that the factor describing ratio of the measured permeation fluxes (0.633) is due almost entirely to the differences in D_{eff}. That is to say that k_{abs}, k_{des}, and k_r do not appear to be appreciably different. Therefore, the relationship presented in Equation 36 may be used to calculate what an equivalent hydrogen permeation flux would be for the 1080 steel prestressing strand for a given hydrogen sensor reading.

The magnitude of the measured permeation fluxes was subject to the detection limits of the ZRA/hydrogen sensor setup. These experimentally determined detection limits were based on time-dependent variations in the data resulting from electrical noise and temperature-induced fluctuations. These fluctuations resulted in a minimum detectible flux and corresponding steady state steel lattice hydrogen concentration of 5.1×10^{-13} mol/cm^{2}s and 6.9×10^{-9} mol/cm^3, respectively, for piles 2 and 3.

Thermal Desorption Spectroscopy to Quantify Trapped Hydrogen Concentrations

Although hydrogen permeation experiments can give quantitative information on the mobile hydrogen concentration and effective diffusivity, it can only indirectly yield information on hydrogen trapping within the microstructure. As such, thermal desorption spectroscopy was used to assess hydrogen trapping and partitioning within the prestressing steel. A schematic of the system itself is presented in Figure 4.17.

---

[9] Permeation foils were verified to be bulk diffusion controlled and not surface limited.

Diffusion controlled egress of hydrogen from a plate containing a uniform initial steel lattice hydrogen concentration, C_H, and a thermal equilibrium hydrogen concentration, C_o, is described by the relation (Flynn, 1964)

$$\frac{\partial C_H}{\partial t} = -\alpha^2 D_{eff}(C_H - C_o) \tag{37}$$

where D_{eff} is the effective hydrogen diffusivity, α = a geometric factor (equal to $\pi/2d$ for an infinite plate of thickness d), and t = time.

If we consider the case of a single trap, C_H can be expressed as the sum of the lattice hydrogen concentration and the concentration of trapped hydrogen. In addition, in the presence of a trap site, the effective hydrogen diffusivity, D_{eff}, will be reduced relative to the hydrogen lattice diffusivity for a trap free matrix, $D_{lattice}$, according to the relation (Oriani, 1970)

$$D_{eff} = \frac{D_{lattice}}{\left(1 + \left(\frac{k_t}{k_d}\right)\left(\frac{N_T}{N_L}\right)\right)} \quad where \quad \frac{k_t}{k_d} = \frac{1}{\gamma}\exp\left(\frac{E_b}{KT}\right) \tag{38}$$

where k_t is the trapping rate constant, k_d the detrapping rate constant, N_T the concentration of trap sites, N_L the concentration of lattice sites, γ the ratio of frequency factors and entropy terms for trapping and detrapping, E_b is the trap binding energy, and T the temperature. This is illustrated schematically in Figure 4.18.

Combining these expressions, the desorption of hydrogen from a plate in the presence of a single trap is defined by the combination of the material parameters γ, E_b, N_T, N_L, $D_{lattice}$, in addition to the plate geometry and the temperature. Recalling that the lattice diffusivity may be expressed as

$$D_{eff} = D_o \exp\left(-\frac{E_m}{KT}\right) \tag{39}$$

we arrive at the relation (Ono, 1992)

$$\frac{\Delta C_H(t_n, t_{n-1})}{\Delta t_{n,n-1}} = C_H(t_n) - C_H(t_{n-1}) = \alpha^2 D_{eff}(t_{n-1})[C_H(t_{n-1}) - C_o(t_{n-1})] \tag{40}$$

From this expression, it is possible to calculate theoretical desorption spectra, where the desorption rate is defined by

32

$$\frac{\partial C_H}{\partial t} = -\left(\frac{\pi}{2d}\right)^2 D_o \exp\left(-\frac{E_m}{KT}\right)\left(\frac{1}{1+\frac{1}{\gamma}\left(\frac{N_T}{N_L}\right)\exp\left(\frac{E_b}{KT}\right)}\right)(C_H-C_o)$$

(41)

At this point, the sensitivity of the thermal desorption process to variations in the various material parameters may be evaluated, as presented in Figures 4.19 though 4.23. Unless otherwise noted in the figures, the parameters used to calculate the theoretical spectra were as follows: $d = 1$ mm, $D_o = 1.83 \times 10^{-8}$ m^2/s, $E_m = 0.189$ eV/atom, $\gamma = 1.25$, $E_B = 0.311$ eV/atom, $C_H{}^o = 200$ wt. ppb (200×10^{-9} g H/g sample), $\phi = 10$ °C/min, and $N_T/N_L = 1 \times 10^{-4}$ trap site/lattice site.

Figure 4.19 presents the effect of an increasingly large trap binding energy. It can be seen in the figure that as the binding energy becomes large, relative to the migration energy for lattice diffusion of hydrogen, the desorption peak associated with the trap site becomes sharper and shifts to higher temperatures. Similarly, if the migration energy for diffusion of hydrogen through the metal lattice is increased (Figure 4.20), becoming large relative to the binding energy of the trap site, the desorption peak associated with the trap site broadens and is shifted to higher temperatures.

Increasing the concentration of trapped hydrogen (i.e., increasing trap coverage, θ_T, assuming that the binding energy is not a strong function of θ_T), the size of the desorption peak associated with the trap site increases, but the temperatures and shape of the peak remain unaltered (Figure 4.21). If, on the other hand, the concentration of hydrogen trap sites (relative to the number of lattice hydrogen sites) is increased (i.e., increasing N_T/N_L), as illustrated in Figure 4.22, the peak shape becomes more gaussian (more regular than the typical asymmetric, double sigmoidal peak shape) and is shifted to higher temperatures.

Finally, if the thermal ramp rate (rate of change of the temperature during the acquisition of the TDS spectra) is increased (Figure 4.23), the peak is observed after shorter times (but higher temperatures) and is sharpened.

Several important pieces of information may be obtained from TDS spectra. The first, and most obvious, is the way with which trapped hydrogen is partitioned throughout the material under investigation. This can be accomplished by careful microstructural modification (adding and removing trap sites, although observing the effect on the spectra). Actual trapped hydrogen concentrations and corresponding coverages may be determined by integrating the area under a particular desorption peak combined with a knowledge of the relative density of that trap site. Finally, it is possible to determine the binding energy associated with each trap site, the calculation of which requires a more careful consideration of the desorption process itself. Detrapping and diffusion of hydrogen from a trap site within a metal matrix is a first order process described by the following reaction:

33

$$H_{trap} \overset{E_b}{\to} \square_{trap} + H_{lattice} \overset{E_m}{\to} H_{lattice} \overset{E_{des}}{\to} H_{ads} \qquad (42)$$
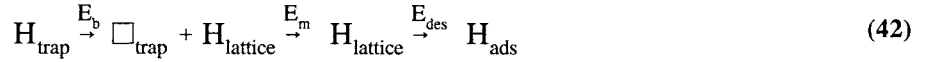
Surface recombinative desorption is a second order process, represented by the following reaction:

$$2H_{ads} \overset{E_{rec}}{\to} H_2 \text{ (gas)} \qquad (43)$$

The order of the controlling step (i.e., detrapping and diffusion (first order) or recombination (second order)) for the desorption process may also be obtained from the desorption spectra. In the case of a first order process, the desorption peak associated with a particular trap site should be a skewed gaussian shape (in particular, asymmetric double sigmoidal) and as the trapped hydrogen concentration increases, the position of the peak should not change (Woodruff, 1986). For a second order process, desorption peaks should be gaussian in shape and shift to lower temperatures as the trapped hydrogen concentration is increased (Woodruff, 1986). In the case of carbon steels, such as the 1080 steel investigated in this study, desorption is a first order process, as demonstrated in this (as will be illustrated) and other studies (Choo, 1982; Hong, 1983; Lee, 1982, 1984). The hydrogen detrapping and desorption rate from such processes can be represented through an Arrhenius expression

$$\frac{dx_d}{dt} = A(1-x_d)^n \exp\left(-\frac{E_a}{RT}\right) \qquad (44)$$

where n is the reaction order, E_a the activation energy for desorption (taken to be equivalent to $E_b + E_m$, since E_{des} and E_{rec} are observed to be small for iron and steel), E_b is the trap site binding energy, E_m the migration energy for lattice diffusion of hydrogen, and x_d is the fraction of hydrogen desorbed.

Differentiating the equation with respect to time, we obtain

$$\frac{d}{dt}\left(\frac{dx_d}{dt}\right) = \left(\frac{(E_m+E_b)\phi}{RT^2} - An(1-x_d)^{n-1}\exp\left(-\frac{(E_b+E_m)}{RT}\right)\right)\left(\frac{dx_d}{dt}\right) \qquad (45)$$

where ϕ is equivalent to dT/dt, the heating ramp rate.

If we then consider the time at which the desorption rate defined in Equation 44 is a maximum, the time derivative of the desorption rate (Equation 45) is equal to zero. As a result, the following expression is obtained

$$\frac{(E_b+E_m)\phi}{RT_{max}^2} = An(1-x_d)^{n-1}\exp\left(-\frac{(E_b+E_m)}{RT_{max}}\right) \qquad (46)$$

34

Since it has been demonstrated by Kissenger (1954) that at $T = T_{max}$, the product $n(1-x_d)^{n-1}$ is independent of the heating ramp rate, and approximately equal to unity for all n, Equation 46 may be further simplified to

$$\frac{\partial\left(\ln\left(\frac{\phi}{T_{max}^2}\right)\right)}{\partial\left(\frac{1}{T_{max}}\right)} = -\frac{(E_b + E_m)}{R} \qquad (47)$$

Thus, a plot of $\ln(\phi/T_{max}^2)$ vs. $1/T_{max}$ will be linear with a slope of $-(E_b + E_m)/R$. Combining the slope obtained in this manner with a previously determined E_m, the trap site binding energy, E_b, may be determined.

In this report, TDS will be used to quantify the trapped hydrogen concentration just as electrochemical permeation was used to quantify mobile hydrogen concentrations. Once completed, the overall hydrogen concentration may be expressed using the relation

$$C_{total} = C_{lattice} + \Sigma C_T^i = C_{lattice} + \Sigma \theta_T^i N_T^i \qquad (48)$$

where C_{total} is the total hydrogen concentration in terms of atoms hydrogen per unit volume of metal, $C_{lattice}$ is the mobile hydrogen concentration in terms of atoms hydrogen per unit volume of metal, C_T^i is the hydrogen concentration (i.e., number of hydrogen atoms) trapped at trap site i, and θ_T^i is hydrogen coverage of trap site i (ratio of occupied to unoccupied trap sites).

Taking the analysis one step further, the actual trap site coverage anticipated for a given mobile lattice hydrogen concentration may be calculated using the binding energies determined via the expression

$$\left(\frac{\theta_T}{1 - \theta_T}\right) = \left(\frac{\theta_L}{1 - \theta_L}\right) \exp\left(\frac{E_B}{RT}\right) \qquad (49)$$

where θ_L is the lattice hydrogen coverage.

Determining the Fracture Initiation Stress for Notched Tensile Bars

As no samples of failed tendon were available for study from the field, it was unclear what the appropriate flaw geometry would be for the prestressing steel tendon. In the event of localized corrosion (e.g., pitting, crevice corrosion), it would be anticipated that some sort of notch would be present, as discussed. However, it has also been suggested (Athanassiadis, 1981)

that fatigue cracks may be present within the reinforcement and that initiation of a hydrogen crack might occur at these sites. In this study, two different notch acuities were examined in addition to fatigue precracked samples. This was done technologically in an effort to cover the range of all possible defects. Mechanistically, this was done to assess if variation in the plastic zone size, and thus at risk material volume, influences the observed critical hydrogen concentration for embrittlement or fracture. In addition, these tests enabled an investigation of the effects of the level of stress concentration on the fracture mode/path, though admittedly, the latter two goals overlap.

CERT experiments were performed on notched tensile bars with an as machined (32 RMS) surface finish and plastic constraint factors (pcf) of 1.08 and 1.50 to define the local stresses and strains at crack initiation (Figures 4.24a and 4.24b). As a point of reference, the pcf for a sharp crack is 2.50 and for an unnotched sample, 0.33. These bars were machined from the center strand of the prestressing tendon. All samples were degreased ultrasonically in methanol and the dimensions documented prior to use. Several experiments were performed on uncharged notched as well as smooth tensile bars in air to establish the baseline tensile strength and plastic flow properties of the steel as discussed previously. CERT Testing was then performed at a series of applied cathodic potentials within saturated $Ca(OH)_2$, ASTM artificial ocean water, the buffered pH 4 and 6 environments, and the acidic H_2S containing environment. In addition, mortar covered CERT samples immersed in ASTM artificial ocean water were also evaluated. All solutions were deaerated prior to, and throughout the electrochemical charging and mechanical testing of each tensile bar. All samples were charged for 12 hours prior to testing, as well as throughout the CERT experiment. The precharge duration was selected to ensure a uniform steady state steel lattice hydrogen concentration throughout the bar (such that concentration at the center of the bar was at least 95% of that at the surface) prior to the initiation of the test assuming a conservative hydrogen diffusivity of 5×10^{-7} cm^2/s. In addition, although the CERT samples were being precharged as well as although the test was in progress, the solution was continuously recirculated via a peristaltic pump to maintain a constant surface pH. A schematic of the cell is presented in Figure 4.25. All tests were performed at a cross-head displacement rate of 1.71×10^{-8} m/s, a rate demonstrated to maximize the observed hydrogen embrittlement effects for prestressing strands by Hartt et al. (Toribio, 1991a, 1991b; Hartt, 1993).

Stress and strain distributions within the notched tensile bars were assessed via FEM analysis at various applied remote section stresses. ABAQUS™[10] was used to conduct an elastic-plastic analysis at various remotely applied loads from which the relevant local stress and strain distributions were obtained, using yield (σ_{YS} = 1696 MPa, E = 184.9 GPa) and flow property data from smooth tensile bars (i.e., true stress-true strain curve). A mesh containing 35 divisions along the notch root for the bluntly notched samples and 20 divisions for the sharper notch were used. Mesh sizes were selected such that further increases in resolution did not result in any change in the results.

---

[10] ABAQUS™ FEM Analysis Software, Hibbitt, Karlsson, & Sorenson, Inc., Pawtucket, Rhode Island.

From the finite element analysis, it was possible to obtain the local stress and strain distributions in front of the notch, in the plane normal to the notch root (see Figure 4.25). The maximum longitudinal stress as a function of distance from the notch root is presented in Figures 4.26 and 4.27 for the blunt and sharp notches, respectively. As can be seen in the figures, the region of elevated stress is much broader at a given remote applied stress for the blunt notch. In terms of the maximum longitudinal stress, a higher peak stress level was achieved for the sharp notch, but the radial dimension over which the stress was elevated was smaller, as illustrated in Figures 4.28. Moreover, the position of the maximum longitudinal stress was a greater distance from the notch root for the bluntly notched sample at a given remote stress, as shown in Figure 4.29. Figure 4.30 presents a comparison of the longitudinal stress for blunt and sharp notched samples at an equivalent remote applied stress, illustrating these points.

The maximum shear stress (Tresca, $\tau_{max}=(\tau_{max} - \tau_{min})/2$), τ_{zr}, where z is parallel with the tensile axis and r the radial direction, can also be determined and is presented in Figures 4.31 and 4.32 for the bluntly and sharply notched specimens, respectively. As can be seen in the figures, a higher shear stress is achieved at the specimen surface in the case of the sharply notched specimen, though the depth of the region where the shear stress is accentuated by the notch is smaller. Also, the larger degree of stress triaxiality produced by the sharp notch reduces the overall magnitude of the shear stress within the center of the bar. These effects are further demonstrated in Figure 4.33 that compares the distribution of the maximum shear stress at a remotely applied load of 806 MPa for the blunt and sharp notch.

The effective plastic strain, calculated through the relation

$$\varepsilon_{eff} = \frac{\sqrt{2}}{3}((\varepsilon_1 - \varepsilon_2)^2 + (\varepsilon_1 - \varepsilon_3)^2 + (\varepsilon_2 - \varepsilon_3)^2)^{\frac{1}{2}} \qquad (50)$$

where ε_i represent the principal strains, is plotted as a function of distance from the notch root for the blunt and sharp notches is presented in Figures 4.34 and 4.35, respectively. As can be seen in the figures, and is presented more clearly in Figure 4.36, the size (radial depth in from notch root) of the plastic zone in the plane of the notch is greater for the bluntly notched specimen at a given applied remote stress. As a result, assuming that crack initiation occurs at some microstructurally significant region within the plastic zone, the effective volume at risk is greater for the blunt notch than the sharp one. However, the magnitude of the effective strains achieved within the plastic zone at a given position is higher for the sharply notched specimens by a factor of nearly 3 for a given applied remote stress.

Determining Threshold Stress Intensity for Crack Initiation

Sample Design and Data Acquisition Procedures

Determining K_{IHE} was accomplished via experiments performed on fatigue precracked specimens. These experiments also served to assess the effect of further reducing the at-risk

volume by reducing the plastic zone size for a given applied remote stress and raising the local tensile stress to 3 to 5 times the yield strength. It also served to increase the range of flaw geometries for which the relationship between the critical fracture initiation behavior and steady state steel lattice hydrogen concentration could be assessed. Unfortunately, because of the geometry of the prestressing strand, machining of standard fracture mechanics specimens, such as a compact tension specimen, was not feasible. As a result, chord notched tensile bars, as illustrated in Figure 4.37, were used. The notches were electrically discharge machined (EDM) with a root radius of 4 mils (0.0102 cm).

Crack initiation and growth was monitored using a direct current potential drop (DCPD) system. Potential leads consisted of PTFE coated copper wires that were spot welded 5 to 10 mils (0.0127 to .0254 cm) from the center of the EDM notch. A current of 7.5 A was applied. The direction of the current was not switched, as the crack voltage appeared to be stable with time. Based on the long term stability of the crack voltage (Figure 4.38), subtraction of the thermal voltage by reversing the direction of DCPD current flow was deemed unnecessary. Potential measurement was conducted using a Measurements Group model 2314 signal conditioning amplifier in conjunction with a Metrabyte DAS-16 data acquisition board. Data were acquired at a rate of 1 point every other second using an amplification factor of 4000x to 6000x.

Each sample was fatigue precracked under load control using an Instron servo hydraulic system. A 10-Hz sinusoidal waveform with a peak to peak amplitude of 1 kip (4448 N) was applied. An initial offset of 50 lb (222 N) was used to prevent compression of the sample during precracking. Precracks were semicircular in nature with a depth of 0.5 mm at the crack center (corresponding to a 90 μV change in DCPD crack potential), as illustrated in Figure 4.39.

Crack initiation toughness was determined by monitoring the DCPD signal although applying progressively increasing load steps. The actual load step waveform is illustrated in Figure 4.40. The load was first ramped from a preload of 400 lb (1780 N) to an initial load of 500 lb (2224 N). The load was then progressively increased in 100-lb increments until crack initiation occurred. Each load increase was in the form of a ramp over 5 minutes. Each load was held for sufficient time to allow stress assisted, diffusive redistribution of hydrogen in front of the crack tip. If we consider a diffusive process, the average time for a hydrogen atom to diffuse a distance d may be expressed as

$$t = \frac{d^2}{\pi D} \tag{51}$$

where D is the diffusivity, and t the time. It was assumed that the hydrogen had to diffuse a distance equivalent to the position of the maximum hydrostatic stress in front of the sharp notch, or approximately 0.2 mm based on the FEM data reported. Using Equation 51 and the effective diffusivity of hydrogen in the prestressing steel of 6.72 x 10^{-7} cm^2/s determined, this results in an average time of 3 minutes, 10 seconds. As a result, each load was held for 30 minutes

38

(approximately 10 times the theoretical time required for hydrogen redistribution) after which it was increased to the next level.

Experiments were performed in a saturated $Ca(OH)_2$ environment, prepared as detailed, within the same cell as used for the CERT experiments. The solution was similarly stirred via a recirculation system. Experiments were conducted on uncharged specimens, as well as steady state steel lattice hydrogen concentrations of 5 x 10^{-7}, 2 x 10^{-6}, and 2 x 10^{-5} mol/cm^3 (0.064, 0.254, and 2.54 ppm, respectively). All hydrogen charged samples were precharged for 12 hours prior to testing, allowing the establishment of a uniform hydrogen concentration throughout the tensile bar. The same charging potential used to precharge the sample was then applied throughout the course of the tensile experiment. Thus, the electrochemical and environmental conditions were controlled such that (1) the applied potentials were highly cathodic in nature, and (2) the environment (saturated $Ca(OH)_2$) was buffered against substantial pH changes. In addition, it should be noted that the effective diffusivity for hydrogen in pearlitic steel is relatively fast when considering the duration of these experiments, allowing diffusive redistribution of the mobile hydrogen within the stress field in front of the crack tip in short times. The combination of the aforementioned conditions ensured that the hydrogen concentration in front of the notch was determined by the bulk hydrogen concentration, not enhanced or inhibited by charging at the crack tip.

Calculating the Threshold Stress Intensity

Although the EDM notched and precracked samples used in this study are nonstandard in nature from the standpoint of typical fracture mechanics type experiments (i.e., differ greatly from a compact tension or double cantilever beam specimen), they do more closely resemble cracking experienced in many actual engineering systems (e.g., aircraft systems, offshore oil drilling, piping systems [Forman, 1986]) and for this reason have seen widespread application. As a result, numerous researchers have attempted to develop solutions for the stress intensity for elliptical and straight fronted cracks within cylindrical tension samples. Typically, analyses are performed at two locations as illustrated in Figure 4.41, at the center of the crack (location A) and at the intersection of the edge of the crack front with the edge of the specimen (typically referred to as location B). FEM analyses (Caspers, 1986, 1987; Blackburn, 1976; Carpentieri, 1992; Athanassiadis, 1981; Levan, 1993; Si, 1990; Raju, 1986) are typically used to calculate the boundary correction factor used to address the nature of the crack. These relationships are of the general form (Si, 1990)

$$K_{IC} = \sigma_i F \sqrt{\pi a} \tag{52}$$

where σ_i is the remote applied stress, a the crack length, and F the boundary correction factor. For a semicircular crack front, the maximum stress intensity is achieved at location B, at the surface. As the shape of the crack front approaches that of the straight crack, the position of the maximum stress intensity moves in toward the center of the crack front (Location A).

39

Eventually, for a straight fronted crack, the stress intensity is roughly constant along the entire crack front.

Solutions developed for straight fronted cracks, by nature of the fact that the stress intensity is assumed to be constant along the crack front, are frequently more tractable mathematically than similar solutions for elliptical cracks. One such solution offered by Blackburn et al. (1976) based on an FEM model of a straight-fronted crack in a cylindrical body is

$$K_I = \frac{5(1-\nu^2)\sigma^2}{3E}\left[\frac{\pi}{32}D^3 - \frac{1}{16}D^3\sin^{-1}\left(1-\frac{2\ell}{D}\right) - \frac{1}{8}\left(1-\frac{2\ell}{D}\right)\ell^{\frac{1}{2}}(D-\ell)^{\frac{1}{2}}D - \frac{1}{3}\ell^{\frac{3}{2}}(D-\ell)^{\frac{3}{2}}\right] \qquad (53)$$

where σ is the remotely applied stress, ℓ is the maximum depth of the crack front (equal to the combined depth of the EDM notch and fatigue precrack), ν is Poisson's ratio, D is the overall diameter of the cylinder, and E the Young's modulus of the material.

Attempts to calculate solutions for the case of an elliptically shaped (sometimes called an almond shaped crack) are complicated by the need to account for the varying geometry of the crack front. As a result, tables are typically constructed of normalized K_I solutions for varying crack front geometries without offering a numerical solution, hindering their application to other systems. One solution, presented by Raju and Newman (1986) was calculated for an elliptically fronted crack via FEM of the general form

$$K_I = \left(\sigma_i\sqrt{\pi\frac{a}{Q}}\right)F \qquad (54)$$

where σ_i is the remotely applied stress, a is the maximum crack depth, Q is a shape factor accounting for the elliptical crack front, and F a boundary correction factor, again, accounting for the geometry of the crack front. Q is then expressed as a function of the crack length along the sample diameter (c) and the maximum crack depth (a) through the relationship

$$Q = 1+1.464\left(\frac{a}{c}\right)^{1.65} \qquad \text{for } \frac{a}{c} \leq 1 \qquad (55)$$

$$Q = 1+1.464\left(\frac{c}{a}\right)^{1.65} \qquad \text{for } \frac{a}{c} \geq 1 \qquad (56)$$

F, the boundary correction factor, was then calculated via FEM and tabulated for a series of differing elliptical geometries (Table 4.6). As such, application of this solution requires first characterizing the crack front geometry, and then extrapolating an appropriate F factor from the tabulated values for a similar geometry. It is this latter solution that will be used in this study.

40

Once the stress intensity at failure is calculated, it must be determined if the resulting stress intensity is, in fact, a valid determination of K_{IC} or K_{IEAC}. In order for this to be true, the size of the plastic zone in front of the fatigue precrack upon crack initiation must be small relative to the size of the advancing crack, a, and the thickness of the tensile specimen, t. Quantitatively (from ASTM E399 and ASTM E1681), this can be expressed as

$$t \text{ and } a \geq 2.5 \left(\frac{K_{Applied}}{\sigma_{YS}} \right)^2 \tag{57}$$

In the case of typical fracture mechanics specimens (e.g., compact tension, double cantilever beam, wedge opening load, etc.) the crack length is readily measured. For round tensile specimens with a semicircular crack, calculation is somewhat less clear, and in this study will be assumed to be equivalent to the maximum depth of the crack (point A in Figure 4.41). Based upon this assumption, for a typical crack length (for this study) of 1.7 mm, $K_{Applied}$ must be less than or equal to 45 MPa$\sqrt{m}$ to be a valid determination of K_{IC} or K_{IHE}. For applied stress intensities in excess of this value, $K_{Applied}$ is equivalent to K_Q and is not a valid determination of K_{IC} or K_{IHE}. Thus, based upon literature values for K_{IC} of prestressing tendon (Table 4.2) it will not be possible to obtain a valid K_{IC} in the uncharged case. However, considering the microstructure of the prestressing tendon (i.e., alternating lamellae of ferrite and cementite), the deforming phase (i.e., ferrite) is observed to be highly constrained by the cementite lamellae, behaving much like a metal matrix composite. As such, it is anticipated that there will be little, if any, difference is the obtained stress intensity as a function of the level of constraint determined by the geometry of the test specimen (i.e., a much higher level of constraint in imposed by the microstructure than could be achieved by specimen geometry). As such, the determined K_{IC} should be relatively insensitive to specimen thickness (i.e., Equation 57 is not strictly applicable) as has been found for metal matrix composites (Somerday, 1994). Thus, valid (though nonstandard) K_{IC} results may be achieved for values of K_Q as high as 90 MPa$\sqrt{m}$.

Simulated Occluded Geometries and Crevice Corrosion

It has been demonstrated in the literature that corrosion initiation of the steel reinforcing tendon within a prestressed concrete structure occurs at the many occluded geometries along the reinforcement (Gonzalez, 1993; Otero, 1990). Since prestressing steel strand is typically a seven-wire, braided strand, there are many intrinsic steel/steel occluded cells formed along the length of each reinforcing tendon. In addition, whenever the aggregate present within the concrete comes into contact with the braided strand, an occluded cell is formed.

As discussed, it is reasonable to expect that the local environment (i.e., Cl^- concentration, O_2 concentration, and pH) within a marine bridge pile is a function of vertical position. In order to quantify the local acidity and Cl^- content that may be present within a laboratory-scale pile, a

41

series of simulated steel/concrete interface experiments was conducted to observe changes in the local pH upon the initiation of corrosion and subsequent ferrous ion hydrolysis.

The first such experiment was performed to investigate the pH levels that would be achieved in a simulated concrete pore solution as the ferrous ion concentration was increased, presumably because of corrosion. This was first investigated through the conduction of a titration experiment. In this test, ferrous ions (via an 0.2 M $FeCl_2$ solution) were gradually titrated into a saturated calcium hydroxide solution although simultaneously monitoring the pH.

In order to examine if similar behavior could be achieved within a crevice, an occluded-cell geometry (Brown, 1971; Pourbaix, 1971) formed by inserting a glass pH electrode (diameter of 2.10 mm) into a hole (No. 43 drill bit, hole diameter approximately 2.37 mm) drilled in a block of SAE/AISI 1080 steel (see Figure 4.42) immersed in a chloride-contaminated, pore solution analog. The bulk environment in which the pH electrode and steel block assembly was immersed consisted of saturated $Ca(OH)_2$ with the addition of 0.5 M NaCl. Access of the crevice to the external solution occurred along the gap between the pH electrode and the drilled steel. The bulk solution was exposed to air throughout the experimentation. Testing was performed at applied anodic potentials of -300, -400, -500, -550, and -600 mV_{SCE}. In each case, the pH as a function of time within the occluded cell geometry was measured. Additional tests were performed with an experimental setup that allowed simultaneous monitoring of the corrosion current in addition to the pH of the occluded environment. A potentiostat[11] compatible with a grounded working electrode was used, eliminating cross-talk and ground loop problems.

When CP is applied to a concrete structure, it is reasonable to expect that the observed potential will become increasingly negative with time. This potential shift is a consequence of the depletion of the initial concentration of dissolved oxygen within the pore solution by the CP current, combined with the slow rate of its replenishment via diffusion from the external environment. In order to examine this effect, a single strand of prestressing tendon with a 1.25 cm coverage of mortar was cathodically polarized galvanostatically although immersed in ASTM artificial ocean water. The ASTM ocean water was ambiently aerated (i.e., the solution was atmospherically exposed) during the course of the experiment, and the resultant local applied potential was monitored.

Laboratory-scale Piles

A series of laboratory-scale piles was constructed in order to establish positional variations in the local environment at the steel/concrete interface as well as the local applied level of CP along the reinforcement. In addition, the laboratory-scale piles, in combination with mechanical testing and Devanathan/Stachurski permeation experiments, enabled determination of when a critical combination of stress and lattice hydrogen concentration existed at some point along the tendon such that embrittlement had occurred. Each of the laboratory-scale piles was

---

[11] EG&G PAR model 253 (Versastat) in "float" mode.

constructed using a Virginia Department of Transportation standard A-5 concrete mix design (Virginia Department of Transportation, 1991) (see Table 4.7) using type-III portland cement to which a quantity of Cl^- 200% greater than the threshold concentration for corrosion initiation had been added (0.033 wt% Cl^- or 1.26 kg Cl^-/m^3 of concrete). Cl^- was added as NaCl to the mix water prior to mixing the concrete. After casting (with the segments of reinforcement unstressed), the concrete piles were allowed to cure for 28 days under controlled environmental conditions (97 ± 3% relative humidity, 22.7 ± 1.67 °C) after which it was allowed to dry for 1 day. The top, base, and two of the four vertical sides of each pile were coated with a marine masking epoxy.[12] As a result, the tendon within the pile simulates a corner strand within an actual pile, maintaining a 5.1 cm coverage of concrete over the reinforcement on all environmentally-exposed sides. These piles were instrumented with pH sensors, reference electrodes, and hydrogen sensors, all of which were monitored throughout the course of each experiment. The embedded pH sensor assembly consisted of a solid state, field effect transistor (FET) pH electrode (5.20 mm diameter) that was placed within a steel occluded cell geometry formed by drilling a hole (5.40 mm diameter) within a piece of undrawn prestressing steel tendon (average crevice gap of 0.10 mm) to simulate the occluded cell geometries present along an actual prestressing tendon, as illustrated in Figure 4.43. This occluded cell was then filled with pore solution and provided an instrumented simulation of the occluded geometries present along an actual prestressing tendon. The reference electrodes were standard, commercially available, embeddable MnO_2 (+140 to +160 mV vs. SCE) electrodes. MnO_2 reference electrodes were selected based on their documented durability and long term stability when embedded in concrete (Williams, 1995; Arup, 1997). By embedding the reference electrodes, IR drop through the concrete was minimized, allowing true current-on potentials to be monitored and compared to the -780 and -900 mV_{SCE} criteria. Finally, each hydrogen sensor consisted of a commercially available, self-contained Devanathan/Stachurski cell using an 0.025-cm-thick, mild steel (0.023% C, 0.19% Mn, 0.012% S, plus other minor constituents with the balance being Fe as presented in Table 4.1) permeation window, functioning as discussed in the preceding section and elsewhere (Devanathan, 1962, 1964). The charging surfaces of the hydrogen sensors were electrically connected to the prestressing tendon such that both the strand and the hydrogen sensors would experience the same hydrogen overpotential, and corresponding cathodic reaction rate, at any given time. These hydrogen sensors, when combined with an appropriate calibration relationship as detailed, enable the determination of the mobile hydrogen concentration within the prestressing steel.

Each of the three piles discussed consisted of a continuous segment of prestressing tendon along with a combination of the sensors discussed. The top, base, and two of the four vertical sides of each pile were coated with a marine masking epoxy, as mentioned. Each pile was then partially immersed in aerated ASTM artificial ocean water. Two of the piles were outfitted with a skirt anode made of platinized titanium mesh placed in the splash zone, extending 8.9 cm below and 16.5 cm above the waterline. The anode was held in place using wooden planks. A layer of sponge was placed between the wooden planks and the concrete,

---

[12] Interlux marine masking epoxy, Courtaulds Coatings, Inc., Union, NJ 07083.

ensuring the presence of an ionic path between the anode and the concrete. Figure 4.44 (pile 1), Figure 4.45 (pile 2), and Figure 4.46 (pile 3) present schematics of the three pile designs used in this study.

As can be seen in each of the figures, sensor arrays were placed within three discreet regions. These regions, denoted as the submerged, splash, and atmospheric zones were selected based on work conducted by Hartt et al. (Hartt, 1994; Pangrazzi, 1994; Chaix, 1995). Hartt found that the reinforcement experienced considerably different conditions in the submerged zone below the waterline to the splash zone just above the waterline compared to the atmospheric zone far above the waterline, as discussed.

After curing for 28 days as discussed, pile 1 (Figure 4.44) was partially immersed in ASTM ocean water and monitored. The pH electrode was located 30.5 cm above the waterline. A similar procedure was followed for pile 2 (Figure 4.45). In this case, after coating and immersing in ASTM artificial ocean water, the pile was allowed to stabilize for two weeks, after which a series of potentiostatic and galvanostatic polarizations were applied, each for a period of 2 weeks. Upon completion of each polarization, the CP level was immediately stepped to the next higher level. Finally, pile 3 (Figure 4.46) was allowed to stabilize although partially immersed in ASTM artificial ocean water for 120 days. Once stabilized, impressed current CP was applied. Each current density was applied for up to 48 days to ensure that the pile stabilized at each current density. After stabilization, the pile was allowed to depolarize for three days to establish whether the 100 mV depolarization criterion could be met after both a 4-hour as well as a longer term depolarization. The next current density was applied after this stabilization period. Reported applied cathodic current densities will be presented in terms of the current per unit area of reinforcement within each of the laboratory-scale piles discussed.

Comparing piles 2 and 3, as will be done, requires an understanding of the subtle differences between the two piles and the CP applied to each pile. Both piles were constructed using an identical concrete mix design, had the same degree of concrete cover over the reinforcement, and contained segments of reinforcing strand taken from the same source. As is clearly seen when comparing pile 2 (Figure 4.45) and pile 3 (Figure 4.46), pile 3 is much greater in height. Consequently, larger total cathodic currents must be applied to achieve the same average cathodic current density on the reinforcement. As a result, the local current density at a fixed position relative to the waterline may be greater in pile 3 than pile 2 for a given average cathodic current density. Note that this would not be the case if the local applied current densities were extremely uniform, which is unlikely as detailed. In addition, the longer stabilization times allowed for pile 3 resulted in lower internal current-on potentials as a function of position at a given applied CP level because of the complete stabilization of the pile (after oxygen depletion, etc.). The difference is accentuated at low cathodic current densities where stabilization of the pile occurred more slowly, and as such was not achieved at low applied current densities for pile 2 in 2 weeks.

RESULTS AND DISCUSSION

Understanding the Cathodic Reaction Kinetics on Iron and Steel within Simulated Pore Solutions

To determine the effects of CP of steel within various solutions, basic cathodic reaction kinetics must be understood. This is particularly true in the case of this research, where the kinetics not only of the hydrogen evolution reaction must be understood, but also the absorption efficiency of hydrogen into the steel lattice. In the literature, it has been demonstrated that hydrogen absorption is enhanced within alkaline solutions similar to those investigated in this study. For example, Flis and Zakroczymski (1992) demonstrated that hydrogen absorption was enhanced at low overpotentials in both neutral and alkaline sodium hydroxide, carbonate/bicarbonate, phosphate, and acetate solutions. They theorized that the enhanced absorption was the result of an activation of the metal surface because of enhanced oxide dissolution within these environments.

Isecke and Mietz (1993) also performed a series of hydrogen permeation experiments in solutions containing calcium hydroxide, calcium hydroxide + sodium chloride, sodium carbonate/bicarbonate, as well as within solutions containing a suspension of cement. They found that hydrogen permeation was further enhanced in the cement and chloride-contaminated calcium hydroxide solutions over that of the sodium carbonate/bicarbonate solution. No effort was made to determine the mechanism behind this increased absorption.

In light of this information, it has been suggested that $Ca^{(II)}$, in the form of $Ca(OH)_2$, is a recombination poison for hydrogen absorption into iron (Lillard, 1996). To verify this claim,t the basic cathodic electrochemistry of the steel/$Ca(OH)_2$ system must be understood. Potentiodynamic scans were used to establish the basic cathodic kinetics of the prestressing tendon within $Ca(OH)_2$ and other pore solution analogs to better understand these kinetics and to establish if there were any differences between the steel and the hydrogen permeation sensors in terms of their cathodic behavior.

Potentiodynamic Polarization of Iron and Steel in Pore Solution Analogs

Figure 4.15 presents potentiodynamic scans performed on the 99.5% iron and the 1080 steel used in the prestressing strand in an 0.025 M, saturated $Ca(OH)_2$ solution. As can be seen in the figure, increased cathodic polarization results in the achievement of a diffusionally limited oxygen reduction current density until a potential is achieved that is sufficiently negative for the water reduction reaction to take place. In the water reduction region, it can be seen that the two materials behave essentially identically.

Polarization scans performed in saturated $Ca(OH)_2$ + 0.3 M NaCl are presented in Figure 5.1. Again, increasing cathodic polarization results in the achievement of a diffusionally limited

45

current density until a sufficiently negative potential is achieved at which point water reduction begins. As with the chloride-free environment, it again can be seen that the 1080 steel and the 99.5% iron behave nominally identically. Moreover, comparison of the chloride free to the chloride-contaminated environments illustrates that chloride, in and of itself, does not alter the kinetics of the hydrogen evolution reaction.

Polarization scans performed in pH 12.5, 0.1 M NaOH are presented in Figure 5.2. Again, increasing cathodic polarization results in the achievement of a diffusionally limited oxygen reduction current density until a sufficiently negative potential is achieved at which point water reduction begins. As with the chloride free environment, it again can be seen that the 1080 steel and the 99.5% iron behave nominally identically.

Finally, a summary of all the polarization scans performed on the 1080 steel are presented in Figure 5.3. As can be seen in the figure, all of the alkaline NaOH and $Ca(OH)_2$ containing environments perform similarly at large negative potentials where the HER is the dominant mechanism. ASTM ocean water, a buffered, high chloride, pH 8.2 environment, did behave differently, as illustrated in the figure.

Based on the polarization scans, no information is provided regarding why hydrogen absorption would be enhanced within a $Ca(OH)_2$ containing environment. However, consideration of the nature of a $Ca(OH)_2$ solution reveals that a polarization scan within a stagnant cell may not be sufficient to reveal differences in the cathodic reaction kinetics, as the surface pH, and as such the true applied overpotential, is not well defined. In terms of the concentration of dissolved $Ca(OH)_2$ that can be achieved at room temperature, we find that $Ca(OH)_2$ is only sparingly soluble in alkaline water at room temperature (solubility of approximately 25 mM at pH 12.6), with the solubility decreasing dramatically with increased pH, in accordance with the following solubility relationship (Pourbaix, 1974)

$$Log[Ca^{2+}] = 22.91 - 2pH \qquad (58)$$

where the concentration of Ca^{2+} is in moles/liter. In a system where a cathodic current is applied, the local pH at the metal surface will be increased because of hydroxyl production. As a result, if a saturated solution, such as the pore solution analog often used within the literature as well as this study, is used as the electrolyte, $Ca(OH)_2$ precipitation will take place at the metal surface. The result of this precipitation is a thin adherent layer of $Ca(OH)_2$. In order to assess if the precipitation of $Ca(OH)_2$ had an effect on the cathodic hydrogen evolution kinetics, rotating disk electrode experiments were conducted, allowing the surface pH to be quantified and controlled.

Controlling the Diffusive Boundary Layer Thickness with an RDE

E-log(i) curves were experimentally determined and corrected for both pH and IR voltage error, allowing true cathodic η vs. Log(i) plots to be constructed, as discussed. Through this

46

technique, a series of different environments may be compared on a common, true hydrogen overpotential scale. Figure 5.4 presents RDE experiments performed using a 99.9% Fe electrode in saturated $Ca(OH)_2$ at pH 12.6, 25 mM $Ca(OH)_2$ at pH 9.2 (previously saturated at pH 12.6, filtered, then pH adjusted to 9.2 with HCl), and NaOH at pH 12.5. Also shown in the figure are the calculated surface pH's for each environment at each applied cathodic current density. Two important pieces of information may be acquired from the figure. First, it is clear that precipitation of a $Ca(OH)_2$ film does not result in a significant alteration in the cathodic kinetics. Second, the cathodic kinetics within the three alkaline environments investigated are, indeed, nominally identical. In other words, within experimental error, for a given true applied hydrogen overpotential, the hydrogen production rate is similar for each of the environments investigated, even though the hydrogen absorption rate (and thus the steady state steel lattice hydrogen concentration achieved) may differ.

Hydrogen Production and Absorption Kinetics for Fully Pearlitic 1080 Steel

Devanathan/Stachurski permeation experiments were performed on SAE/AISI 1080 steel foils within environments identical to those used for CERT testing. Each environment and its justification for use as a pore solution analog is presented in Table 5.1.

Representative rise and decay transients for a 14 mil (0.036 cm) 1080 steel foil are presented in Figure 5.5. Each transient was analyzed as outlined in the experimental methodology section, calculating the effective diffusivity and steady state steel lattice hydrogen concentration for each applied cathodic current density using the method of McBreen, Nanis, and Beck, as illustrated in Figure 4.10, and Fick's first law, presented in Equation 33, respectively.

The steady state steel lattice hydrogen concentrations, calculated using Equation 33, as a function of applied cathodic potential or overpotential are presented in Figures 5.6 through 5.9. As is clearly illustrated, in cases where the pH of the environment is below that of saturated calcium hydroxide (i.e., pH < 12.5), hydrogen permeation was observed at potentials considerably more positive (e.g., Figure 5.9) than the -900 mV_{SCE} threshold potential for embrittlement proposed in the literature for $Ca(OH)_2$+HCl solutions of similar pH (Hartt, 1993). Moreover, Figures 5.6 through 5.9 indicate that steady state steel lattice hydrogen concentrations comparable to those achieved at applied potentials more negative than -980 mV_{SCE} in saturated $Ca(OH)_2$ where hydrogen embrittlement was observed (Hartt, 1994; Pangrazzi, 1994) are possible at more positive potentials in other relevant environments. For example, consider a hydrogen concentration of 5 x 10^{-7} mol/cm^3, which will be revealed as an embrittling concentration, and compare it to the permeation results. As can be seen in Figure 5.10, this embrittling steady state steel lattice hydrogen concentration is achieved at an applied potential of -1.007 V_{SCE} in saturated $Ca(OH)_2$, and would be accounted for (i.e., identified as an embrittling potential) by Hartt's absolute potential criterion. Note that this concentration is achieved at a very low cathodic current density of approximately 1.0 $\mu A/cm^2$. However, this same concentration is achieved at an applied potential of -0.876 V_{SCE} in ASTM artificial ocean water,

and an applied potential of -0.710 V_{SCE} in the pH 6 buffered environment, albeit at a higher applied cathodic current density, neither of which would be anticipated as being embrittling based on Hartt's criterion. From the permeation results for each environment, it is possible to calculate a relationship expressing the steady state steel lattice hydrogen concentration that would be achieved for a given applied potential. By correcting the applied potential to address the changes that will occur in the pH at the surface, it is possible to calculate the true applied overpotential, allowing the construction of applied overpotential vs. C_H plots. Using such relationships, it is possible to determine hydrogen concentrations for lower applied potentials, approaching the reversible electrode potential, where permeation fluxes were below the detection limits of the instrumentation. These relationships, here in the form of linear regressions, are given in terms of cathodic overpotential, η, in V, as follows (where C_H is in mol H/cm^3):

for saturated $Ca(OH)_2$

$$\log(C_H) = -6.50 - 6.94 \ \eta_{Applied} \tag{59}$$

for mortar-covered samples immersed in ASTM ocean water[13]

$$\log(C_H) = -8.27 - 2.13 \ E_{Applied} \tag{60}$$

for ASTM artificial ocean water

$$\log(C_H) = -6.75 - 2.98 \ \eta_{Applied} \tag{61}$$

and for the pH 6, buffered environment

$$\log(C_H) = -6.32 - 1.42 \ \eta_{Applied} \tag{62}$$

The results clearly indicate that C_H increases more strongly as a function of $\eta_{applied}$ in $Ca(OH)_2$. The next environment more favorable toward hydrogen uptake is mortar cover, followed by ASTM artificial ocean water. This is also indicated in Figure 5.11, illustrating the steady state permeation flux density, J_{ss}, as a function of the surface and IR corrected true $\eta_{applied}$ for each of the aforementioned environments. It can be seen in the figure that for a given hydrogen overpotential (corresponding to a thermodynamic driving force) a larger J_{ss}, and consequently a larger C_H, is achieved in saturated $Ca(OH)_2$, followed by ASTM artificial ocean water, and the pH 6 environment.

---

[13] The expression derived for the mortar-covered samples is in terms of the applied potential rather than overpotential as in the other relations. This is because of the fact that the surface pH could not be accurately monitored or maintained at the steel/mortar interface. As a result, it is likely that the surface pH increased with increasing applied cathodic current density. Since the overpotential is a direct function of the pH, its calculation was not possible.

Hydrogen Partitioning Within the Prestressing Steel as a Function of the Uniform Lattice Concentration

Thermal desorption spectroscopy (TDS) experiments were performed to quantify the nature of the trapped hydrogen concentration within the prestressing steel in terms of its partitioning between various trap sites. Prior to performing each TDS experiment, sufficient time was allowed for the lattice hydrogen to completely diffuse out of the sample. As such, each peak observed within a TDS spectra corresponds to a specific trap site within the steel, and not lattice hydrogen still present within the metal matrix. Figure 5.12 presents the desorption spectra for samples charged to a series of uniform steel lattice hydrogen concentrations, bracketing those that will later be used for mechanical testing. As can be seen in the figure, there are at least three distinct trapping sites within the prestressing tendon. Identification of these trap sites requires quantification of the binding energy associated with each peak.

Figure 5.13 presents TDS spectra for a sample charged to a uniform lattice hydrogen concentration of 2×10^{-5} mol H/cm^3 and temperature programmed desorption at ramp rates of 2.5, 5, 7.5, and 10 °C/min. By performing a peak fit to each of the peaks within the spectra in this Figure, it is possible to determine the temperature of the maximum desorption rate for each of the trap sites and their associated desorption peak. This data can then be plotted as discussed and presented in Figure 5.14. The slope of the line defined by each curve in Figure 5.14 is equivalent to the E_a/R where E_a is the activation energy for desorption (equivalent to the sum of E_m and E_b) and R is the gas constant. The results from such an analysis are presented in Table 5.2. Note that a greater temperature of maximum desorption corresponds to a greater trap site binding energy. Comparing this information to the desorption spectra, in particular to Figure 5.12, it can be seen that the stronger trap sites (i.e., higher binding energy) tend to retain more hydrogen, even in the as received, uncharged case. Also listed in the table is the likely identification of each trap site, based on literature data presented in Table 5.3.

Using the binding energies determined, it is then possible, through Equation 49, to calculate the anticipated coverage of each trap site for a given steady state steel lattice hydrogen concentration. Figure 5.14b presents the trap coverage for each of the trap sites present within the prestressing tendon as a function of the lattice coverage. As can be seen in the figure, the trap site coverage for Fe/Fe_3C interfaces[14] increases from 0.0005 at a lattice concentration of 5×10^{-7} mol/cm^3 to 0.022 at a lattice coverage of 2×10^{-5} mol/cm^3. The coverage of dislocations similarly increases with increasing lattice hydrogen concentration, increasing from 0.002 to

---

[14] Although the lowest energy site has been tentatively identified as Fe/Fe_3C interfaces from the literature, it is not clear whether the hydrogen is trapped at the interface or within the cementite at individual carbon atoms. Considering a lattice hydrogen concentration of 2×10^{-5} mol/cm^3, the coverage of the Fe/Fe_3C trap site is found to be 0.02. Based upon this coverage, if one hydrogen atom were trapped at each carbon atom within the cementite, there should be 1.024×10^{-4} mol H/cm^3 Fe. However, from the TDS spectra 5.885×10^{-7} mol H/cm^3 Fe are found at this trap site. As such, it is reasonable to assume that hydrogen is in fact trapped at the interface, and not within the cementite lamellae.

0.083 over the same range of concentrations. The coverage of the strongest trap site, corresponding to microvoids, increases from 0.022 to 0.508 over the same range of lattice compositions.

In addition to the relative partitioning of the trapped hydrogen for a given steel lattice hydrogen concentration, it is also important to define how the concentration at a given trap site changes with varying steady state steel lattice hydrogen concentration. Such information can later be related to the mechanical behavior of the reinforcement. The low temperature and high temperature peaks correspond to hydrogen trapped at α-Fe/Fe$_3$C interfaces and microvoids, respectively, based upon comparison of the activation energy for desorption to values within the literature, as shown in Table 5.2. The medium temperature peak corresponds to dislocations. From the desorption spectra presented in Figure 5.13, it can be seen that the trapped hydrogen concentration at α-Fe/Fe$_3$C interfaces and microvoids increases with increasing lattice hydrogen concentration.

Hydrogen Embrittlement of the Drawn, Pearlitic Wire Used as Prestressing Steel

This section addresses relationships between the fracture initiation stress (σ_F) and stress intensity (K_{IHE}) and the steady state steel lattice hydrogen concentration, C_H. Doing so involves not only the determination of the actual remotely applied and local stress or strain at crack initiation for a given overpotential in each environment, but also quantification of the corresponding steady state steel lattice hydrogen concentration for each cathodic overpotential. This quantification of the corresponding steady state steel lattice hydrogen concentration is possible using the relationships presented in Equations 59 to 62.

Crack Initiation From a Notch Simulating a Physical Defect Along the Prestressing Strand

In order to determine the critical concentration of hydrogen required for embrittlement, it is essential that the relationship between the locally applied stress (in front of a notch or crack) required for initiation as a function of hydrogen concentration be defined. In this study, this issue was addressed by performing mechanical testing on a series of both notched and precracked specimens as a function of hydrogen concentration. As a result, two notch geometries (plastic constraint factors of 1.08 and 1.27), in addition to a fatigue pre cracked sample, were investigated in this study. These samples were evaluated uncharged in lab air as well as at a series of steady state steel lattice hydrogen concentrations achieved via cathodic polarization in relevant environments.

A number of CERT experiments were also performed on doubly notched tensile specimens (using both notch acuities). In these experiments, as well as in experiments where the test was halted close to, but preceding, failure of the tensile bar, it was hoped that the point of crack initiation would be determined. However, serial sectioning of all of the aforementioned

50

samples failed to reveal any subcritical cracking beneath the notch. This is likely the result of the fine pearlitic microstructure of the prestressing strand. A similar result was achieved by Kavishe and Baker (1986) using notched bend bars. Although documentation of subcritical cracking beneath the notch in coarse pearlitic microstructures was enabled, microstructures with an increasingly fine interlamellar spacing did not exhibit any subcritical cracking beneath the notch root.

Fracture Initiation from a Bluntly Notched Tensile Bar

Bluntly notched tensile bars (plastic constraint factor or 1.08, pictured in Figure 4.24a) were evaluated in a series of relevant environments, as detailed. These tests were performed to assess not only the fracture initiation stress of the reinforcement as a function of steady state steel lattice hydrogen concentration, but also to assess if there were any effects of environment discrete from the hydrogen effect. As such, CERT experiments were performed at various applied cathodic potentials within the environments detailed in Table 5.1. The results of these tests, in terms of the fracture stress as a function of the applied potential, are presented in Figures 5.15 through 5.18. It can be seen in the figures that a lower remote stress (and corresponding maximum longitudinal stress) is required for fracture initiation as the applied potential becomes increasingly negative below the reversible potential for the hydrogen evolution reaction in each environment. These potentials were then converted into equivalent steady state steel lattice hydrogen concentrations through relationships defined between the applied hydrogen overpotential and the resultant steady state steel lattice hydrogen concentration by the Devanathan/Stachurski permeation experiments (Equations 59 through 62). Once each tensile test was performed, information such as the maximum longitudinal stress and the depth of the plastic zone at failure was calculated via FEM calculations detailed.

Figure 5.19 presents a summary of the applied remote stress and corresponding maximum longitudinal stress as a function of the steady state steel lattice hydrogen concentration for CERT experiments conducted in each of the environments listed in Table 5.1. The threshold hydrogen concentration, C_0, required to produce embrittlement can also be obtained from the plot, and is found to be approximately 2×10^{-7} mol/cm^3 (0.0254 wt ppm). An empirical relationship of the general form

$$\sigma_F \ (MPa) \ = \ \sigma_0 - \alpha Log\left(\frac{C_H}{C_0}\right) \tag{63}$$

may also be derived from the data and is found to be

$$\sigma_F \ (MPa) \ = \ 2599 \ \pm \ 155 \ - \ 231.5 Log\left(\frac{C_H}{2x10^{-7}}\right) \tag{64}$$

51

Since all data fit within this band, it is clear that the degree of embrittlement of the prestressing tendon for a given hydrogen concentration is a function only of $\log(C_H)$, and is independent of the environment in which the test was performed. Other researchers have arrived at similar conclusions for hydrogen embrittled steels (Gangloff, 1986; Yamakawa, 1984). This independence from external environment gives the experimentalist the freedom to utilize experiments in one environment to predict behavior in another environment, provided that the steady state steel lattice hydrogen concentration is known in the second environment.

Figures 5.20a and b present the radial depth of the plastic zone at the maximum applied load (initiation conditions) and the position of the maximum hydrostatic tension as a function of the steady state steel lattice hydrogen concentration for the bluntly notched tensile bars. Similar relationships to Equation 63 may also be derived to express both the achieved plastic zone size at failure, r_p, and the depth of the maximum hydrostatic tension as a function of the steady state steel lattice hydrogen concentration. As is indicated in the figure, these relationships are found to be

$$r_p \; (mm) \; = \; 0.491 \; - \; 0.133 Log\left(\frac{C_H}{2.0x10^{-7}} \right) \tag{65}$$

where r_p is the radial depth of the plastic zone in mm, and C_H the steady state steel lattice

$$Depth \; of \; Hydrostatic \; (mm) \; = \; 0.328 \; - \; 0.085 Log\left(\frac{C_H}{2.00x10^{-7}} \right) \tag{66}$$

hydrogen concentration in mols/cm^3. Even at the highest hydrogen concentrations, which resulted in the lowest breaking loads, the steel experienced plastic deformation near the notch root. The size of the plastic zone (as well as the corresponding position of maximum longitudinal and hydrostatic stress) was large relative to the pearlite colony size and inclusion spacing reported, as indicated in Figure 5.20.

Fracture Initiation from a Sharply Notched Tensile Bar

The sharply notched tensile bars were all tested in saturated $Ca(OH)_2$ since the embrittlement of the prestressing steel was demonstrated to be independent of the environment in which the test was performed. The fracture initiation stress as a function of the steady state steel lattice hydrogen concentration is presented in Figure 5.21a. It can be seen in the figure that the sharp notch has much less scatter than the blunt notch.

It is possible to extract both a threshold hydrogen concentration for embrittlement as well as a relationship between the steady state steel lattice hydrogen concentration and the fracture initiation stress, as was done for the bluntly notched tensile bars. The threshold hydrogen concentration, C_o, was found to be 3.25×10^{-7} mol/cm^3 (0.0413 ppm). The empirical relationship

established between the fracture initiation stress and the steady state steel lattice hydrogen concentration was found to be

$$\sigma_F \ (MPa) = 3021.6 \pm 132 - 366.4 Log\left(\frac{C_H}{3.25 \times 10^{-7}}\right) \tag{67}$$

The value of σ_0 is elevated over that of the bluntly notched tensile bars, and σ_F declines more rapidly with increasing hydrogen concentration. This elevation of the former quantity is because of the enhanced notch work hardening of the sharper notch that in turn increases the peak stress in air. Since there is greater uncertainty in the data from the blunt notch than the sharp notch, it seems reasonable that the results from CERT of the sharp notch more accurately reflect the behavior of the prestressing steel.

Comparison of the blunt and sharp notch test results for $Ca(OH)_2$ is presented in Figure 5.21b. As can be seen in the figure, although the slopes of the best fit lines describing the fracture initiation stress/hydrogen concentration relationship for blunt and sharp notches is roughly equivalent, the results for the sharp notch is offset to higher stresses. In other words, for a given steady state steel lattice hydrogen concentration, a higher local crack initiation stress is observed for the sharp notch. This offset is the result of the higher level of constraint placed on the steel by the sharp notch.

Figures 5.22a and b present the achieved plastic zone depth at the maximum applied remote stress and the depth of the maximum hydrostatic tension as a function of the steady state steel lattice hydrogen concentration for the sharply notched tensile bars. A similar relationship to Equation 64 may also be derived to express the plastic zone size at failure, r_p, and the depth of the maximum hydrostatic tension as a function of the steady state steel lattice hydrogen concentration. As is indicated on the figure, these relationships are found to be

$$r_p \ (mm) = 0.254 - 0.085 Log\left(\frac{C_H}{3.25 \times 10^{-7}}\right) \tag{68}$$

$$Depth \ of \ Hydrostatic \ (mm) = 0.208 - 0.061 Log\left(\frac{C_H}{3.25 \times 10^{-7}}\right) \tag{69}$$

where r_p is the radial depth of the plastic zone in mm and C_H the steady state steel lattice hydrogen concentration in mol/cm^3. As with the blunt notch, both the plastic zone depth and the depth of the maximum hydrostatic tension was large relative to the size of all microstructurally significant features (i.e., pearlite colony and inclusion spacing).

53

K_{IC}, the stress intensity for hydrogen crack initiation, was calculated using the method of Raju and Newman, as discussed. Figure 5.23 presents the crack voltage as a function of time along with the applied load. Crack initiation was assumed to take place at the load that resulted in a change in slope of the crack voltage with time, as illustrated in the figure. In actuality, crack initiation likely occurred during the load ramp immediately prior to the load plateau at which the change in slope of the DCPD potential was observed. As a result, the calculated stress intensity must be viewed as an upper limit. The initial crack growth was within the same plane as the fatigue precrack (i.e., mode I) but later transitioned to cracking that was parallel to the tensile axis. Figure 5.24 presents the calculated value of K_{IHE} as a function of the steady state steel lattice hydrogen concentration. The stress intensity was calculated for the surface of the bar (Location A in Figure 4.41) and the center of the fatigue precrack (Location B in Figure 4.41) since the actual site of initiation could not be determined from the fracture surfaces. As can be seen in the figure, a reduction of 15% in K_{IC} is observed at a hydrogen concentration of 2×10^{-7} mol/m^3, the concentration below which embrittlement was not observed. This threshold is comparable to that observed for the blunt (2×10^{-7} mol/cm^3) and sharp (5×10^{-7} mol/cm^3) notched tensile bars. As can be seen in the figure, although the prestressing steel is embrittled by hydrogen, the effect is not nearly as dramatic as for a quench and tempered steel of equivalent yield strength and comparable lattice hydrogen concentrations, where K_{IHE} values on the order of 20 MPa$\sqrt{m}$ are not uncommon (Gangloff, 1986).

Fractography for Smooth, Notched, and Precracked Tensile Bars

Little has been presented in the literature discussing the fracture behavior of the heavily cold worked pearlitic material commonly applied as prestressing steel. However, much work has been completed identifying the mode and mechanism of fracture for isotropic pearlitic eutectoid steels (i.e., as transformed microstructure). The work that has been done, predominantly by Toribio and coworkers (Toribio, 1991a, 1991b, 1992a, 1992b, 1993, 1994, 1996) has identified several differences between isotropic and cold worked materials. First, fracture of the drawn material in air is predominantly ductile in nature (MVC) with less cleavage than would be observed for an isotropic pearlitic steel of the same composition and the same level of constraint. Second, because of the highly anisotropic microstructure of the drawn wire, there is a large degree of secondary cracking parallel to the drawing axis (i.e., longitudinal splitting) that is not observed in the case of the isotropic wire. Finally, there does not appear to be a change in the microscopic mode of fracture with increased hydrogen concentration for the cold worked steel, though the size of the region reported to be TTS does increase with C_H. In contrast, an increased amount of cleavage is observed with increasing hydrogen concentration and/or level of constraint in the case of isotropic pearlitic steels. In addition, a larger decrease in K_{TH} with increased hydrogen concentration is achieved for the isotropic case.

The following section presents a more detailed fractographic study of the cold drawn prestressing steel at various steady state steel lattice hydrogen concentrations. An effort is made to point out the distinguishing characteristics, and discuss how they relate to the underlying microstructure of the material. There were no differences observed, either macroscopically or microscopically, between the fracture surfaces for the blunt or sharp notched specimens. Therefore, a general description of the behavior for both at each hydrogen concentration is presented without distinguishing between the blunt and sharp notch.

Uncharged and Low C_H ($5x10^{-7}$ mol/cm^3 or 0.0635 ppm)

Figure 5.25 presents an overview of the fracture surface for an uncharged, smooth diameter tensile bar. Overall, the fracture surface is best described as a classic cup and cone ductile fracture. There are a number of features of note on this fracture surface. First, the center of the bar is uniformly ductile in nature (Figure 5.26), and is presumably the location of crack initiation. Progressing radially out from the center of the bar is a series of longitudinal cracks (i.e., cracks parallel with the drawing axis), seen in Figure 5.27. At higher magnification, numerous smaller longitudinal splits, the spacing of which is comparable to the pearlite subcolony size discussed, can be observed, though the bulk of the fracture surface is still uniformly ductile (MVC) as shown in Figure 5.28. Finally, around the periphery of the fracture surface is a shear lip (presumably the result of shear overload at failure) that is microscopically uniform MVC as presented in Figure 5.29.

The notched tensile bars (i.e., bluntly and sharply notched) exhibited nominally identical behavior in terms of both the macroscopic and microscopic features of the fracture surface when tested in air. Figure 5.30 presents an overview of the typical fracture surface for as received and low hydrogen concentration tests. As can be seen in the figure, there are three distinct macroscopic regions of the fracture surface. The first is a large tortuous region oriented at a large angle (approximately 70 degrees) to the tensile axis, as shown from a vantage point parallel to and perpendicular to the tensile axis in Figures 5.31a and 5.31b, respectively (Location of following figures indicated on Figure 5.30). Closer inspection of this tortuous region reveals that it is actually terraced in nature, having been the results of longitudinal splitting, which appears to be brittle in nature (Figure 5.31a), linked together by ductile and, in some cases, brittle (i.e., cleavage) plateau regions (Figure 5.32a and 5.32b, respectively). Relating this tortuous region to the microstructure of the steel, we find that the size of the ledge and terrace regions is similar to the pearlite colony size (on the order of 10 to 20 μm).

The second region of the tensile bar is a small edge region, or lip, along portions of the circumference of the tensile bar (predominantly at the edge of the tortuous region), also oriented at an angle roughly 45 degrees to the tensile axis (Figure 5.33a). Closer inspection of this region reveals many small areas that are composed of numerous lamellar voids 90 to 140 nm in width, which is roughly equivalent to the interlamellar spacing of the pearlite (95 nm) presented (Figure 5.33b). These latter regions are likely the result of the tensile shear cracking process proposed by

55

Miller and Smith (1970). The third major region of the fracture surface is a large, smooth region oriented 45 degrees to the tensile axis, which appears macroscopically ductile in nature (Figure 5.34). This latter region is likely the result of shear overload during the ductile fast fracture of the remaining ligaments of the tensile bar. Experiments conducted on the uncharged, notched tensile bars at liquid nitrogen temperatures behaved nominally identical with those performed at room temperature, with no change in the degree of cleavage fracture.

The fracture surface of the precracked samples, although macroscopically much different than the notched tensile bars, shares many of their significant microscopic features. An overview of a fracture surface for a precracked specimen tested in air is presented in Figures 5.35a and 5.35b (looking down parallel to the tensile axis and at an angle, respectively). A representative view of the fatigue precrack is pictured in Figure 5.36. Along the edge of the fatigue precrack, numerous sites of mode I crack initiation can be seen (Figure 5.37a). Upon closer inspection of these initiation sites, we see they are composed of an array of lamellar voids (Figure 5.37b) much like the small lip region in the notched tensile bars. Beyond these initiation sites, the advancing crack rapidly turns parallel with the tensile axis, as illustrated in Figure 5.35b. Close inspection of the crack surface once it has become parallel with the tensile axis (Figure 5.38a) shows that it is the result of longitudinal splitting of the tensile bar because of the highly anisotropic nature of the drawn pearlitic steel (i.e., alignment of pearlite lamellae parallel to the wire axis). As such, this region is similar in appearance to the tortuous region pictured for the notched tensile bars, being terraced in nature, with numerous plateau regions, both ductile and brittle in nature (Figure 5.38b). Beyond this tortuous region, the fracture surface becomes smooth and microscopically ductile in nature (Figure 5.39), the result of rapid ductile overload of the remaining ligament.

Moderate C_H ($2x10^{-6}$ mol/cm^3 or 0.254 ppm)

An overview of a notched tensile sample containing 2×10^{-6} mol/cm^3 hydrogen is presented in Figure 5.40. Recall that charging the tensile bars to this steady state steel lattice hydrogen concentration resulted in a 20% decrease in the remote stress at failure. Comparing the overall fractography of these samples to the lower hydrogen concentration, several observations may be made. First, it is clearly evident that more extensive longitudinal splitting is occurring as the hydrogen concentration is increased, as illustrated in the angle view of the fracture surface presented in Figure 5.41. In addition, though the smooth and tortuous regions present at the lower hydrogen concentration are still present, the distinction between the two is becoming less pronounced. Finally, within the microscopically ductile edge region (around portions of the circumference of the tensile bar, particularly along the edge of the tortuous region), or lip, (Figure 5.42a) much more of the lamellar void regions (as presented for the lower C_H) is evident at this hydrogen concentration as compared to the lower hydrogen concentrations and the uncharged case, though the dimensions of the actual voids are unchanged (Figure 5.42b).

As before, the precracked specimens possessed similar features microscopically. Figure 5.43a and 5.43b present an overview of the fracture surface. As can be seen in the figures, the

advancing crack rapidly turned to a direction approximately parallel to the tensile axis. As can be seen in Figure 5.44, there were numerous sites along the front of the fatigue precrack where a mode I crack was initiated. Microscopically, these sites were composed of lamellar voids (Figure 5.45) as seen in the lip regions for the notched tensile bars. These regions are likely shear cracks as proposed by Miller and discussed. Looking more closely at the fracture surface once the crack turned roughly parallel to the tensile axis (Figure 5.46), we see that it again appears similar to the tortuous regions described.

High C_H ($2x10^{-5}$ mol/cm^3 or 2.54 ppm)

An overview of a notched tensile sample containing 2×10^{-5} mol/cm^3 hydrogen is presented in Figure 5.47. Comparing this to the samples of lower C_H, several differences are evident. First, it is evident that the large, macroscopically smooth, shear overload region oriented at 45 degrees to the tensile axis has largely vanished, though numerous smaller regions are still present. In addition, longitudinal splitting has become still more pronounced. The nature of the splitting itself has changed, however, and it now appears microscopically ductile, as illustrated in Figure 5.48. Finally, the microscopically ductile, "lip" region found on the other samples, though it is still seen here, appears to be smaller, in terms of its radial depth from the notch root, than at lower C_H levels, in addition to possessing a large number of longitudinal cracks, as illustrated in Figure 5.49a. Closer inspection of this region reveals extensive regions containing arrays of lamellar voids as presented, seen in Figure 5.49b. In addition, these regions progress further into the tensile bar, well beyond the lip region. Little cleavage is visible at this elevated hydrogen concentration.

An overview of a similarly hydrogen charged, precracked specimen is pictured in Figures 5.50a and 5.50b. Again, the fracture surface for the fatigue precracked specimen has many of the microscopic features present in the notched specimens. These regions include the initiation regions in front of the fatigue precrack (Figure 5.51a), which, upon closer inspection, are revealed to be composed of numerous lamellar voids (Figure 5.51b), the size of which is approximately equivalent to the interlamellar spacing of the pearlite. Beyond these initiation sites, the advancing crack turns roughly parallel to the tensile axis, and appears similar to the tortuous region (Figure 5.52a and 5.52b) discussed. Beyond this tortuous region is a smooth, MVC region resulting from catastrophic shear overload of the remaining ligament.

Proposed Mechanism for Hydrogen Induced Failure of Prestressing Steel

As was discussed, it has been shown in the literature that for isotropic pearlitic microstructures, failure is predominantly brittle in nature, with cleavage crack initiation occurring at either shear cracks, formed by the mechanism proposed by Miller and Smith (1970), or fractured MnS inclusions (Lewandowski, 1987). Upon hydrogen charging, however, isotropic pearlitic structures are seen to initiate cracks in a microscopically ductile fracture mode and to

57

propagate cracks by brittle cleavage in mode I (Toribio, 1991, 1992, 1993, 1994, 1996). In cold drawn steels, hydrogen promotes an increase in uniformly ductile, tearing topography surface (TTS) fracture according to Toribio (1991, 1992, 1993, 1994, 1996) and shear cracking of the pearlite lamellae, as proposed by Miller (1970). As was illustrated, the latter were always observed near the surface of the notch or edge of the fatigue precrack, where both the maximum shear stress and the longitudinal tensile stress were maximized. Recall that the Miller proposed shear cracking process involves the formation of slip bands within the ferrite lamellae within a plane close to 45 degrees from the tensile axis, possibly along {112} planes, which on average would be oriented 55 degrees from the tensile axis, forming physical defects within the cementite lamellae and later resulting in their tensile fracture.[15] These failed cementite lamellae subsequently act as void nuclei within the ferrite lamellae. Voids nucleated in this manner then grow within the ferrite lamellae and link up to form a macroscopic crack, as illustrated in Figure 1.11. Thus, the Miller process requires a large *tensile stress* to fail the cementite lamellae, as well as a high *shear stress* to promote void growth and link up through the ferrite. This result is similar to that of Lewandowski for isotropic pearlitic microstructures where crack initiation was observed to occur closer to the notch root than the position of the maximum longitudinal stress (Lewandowski, 1987). Based on the observed increase in the extent of shear cracking and reduction in the fracture initiation stress or stress intensity with increased hydrogen concentration, it seems likely that hydrogen either reduces the fracture stress of the cementite lamellae that in turn act as void nuclei, or it assists in the void growth and link up stage of the Miller shear cracking process.

In both isotropic and cold worked pearlitic steels, hydrogen charging results in two types of ductile fracture modes (defined as Miller shear cracking and TTS). This increase in ductile nature is to be expected when the effects of hydrogen on steels such as these are considered. Oriani and Josephic (1979) found for pearlitic 1045 steel that hydrogen reduced the lattice cohesion strength (i.e., decohesion occurs at a lower applied stress with increasing hydrogen concentration), with increased hydrogen concentration resulting in a further decrease in the cohesive strength of the alloy. As a result, void nucleation at ferrite/cementite interfaces, followed by growth within the ferrite is assisted. Thus more numerous (because of enhanced void nucleation) larger (because of enhanced void growth) voids are formed for a given macroscopic strain, leading to failure at lower macroscopic strains with increased hydrogen concentration. Cialone and Asaro (1979) found for spheroidized 1090 steel that void nucleation at Fe_3C interfaces was enhanced by hydrogen, as were the latter stages of void growth and coalescence. They then went on to speculate that the mechanism may be because of high hydrogen pressures achieved within the voids, but stated that their results were unable to conclusively determine the mechanism. Garber et al. (1981) also found that hydrogen assisted the latter stages of void linkup, but they stated that there was little effect on the earlier stages of

---

[15] The actual mechanism by which the cementite lamellae deform and fracture is unclear. The literature suggests that as the thickness of the cementite lamellae decreases, overall deformation of the pearlite is more uniform, and the cementite may behave in a ductile manner, necking down to failure rather than fracturing in a brittle manner (Porter, 1978).

void nucleation and growth. Finally, work conducted by Onyewuenyi and Hirth (1966) on spheroidized 1090 steel found that increased hydrogen resulted in increased dislocation injection from second phase particles within the ferritic matrix, and that hydrogen enhanced the mobility of screw dislocations.

To summarize these findings, hydrogen has the effect of stimulating plastic flow, through enhanced dislocation generation, enhanced void nucleation, and accelerated void growth at α-Fe/Fe_3C interfaces. As a result, ductile failure may be achieved at lower global strains, and thus lower remotely applied stresses.

If we consider the case of the drawn pearlitic microstructure, we see that from the outset in the uncharged case, the fracture is predominantly ductile in nature. This ductile behavior is in stark contrast with the undrawn case, where the fracture mode has been found to be predominantly cleavage under high constraint (Park, 1979; Lewandowski, 1987). The microstructure of the drawn pearlitic wire is composed of fragmented cementite and ferrite lamellae, the latter of which contains an extensive dislocation network, and both of which are aligned parallel to the drawing axis (Embury, 1966). As such, there are numerous microvoid nucleation sites (i.e., microcracks, small cementite lamellae fragments) located throughout the microstructure (Embury, 1966; Chandhok, 1966). In addition, numerous inclusions (MnS and Ca rich) are present throughout the microstructure. However, in all cases (hydrogen charged or otherwise) the plastic zone size was very large relative to the spacing of these inclusions throughout the microstructure, as well as the size of pearlite colonies (Figure 4.1). As a result, the at-risk volume of the microstructure in front of the notch root or fatigue precrack will contain many of the aforementioned fatal crack initiating flaws (i.e., cracked inclusions or appropriately aligned pearlite colonies). Based upon the fractography presented, it is unlikely that either cracked MnS or Ca rich inclusions serve as the predominant fracture initiation site in these steels, as even though there would be numerous such sites within the at-risk volume in front of the notch or fatigue pre-crack, no cracking that could be attributed to such sites was observed. Based on the observations made in this study for uncharged specimens, it appears that crack initiation occurs by the formation of shear cracks oriented at approximately 45 degrees from the tensile axis (which is in turn parallel to the cementite lamellae's long axis) as proposed by Miller and Smith (1970), around the periphery of the tensile bar within the plastic zone (i.e., within the microscopically ductile, lip region described). This is illustrated in Figure 5.52c that illustrates the numerous shear cracks emanating from an advancing fatigue pre-crack. As is also presented in the Figure, upon initiation of a mode I crack, the advancing crack rapidly turns parallel with the tensile axis. Considering the angle of these shear cracks, we see that they are oriented 45 degrees from the tensile axis, similar to the shear cracks observed by Miller, as illustrated in Figure 5.52d.

From the literature, recall that the α-Fe/Fe_3C interface is a site of enhanced void nucleation. The question remains, does hydrogen accumulate there? Recalling the results from TDS analysis of the cold drawn steels presented, the hydrogen concentrations, and hence coverage (θ_T), of trap sites identified as α-Fe/Fe_3C interfaces and microvoids increase as the

lattice hydrogen concentration is increased. Figures 5.52e and 5.52f present the fracture initiation stress as a function of the hydrogen trap coverage at α-Fe/Fe$_3$C interfaces and microvoids, respectively. From the figures it can be seen that although the steady state lattice hydrogen concentrations (and corresponding lattice site coverage) are low, the coverage of the significant trap sites is, by comparison, relatively high. Embrittlement of the prestressing steel was realized (in terms of a reduction of the stress to nucleate a crack) at a trap site coverage of 0.0002 for Fe/Fe$_3$C interfaces, and 0.01 for microvoids. For comparison, the corresponding lattice concentration and coverage were 2×10^{-7} mol/cm^3 and 9.45×10^{-7}, respectively. As such, hydrogen is seen to be a very potent embrittler for these steels.

Once shear cracks have been initiated, they propagate to an undefined microstructural defect oriented parallel to the tensile axis that, in turn, triggers longitudinal cracking at an apparently low applied normal stress in the transverse direction (i.e., perpendicular to the tensile axis) relative to the combined shear stress/normal stress required to initiate Miller shear cracking. This longitudinal cracking is, in essence, propagation of a brittle crack parallel to the drawing axis, as a result of the highly anisotropic microstructure. In particular, the longitudinal splitting is likely along the boundary between adjacent pearlite colonies that were in turn a result of the drawing process (Hosford, 1964). Thus the longitudinal splitting may be viewed as the arrest of the advancing shear crack at the edge of a pearlite subcolony by the highly aligned microstructure. This longitudinal splitting continues as the tortuous region discussed is formed. Eventually, the shear stress in the remaining ligament exceeds the strength of material, and catastrophic ductile shear overload of the remaining ligament or ligaments between longitudinal splits of the tensile bar results.

Considering the micromechanisms of crack nucleation, as the prestressing steel is hydrogen charged, microplastic deformation becomes more pronounced, via an enhancement of both void nucleation at ferrite/cementite interfaces and void propagation through the ferrite lamellae. As a result, it is not unreasonable to consider that hydrogen either reduces the cohesive strength of the latter interfaces and enhances void nucleation, or enhances void growth, through either an internal pressure mechanism as proposed by Beachem (1972) or by reducing the cohesive strength of the metal lattice. Thus, a shear crack is nucleated and grown at a lower remotely applied stress (and hence strain). This increased microplastic deformation is particularly evident at very high hydrogen concentrations, where even the longitudinal secondary cracking appears to be ductile in nature (e.g., Figures 5.38 and 5.46).

Relevant Conclusions Relating to the Properties of the Prestressing Strand

Hydrogen absorption rates in iron and prestressing steel are not solely a function of the solution pH and applied overpotentia, but instead are also dependent on the composition of the cathodic polarization (catholyte) solution. Hydrogen permeation is greater in saturated Ca(OH)$_2$ than in NaOH at an equivalent pH. Moreover, hydrogen permeation rates through iron and steel were enhanced by the presence of a mortar cover, at least 2.5 times that in NaOH solution at the

same cathodic current density. Ca^{2+} in the form of $Ca(OH)_2$ is a hydrogen recombination poison and enhances hydrogen entry. As a consequence, hydrogen absorption in laboratory simulants of concrete pore solutions will be extremely dependent on the exact chemistry of that solution.

The root cause of embrittlement of prestressing steel is the steady state steel lattice hydrogen concentration achieved through cathodic polarization, irrespective of the exact concrete pore solution or simulated crevice solution in which the steel was evaluated. Although simulated pore and local crevice site solutions with different pH values resulted in differing critical or threshold potentials for embrittlement, they all resulted in a threshold hydrogen concentration (2×10^{-7} mol/cm^3) for reduction of the fracture initiation stress of a bluntly notched steel from the values obtained in air. A universal relationship between a prestressing steel's absorbed mobile hydrogen concentration and the local fracture initiation stress was established. The relationship is of the form $\sigma_i = \sigma_{air} - \alpha \log (C_H/C_H^\circ)$, where σ_i is the local fracture initiation stress, C_H, is the steel hydrogen concentration, and C_H° is the hydrogen concentration below which hydrogen has no influence on fracture initiation. The critical concentration was established to be ~2×10^{-7} mol H/cm^3. Specifically, the exact lower bound relationship was σ_i (MPa) = 2599 - 231.5 $\log (C_H/2 \times 10^{-7})$ for the blunt notch configuration used. This relationship was independent of the simulated pore solution in which the material was evaluated. The technological significance of this relationship is that different simulated pore and local occluded site solutions may yield different precise cathodic current densities and potentials that are required to achieve the aforementioned critical hydrogen concentration. Therefore, the applied potential, in and of itself, is insufficient to define the threshold for hydrogen embrittlement, although the critical hydrogen concentration achieved within the prestressing steel is a single parameter that is.

Three discrete hydrogen trap sites exist within the prestressing steel microstructure, identified at α-Fe/Fe$_3$C interfaces, microvoids, and dislocations. The concentration trapped at the former two sites increases markedly with increasing lattice hydrogen concentration. Thermal desorption spectroscopy experiments demonstrated that three distinct trap sites exist within the prestressing steel microstructure. Based on comparison with literature data for similar carbon steels, these trap sites have been identified as α-Fe/Fe$_3$C interfaces, microvoids, and dislocations. The concentration trapped at the former two has been demonstrated to increase significantly with increasing lattice hydrogen concentration, although the concentration at dislocations appeared to remain essentially constant.

Crack initiation within the heavily cold worked pearlitic steels used as prestressing tendon occurs through the formation of shear cracks (Miller, 1970) that in turn trigger longitudinal splitting, followed by ductile overload of the remaining ligament of the tensile bar. This process is assisted by hydrogen that either reduces the cohesive strength of the Fe/Fe$_3$C interface or assists void growth and linkup. Crack initiation within cold drawn, fully pearlitic steels is seen to take place near the notch root or edge of the fatigue precrack, where both the hydrostatic tensile stress and the maximum shear stress are maximized. From TDS, it was established that the coverage of both Fe/Fe$_3$C and microvoid trap sites increases markedly with

increased lattice hydrogen concentration. Shear cracking, as proposed by Miller, begins with the tensile failure of cementite lamellae within the steel. These failed lamellae then act as void nucleation sites within the ferrite lamellae. The voids nucleated at such sites then grow through the ferrite lamellae until they link up and form a macroscopic crack. Once such a crack forms, it continues to grow until reaching a microstructural defect oriented parallel to the wire axis, such as a pearlite subcolony interface, as discussed, triggering longitudinal splitting. The latter process continues until the stress within the remaining ligament becomes sufficiently large to trigger ductile overload.

Based on the results of this study, hydrogen enhances the ductile nature of the pearlite, enhancing either void nucleation (by reducing the cohesive strength of the metal matrix) or propagation (through an internal pressure model as proposed by Beachem).

Developing Local pH Within Occluded Geometries Along the Tendon

The environment within a reinforced concrete structure prior to the initiation of corrosion, such as a marine bridge pile, varies with both position as well as time. Initially, the environment at the steel/concrete interface is highly alkaline (pH >12.5) containing Na^+, K^+, Ca^{2+}, SO_4^{2-}, and OH^- as well as a number of other minor constituents (Rechenberg, 1983; Wheat, 1985; Diamond, 1975; Andersson, 1989). Because of the environmental conditions to which a bridge pile is exposed (i.e., partially immersed in ocean water), variations in Cl^-, CO_2, and O_2 concentration will also occur as a function of position. The result of these positional chemical variations is the accentuation of corrosion in certain regions of the pile. More specifically, a larger degree of corrosion is observed in the splash and atmospheric zones as compared to the submerged zone (Pangrazzi, 1994).

As mentioned previously, upon the initiation of crevice corrosion within an occluded cell or general corrosion along the reinforcing tendon, ferrous ions will be produced that will subsequently hydrolyze, reducing the pH according to the relation

$$pH = 6.64 - \frac{1}{2}\log[Fe^{2+}] \tag{70}$$

To demonstrate this, ferrous ions (as 0.2 M $FeCl_2$) were gradually titrated into a saturated (approximately 0.025 M), filtered $Ca(OH)_2$ solution. As can be seen in Figure 5.53, upon attaining a sufficiently large concentration of Fe^{2+}, the solution rapidly acidified, following a theoretical relationship (Equation 68) (Sedriks, 1996) as illustrated in the figure. Also shown in the figure is the anticipated reduction of the local pH to below 3 if ferrous (Fe^{2+}) ions have oxidized to ferric (Fe^{3+}) and subsequently hydrolyze as has been argued to occur within the atmospheric zone by Otero et al. (1990).

A similar result was achieved when a prestressing steel crevice was placed and potentiostatically polarized within a simulated pore solution consisting of aerated, saturated

Ca(OH)$_2$ + 0.5 M NaCl, and instrumented with a micro-pH electrode. Upon initiation of corrosion within the occluded cell, the pH rapidly decreased to a value of 6 and below, following a trend nearly identical to that observed for the FeCl$_2$ titration experiment as can be seen in Figure 5.54. Additional experiments were performed using a pH electrode assembly identical to that embedded within the concrete piles. In these experiments, provisions were made such that the applied current density could also be monitored (i.e., a potentiostat capable of accommodating a grounded working electrode was used). As can be seen in Figure 5.55 for such an experiment performed at -400 mV$_{SCE}$ in the chloride-contaminated pore solution analog, the initiation of crevice corrosion was accompanied by both a decrease in the pH of the occluded geometry and an increase in the applied current density from the crevice. Applied potentials ranging from -350 to -600 mV$_{SCE}$ were investigated. At potentials more negative than -600 mV$_{SCE}$, crevice corrosion initiation did not occur, allowing -550 mV$_{SCE}$ to be viewed as an approximate threshold potential for crevice corrosion initiation.

Although the anticipated crevice corrosion and accompanying pH drop were readily observed in simulated pore solutions, the next step was to establish if the same phenomenon would occur within a chloride-contaminated concrete structure. As such, the pH sensor assembly pictured in Figure 4.43 was embedded within a chloride-contaminated, laboratory-scale pile. Figure 5.56 illustrates the measured pH as a function of time for pile 1 (Figure 4.44). As can be seen in Figure 5.56, after approximately 8 days of immersion, the local pH began to decrease, indicative of crevice corrosion initiation and ferrous ion hydrolysis. The pH continued to decrease until achieving a pH of approximately 6 to 7, similar to that observed in the simulated crevices illustrated (Figures 5.53 and 5.54). A similar result was observed at the pH sensors placed in pile 3 (Figure 4.46). Local pH levels as low as 5.5 were observed throughout the pile between 47 and 141 days, consistent with the results illustrated in Figure 5.56. It should be noted that the bulk pH, as measured by a pH electrode within the bulk concrete (and not within an occluded geometry), remained a highly alkaline 13.5 throughout the test.

To summarize, once corrosion has been initiated at a point on the reinforcement, the local pH may be reduced because of ferrous ion hydrolysis

$$Fe^{2+} + 2H_2O \rightarrow Fe(OH)_2 + 2H^+ \tag{71}$$

As the reversible potential for hydrogen production is a direct function of the pH, it will vary with position accordingly. As such, once the reversible potential for hydrogen production is exceeded by the applied CP at a position along the pile, net hydrogen production and the possible embrittlement of the pile may result.[16] The implications of this for a potential-based CP criterion are clear. Since the environment is a function of position, and as such the reversible potential for hydrogen production is as well, there may not be a single universally applicable reversible potential that, when not exceeded, will ensure adequate CP of the reinforcement in terms of

---

[16] Hydrogen production and permeation is also possible at underpotentials (i.e., potentials less negative than the reversible electrode potential). This effect is well known for the Pd electrode, where permeation experiments are often conducted at underpotentials to avoid hydriding the Pd electrode.

eliminating corrosion although avoiding the potential embrittlement of the reinforcement at all points in the pile.

Oxygen Depletion at the Steel/Concrete Interface

A prestressing steel strand with a 1.25 cm mortar cover was immersed in ASTM artificial ocean water and cathodically protected. As can be seen in Figure 5.57, for a constant applied cathodic current density, the observed potential decreases with time and then plateaus. This decrease in potential is the result of the gradual depletion of dissolved oxygen within the pore solution at the steel/concrete interface. For low applied cathodic current densities, the rate of diffusion of dissolved oxygen to the steel surface is sufficiently quick to support the reaction rate being driven at the steel/concrete interface. If the applied cathodic current density is increased such that the diffusional transport of oxygen through the concrete pore solution is insufficient to support the cathodic reaction rate being driven on the steel surface, the potential becomes increasingly negative such that water reduction will become a thermodynamically viable reaction. With increased polarization, the HER will then become the dominant cathodic reaction, as is illustrated in the figure for a relatively modest level of CP levels. It should be noted that the mortar coverage used in this experiment is considerably less than the 5 cm required for atmospherically exposed concrete structures. This reduced coverage will result in a less severe condition (oxygen transport flux densities will be higher) than in an actual pile, where oxygen depletion will occur at much lower applied cathodic current densities, as will be illustrated.

To summarize, oxygen availability will be considerably greater initially than for the deaerated solutions investigated in the section within a concrete structure. As a result, the dominant reaction at the steel/concrete interface will be oxygen reduction until the dissolved oxygen concentration is depleted upon application of CP at low local cathodic current densities. This depletion is anticipated, as oxygen transport through the liquid saturated pore structure within the concrete (approximately 10^{-5} cm^2/s) is slow relative to its rate of consumption at the steel/concrete interface.

Simulating a Chloride-Contaminated, Prestressed Marine Bridge Pile

To apply information relating the threshold stress intensity, K_{TH}, or fracture initiation stress, σ_i, to the steady state steel lattice hydrogen concentration, C_H, in prestressing steel within an actual prestressed concrete structure, and determine safe CP procedures, the next step is to determine the level of CP (e.g., i_{cath}, $\eta_{applied}$, and C_H) applied as a function of position within a marine bridge pile. To accomplish this, a series of laboratory-scale piles was constructed and subjected to varying levels of CP.

Upon immersion in ASTM artificial ocean water, the open circuit potentials of the piles were allowed to stabilize. Figure 5.58 presents the internally measured open circuit potentials as a function of vertical position within pile 3 (illustrated in Figure 4.46). Also presented in the figure are the critical potentials above which pitting and crevice corrosion were initiated in saturated $Ca(OH)_2$ solutions containing additions of 0.3 and 0.5 M NaCl, respectively. These critical potentials were determined via potentiodynamic scans for the former (see Figure 5.59), and through the crevice corrosion experiments discussed for the latter. As can be seen in the figure, the potentials were initially very similar for each level, and in all cases more positive than the threshold potential for crevice corrosion in the aforementioned chloride-contaminated pore solution analog. After an induction period, increased corrosion initiation was observed via a decrease in the measured local potentials throughout the pile. At that point, approximately 40 days into the test, the potentials began to become more negative. The pile was then allowed to stabilize for an additional 80 days. Potentials ranging from -342 to -359 mV_{SCE} (-487 to -494 mV_{MnO2}) were observed for the submerged and splash zones (levels 4, 5, and 6) although potentials ranging from -246 to -285 mV_{SCE} (-391 to -429 mV_{MnO2}) were observed in the atmospheric zone (levels 1, 2, and 3) as can be seen in the Figure.

Comparison of the observed local open circuit potentials to the previously discussed threshold potentials for pitting and the initiation of crevice corrosion reveals several important pieces of information. First, it is clear that the potentials are all significantly less positive than the pitting potential, and as such it is unlikely that pitting has taken place at any point along the reinforcement. On the other hand, all of the internal potentials were more positive then the crevice corrosion initiation potential determined. As such, it is likely that crevice corrosion has initiated within the occluded geometries throughout the prestressing tendon. Thus, it should be anticipated that the local environment at the steel/concrete interface will deviate significantly from the bulk concrete environment and is likely more acidic because of ferrous ion hydrolysis as discussed.

Another variation in the local environment may be brought about by the CP current itself. Although initially the cathodic reaction on the reinforcement will be the oxygen reduction reaction, with time the O_2 available at the steel/concrete interface will be consumed and hydroxyl ions produced. The result of this process will be a negative shift in the measured potential until the reversible potential for water reduction is reached, and net hydrogen production occurs. This is illustrated in Figure 5.60, where upon application of a modest level of CP (in this case an applied cathodic current density of 0.66 $\mu A/cm^2$), the current-on potential of the reinforcement, as measured by embedded reference electrodes, was seen to decrease.[17] With time, this potential became negative enough to allow hydrogen production, as evidenced by the measurement of permeation at the hydrogen sensors at this current density, as illustrated.

---

[17] This same trend was also observed for all applied cathodic current densities, the results of which are presented in Appendix C.

Local current and potential distributions. CP was applied galvanostatically to piles 2 and 3 via a platinized titanium skirt anode at a series of current densities. For pile 2 (Figure 4.45), cathodic current densities[18] of 1, 1.5, 2, and 2.5 $\mu A/cm^2$ were each applied for a period of two weeks. For pile 3 (Figure 4.46), it was recognized that the 2-week time period was insufficient for the pile to stabilize at low current densities (< 2 $\mu A/cm^2$). As a result, current densities of 0.1, 0.33, 0.66, 1.0, 1.33, 1.66, 2.00, 2.5, and 3.00 $\mu A/cm^2$ were applied, each for 48 days.

Figure 5.60 presents representative potential data as a function of time for the polarization of pile 3 (Figure 4.46),[19] in this case for a current density of 0.66 $\mu A/cm^2$. In the figure, it can be seen that more than 40 days were required for the potentials to stabilize. At current densities of 2.0 and 2.5 $\mu A/cm^2$, pile 2 (Figure 4.45) was able to stabilize well within the 2-week period, as illustrated in Figures 5.61 and 5.62, respectively. After applying each current density until stabilization (or 2 weeks, for pile 2), application of the CP current was ceased, and the piles were allowed to depolarize. Figure 5.63 shows representative current-off potential data for the depolarization of pile 3 (Figure 4.46) from a current density of 0.66 $\mu A/cm^2$. Although the pile depolarized significantly after 5 hours, several days were required for the pile to stabilize. As the applied current density increased, the actual time required to completely depolarize also increased, exceeding a week at a current density of 3.00 $\mu A/cm^2$ as is illustrated in Appendix 1. The current-on local potentials achieved as a function of vertical position for piles 2 and 3 (Figures 4.45 and 4.46) at each applied current density are presented in Figures 5.64 and 5.65. As the applied current density was increased, the current-on, local potentials became progressively more negative, indicative of oxygen depletion at the steel/concrete interface as discussed. Also noted on each of the aforementioned figures is the current density at which a measurable hydrogen permeation flux was observed for each sensor level. As can be seen in the figures, area averaged current densities as low as 0.33 $\mu A/cm^2$ resulted in a measurable permeation flux in regions 25 to 50 cm above the waterline in pile 3. Figure 5.66 presents the magnitude of the achieved depolarization (instant-off potential - depolarized potential) as a function of vertical position in pile 3 (Figure 4.46). From Figure 5.66, it is clear that for a skirt anode placed at the waterline, the 100 mV depolarization criterion can be achieved at positions 25 cm above the waterline and all positions below the waterline at an applied current density of 0.33 $\mu A/cm^2$. However, it can be seen that a current density of 1 $\mu A/cm^2$ or greater is required to achieve a comparable depolarization at positions 50 and 75 cm above the waterline. In all three of the figures (5.64-5.66), the nonuniform nature of the applied CP is clearly presented. This nonuniformity is because of the ease with which CP current is thrown into the conductive submerged and splash zones as compared to the more resistive atmospheric zone.

---

[18] All applied cathodic current densities are normalized per unit area of steel reinforcement.

[19] The MnO_2 reference electrodes were embedded very close to the tendons within each pile, there is essentially no difference between the current-on and instant-off potentials. In other words, the contribution to the observed potential because of IR is negligible, and the measured potentials are essentially "IR free."

Potentiodynamic polarization scans were performed on each sensor at each level upon the completion of the CP program, as illustrated in Figure 5.67. These polarization curves may be used to calculate an approximate local cathodic current density at each sensor level for a given average applied CP level. By taking the IR corrected applied cathodic potential as a function of vertical position for the pile from Figure 5.68, the locally applied current density may be approximated by observing the corresponding current density for that same applied potential on the IR corrected, potentiodynamic polarization curve developed for each sensor level (Figure 5.67). Figure 5.68 presents the local current densities for the entire pile as a function of the area averaged applied CP level. As can be seen in the figure, the nonuniform resistivity of the concrete pile restricts the ability to throw appreciable protection current into the highly resistive atmospheric zone, as was concluded based upon the potential measurements described previously. In Figure 5.69, the local current density at each level is presented as a function of the applied CP level. Again, little CP current was able to be supplied to the highly resistive atmospheric zone 50 cm and above the waterline. This figure also illustrates that the bulk of the CP current is applied to the region near the anode, with the local current densities dropping off above and far below the anode. From these data it is evident that local current densities >20 $\mu A/cm^2$ can occur in the region 25 cm above to 25 cm below the waterline at an area averaged cathodic current density of 1 $\mu A/cm^2$, an anticipated protection level in field applications.

Local Hydrogen Production, Absorption, and Achieved Hydrogen Concentrations

As discussed, hydrogen sensors were placed within the submerged, splash and atmospheric zones of piles 2 and 3 (Figures 4.45 and 4.46). By monitoring the hydrogen oxidation current output of each sensor via a zero resistance ammeter (ZRA), it was possible to observe when hydrogen permeation was taking place. Measurement of exact hydrogen permeation fluxes from the hydrogen sensors was confirmed through the use of decay transients obtained upon switching off each applied cathodic current density.[20] A representative rise and decay transient for one of the hydrogen sensors is illustrated in Figure 5.70a and 5.70b. Note the similarity of this rise transient to those observed with the Devanathan/Stachurski permeation technique illustrated in Figure 5.5.[21] This method was used to address any drift in the background current of each sensor as a function of time. Figures 5.71 and 5.72 present the observed steady state hydrogen permeation fluxes for each sensor at each level within piles 2 and

---

[20] Taking the difference between the steady state permeation flux before the cathodic charging current is turned off and the residual permeation flux once the embedded steel hydrogen sensor has depolarized from the applied cathodic potential (i.e., the decay transient method) is a common approach[20,21] to ensure valid permeation flux measurements. This technique is preferred to the rise transient technique since complicating factors such as oxide reduction and irreversible trapping are avoided.

[21] The rise and decay transients observed for the hydrogen sensors appear to be spread out over time when compared to those for a typical Devanathan/Stachurski experiment. This is because of time dependant variation of the boundary condition at the charging surface (i.e., the applied cathodic potential) of the hydrogen sensors during the application of each CP level. As a result, the effective charging current density (i.e., portion of the local applied current density because of the HER) is increasing with time.

3 (Figures 4.45 and 4.46) as a function of the applied CP current density.[22] These fluxes were then converted, as discussed in the experimental methodology section, into equivalent hydrogen concentrations present within the prestressing strand, as presented in Figures 5.74 and 5.75. As can be seen in Figure 5.50, for pile 2 (Figure 4.45), hydrogen permeation was observed in the splash zone at an applied current density of 1 μA/cm^2 (internally measured potential of -522 mV$_{SCE}$) and in the submerged zone 30 cm below the waterline at an applied current density of 2 μA/cm^2 (internal potentials of -711 and -942 mV$_{SCE}$ for the splash and submerged zones, respectively). Hydrogen permeation in excess of the most conservative detection limit was not observed in the atmospheric zone 30 cm above the waterline in pile 2 until the application of a current density of 2.5 μA/cm^2.

In pile 3 (Figure 4.46) permeation just in excess of the detection limit was observed 25 and 50 cm above the waterline (internal potentials of -270 and -313 mV$_{SCE}$) at an applied current density of 0.33 μA/cm^2, and at all levels, save the position 75 cm above the waterline, at an applied current density of 1.00 μA/cm^2. No measurements were possible at the waterline because of failure of that particular hydrogen sensor. The higher permeation fluxes in the submerged zones at high applied cathodic current densities are the result of the greater extent of CP achieved (Figure 5.65) due the high conductivity of the concrete at these positions. Permeation first occurs at lower current densities in the atmospheric zones because of increased acidity at the steel/concrete interface, but the lower concrete conductivity at these positions limits the degree of additional cathodic polarization as the applied cathodic current is increased (Figures 5.65 and 5.66). Moreover, Equation 62 illustrates that C_H rises slowly with cathodic overpotential in acidified Ca$^{(II)}$ environments (also shown in Figure 5.10). No permeation was observed in excess of the detection limit at the sensor located 75 cm above the waterline because of the poor throwing power of the CP in the drier, and hence less conductive, concrete at this elevation (Williams, 1995).

Applying Accepted CP Criteria

Currently, several CP criteria are used to define the adequate CP levels within an atmospherically exposed, steel-reinforced concrete structure. The first is known as the 100 mV depolarization criterion (NACE, 1990). In this technique, the structure is polarized such that the difference between the current-on and the completely depolarized potentials is at least 100 mV in magnitude, though some researchers have demonstrated that 100 mV of depolarization is inadequate and that 200 mV or more may be required (Funahashi, 1991). The second criterion is an absolute potential based criterion in which the reinforcement is polarized to a potential more negative than the reversible potential for iron oxidation (-780 mV$_{SCE}$) (Funahashi, 1991). In applying either of these criteria, care must be taken to ensure that the structure is not

---

[22] The claim that the application of CP will eventually increase the local pH of the acidified interfacial environment, shutting off hydrogen permeation, was not observed. That is to say that steady state hydrogen permeation fluxes were maintained over long time periods in all but a few instances, as illustrated in Figure 5.73a and 5.73b for applied current densities of 1 and 2 μA/cm^2.

overprotected, resulting in the production of cathodic hydrogen and the subsequent embrittlement of the reinforcing steel. In other words, can a pile be cathodically protected such that corrosion is abated in the high corrosion splash zone without the production of a steady state steel lattice hydrogen concentration in excess of $C_H^{critical}$ (e.g., 2 x 10^{-7} mol/cm^3 for bluntly notched specimens, as will be detailed) at some position in the reinforcement? Hartt et al. (1993) have proposed a CP safe-limit. This safe-limit is based upon constant extension rate experiments performed by Hartt et al. (1993) and Parkins et al. (1982) on prestressing steel tendon in saturated Ca(OH)$_2$ at various pH levels. It was concluded that if the applied potential is held to values more positive than -900 mV$_{SCE}$ (the thermodynamic reversible potential for hydrogen production, upon which this criterion is based, is -981 mV$_{SCE}$ at pH 12.5), minimal hydrogen embrittlement occurs. Hereinafter, these potentials (i.e., -780 and -900 mV$_{SCE}$) will be known as "potential thresholds."

Tables 5.4 and 5.5 compare the achieved levels of CP as a function of vertical position with the aforementioned CP criteria for piles 2 and 3 (Figures 4.45 and 4.46), respectively. Recall that there are several differences in the CP procedures applied to piles 2 and 3. The most significant of these is the longer stabilization time allowed for pile 3 (48 days versus 14 days). As a result, more negative applied potentials will be achieved for a given cathodic current density in pile 3 when compared to pile 2. In addition, since pile 3 is considerably taller than pile 2, with larger regions both above and below the waterline, the actual local current densities may differ from those in pile 2, given the anticipated extremely nonuniform current distributions found within a marine bridge pile, for a corresponding average applied cathodic current density.

100 mV and 200 mV depolarization criteria. As can be seen in Table 5.4, the 100 mV depolarization criterion is met at all sensor levels in pile 2 for all applied cathodic current densities ranging from 1 to 2.5 μA/cm^2 (1 μA/cm^2 was the lowest CP level applied to pile 2).

In the case of pile 3, 100 mV of depolarization was achieved at a lower applied current density than that seen by pile 2, the result of the longer stabilization time allowed for pile 3. The 100 mV criterion was met in pile 3 at all levels, save the atmospheric level 75 cm above the waterline, at current densities equivalent to and greater than 0.33 μA/cm^2. 100 mV of depolarization was achieved 75 cm above the waterline (as well as at all other levels) at an applied current density of 1 μA/cm^2. If it is instead assumed that 200 mV of depolarization is required, it can be seen that this criterion was met at all positions within pile 2 at an applied current density of 1 μA/cm^2. For pile 3, the 200 mV criterion was met at and below the waterline at 0.66 μA/cm^2, 25 cm above the waterline at 1 μA/cm^2 (as well as for all positions at and below the waterline), 50 cm above the waterline at 1.66 μA/cm^2, and finally, 75 cm above the waterline at an applied current density of 2.5 μA/cm^2.

Absolute potential (-780 mV$_{SCE}$) criterion. The absolute potential criterion (-780 mV$_{SCE}$) is met for pile 2 (Table 5.4) at an area averaged current density of 2 μA/cm^2 in the submerged (30 cm below the waterline) and splash zones (at the waterline). This criterion was also achieved at a current density of 2.5 μA/cm^2 in the atmospheric zone, 30 cm above the

waterline (Table 5.4). In pile 3 (Table 5.5), the absolute potential criterion is met only in the submerged zone (25 and 50 cm below the waterline) at a current density of 1 μA/cm^2, and within the splash zone at an applied current density of 1.33 μA/cm^2. Again, the criterion was met at a lower applied current density for pile 3 as a result of the longer stabilization time allowed for that pile. The -900 mV$_{SCE}$ overprotection criterion proposed by Hartt is not exceeded for any condition except in the submerged zone of pile 2 (Figure 4.45) at an applied current density of 2 μA/cm^2, and in the splash zone at an applied current density of 2.5 μA/cm^2. In pile 3 (Figure 4.46), the -900 mV$_{SCE}$ criterion was exceeded within the submerged zone (25 and 50 cm below the waterline) at applied current densities in excess of 1.66, 2.00, 2.50, and 3.00 μA/cm^2, and within the splash zone at a current density of 1.66 μA/cm^2. Hydrogen production was observed under many of the CP levels investigated, though the magnitude of the corresponding hydrogen concentrations was often below the threshold concentrations for embrittlement that will be discussed.

Conclusions From Pile Results

Several laboratory-scale piles have been constructed and cathodically polarized in an effort to assess the local environmental and electrochemical conditions at the steel/concrete interface within the pile. There are three primary conclusions that may be drawn from these results:

1. Polarization of laboratory-scale piles to very low applied current densities (0.33 μA/cm^2 and greater) resulted in a cathodic reaction rate at the steel/concrete interface that exceeded the rate with which oxygen could diffuse to that interface. As a result, hydrogen production became a viable cathodic reaction, introducing the potential for hydrogen production, absorption, and the subsequent embrittlement of the reinforcement;

2. It was not possible to achieve many of the accepted "sufficient protection criteria," such as the 200 mV depolarization criterion or absolute potential criterion, throughout the pile without hydrogen production at some point near or below the waterline within the pile;

3. Although quantitative information on the hydrogen concentrations within the prestressing strand has been obtained, a comparison to fracture initiation and threshold stress intensity as a function of C_H is required to assess the implications of those hydrogen concentrations on the mechanical strength of the reinforcement, in order to establish whether or not embrittlement has taken place. This comparison revealed that achievement of sufficient protection throughout the entire pile according to any of the criteria more substantial than the 100 mV depolarization criterion was not possible without the production of an embrittling hydrogen concentration at some point within the pile. In fact, it was not possible to achieve any of the protection

70

criteria without the observance of a measurable permeation flux at some point within the pile.

Detecting Hydrogen Production and the Magnitude of Achieved Concentrations

Hydrogen production was observed at relatively low applied cathodic current densities for both pile 2 and pile 3. In pile 2, hydrogen permeation was observed at the hydrogen sensor within the splash zone at an applied cathodic current density of 1 $\mu A/cm^2$. Polarization to 2 $\mu A/cm^2$ resulted in the detection of hydrogen permeation within the submerged zone 30 cm below the waterline. Finally, hydrogen permeation was observed at all sensor levels for an applied cathodic current density of 2.5 $\mu A/cm^2$.

Comparing the observed hydrogen concentrations to our previously determined threshold concentrations for embrittlement, we see that only at an applied cathodic current density of 2.5 $\mu A/cm^2$ was this threshold exceeded, and only within the submerged zone 30 cm below the waterline.

In pile 3, hydrogen permeation was observed 25 and 50 cm above the waterline at an applied cathodic current density of 0.33 $\mu A/cm^2$. Note again that the hydrogen sensor located at the waterline within this pile malfunctioned prior to the application of CP. Further polarization to 0.66 $\mu A/cm^2$ leads to hydrogen permeation 50 cm below the waterline. Finally, upon polarization to 1.00 $\mu A/cm^2$, permeation was observed at all sensor levels save the one 75 cm above the waterline. Hydrogen permeation was never observed at the sensor level 75 cm above the waterline, because of the difficulty in throwing sufficient CP through the highly resistive atmospheric zone to this level.

Comparing the hydrogen concentrations achieved to the critical hydrogen concentrations required for embrittlement, we see that the threshold for bluntly notched tensile bars (the lowest, and thus most conservative) was exceeded within the submerged zone 50 cm below the waterline at an applied cathodic current density of 1.33 $\mu A/cm^2$. Further polarization to 1.66 $\mu A/cm^2$ resulted in the exceeding of the same threshold 25 cm below the waterline. Polarization to higher levels, although it did increase the concentrations achieved throughout the pile, did not result in the detection of an embrittling concentration at any other functional sensor level within the pile.

To summarize, the results suggest that hydrogen production and uptake can occur at current densities as low as 0.33 $\mu A/cm^2$, but that the critical hydrogen concentration established for bluntly notched prestressing steel is not exceeded in the reinforcement at CP levels as high as 1 $\mu A/cm^2$. Application of larger applied current densities (1.33 $\mu A/cm^2$ and greater) did, however, result in significant local steady state steel lattice hydrogen concentrations. Here, the applied potentials were more negative than -900 mV_{SCE}. Therefore, in answer to the critical question posed, adequate CP (according to the either the 100 mV depolarization or the -780 mV

71

absolute potential CP criteria) cannot be achieved without some hydrogen production and uptake in the prestressing steel. However, it may be possible to achieve adequate CP based on the aforementioned criteria without exceeding the critical hydrogen concentration required for embrittlement of a bluntly notched tensile bar.

Assessing the Implications of Local Hydrogen Concentrations for Actual Piles with a Distribution of Corrosion- and Fatigue-Related Flaws That Concentrate Stress

Hydrogen concentrations that were embrittling in nature (as high as 8×10^{-7} mol/cm^3) were detected within regions near and below the waterline for laboratory-scale concrete piles at CP levels above 1.33 μA/cm^2. However, as discussed, failure of the prestressing tendon depends on a critical combination of local hydrogen concentration *and* local stress. Although the remotely applied stress is well defined (70% of the yield strength, or ~1200 MPa), assessment of the local stress requires that the nature of the corrosion generated defects along the reinforcement be known. This information is generally lacking in the literature for prestressing steels or other carbon steels in alkaline environments.

Pits are found to be hemispherical in nature and of various depths, based on studies performed by Marsh (1988) and Szklarska-Smialowska (1986) for iron in alkaline environments. In Marsh's study, pit depths ranging from 0.2 to 2.5 mm were observed. Within the literature, a number of researchers have calculated the stress intensification factor ($\sigma_{max.\ local}/\sigma_{applied}$) for such geometries (Pilkey, 1997) as illustrated in Figure 8.1. Based upon this information, several scenarios may be envisioned. For example, if a small, sharp pit is present (depth of 0.2 mm yielding a d/h of 0.08), the resulting stress concentration factor will be 2.09, and as such a local stress of 2487 MPa will be achieved in front of the pit. Referring back to Figure 5.19, we see that for that local stress, failure of the tendon is likely at a hydrogen concentration of 8×10^{-7} mol/cm^3 (i.e., $\sigma_{local} > \sigma_f$ as determined via CERT experiments). If, on the other hand, a large, blunt pit 2 mm deep were present (d/h = 0.8), the stress concentration factor for the pit would be 1.5, resulting in a local stress of 1785 MPa. Based upon the aforementioned CERT data, a blunt pit 2 mm deep would not result in failure of the tendon for the hydrogen concentrations as high as 8×10^{-7} mol/cm^3 (i.e., local stress is less than the fracture initiation stress). It has also been argued by some researchers that fatigue cracks may be present along the tendon. Conducting a similar analysis as presented, assuming that K_{th} may be described through the expression

$$K_{TH} = A\ \sigma_{70\%YS} \sqrt{\pi a}$$ (72)

where A is a geometric factor, assumed to be 1 for this calculation. Based upon the K_{IHE} for the prestressing tendon at a hydrogen concentration of 8×10^{-7} mol/cm^3 of 50 MPa$\sqrt{m}$ (Figure 5.24), crack lengths of 0.5 mm or greater will result in a sufficiently high local stress to cause failure of the tendon. At this point it should also be noted that higher hydrogen concentrations will result in further reductions in the stress or stress intensity required to break a tendon, as illustrated in Figures 5.19, 5.21, and 5.24. Consequently, as the hydrogen concentration increases, a

72

decreasingly sharp flaw is required to achieve a local stress of sufficient magnitude to initiate a crack.

The implications of a failed tendon should also be considered. If a single tendon fails, a portion of the load carried by that tendon will be transferred to the other tendons within the pile. As a result, a higher effective load (and corresponding local stress) will be applied to the other tendons. As a result, failure of one tendon may result in the sympathetic failure of others because of load transferral.

CONCLUSIONS

* *The local chemical and physical environment of embedded prestressing steels varies with vertical position in a prestressed concrete pile with immersed, splash, and atmospheric zones.* In the immersed zones, pore structures tend to be saturated, leading to low ionic resistivities, low oxygen transport rates, and low carbon dioxide transport rates. Higher ionic resistivities, oxygen, and CO_2 transport rates occur in the splash zone. Corrosion rates are highest in this zone. The highest resistivities are obtained in the atmospheric zone where the concrete is drier. Oxygen and CO_2 transport rates are faster, but the overall moisture content is lower. All three zones appear to be able to support steel-occluded cell formation where acidification because of ferrous and, possibly, ferric ion hydrolysis can lower the local pH at the steel interface.

* *The observed open circuit potential of the reinforcement within the submerged, splash, and atmospheric zones indicates that initiation of localized corrosion within occluded geometries along the reinforcing tendon should be anticipated.* The open circuit potential of the reinforcement at all locations at which it was measured was more negative than the pitting potential in chloride-contaminated pore solutions but more positive than the potential required to initiate crevice corrosion. As a result, although pitting or general corrosion of the reinforcement is unlikely, the initiation of crevice corrosion is to be anticipated, followed by the development of an acidic local environment within the resulting occluded site.

* *The local pH of the concrete/steel or steel/steel occluded interface can drop below 6 because of a sequence of local deaeration, dissolution of iron, ferrous ion hydrolysis, and acidity accumulation at occluded sites during the free corrosion of a concrete pile.* The possibility of crevice corrosion of steel embedded in concrete at the expected open circuit potentials, chloride ion concentrations, and aeration levels confirms this observation. The pH may become more acidic in splash and atmospheric zone owing to the fast vapor phase transport of oxygen through the non-moisture saturated pore structure that in turn results in the oxidation of ferrous ions (Fe^{2+}) to ferric ions (Fe^{3+}). In contrast, the pH of a concrete pore solution within the bulk of the concrete may remain at an alkaline pH of 12.6. The ramifications of a local pH that varies with position in a concrete pile is that no single reversible electrode potential for reduction of water exists.

73

- *Current and potential distributions, and the corresponding extent of depolarizations upon removal of cathodic polarization, were nonuniform at vertical positions above the waterline skirt anode in the atmospheric zone.* At distances greater than 30.5 cm above the waterline anode skirt, very little cathodic polarization was achieved, even at high cathodic current densities (e.g., area averaged values >1.5 $\mu A/cm^2$). Resulting depolarization levels were, correspondingly, below 200 mV. In contrast, immersed zones were readily polarized and exhibited large depolarizations. This difference was attributed to the low resistivity of the immersed zone concrete and the high resistivity of the concrete in the atmospheric zone.

- *At modest levels of CP (e.g., area averaged current densities of 0.33 $\mu A/cm^2$ and above) such as might be applied to a prestressing steel in a concrete pile in practice, the rate of cathodic reactions at the steel surface exceeds the rate with which oxygen may diffuse through a standard concrete cover of 5 cm.* This situation results in a decreasing applied current-on potential until a cathodic reaction other than the reduction of water; in this case, the hydrogen evolution reaction becomes thermodynamically possible even at modest impressed current CP levels. This phenomenon occurs more readily in the splash and submerged zones where the water-saturated pore structure within the concrete hinders oxygen diffusion.

- *The minimum accepted depolarization level (i.e., 100 mV) for suppression of corrosion in the splash zone at the waterline could be achieved only under conditions that also resulted in hydrogen production and absorption at some position within the pile.* An area-averaged current density of 0.33 $\mu A/cm^2$ was sufficient to achieve 100 mV of depolarization in the region from 25 cm above to 25 cm below the waterline. However, hydrogen production and absorption in steel were detected at this applied current density at 25 and 50 cm above the waterline. Fortunately, however, absorbed hydrogen concentrations were not of sufficient magnitude to cause embrittlement based on the threshold hydrogen concentrations determined for sharply notched, bluntly notched, and fatigue precracked prestressing steel.

- *The 200 mV depolarization criterion for suppression of corrosion in the splash zone at the waterline could be achieved only under conditions that also resulted in hydrogen production and absorption at some position within the pile.* An area-averaged current density of 1.00 $\mu A/cm^2$ was sufficient to achieve 200 mV of depolarization in the region from 25 cm above to 25 cm below the waterline. However, hydrogen production and absorption in steel were detected at this applied current density at all sensor levels from 50 cm above the waterline to 50 cm below. Fortunately, however, absorbed hydrogen concentrations were not of sufficient magnitude to cause embrittlement based on the threshold hydrogen concentrations determined for sharply notched, bluntly notched, and fatigue precracked prestressing steel. If, however, it was desired to achieve 200 mV of depolarization 50 cm above the waterline (achieved at a current density of 1.66 $\mu A/cm^2$), a hydrogen concentration in excess of the critical concentration for embrittlement of bluntly notched specimens (the most conservative of the criteria determined in this study) was observed 50 cm below the waterline.

- *The absolute potential criterion for mitigation of corrosion (i.e., -780 mV$_{SCE}$) for suppression of corrosion could be achieved only in the splash zone at the waterline under conditions that also caused hydrogen production and absorption such that the critical levels for hydrogen absorption were exceeded at some position within the pile.* Application of a cathodic current density of 2.5 μA/cm² for 14 days was required to achieve adequate CP according to the -780 mV$_{sce}$ criterion in the region from 30 cm above to 30 cm below the waterline. However, polarization to this level resulted in a local hydrogen concentration in excess of the critical hydrogen concentration for crack initiation of 2 x 10^{-7} mol/cm³ determined for bluntly notched prestressing steel, at a position 30 cm below the waterline. Application of a cathodic current density of only 1.33 μA/cm² for 48 days was required to achieve an adequate CP according to the -780 mV$_{sce}$ criterion in the region at and below the waterline. However, polarization to this level resulted in a local hydrogen concentration 50 cm below the waterline in excess of the critical hydrogen concentration for crack initiation of 2 x 10^{-7} mol/cm³ for bluntly notched prestressing steel.

- *Differing threshold potentials for hydrogen embrittlement of a bluntly notched prestressing steel were obtained depending upon the exact chemistry of the simulated pore solution or occluded site solution, particularly its pH.* Specifically, the threshold potential was -980 mV$_{sce}$ in saturated Ca(OH)$_2$, approximately -1.0 V$_{sce}$ for mortar-covered samples immersed in ASTM artificial ocean water, -876 mV$_{sce}$ in ASTM artificial ocean water (pH = 8.2), and approximately -710 mV$_{sce}$ in a simulated occluded crevice site solution at pH = 6. All potentials were IR corrected. Similarly, the applied cathodic current density that produced embrittlement was approximately 1 μA/cm² in saturated Ca(OH)$_2$, ~4 μA/cm² in ASTM ocean water, and ~ 9 μA/cm² in the occluded crevice solution (these differences relate to the efficiency of hydrogen uptake in each solution). Therefore, there is neither a discrete applied potential nor a specific applied current density that may be used as a threshold that would ensure that corrosion is abated throughout the steel-reinforced structure, although at the same time avoiding the embrittlement of the steel reinforcement. For example, use of a safe potential limit of -710 mV$_{sce}$, although ensuring that the reinforcement is not embrittled, does not meet the -780 mV absolute potential criterion that ensures adequate CP, though it may meet the 100 or 200 mV depolarization criteria.

- *The results of this project indicate that a hydrogen concentration-based threshold for the prevention of hydrogen embrittlement can be universally applied to prestressing tendons, whereas a potential-based criterion is not universal and requires an intimate understanding of the local pH as a function of position at the steel interface.* The results of this project have established that the local pH, and therefore hydrogen production rates under CP, may vary with vertical position because of crevice corrosion between strands of prestressing steel wires. Therefore, the safe potential for avoidance of hydrogen production would need to be based on the minimum expected local pH and differs from the -980 mV$_{sce}$ proposed in the literature, assuming saturated Ca(OH)$_2$ as the homogeneous local concrete pore solution. The safe potential based on a Nernst equation (reversible electrode potential for hydrogen production) approach would vary with local pH in the pile. The safe conditions for

avoidance of hydrogen embrittlement have also been investigated. This condition is not based on the threshold potential for hydrogen production but instead is based on the notion that a critical combination of hydrogen concentration and stress state can be defined that initiates steel crack initiation. The CP conditions, applied stress/notch geometry, and pile positions that enable such a critical hydrogen concentration to be attained have been established in laboratory piles. This leads to the distinct possibility of using hydrogen sensors to detect actual steel hydrogen concentrations during the application of CP. The hydrogen concentrations achieved under various levels of CP can then be compared to the critical levels for embrittlement (the most conservative of which was 2×10^{-7} mol/cm^3, determined for bluntly notched prestressing steel). Safe CP limits can thereby be defined using the critical hydrogen concentration as a threshold. This project has also addressed the question of whether adequate levels of CP for suppression of corrosion can be achieved without exceeding this threshold.

- *Currently, we can recommend only that modest levels of impressed current CP (e.g., area averaged current densities of 0.33 μA/cm^2 and below) be applied to cathodically protect prestressing steels in a concrete pile using waterline skirt anodes.* Such a level of CP did not exceed the threshold for embrittlement of a bluntly notched prestressing tendon, the most conservative (i.e., lowest) of the threshold embrittlement levels determined in this study. However, this level of CP should be tested on an actual piles in the field, recognizing the extreme nonuniformity of current and potential distributions.

RECOMMENDATIONS FOR APPLYING THIS RESEARCH

1. *Assess the condition of the pile to be protected.* This research has demonstrated that for a chloride-contaminated, marine bridge pile there will be variations in electrochemical conditions at the steel/concrete interface. As such, it is clear that assessment of the overall condition of the pile to be protected (i.e., anticipated degree of corrosion, positional variations in concrete resistivity, and chloride content) be assessed prior to the application of CP.

2. *Monitor the CP level as a function of position.* The applied CP level as a function of vertical position will vary, both in terms of the applied potential and current density. As a result, monitoring of the CP level as a function of position is crucial to ensure that overprotection and potential embrittlement of the reinforcement is not taking place. In other words, simply measuring an "average" applied current density or potential as is often done in practice is inadequate to prevent overprotection-related damage.

3. *Avoid placing the impressed current anode at or very near the waterline.* Because of the nonuniform resistivity of the concrete, and varying local environment at the steel/concrete interface, positioning of the anode is very important. Placement of the impressed current

anode at or very near the waterline must be avoided because of the lower resistivity of the concrete within regions near and below the waterline, resulting in severe overprotection of those regions prior to the achievement of adequate CP in the splash and atmospheric zones. A better system would include separate anodes and accompanying current rectifiers for regions above and below the waterline.

REFERENCES

Akhurst, K. N. & T. J. Baker (1981). The threshold stress intensity for hydrogen-induced crack growth. *Metallurgical Transactions A* 12A(6):1059-1070.

Alonso, M. C., R. P. M. Procter et al. (1993). Susceptibility to stress corrosion cracking of a prestressing steel in NaHCO$_3$ solutions. *Corrosion Science* 34(6):961-973.

Alp, T., B. Dogan et al. (1987). The effect of microstructure in the hydrogen embrittlement of a gas pipeline steel. *Journal of Materials Science* 22:2105-2112.

Andersson, K., B. Allard et al. (1989). Chemical composition of cement pore solutions. *Cement and Concrete Research* 19(3):327-332.

Arup, H., O. Klinghoffer et al. (1997). *Long term performance of MnO2 reference electrodes.* Corrosion/97, New Orleans, NACE.

Athanassiadis, A., J. Boissenot et al. (1981). Linear elastic fracture mechanics computations of cracked cylindrical tensioned bodies. *International Journal of Fracture* 17(6):553-566.

Beachem, C. (1972). A new model for hydrogen assisted cracking (hydrogen embrittlement). *Metallurgical Transactions* 3(2):437-451.

Bergsma, F., J. W. Boon et al. (1977). Endurance test for determining the susceptibility of prestressing steel to hydrogen embrittlement. *Heron* 22(1):46-76.

Blackburn, W. (1976). Calculation of stress intensity factors for straight cracks in grooved and ungrooved shafts. *Engineering Fracture Mechanics* 8:731-736.

Bockris, J. M., J. McBreen et al. (1965). The hydrogen evolution kinetics and hydrogen entry into a-iron. *Journal of the Electrochemical Society* 112(10):1025-1031.

Brooks, C. & Y. Chawla (1987). Some microstructural observations of the effect of austenite grain and twin boundaries on a moving pearlite interface. *Microstructural Science* 14:159-181.

Brown, B. (1971). Stress corrosion cracking of high strength steels. *The theory of stress corrosion cracking in alloys*. J. Scully (ed.). Leeds, England, W.S. Maney and Sons, Ltd.

Carpinteri, A. (1992). Stress intensity factors for straight-fronted edge cracks in round bars. *Engineering Fracture Mechanics* 42(6):1035-1040.

Caspers, M., C. Mattheck et al. (1986). Fatigue crack propagation in cylindrical bars. *Z. Werkstofftech* 17:327-333.

Caspers, M. & C. Mattheck (1987). Weighted averaged stress intensity factors of circular fronted cracks in cylindrical bars. *Fatigue and Fracture of Engineering Materials and Structures* 9(5):329-341.

Chaix, O., W. H. Hartt et al. (1995). Localized cathodic protection of simulated prestressed concrete pilings in seawater. *Corrosion* 51(5):386-398.

Chandhok, V., A. Kasak et al. (1966). Structures and strengthening mechanisms in carbon steel wire. *Transactions of the ASM* 59:288-301.

Cherry, B. W. & S. M. Price (1980). Pitting, crevice and stress corrosion cracking studies of cold drawn eutectoid steels. *Corrosion Science* 20:1163-1183.

Chin, D. & C. Tsang (1978). Mass transfer to an impinging jet electrode. *Journal of the Electrochemical Society* 125(9):1461-1470.

Choo, W. Y. & J. Y. Lee (1982). Thermal analysis of trapped hydrogen in pure iron. *Metallurgical Transactions A* 13A(2):135-140.

Christensen, B. J., T. O. Mason et al. (1992). Influence of silica fume on the early hydration of portland cement using impedance spectroscopy. *Journal of the Americal Ceramic Society* 75(4):939-945.

Cialone, H. & R. Asaro (1979). The role of hydrogen in the ductile fracture of plain carbon steels. *Metallurgical Transactions A* 10A(3):367-375.

Devanathan, M. A. V. & Z. Stachurski (1962). The adsorption and diffusion of electrolytic hydrogen in palladium. *Proceedings of the Royal Society of Medicine (London)* 270A:90-102.

Devanathan, M. A. V. & Z. Stachurski (1964). The mechanism of hydrogen evolution on iron in acid solutions by determination of permeation rates. *Journal of the Electrochemical Society* 111(5):619-623.

Diamond, S. (1975). Long term status of calcium hydroxide saturation of pore solutions in hardened cements. *Cement and Concrete Research* 5:607-616.

Embury, J. & R. Fisher (1966). The structure and properties of drawn pearlite. *Acta Metallurgica* 14(2):147-159.

Flis, J. & T. Zakroczymski (1992). Enhanced hydrogen entry in iron at low anodic and low cathodic polarizations in neutral and alkaline solutions. *Corrosion* 48(7):530-539.

Flynn, C. (1964). Monodefect annealing kinetics. *Physical Review A* 133(2A):A587-A595.

Funahashi, M. & J. B. Bushman (1991). Technical review of 100mV polarization shift criterion for reinforcing steel in concrete. *Corrosion* 47(5):376-386.

Gangloff, R. (1986). *A Review of the threshold for hydrogen environment embrittlement of steel.* Corrosion Prevention and Control: 33rd Sagamore Army Materials Research Conference, Burlington, VT, U.S. Army Materials Technology Laboratory.

Garber, R., I. Bernstein et al. (1981). Hydrogen assisted ductile fracture of spheroidized carbon steels. *Metallurgical Transactions A* 12A(2):225-234.

Gerberich, W. W. & Y. T. Chen (1975). Hydrogen controlled cracking: An approach to threshold stress intensity. *Metallurgical Transactions A* 6A(2):271-278.

Gileadi, E. (1993). *Electrode kinetics for chemists, chemical engineers, and materials scientists.* New York, VCH Publishers.

Gonzalez, J., A. Molina et al. (1990). On the mechanism of steel corrosion in concrete: the role of oxygen diffusion. *Magazine of Concrete Research* 42(150):23-27.

Gonzalez, J. A., E. Otero et al. (1993). Initial steps of corrosion in the steel/Ca(OH)2 + Cl- system: The roll of heterogeneities on the steel surface and oxygen supply. *Cement and Concrete Research* 23:33-40.

Gratten-Bellew, P. E. (1994). Alkalai contribution from limestone aggregate to pore solution of old concrete. *ACI Materials Journal* 91(2):173-177.

Hansson, C. M. (1995). Concrete: The advanced material of the 21st century. *Metallurgical Transactions A* 26A(6).

Hartt, W. A Critical evaluation of cathodic protection for prestressing steel in concrete. *Corrosion of reinforcement in concrete.* C. T. Page, KWJ; Bamforth, PB. New York, Elsevier Aplied Science: 515-524.

Hartt, W. H., C. C. Kumria et al. (1993). Influence of potential, chlorides, pH, and precharging time on embrittlement of cathodically polarized prestressing steel. *Corrosion* 49(5):377-385.

Hartt, W. H., O. Chaix et al. (1994). *Localized cathodic protection of simulated prestressed concrete pilings in sea water*. Corrosion 94, Baltimore, NACE.

Hillert, M. (1962). The formaition of pearlite. *Decomposition of austenite by diffusional processes*. V. Zackay and H. Aaronson. New York, Interscience:197-247.

Hirth, J. P. (1980). Effects of hydrogen on the properties of iron and steel. *Metallurgical Transactions A* 11A(6):861-890.

Hong, G.-W. & J.-Y. Lee (1983). The interaction of hydrogen with iron oxide inclusions in iron. *Materials Science and Engineering* 61:219-225.

Hong, D., W. Fan et al. (1993). Study and application of impressed current cathodic protection technique for atmospherically exposed salt-contaminated reinforced concrete structures. *ACI Materials Journal* 90(1):3-7.

Hope, B. B. & A. K. C. Ip (1987). Chloride corrosion threshold in concrete. *ACI Materials Journal*:306-314.

Hosford, W. (1964). Microstructural changes during deformation of (011) fiber-textured metals. *Transactions of the Metallurgical society of AIME* 230(2):12-15.

Hyzak, J. M. & I. M. Bernstein (1976). The role of microstructure on the strength and toughness of fully pearlitic steels. *Metallurgical Transactions A* 7A:1217-1224.

Isecke, B. & J. Mietz (1993). The risk of hydrogen embrittlement in high-strength prestressing steels under cathodic protection. *Steel Research* 64(1).

Jeng, H. W., L. H. Chiu et al. (1990). Effect of pearlite morphology on hydrogen permeation, diffusion, and solubility in carbon steels. *Metallurgical Transactions A* 21A:3257-3259.

Johnson, D. L., G. Krauss et al. (1987). Correlation of microstructural parameters and hydrogen permeation in carbon steel. *Metallurgical Transactions A* 18A:717-721.

Kavishe, F. P. L. & T. J. Baker (1986). Micromechanisms of cleavage fracture in fully pearlitic steels. *Materials Science and Technology* 2(6):583-588.

Kessler, R. J., R. G. Powers et al. (1995). Update on sacraficial anode cathodic protection on steel reinforced concrete structures in seawater. *Corrosion 95, Paper 516.* Houston, NACE.

Kissenger, H. (1957). Reaction kinetics in differential thermal analysis. *Analytical Chemistry* 29(11):1702-1706.

Klein, P. A., R. A. Hays et al. (1993). Hydrogen cracking initiation of a high strength steel weldment. *Slow strain rate testing for the evaluation of environmentally induced cracking: Research and engineering applications.* R. D. Kane. Philadelphia, American Society for Testing and Materials, 1210: 202-222.

Kummick, A. J. & H. H. Johnson (1974). Hydrogen transport through annealed and deformed armco iron. *Metallurgical Transactions A* 5(5):1199-1206.

Langstaff, D., G. Meyrick et al. (1981). Hydrogen induced delayed failure of high strength alloy steel wires. *Corrosion* 37(8):429-437.

Lee, J. Y., J. L. Lee et al. (1982). Thermal analysis of trapped hydrogen in AISI 4340 steel. *Current solutions to hydrogen problems in steels.* C. G. Tnterrante and G. M. Pressouyre, ASM: 423-427.

Lee, H. G. & J.-Y. Lee (1984). Hydrogen trapping by TiC particles in iron. *Acta Metallurgica* 32(1):131-136.

Lee, K., J.-Y. Lee et al. (1984). A study of hydrogen-trapping phenomena in AISI 5160 spring steel. *Materials Science and Engineering* 67: 213-220.

Levan, A. & J. Royer (1993). Part-circular surface cracks in round bars under tension, bending and twisting. *International Journal of Fracture* 61:71-99.

Lewandowski, J. J. & A. W. Thompson (1986). Microstructural effects on the cleavage fracture stress of fully pearlitic eutectoid steel. *Metallurgical Transactions A* 17A(10):1769-1786.

Lewandowski, J. J. & A. W. Thompson (1986). Effects of the prior austenite grain size on the ductility of fully pearlitic eutectoid steel. *Metallurgical Transactions A* 17A:461-472.

Lewandowski, J. J. & A. W. Thompson (1987). Micromechanics of cleavage fracture in fully pearlitic microstructures. *Acta Metallurgica* 35(7):1453-1462.

Lillard, R. & J. Scully (1996). Hydrogen absorption in iron exposed to simulated concrete pore solutions. *Corrosion* 52(2):125-137.

Luppo, M. I. & J. Overjero-Garcia (1991). The influence of microstructure on the trapping and diffusion of hydrogen in a low carbon steel. *Corrosion Science* 32(10):1125-1136.

Marandet, B. (1977). Effect of cold work on the dissolution and diffusion of hydrogen in unalloyed carbon steels. *Stress Corrosion Cracking and Hydrogen Embrittlement of Iron Base Alloys (NACE-5)*.

Marsh, G., I. Bland et al. (1988). Statistical study of pit ptopogation in carbon steel under nuclear waste disposal conditions. *British Corrosion Journal* 23(3):157-164.

McBreen, J., L. Nanis et al. (1966). A method for determination of the permeation rate of hydrogen through metal membranes. *Journal of the Electrochemical Society* 113(11): 1218-1222.

McGuinn, K. & J. R. Griffiths (1977). Rational test for stress corrosion crack resistance of cold drawn prestressing tendon. *British Corrosion Journal* 12(3):152-157.

Miller, L. E. & G. C. Smith (1970). Tensile fractures in carbon steel. *Journal of the Iron and Steel Institute* 208(11):998-1005.

Monfore, G. E. & G. J. Verbeck (1960). Corrosion of prestressed wire in concrete. *Journal of the American Concrete Institute* 32(11):491-515.

NACE (1990). *Cathodic protection of reinforcing steel in atmospherically exposed concrete structures.* Houston.

Namboodhiri, T. & L. Nanis (1973). Concentration dependance of hydrogen diffusion in armco iron. *Acta Metallurgica* 21(5):663-672.

Nanis, L. & T. K. G. Namboodhiri (1972). Mathematics of the electrochemical extraction of hydrogen from iron. *Journal of the Electrochemical Society* 119(6):691-694.

Ono, K. & M. Meshii (1992). Hydrogen detrapping from grain boundaries and dislocations in high purity iron. *Acta Metallurgica* 40(6):1357-1364.

Onyewuenyi, O. A. & J. P. Hirth (1981). The effect of hydrogen on microhardness of spheroidized AISI 1090 steel. *Scripta Metallurgica* 15(1):113-118.

Oriani, R. A. (1970). The diffusion and trapping of hydrogen in steel. *Acta Metallurgica* 18(1): 147-157.

Oriani, R. & P. Josephic (1979). Hydrogen enhanced load relaxation in a deformed medium carbon steel. *Acta Metallurgica* 27:997-1005.

Otero, E., J. Gonzalez et al. (1990). *On the generation of local acid pH in concrete structures.* 11th International Corrosion Congress, Florence, Italy, Associazione Italiana di Metallurgia.

Pangrazzi, R., W. H. Hartt et al. (1994). Cathodic polarization and protection of simulated prestressed concrete pilings in seawater. *Corrosion* 50(3):186-196.

Papadakis, V. G., C. G. Vayenas et al. (1989). A reaction engineering approach to the problem of concrete carbonation. *AIChE Journal* 35(10):1639-1650.

Park, Y. J. & I. M. Bernstein (1979). The process of crack initiation and effective grain size for cleavage fracture in pearlitic steel. *Metallurgical Transactions A* 10A(11):1653-1664.

Parkins, R. N., M. Elices et al. (1982). Environment sensitive cracking of prestressing steels. *Corrosion Science* 22(5):379-405.

Pourbaix, M. (1971). *The electrochemical basis for clocalized corrosion.* NACE-3, NACE.

Pourbaix, M. (1974). *Atlas of electrochemical equilibria in aqueous solutions.* Houston, NACE.

Price, S. M. (1984). The effect of sulphides on the passivity, crevice corrosion, and hydrogen embrittlement of steel prestressing tendons. *International Congress on Metallic Corrosion* 2:262-269.

Quick, N. R. & H. H. Johnson (1978). Hydrogen and deuterium in iron, 49-506 C. *Acta Metallurgica* 26:903-907.

Raju, I. & J. Newman (1986). Stress-intensity factors for circumferential surface cracks in pipes and rods under tension and bending. *Fracture Mechanics: Seventeenth Volume.* J. Underwood, R. Chait, C. Smith et al. Philadelphia, ASTM. 905:789-805.

Rathenau, G. & G. Baas (1954). Electron-optical observations of transformations in eutectoid steel. *Acta Metallurgica* 2(10):875-883.

Rechenberg, W. & S. Sprung (1983). Composition of the solution in the hydration of cement. *Cement and Concrete Research* 13:119-126.

Scully, J. R., J. A. Van Der Avyle et al. (1991). The influence of palladium on the hydrogen assisted cracking resistance of PH 13-8 Mo stainless steel. *Metallurgical Transactions A* 22A(10):2429-2444.

Sedriks, A. (1996). *Corrosion of stainless steels.* New York, J. Wiley Interscience.

Si, E. (1990). Stress intensity factors for edge cracks in round bars. *Engineering Fracture Mechanics* 37(4):805-812.

Song, R.-H. & S. Pyun (1990). Hydrogen permeation through a bilayer of Fe/electrodeposited Ni. *Journal of the Electrochemical Society* 137(4):1051-1056.

Szklarska-Smialowska, Z. (1986). *Pitting corrosion of metals.* Houston, NACE.

Thompson, A. & J. Chesnutt (1979). Identification of a fracture mode: the tearing topography surface. *Metallurgical Transactions A* 10A(8):1193-1196.

Thompson, A. W. (1985). Hydrogen assisted fracture at notches. *Materials Science and Technology* 1(9):711-718.

Toribio, J., A. M. Lancha et al. (1991). Hydrogen embrittlement of pearlitic steels: Phenomenological study on notched and precracked specimens. *Corrosion* 47(10):781-791.

Toribio, J., A. M. Lancha et al. (1991). Macroscopic variables governing the microscopic fracture of pearlitic steels. *Materials Science and Engineering A* 145:167-177.

Toribio, J., A. Lancha et al. (1992). The tearing topography surface as the zone associated with hydrogen embrittlement process in pearlitic steel. *Metallurgical Transactions A* 23A(5): 1573-1584.

Toribio, J. & M. Elices (1992). The role of local strain rate in the hydrogen embrittlement of round-notched samples. *Corrosion Science* 33(9):1387-1409.

Toribio, J. (1993). Role of hydrostatic stress in hydrogen diffusion in pearlitic steel. *Journal of Materials Science* 28:2289-2298.

Toribio, J. & A. M. Lancha (1993). Effect of cold drawing on susceptibility to hydrogen embrittlement of prestressing steel. *Materials and Structures* 26(1):30-37.

Toribio, J., A. Lancha et al. (1994). *Hydrogen induced damage in high strength pearlitic steel: Micromechanical effects and continuum mechanics approach.* Hydrogen effects in materials, Jackson Hole, WY, TMS.

Toribio, J. & A. Lancha (1996). Effect of cold drawing on environmentally assisted cracking of cold-drawn steel. *Metallurgical Transactions*:6015-6024.

Townsend, H. J. (1972). Hydrogen sulfide stress corrosion cracking of high strength steel wire. *Corrosion* 28(2):39-46.

Virginia Department of Transportation (1991). *Road and Bridge Specifications,* Richmond.

Vrable, J. B. & B. E. Wilde (1980). Electrical-potential requirements for cathodic protection of steel. *Corrosion* 36(1):18-23.

Wheat, H. G. & Z. Eliezer (1985). Some electrochemical aspects of corrosion of steel in concrete. *Corrosion* 41(11):640-645.

Williams, A. J. (1995). Determination of safe cathodic protection limits for prestressed concrete pilings: Electrochemical conditions in pilings subject to cathodic protection. *Materials Science and Engineering.* Charlottesville, University of Virginia: 249.

Woodruff, D. P. & T. A. Delcher (1986). Desorption spectroscopies. *Modern Techniques of Surface Science:*279-299.

Yamakawa, K. (1984). Critical hydrogen content on hydrogen embrittlement of high strength steel. *International Congress on Metallic Corrosion* 2:254-261.

FIGURES
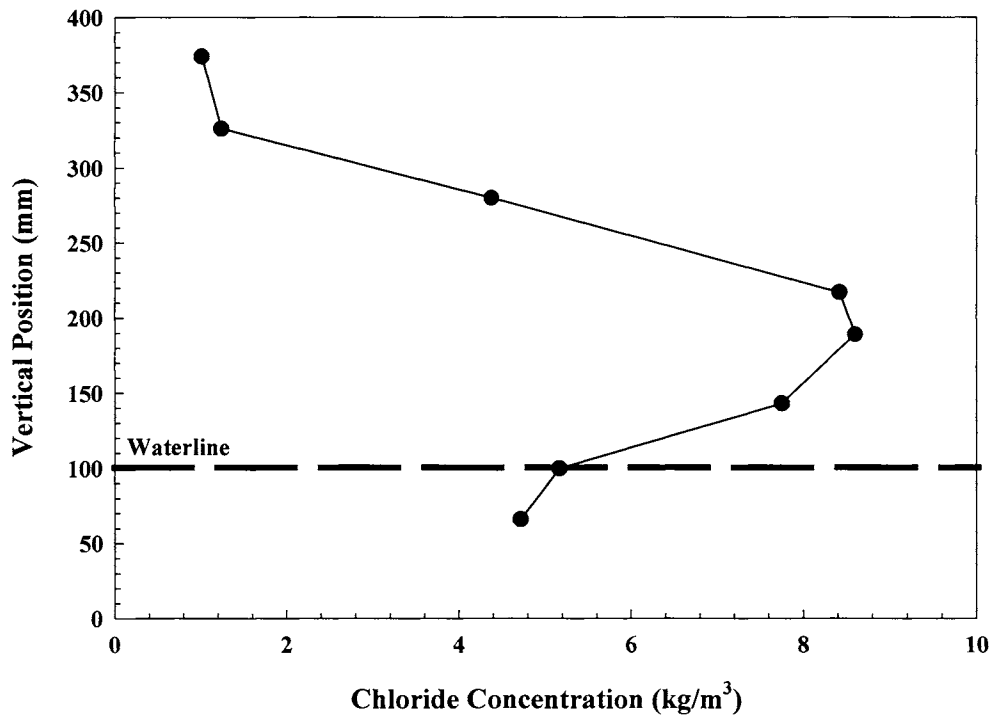
Figure 1.1. Nonuniformity of the chloride concentration within a marine piling as a function of position. (Hartt, 1994).
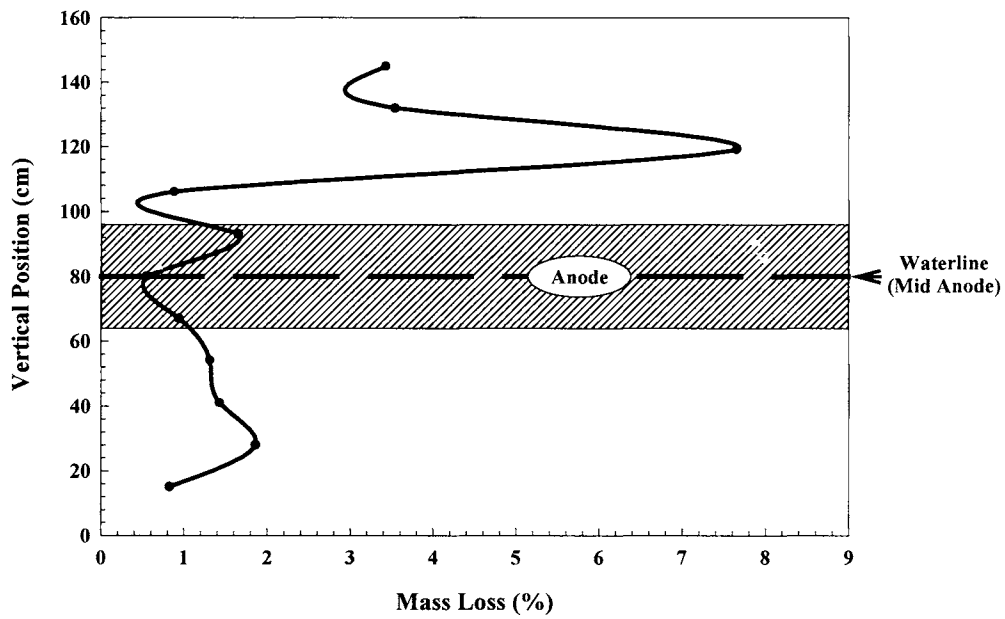
Figure 1.2: Degree of corrosion, expressed as percent weight loss, as a function of position within a marine bridge pile, illustrating the effect of the varying environmental conditions (Hartt, 1994).
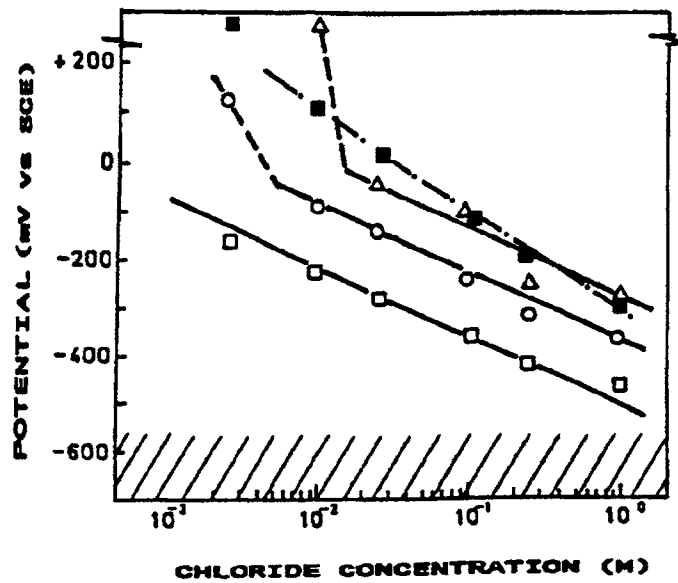
Critical breakdown potential (E_b) of steel in deaerated $Ca(OH)_2$ + Cl⁻
obtained by different electochemical techniques

△   Polarization curves at sweep rate of 0.5 mV s⁻¹
■   Galvanostatic pulse of 10 μA cm⁻² (maximum of the E-t curve)
O   Scratching the electrode surface at imposed potential
□   Galvanostatic pulse of 10 μA cm⁻² (steady potential)

Figure 1.3: Pitting potentials of steel in $Ca(OH)_2$ + x M Cl⁻ solutions as determined via a variety of techniques (Gonzalez, 1993).

E vs. Log I

REBAR POTENTIAL (−Volts)

Point Where Linearity
of the E Log I Plot Begins

Static
Potential
or
E−CORR

Linear Behavior Segment
(Oxygen Reduction)

Hydrogen
Evolution

Extrapolation of Linear Segment

Corrosion Current − I−CORR

Current for Cathodic
Protection − I−PROTECT

Extrapolation of E−CORR

APPLIED C.P. CURRENT (Amperes) − LOG SCALE
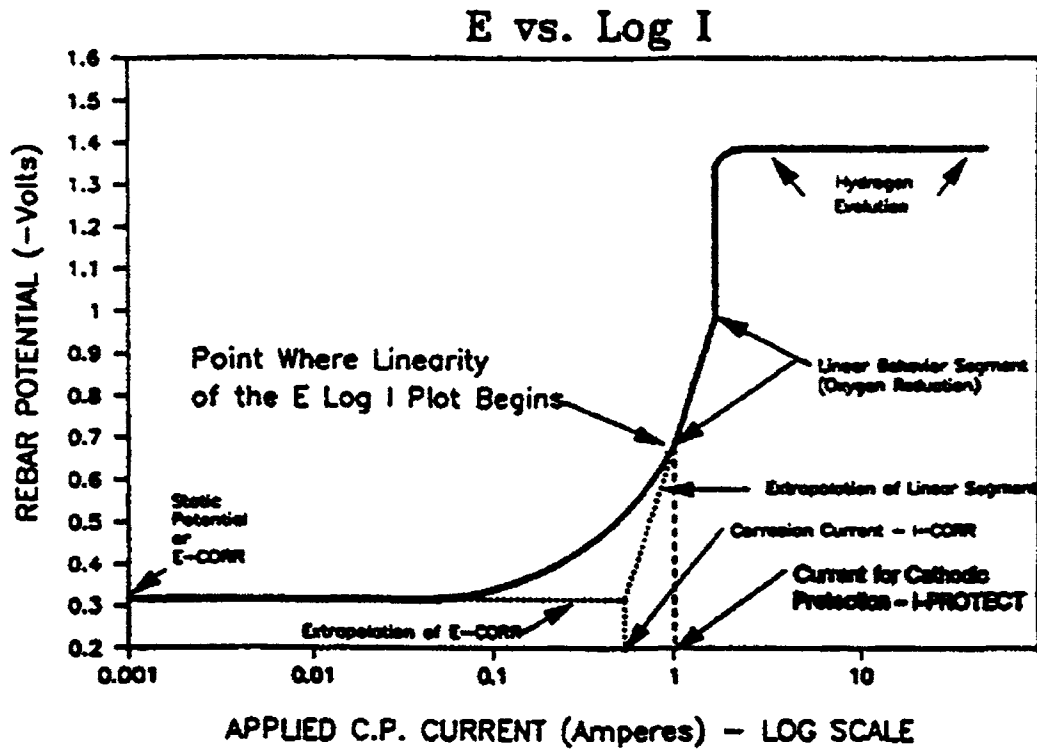
Figure 1.4: Schematic illustrating the determination of the protection potential utilizing the E-Log I technique for atmospherically exposed concrete structures (NACE, 1990).
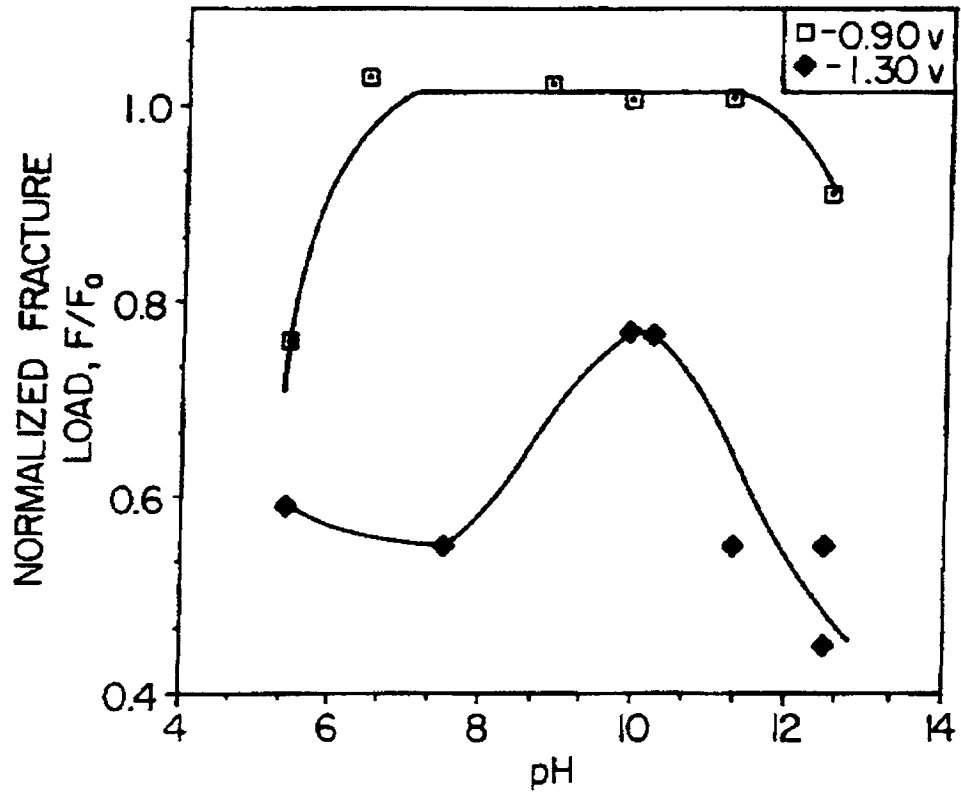
Figure 1.5: Normalized fracture load as a function of pH in $Ca(OH)_2$ x HCl solutions at applied potentials of - 0.9 V_{SCE} and -1.3 V_{SCE} (Hartt, 1994).
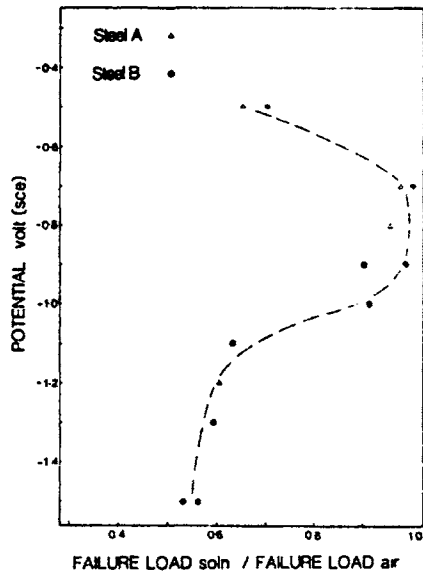
pH 8 to pH 10.5
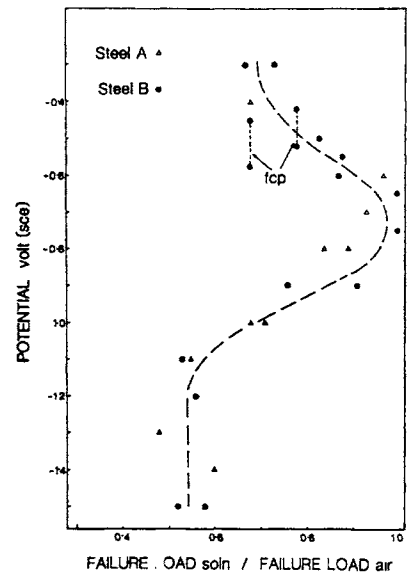
pH 6 to pH 8.5
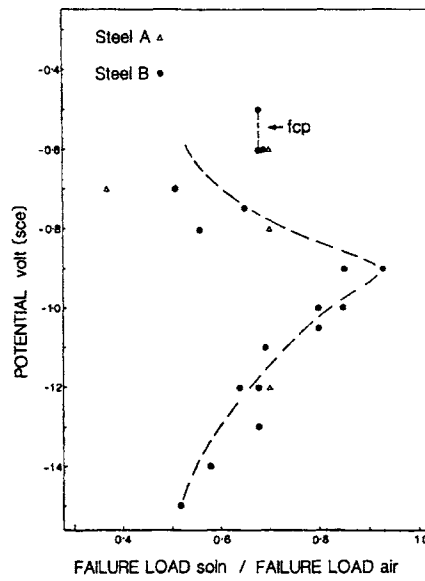
pH 2 to pH 3

Figure 1.6:   Normalized fracture load as a function of pH in $Ca(OH)_2 + x$ HCl solutions (Parkins, 1982).
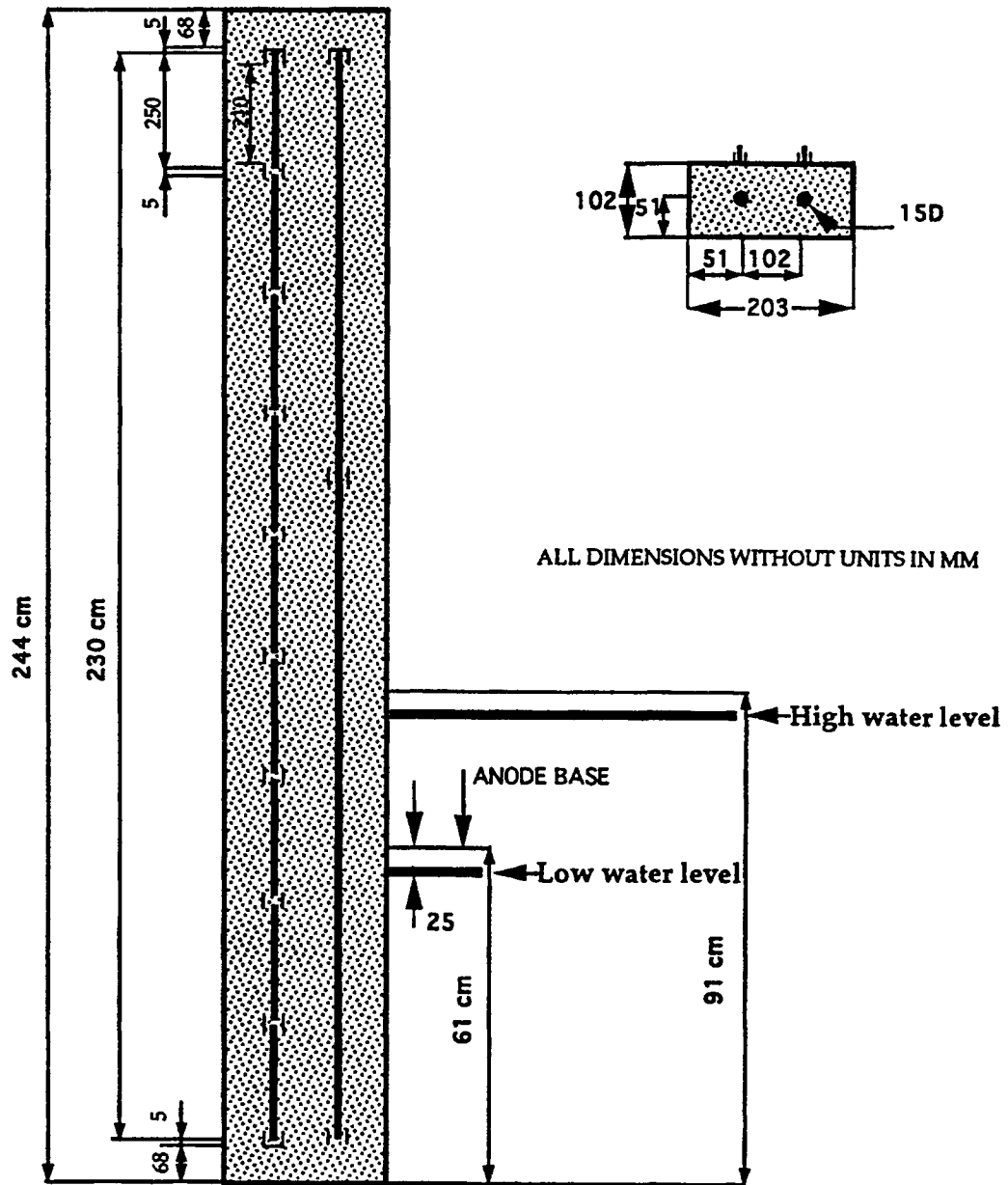
Figure 1.7: Schematic of the laboratory scale piling containing segmented and continuous reinforcement utilized by Hartt et al. (Hartt, 1994).
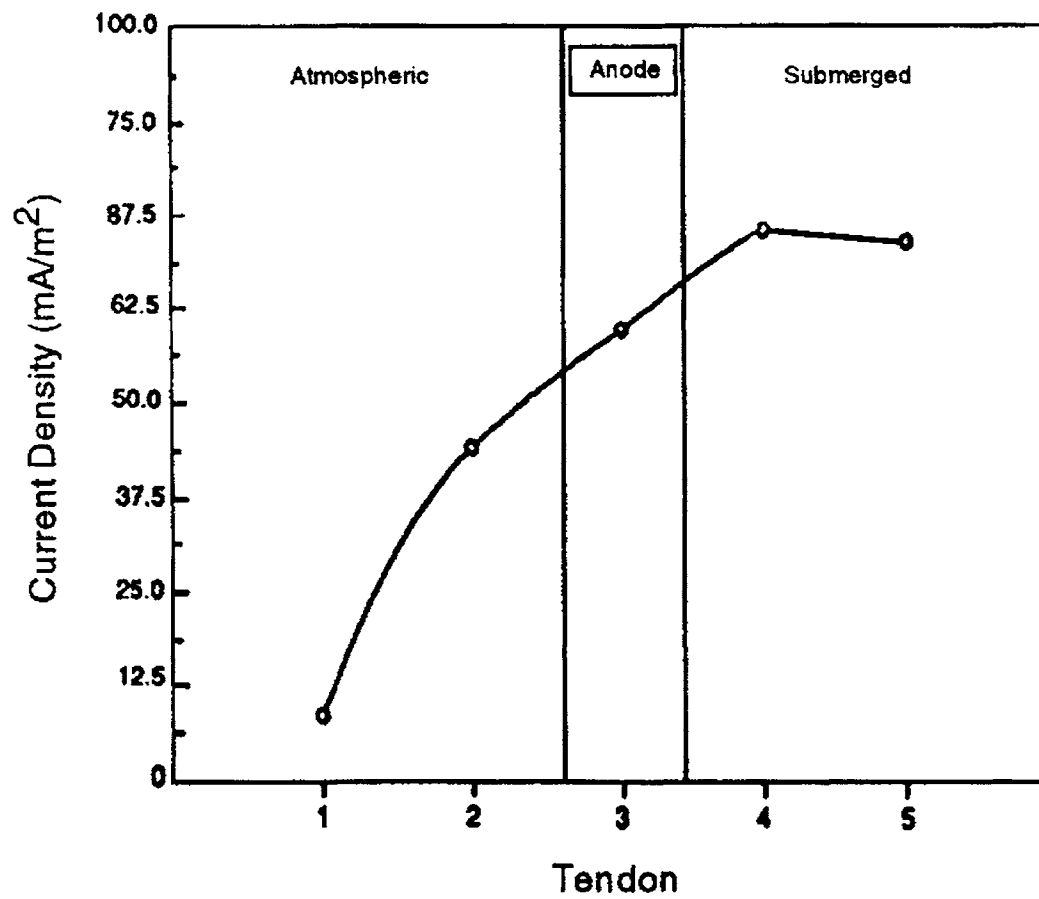
Figure 1.8: Nonuniformity of the local current density distribution for a potentiostatic (constant potential) cathodic protection system, (Pangrazzi, 1994).
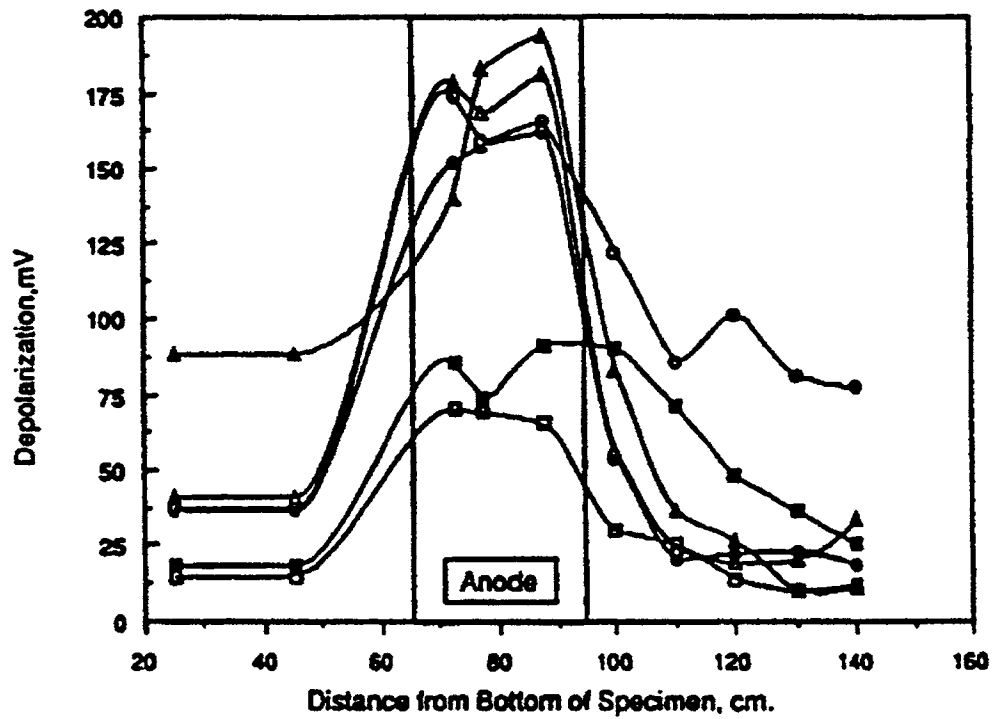
Specimen Number	Potential (mV_SCE)
1	-720
2	-770
3	-850
4	-850
5	-950
6	-1100

Figure 1.9: Nonuniformity of the local applied potentials as a function of position for an impressed current cathodic protection system (Hartt, 1994).
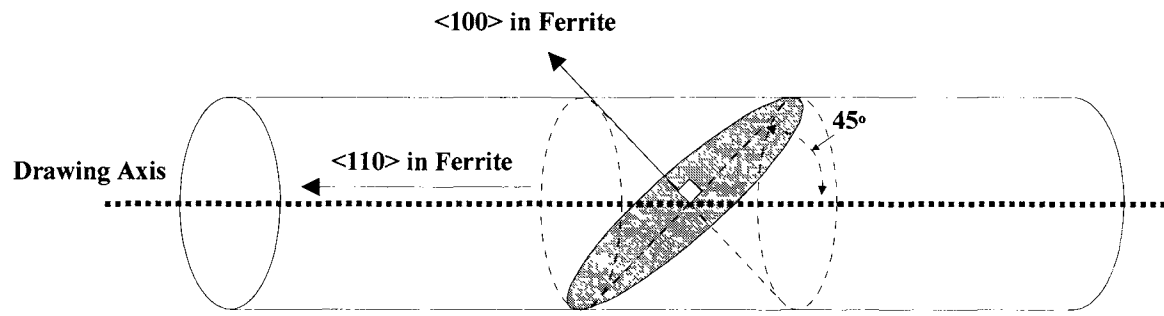
Figure 1.10: Schematic representation of wire texture of pre-stressing strand
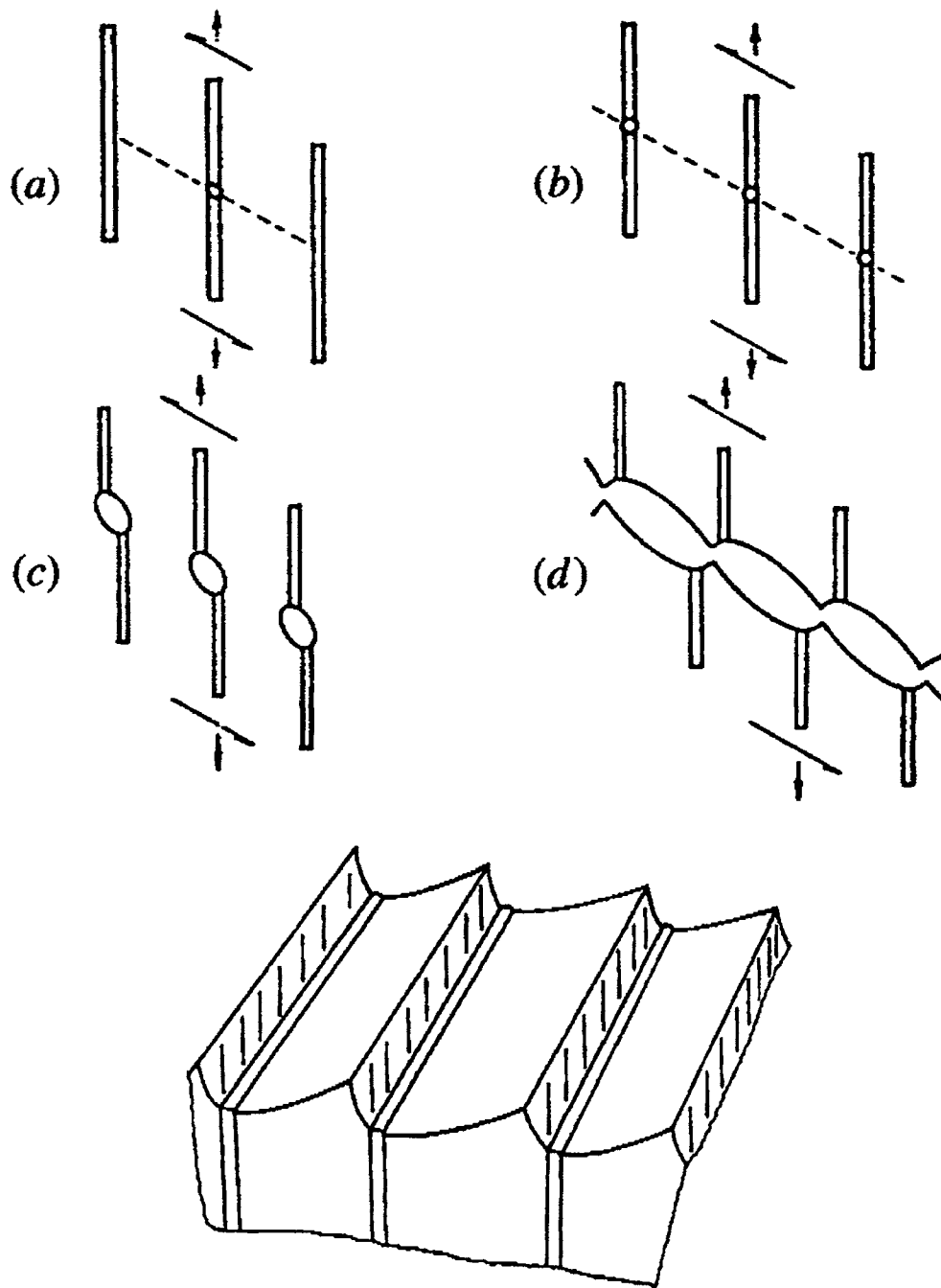
Figure 1.11. Schematic representation of the shear cracking process within pearlitic steels along with the resultant fracture surface. The shear crack process involves the formation of a slip band within the pearlite, resulting in the fracture of a cementite lamellae and the formation of an easy path for further deformation. Increased strain results in the failure of additional cementite lamellae in the slip plane which in turn act as microvoid nucleation sites. These voids then grow to form a macroscopic crack (Miller, 1970).
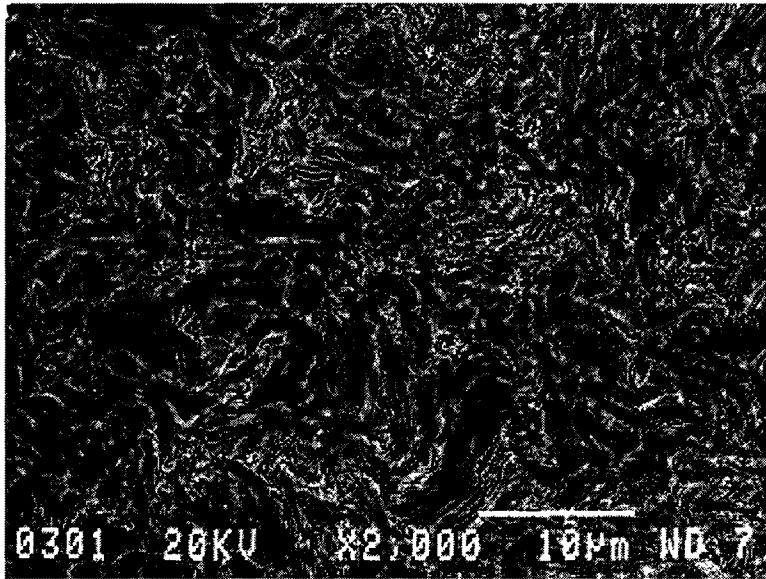
Figure 4.1a: Low magnification view (parallel to the drawing axis) of the microstructure of the drawn, pearlitic prestressing strand.
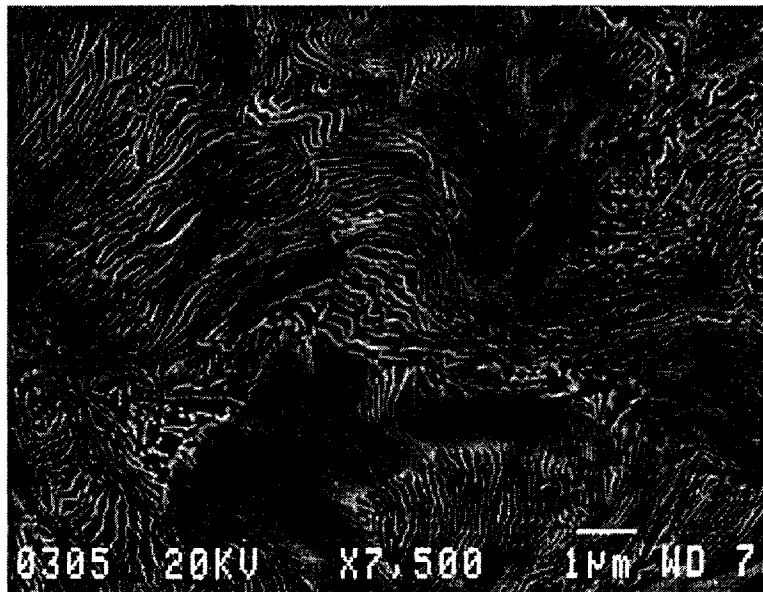
Figure 4.1b: High magnification view (parallel to the drawing axis) of the drawn, pearlitic wire utilized as prestressing strand.
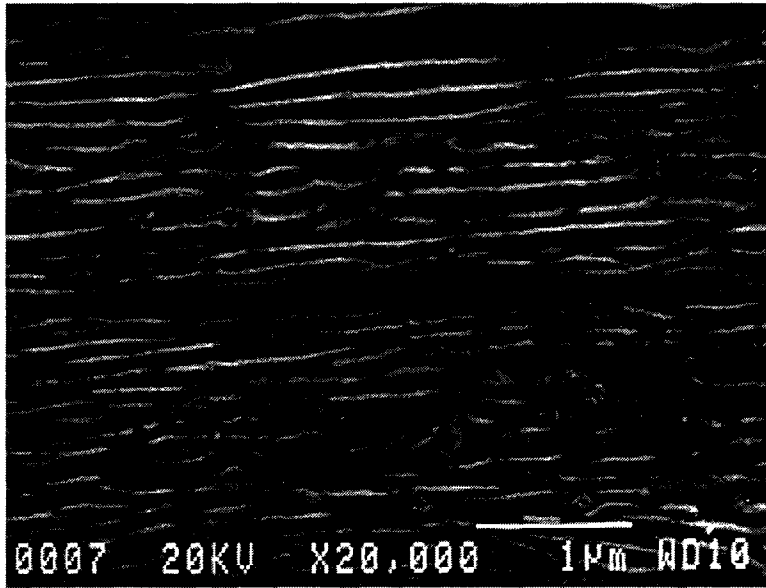
Figure 4.2:   Longitudinal view of an MnS inclusion within the drawn, pearlitic wire.
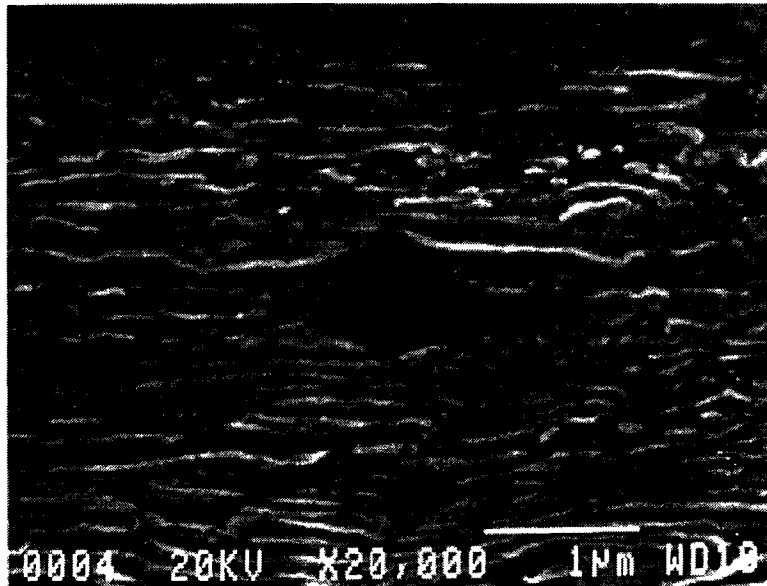
Figure 4.3:   Longitudinal view of a Ca rich inclusion within the drawn, pearlitic wire.
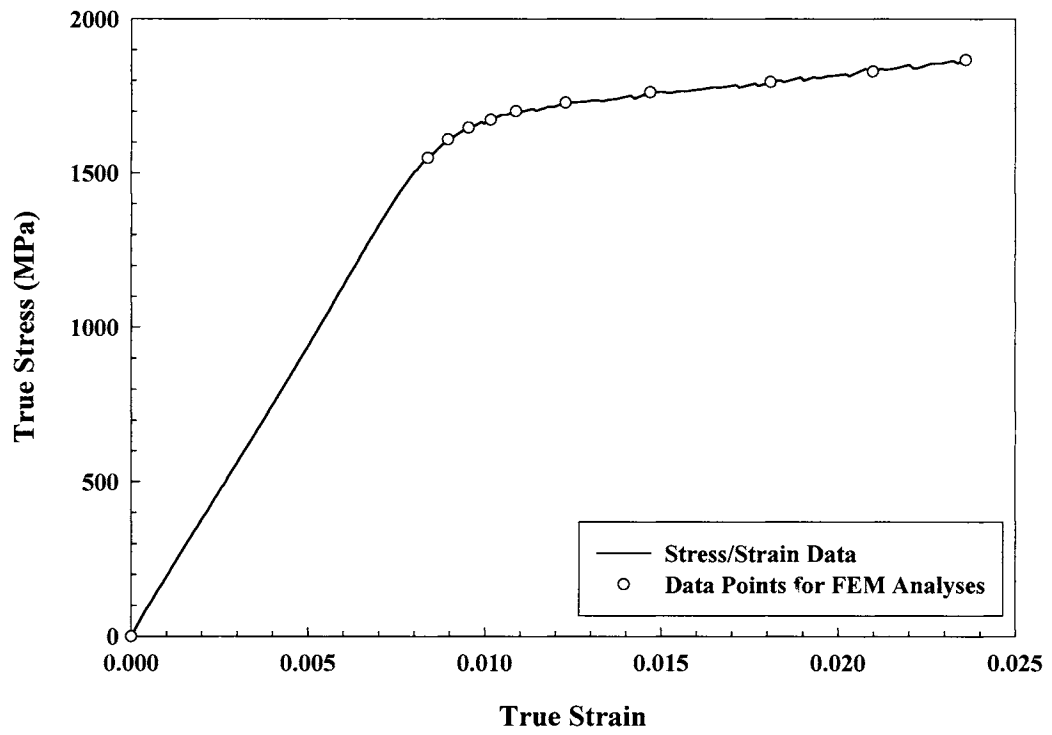
Figure 4.4.   True stress-true strain curve for pre-stressing tendon. Also indicated are the 11 points used to represent this curve for the FEM analyses.
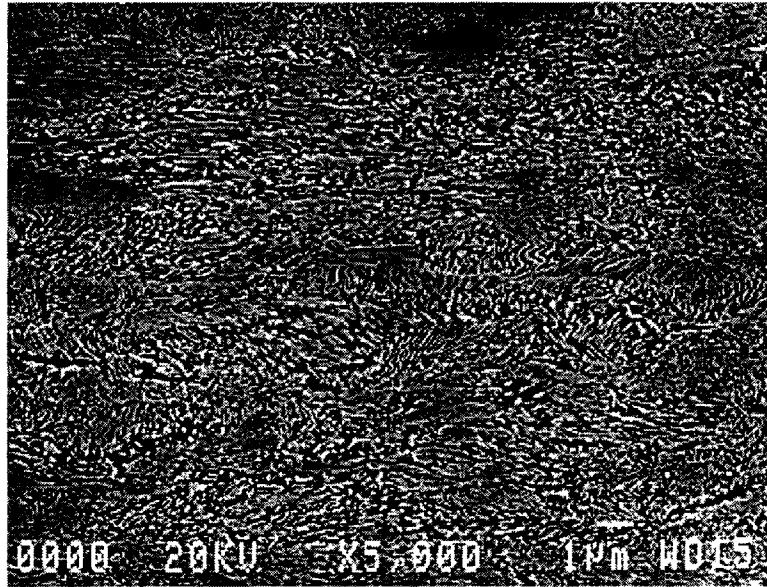
Figure 4.5a: Low magnification view perpendicular to the rolling direction (rolling direction goes into the page) of the rolled 1080 sheet utilized for permeation experiments.
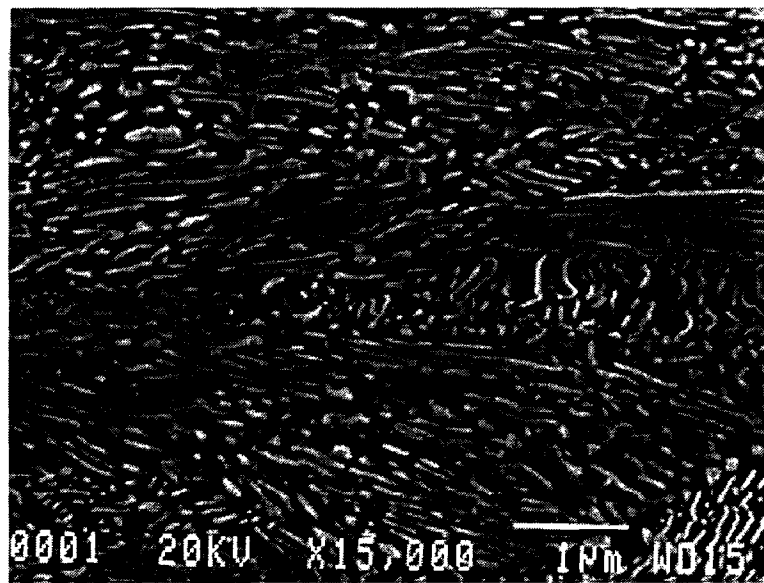
Figure 4.5b: High magnification view perpendicular to the rolling direction of the rolled 1080 sheet utilized for permeation experiments.
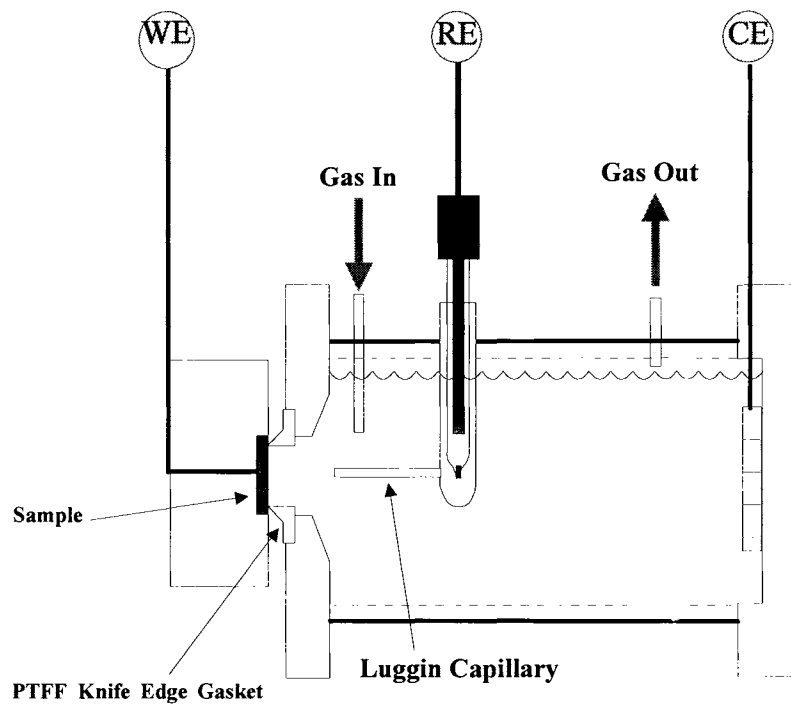
Figure 4.6. Flat cell utilized to perform potentiodynamic experiments. Cell body and end plates were acrylic, and the saturated calomel electrode was typically used as a reference.
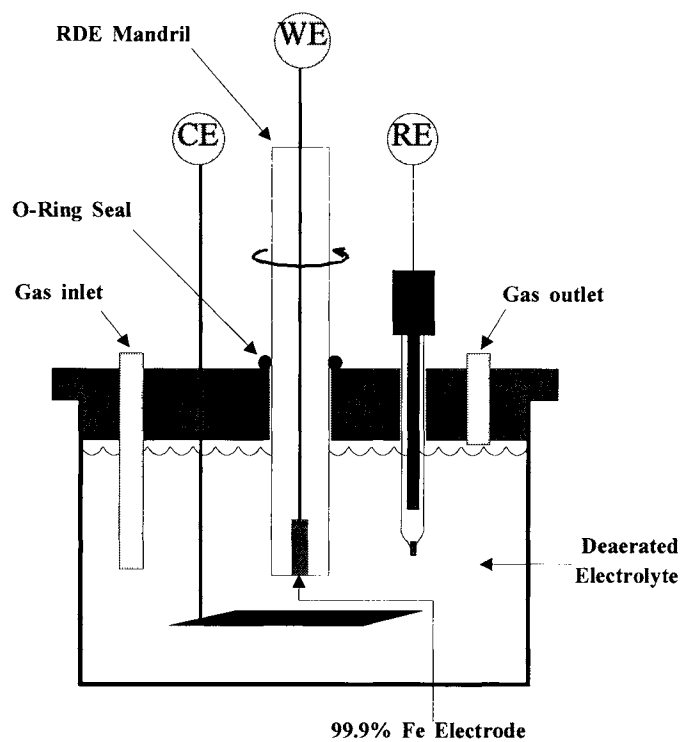
Figure 4.7.   Electrochemical cell utilized for rotating disk electrode experiments. Cell allowed the solution to be deaerated via an o-ring seal on the PTFE sample mandril.
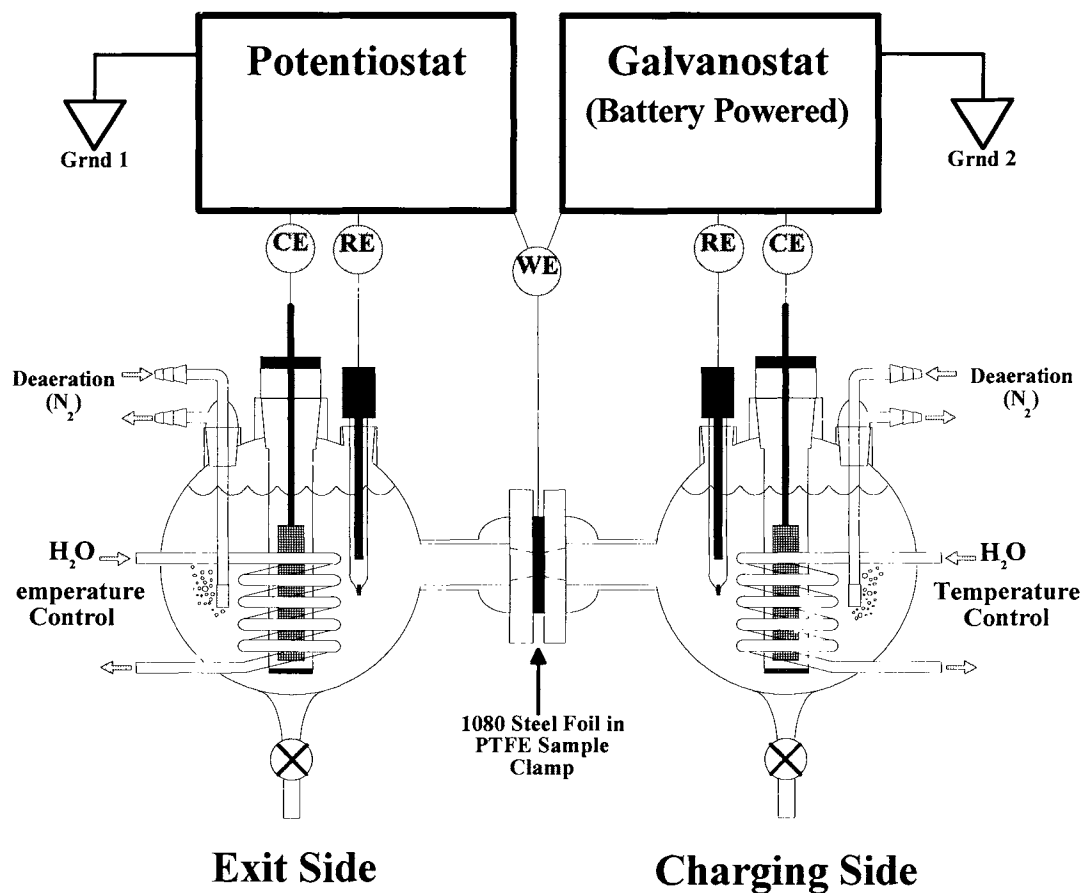
Figure 4.8.   Schematic of the Devanathan/Stachurski cell utilized in hydrogen permeation experiments. Both sides were deaerated and maintained at a constant temperature of 27°C. Exit side solution was pH 12.5 NaOH.

A.

WE RE CE

Solution IN

Deaeration
(N$_2$)

H$_2$O
Temperature
Control

Iron Foil in
PTFE Sample
Clamp

Solution OUT

B.

Jet

v

d

H

Wall Jet Region   Uniform
                   Access
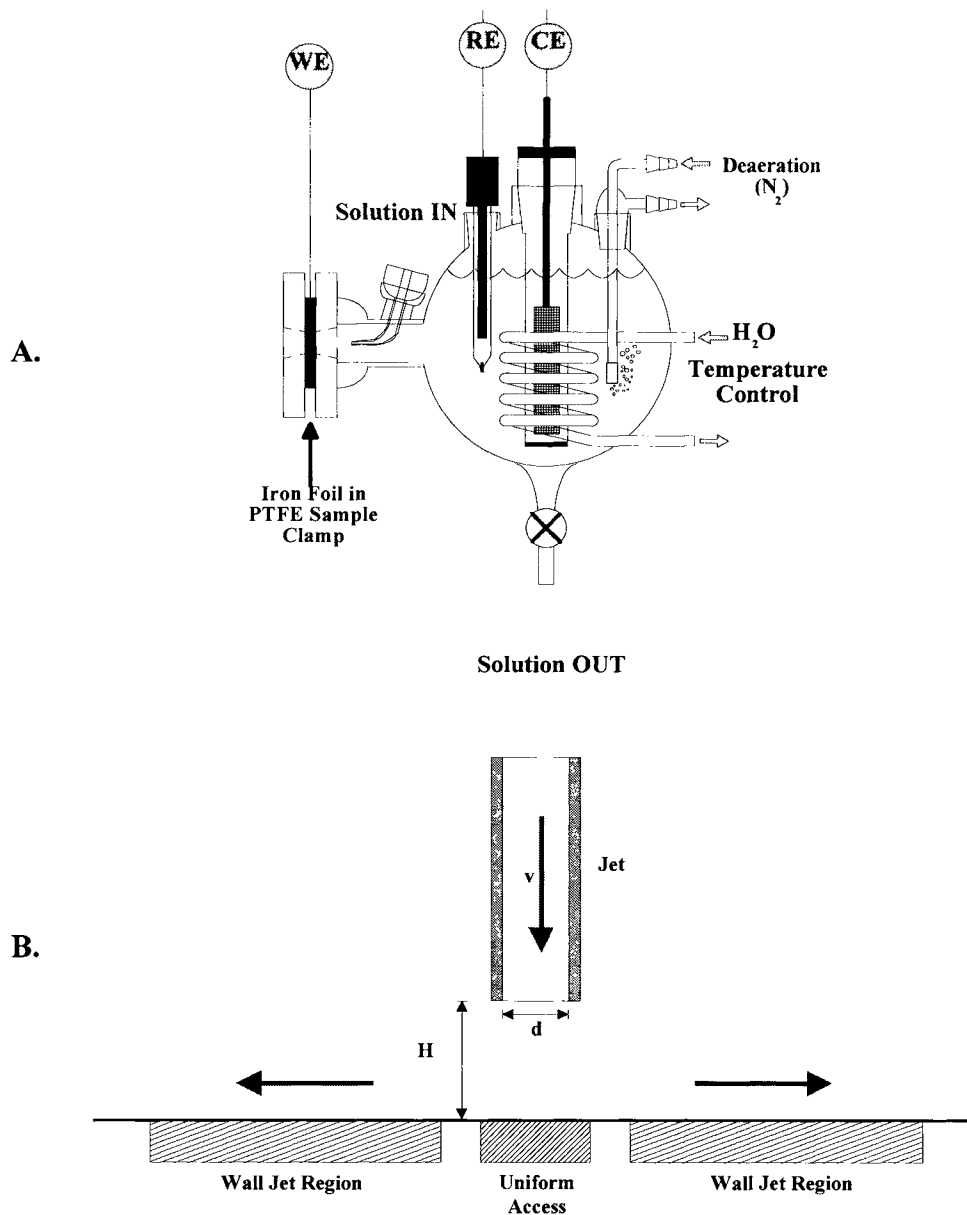
Wall Jet Region

Figure 4.9.   Schematic of (a) the recirculation system utilized to maintain the surface pH on the charging side of the Devanathan/Stachurski cell utilized in hydrogen permeation experiments. (b) Location of the uniform access and wall jet regions for an impinging jet electrode.
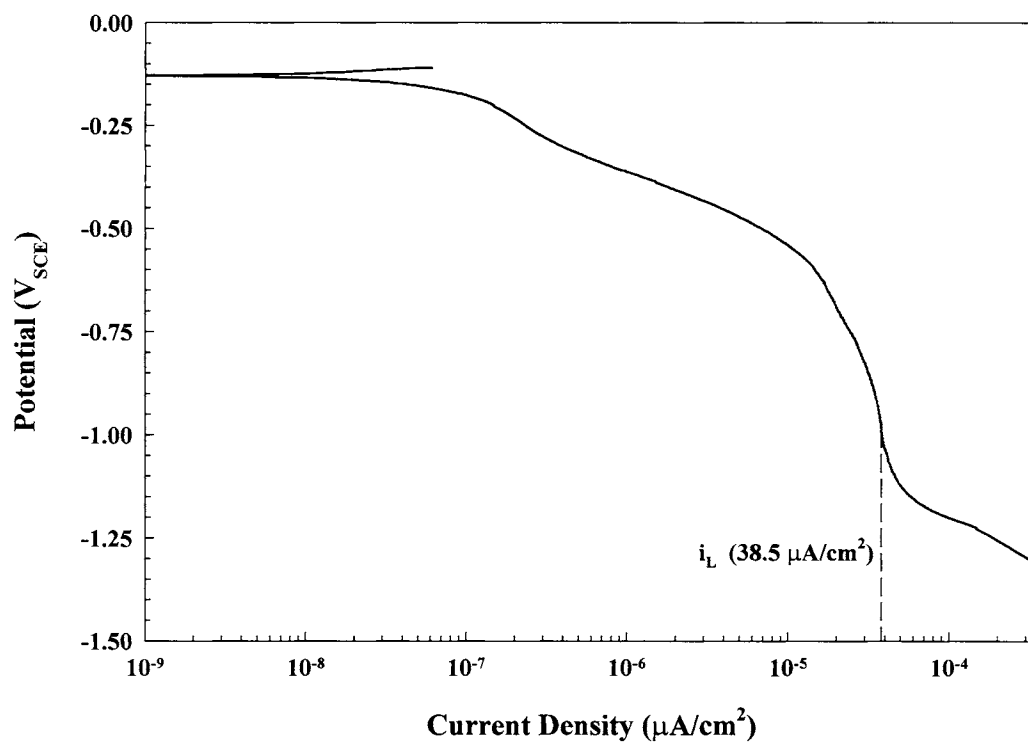
Figure 4.9c. Cathodic polarization scan of an iron foil in deaerated, pH 12.6 NaOH for the impinging jet utilized for Devanathan/Stachurski permeation experiments to determine the diffusionally limited current density of the oxygen reduction reaction.
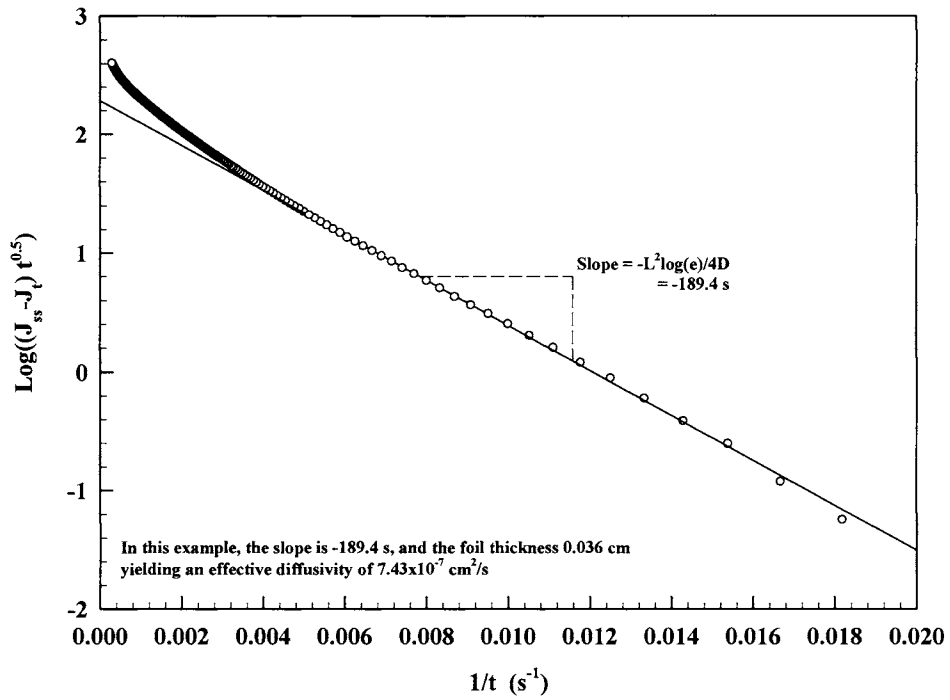
Figure 4.10. Sample calculation of the effective hydrogen diffusivity utilizing the slope technique of McBreen, Nanis, and Beck (1966).
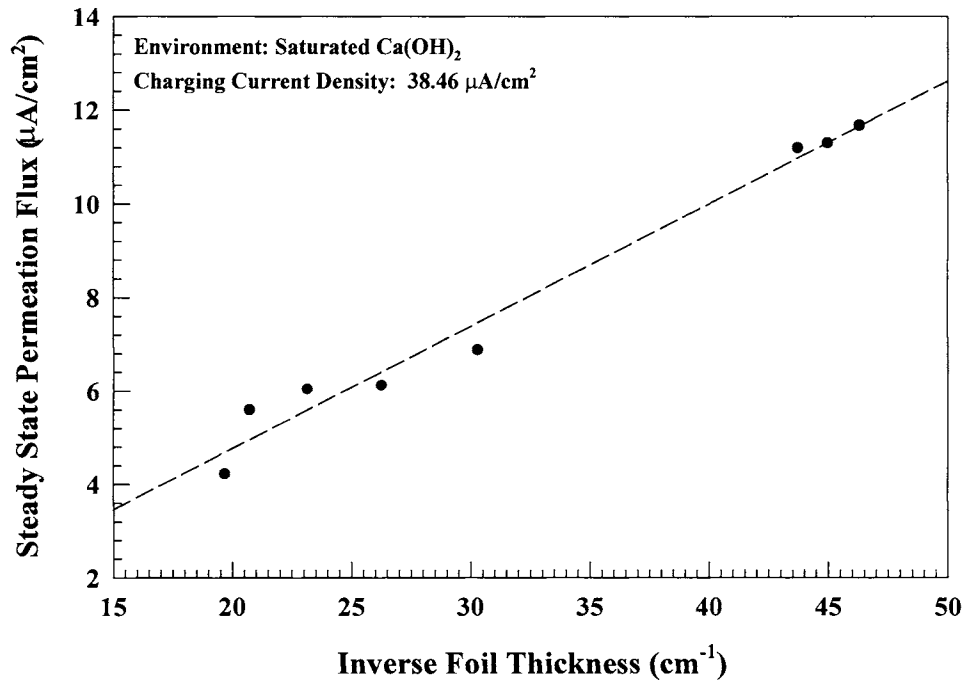
Figure 4.11. Results from Devanathan/Stachurski permeation experiments on SAE/AISI 1080 steel foils in saturated $Ca(OH)_2$ at $27^\circ C$ (300 K) demonstrating the linear relationship between the steady state permeation flux as a function of inverse thickness, confirming that experiments were bulk diffusion controlled.
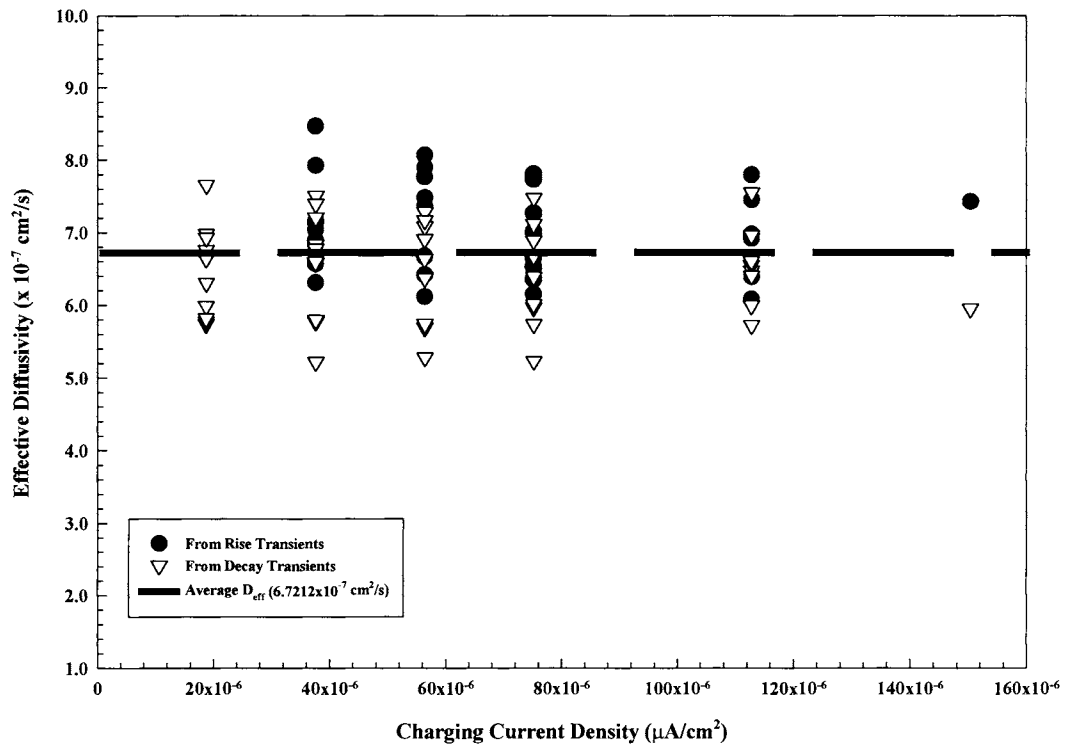
Figure 4.12. Effective diffusivity as a function of charging current density for all foils calculated utilizing the slope method of McBreen et al. From rise and decay transients. Results are from Devanathan/Stachurski permeation experiments on SAE/AISI 1080 steel foils in saturated $Ca(OH)_2$ at 27°C (300 K). The overall average diffusivity for all experiments performed is also shown.
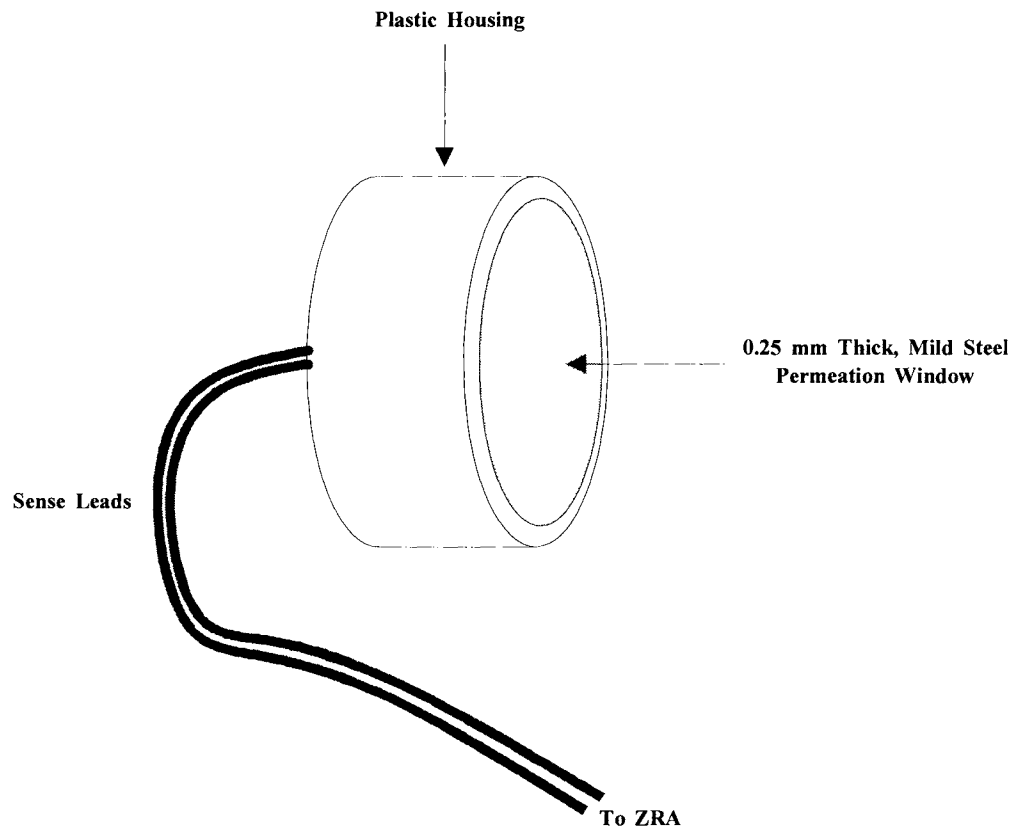
Figure 4.13.   Schematic of the IHS-12 Hydrogen sensor obtained from Force Institute and embedded in laboratory scale pilings.
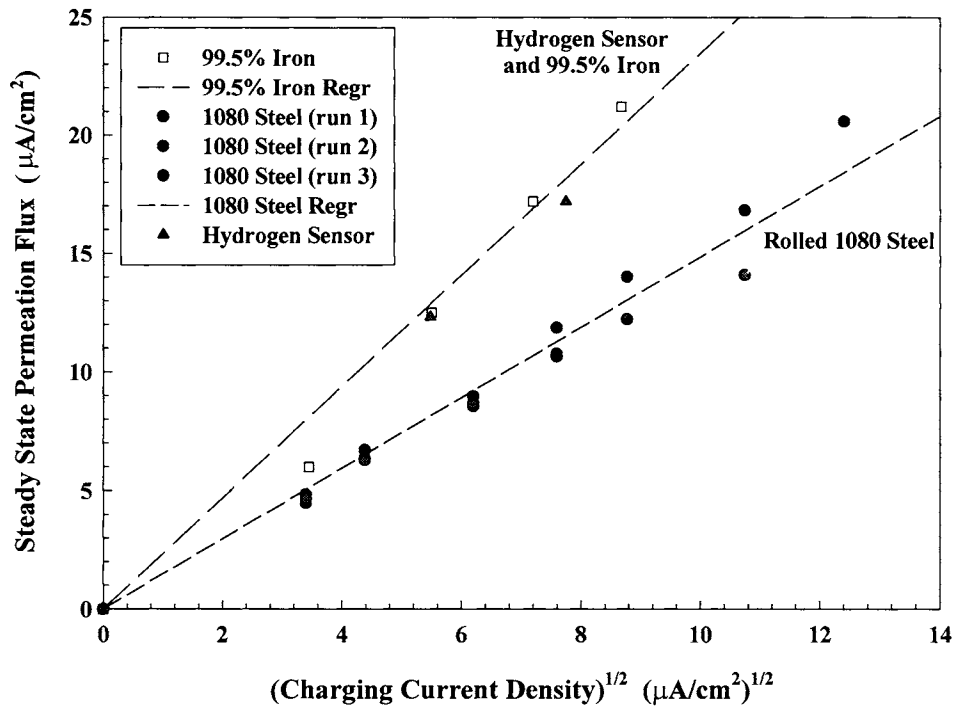
Figure 4.14.   Steady state permeation flux as a function of the square root of the applied charging current density for 99.5% iron and 1080 steel foils in saturated $Ca(OH)_2$. Both foils were 0.025 cm thick and tested at 27°C.
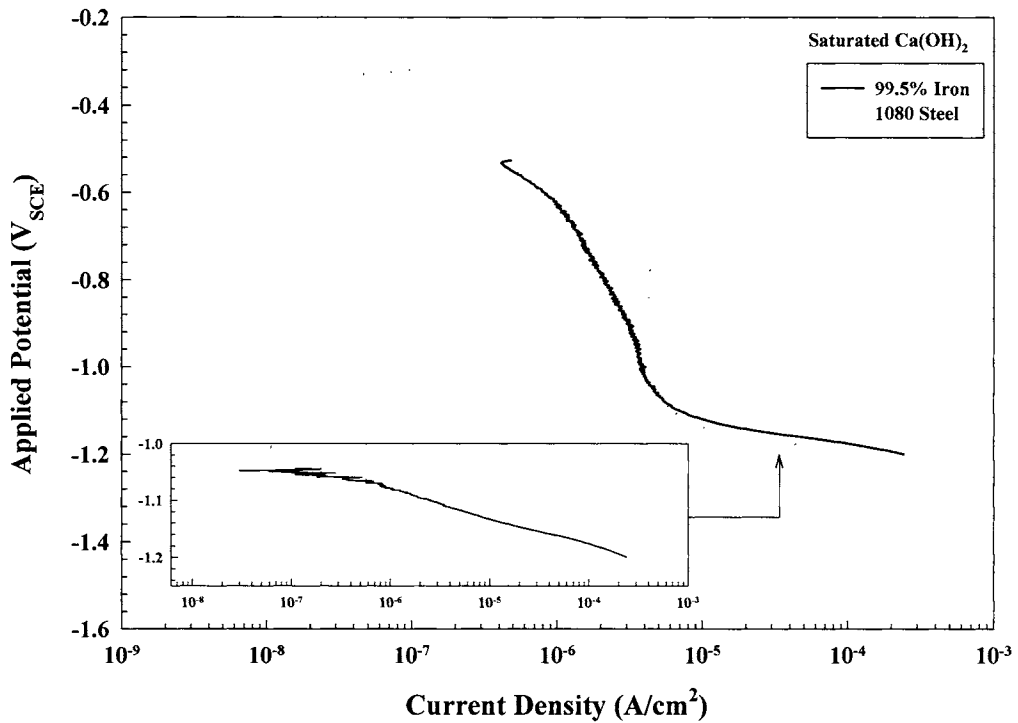
Figure 4.15.   Cathodic polarization behavior of 99.5% iron and 1080 steel in deaerated, saturated $Ca(OH)_2$.
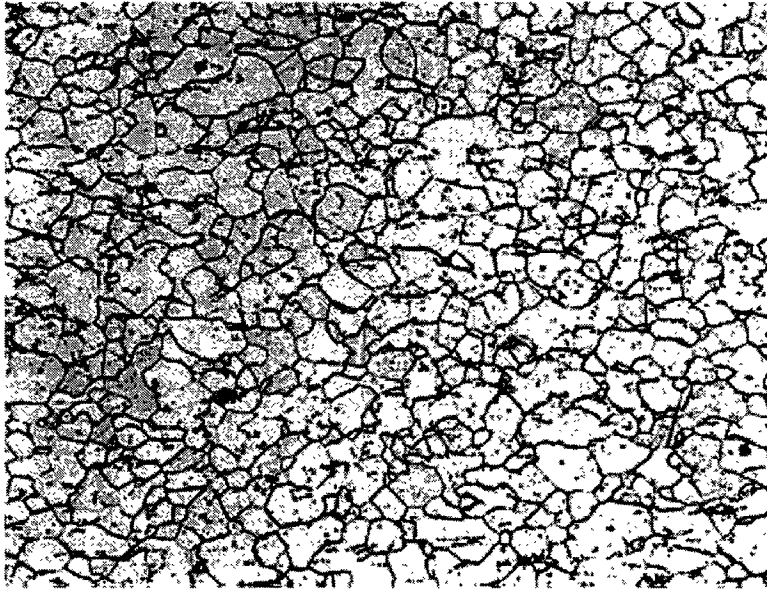
Figure 4.16:   Microstructure of the 99.5% Fe foils utilized in hydrogen permeation experiments.
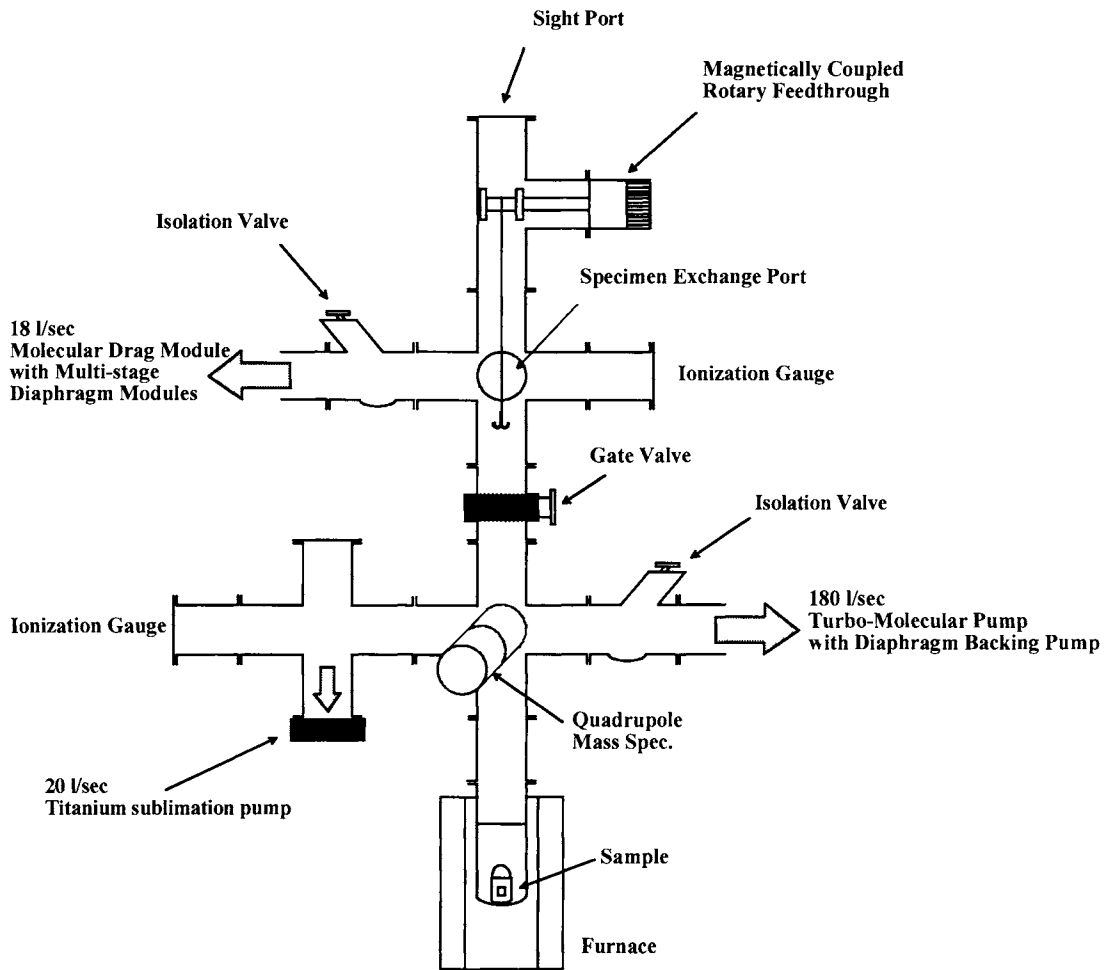
Figure 4.17. Schematic of the thermal desorption spectroscopy system, illustrating the position of various components and their performance characteristics.
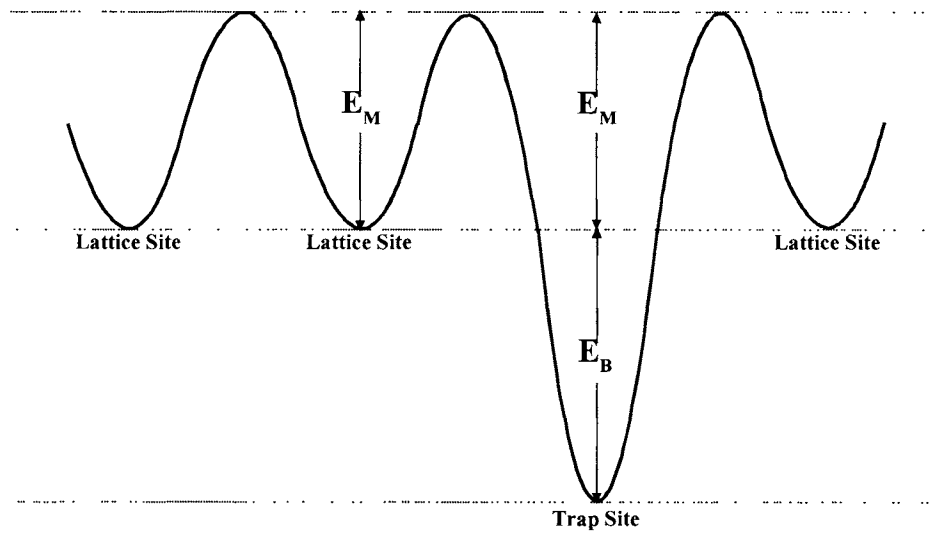
Figure 4.18. Simplified energy level schematic of a trap site within a metal lattice, illustrating the diffusional migration and trap binding energies.
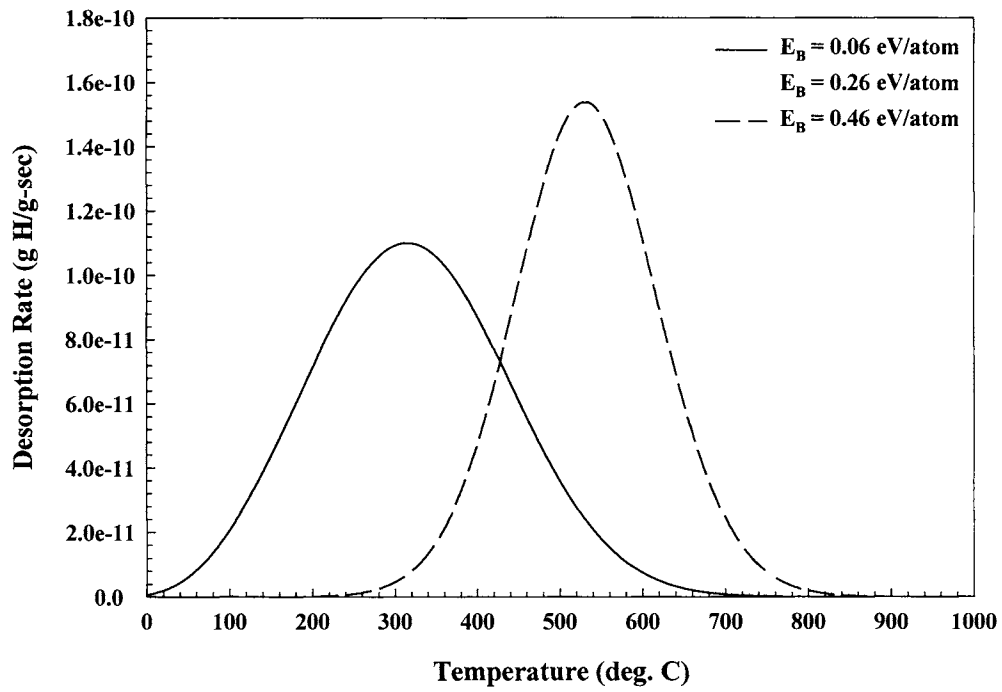
Figure 4.19. Effect of varying binding energy on the overall shape of a theoretical desorption spectra calculated using the method of Ono and Meshii.
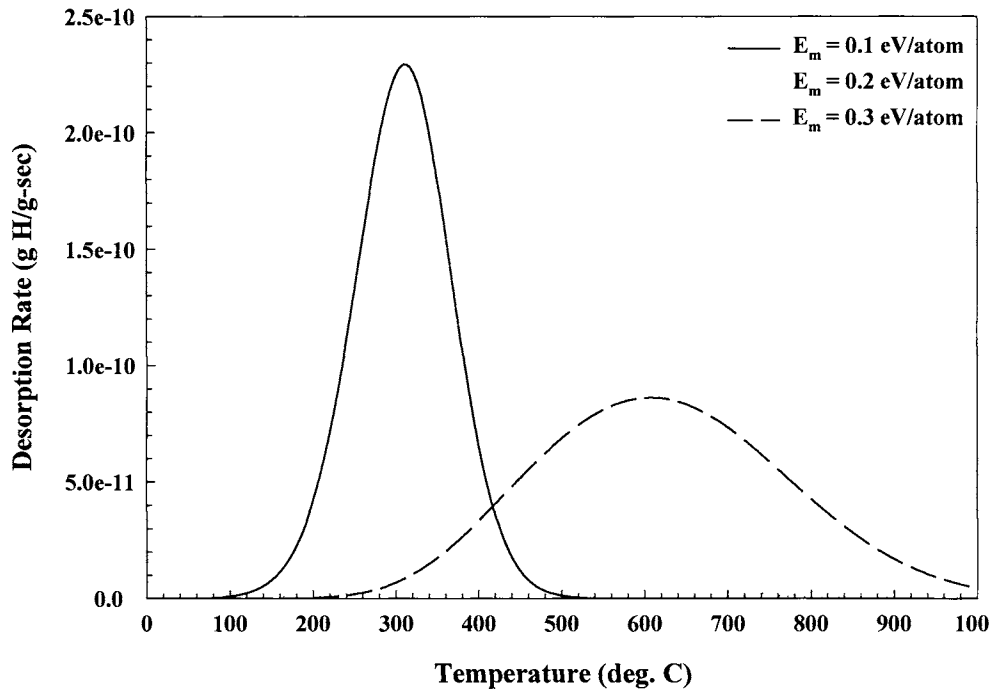
Figure 4.20. Effect of varying migration energy on the overall shape of a theoretical desorption spectra calculated using the method of Ono and Meshii.
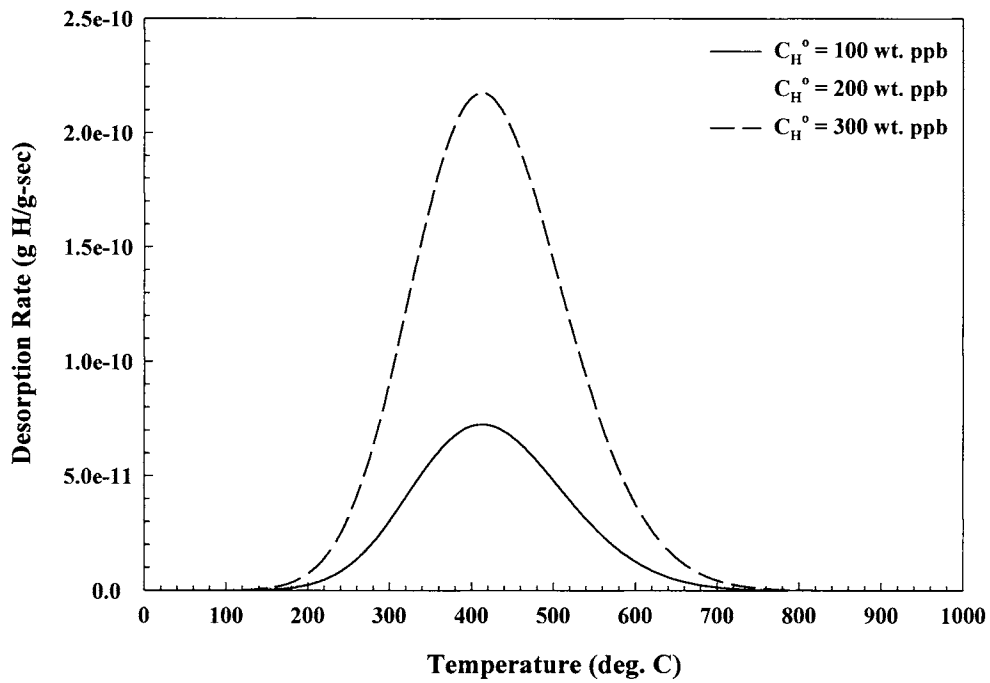
Figure 4.21. Effect of varying trapped hydrogen concentration on the overall shape of a theoretical desorption spectra calculated using the method of Ono and Meshii.
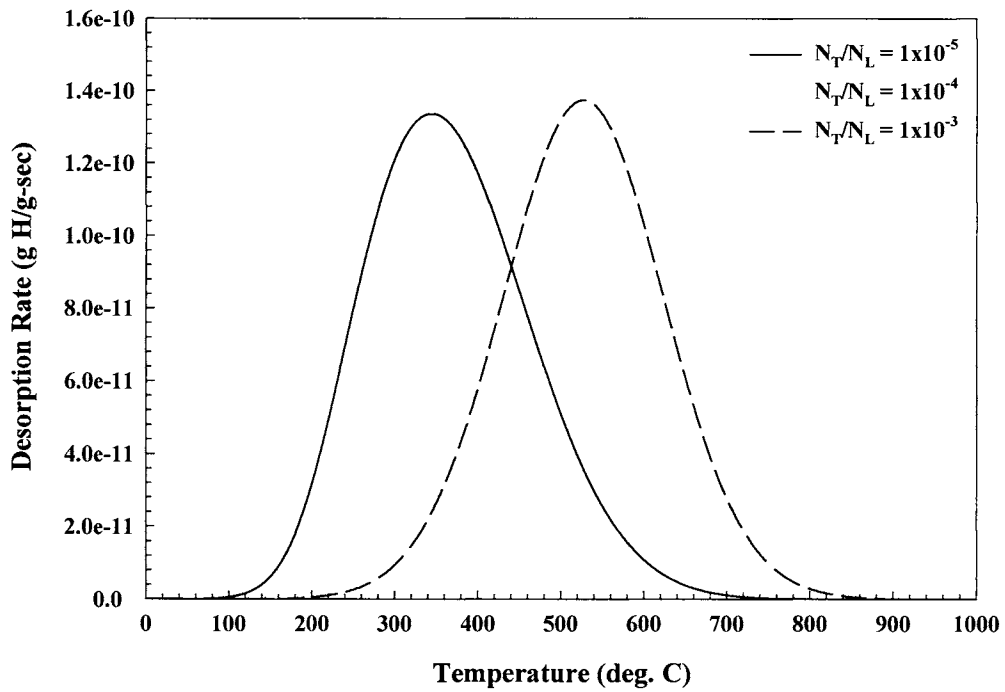
Figure 4.22. Effect of varying the relative concentration of trap sites while maintaining a fixed trapped hydrogen concentration on the overall shape of a theoretical desorption spectra calculated using the method of Ono and Meshii.
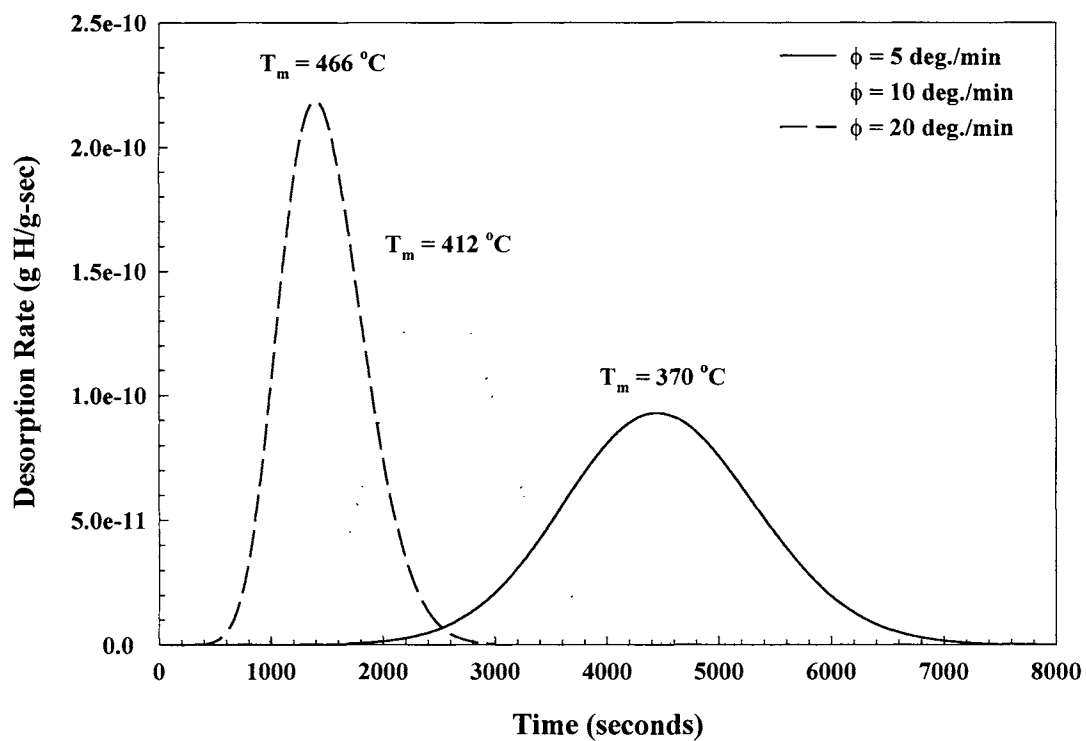
Figure 4.23. Effect of varying the thermal ramp rate on the overall shape of a theoretical desorption spectra calculated using the method of Ono and Meshii.
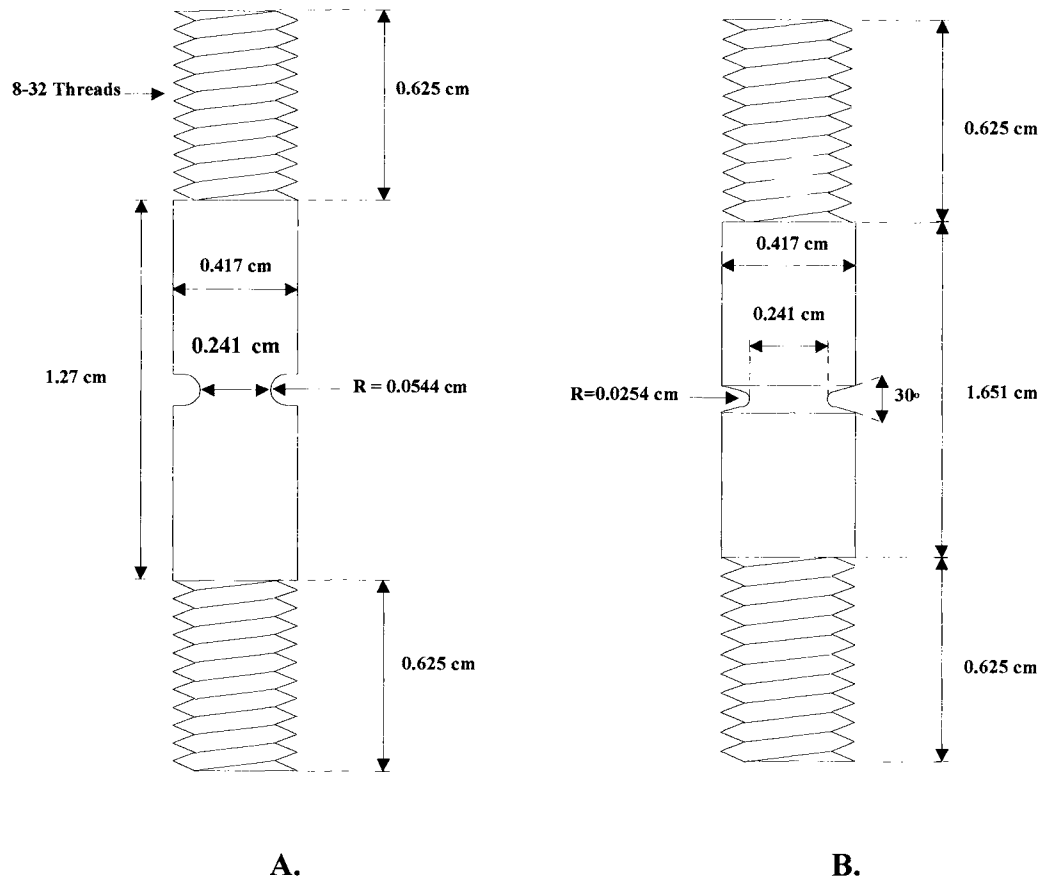
Figure 4.24. Notched tensile bars utilized to perform constant extension rate experiments. Samples with a plastic constraint value of (a) 1.08, and (b) 1.27 are illustrated.
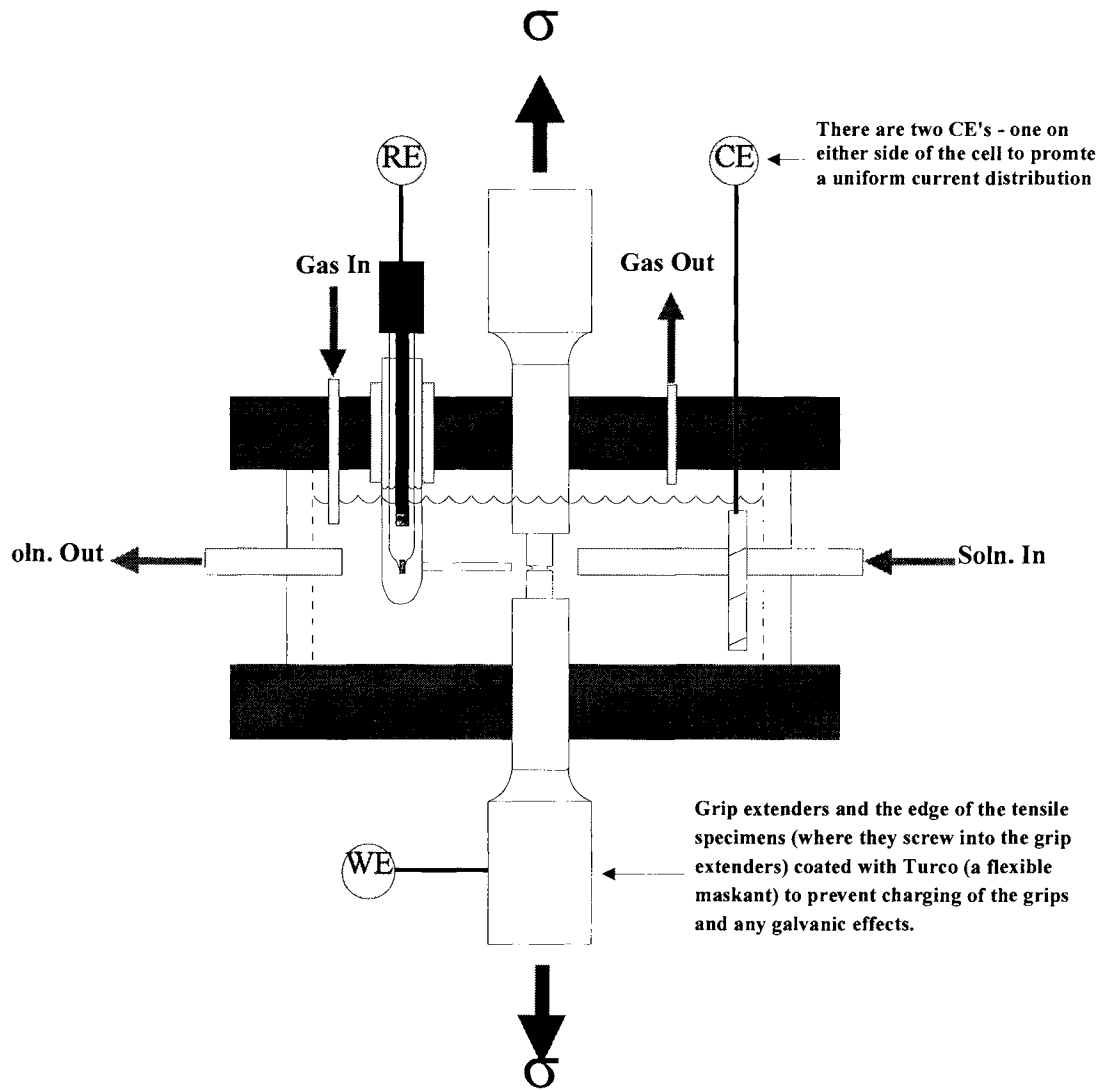
Figure 4.25. Schematic of the cell utilized to perform CERT and short crack fracture experiments. Cell enabled deaeration of the solution throughout the experiment in addition to possessing a recirculation system similar to that utilized for the Devanathan/Stachurski experiments discussed.
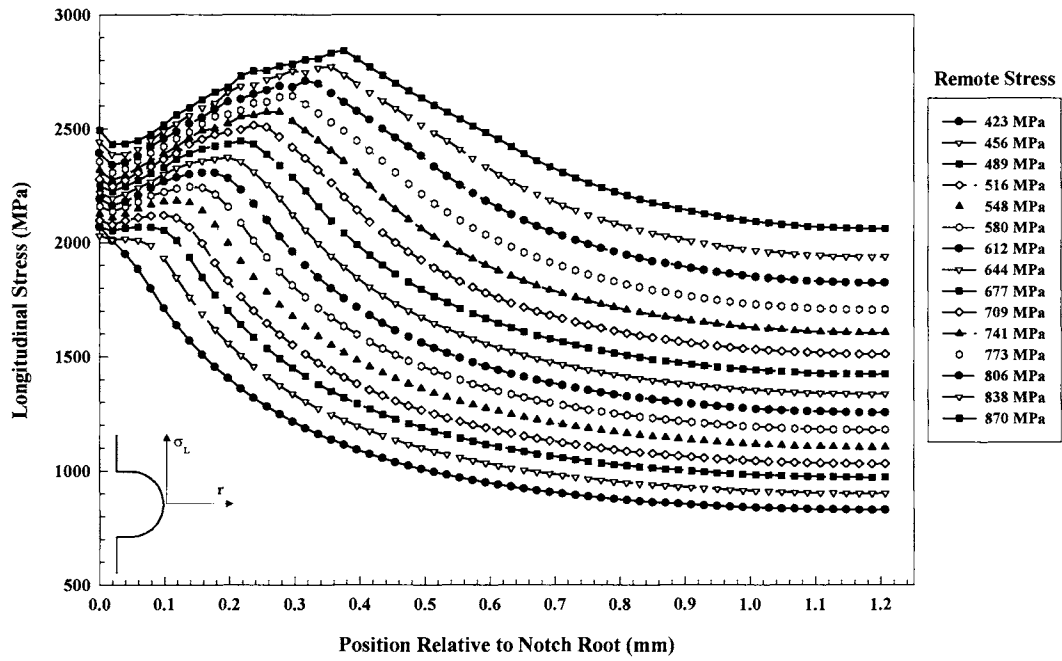
Figure 4.26. Longitudinal stress as a function of position in front of the notch root for the bluntly notched specimens pictured in Figure 4.24a.
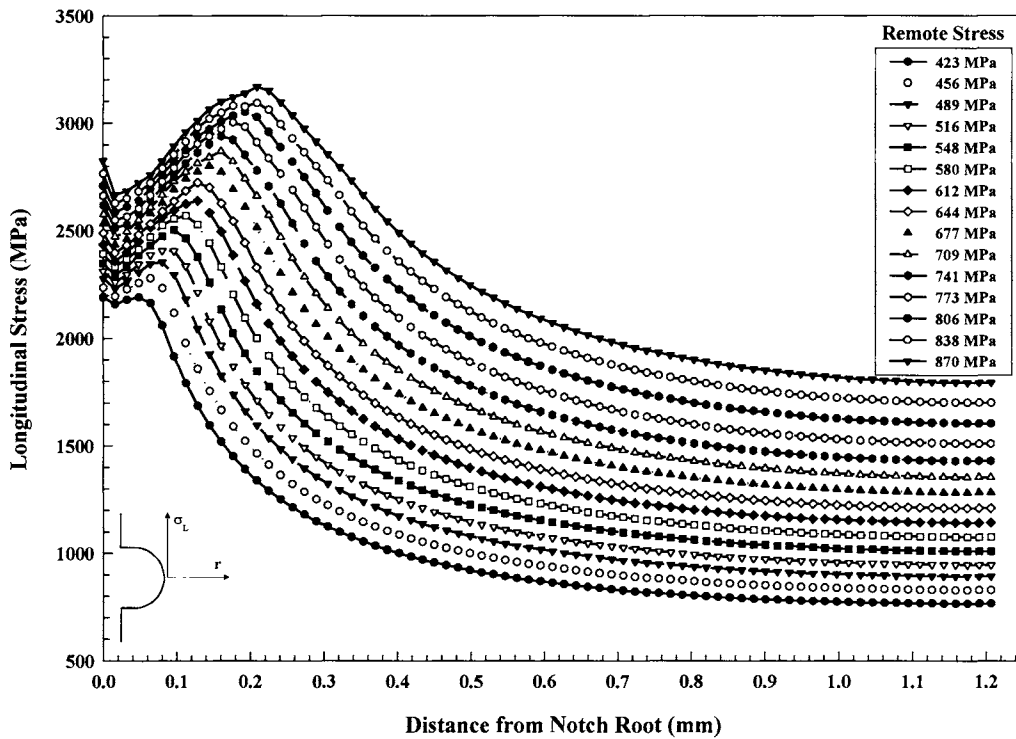
Figure 4.27. Longitudinal stress as a function of position in front of the notch root for the sharply notched specimens pictured in Figure 4.24b.
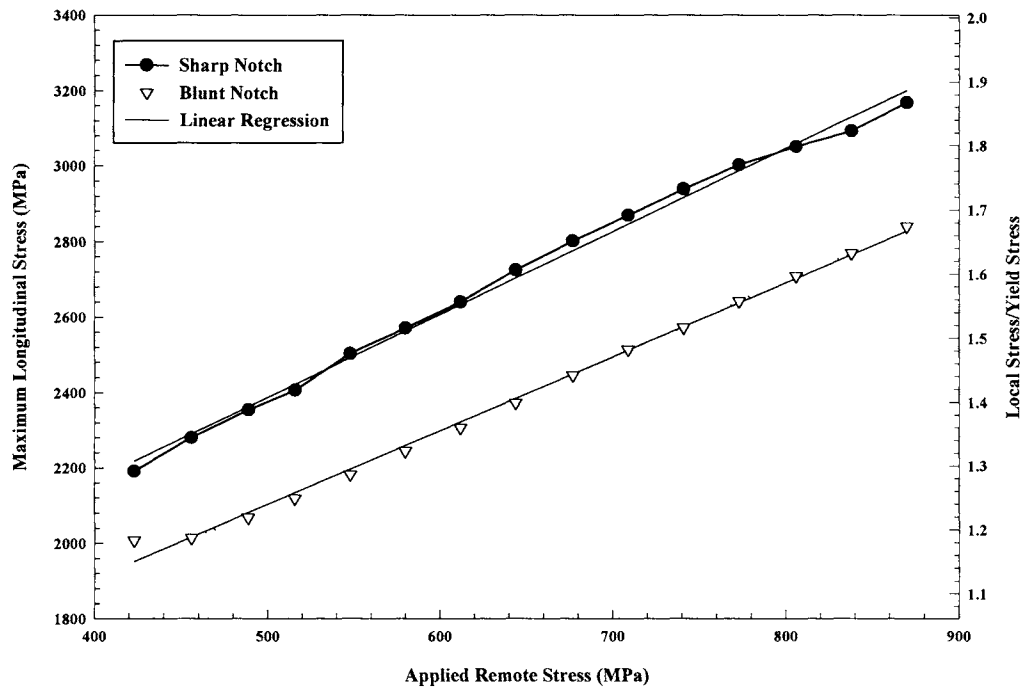
Figure 4.28. Relative position of the maximum longitudinal stress in front of the notch root for the blunt and sharp notched specimens.
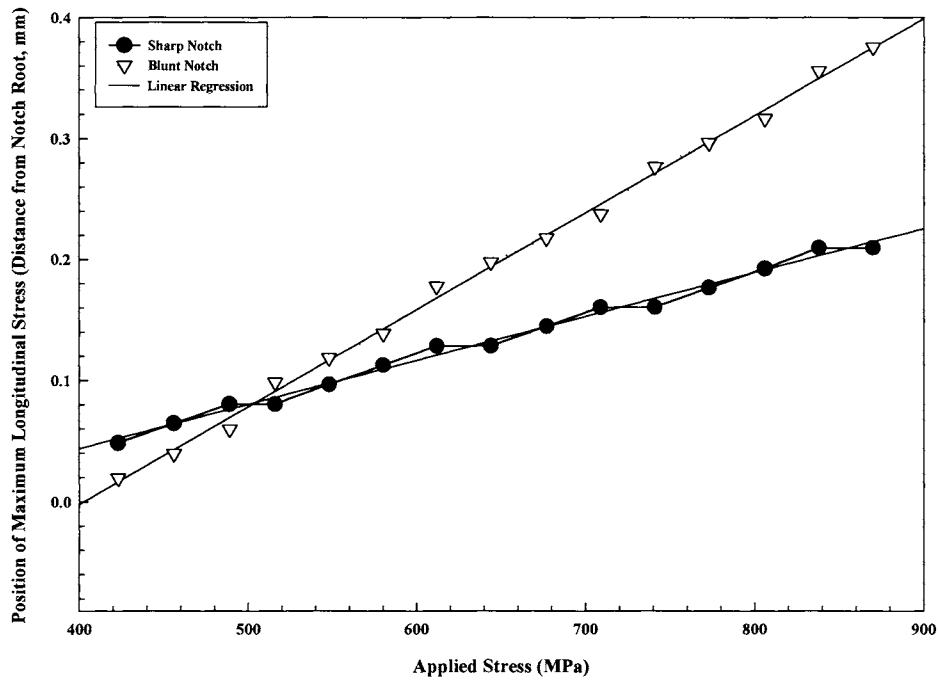
Figure 4.29. Comparison of the longitudinal stress as a function of radial distance from the notch root for the blunt and sharp notched tensile bars at a remote applied stress of 806 MPa.
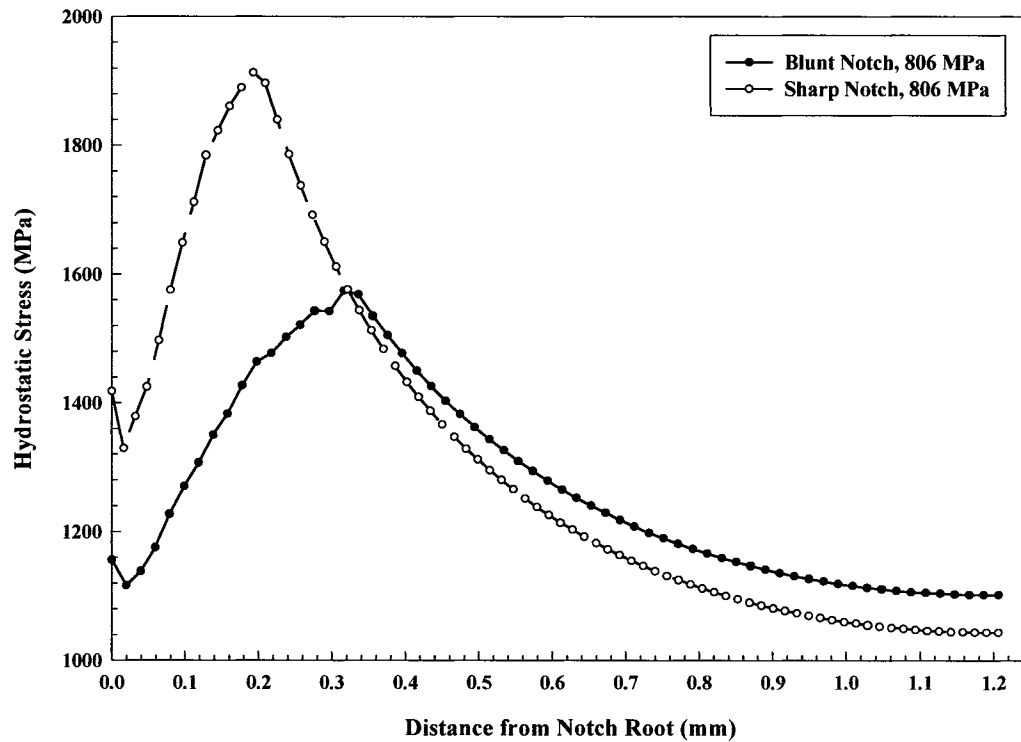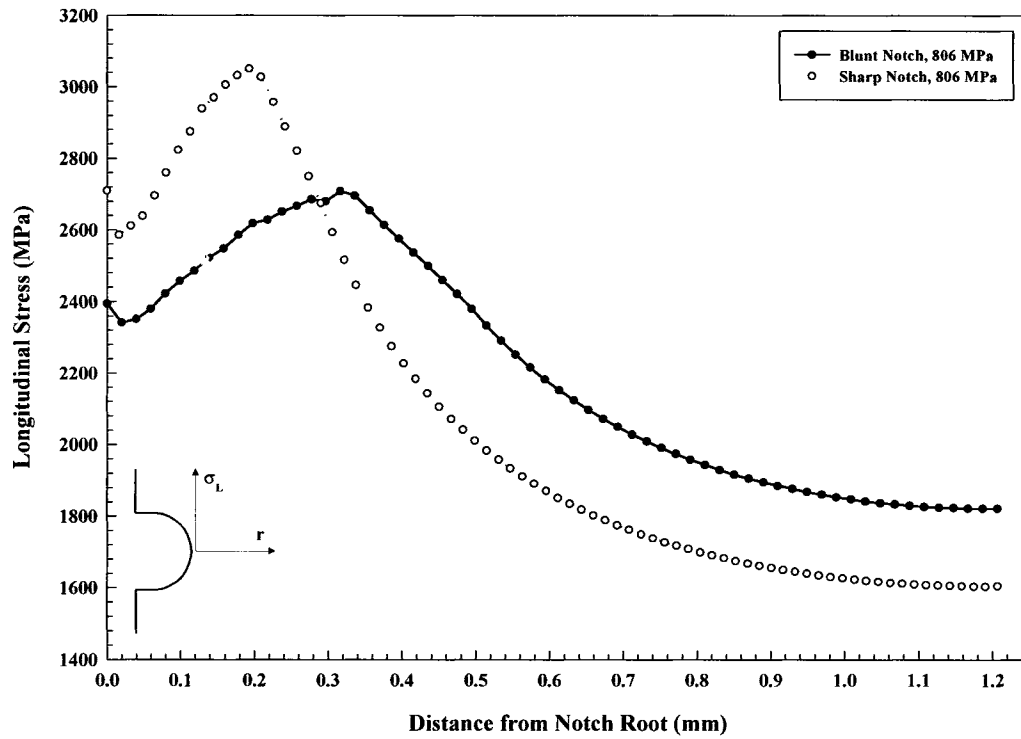
Figure 4.30. Comparison of the maximum longitudinal stress and the hydrostatic stress as a function of remotely applied stress for the blunt and sharp notched tensile bars as a function of radial distance from the notch root.
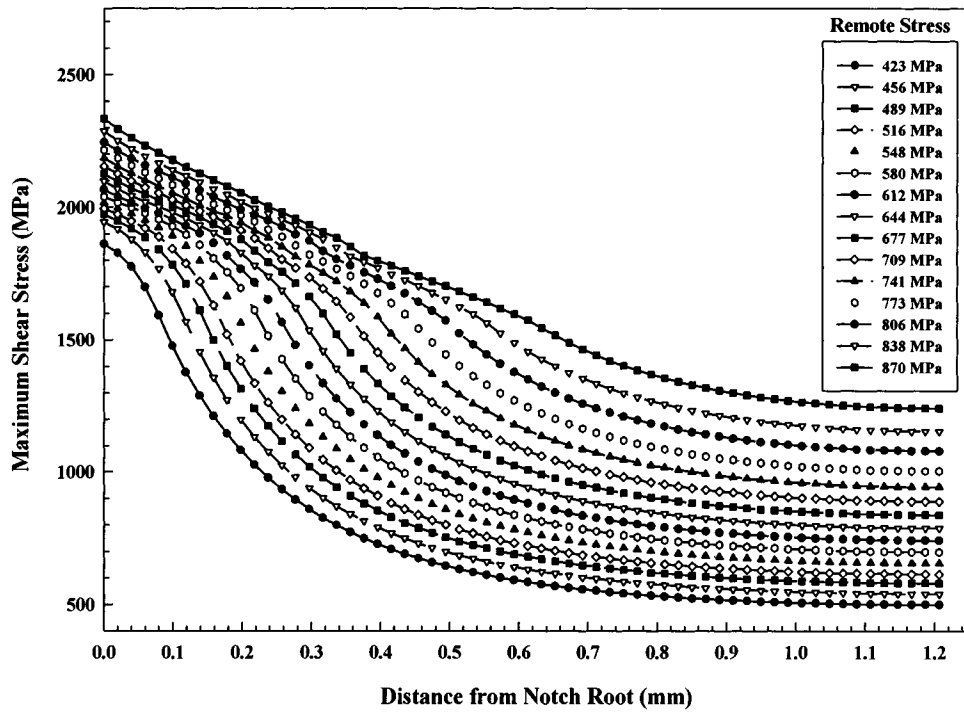
Figure 4.31. Maximum shear stress as a function of radial position from the notch root for the bluntly notched tensile bars.
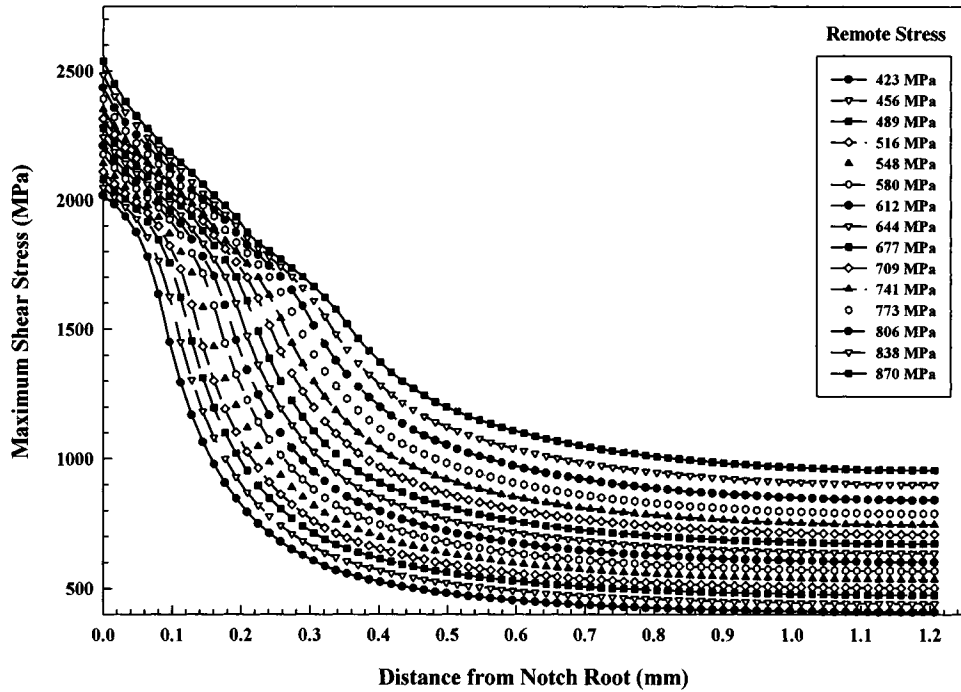
Figure 4.32. Maximum shear stress as a function of radial position from the notch root for the sharply notched tensile bars.
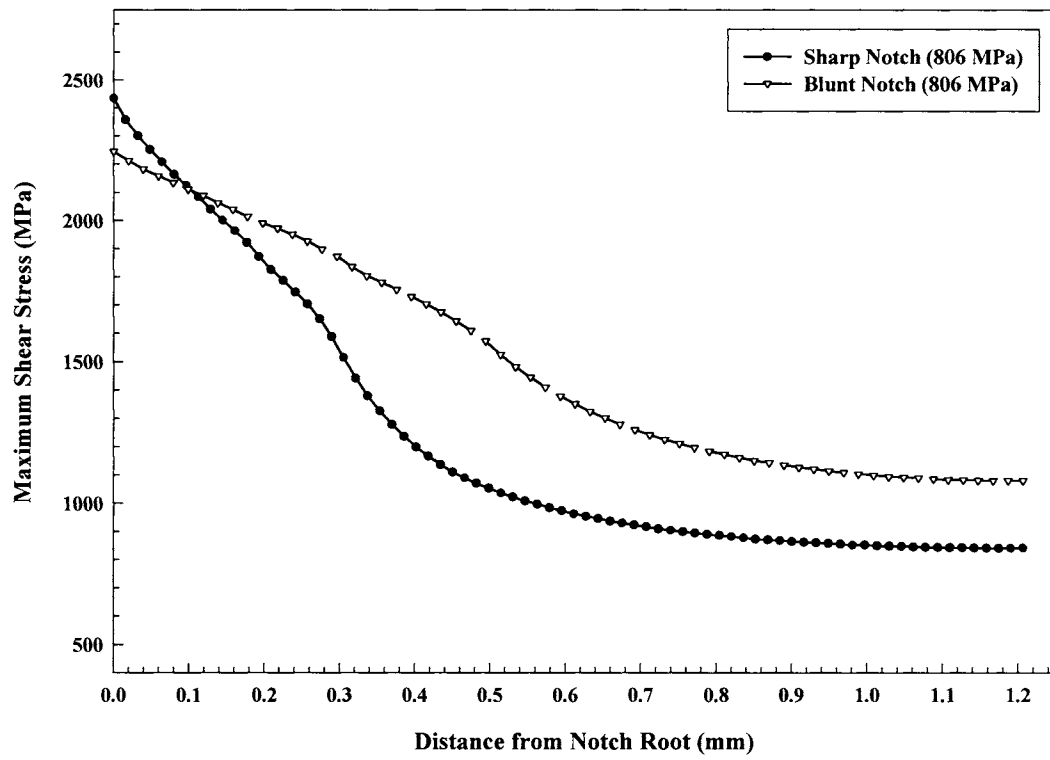
Figure 4.33. Comparison of the position of the maximum shear stress as a function of remotely applied stress for the blunt and sharply notched tensile bars.
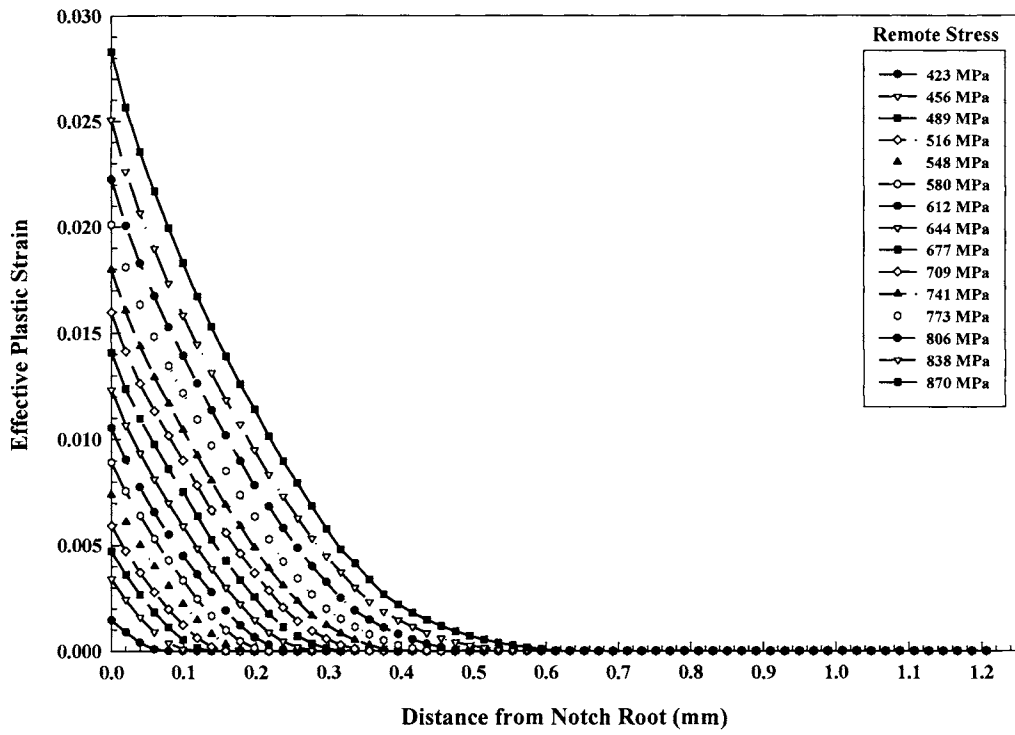
Figure 4.34. Effective plastic strain as a function of radial distance from the notch root for the bluntly notched tensile specimens illustrated in Figure 4.24a.
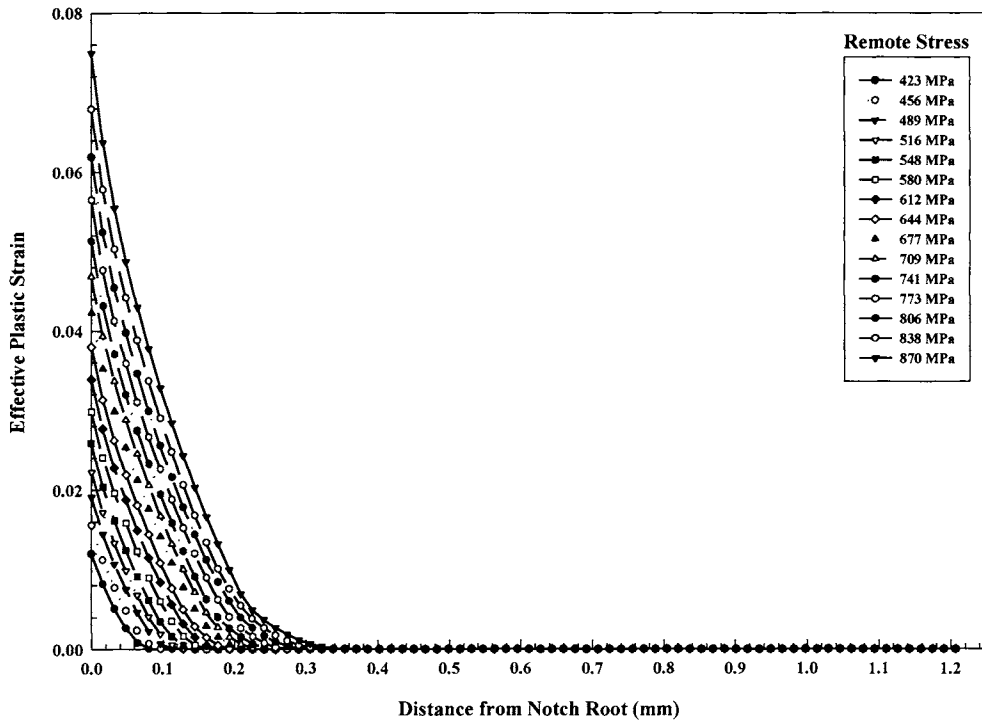
Figure 4.35. Effective plastic strain as a function of distance from the notch root for the sharply notched tensile specimens illustrated in Figure 4.24b.
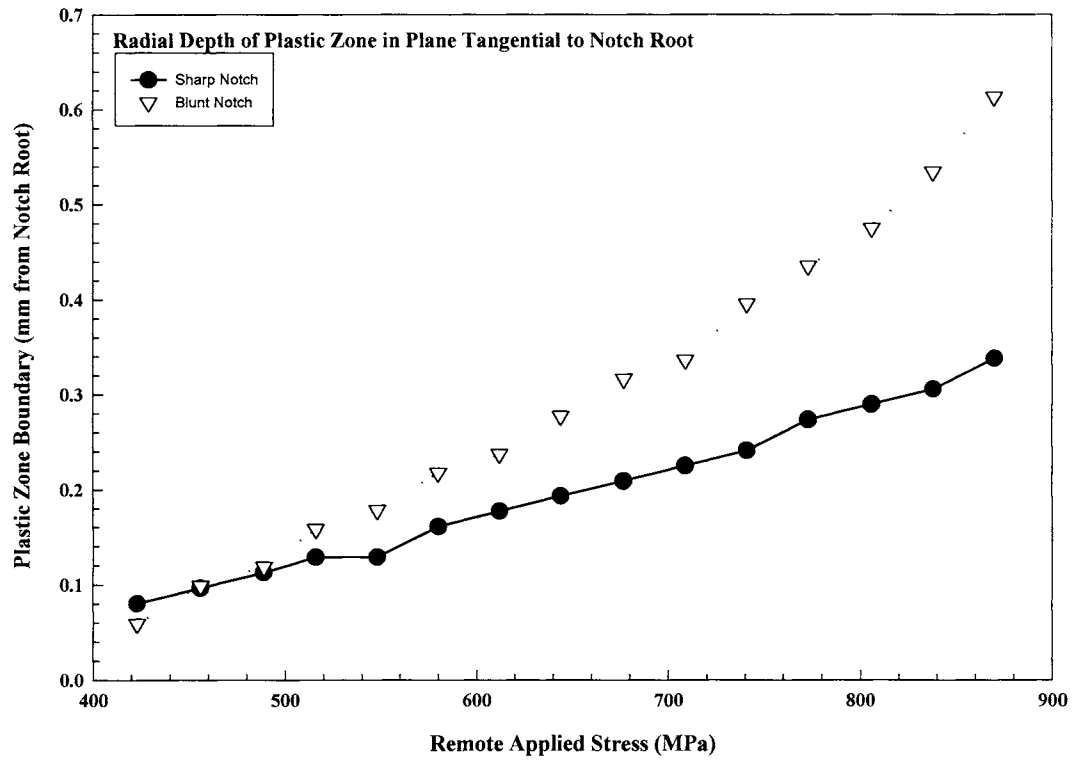
Figure 4.36.   Radial depth of the plastic zone as a function of the remotely applied load for the blunt and sharp notched tensile bars.

8-32 threads

0.164 in. +/- 0.002"
(0.417 cm +/- 0.005 cm)

0.5 in. (1.27 cm)

0.25 in. (0.635 cm)

0.25 in. (0.635 cm)

EDM "chord" notch
(using 0.003" wire)

0.164 in. +/- 0.002"
0.417 cm +/- 0.005 cm)

Notch Depth of 0.0400" +/- 0.0005"
(0.102 cm +/- 0.001 cm)
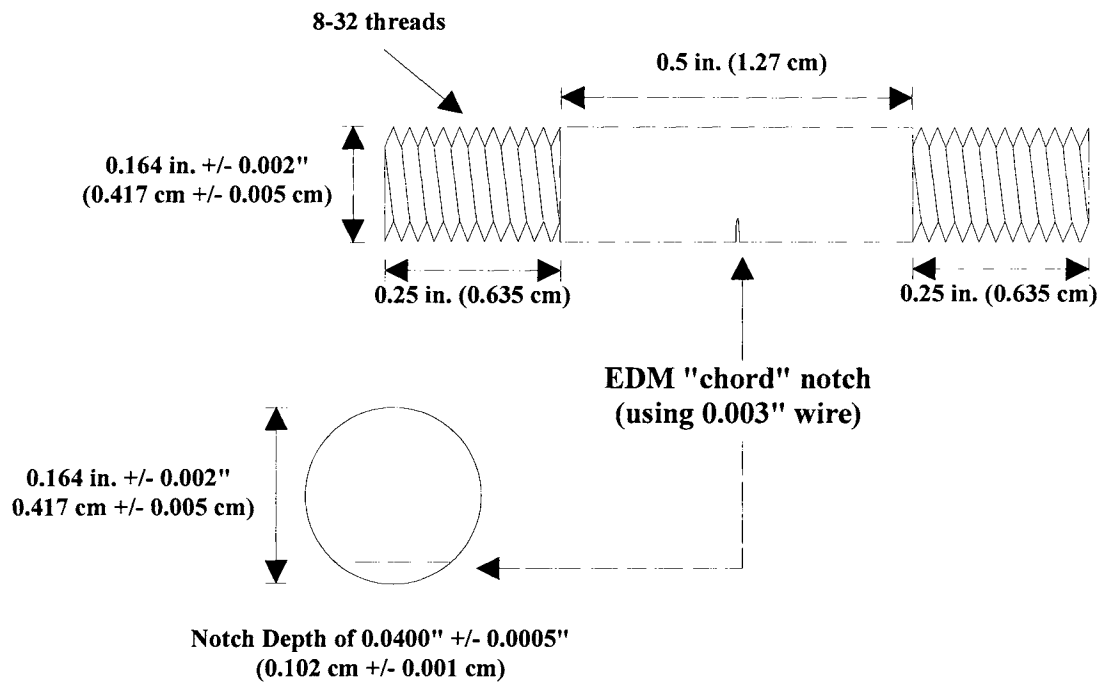
Figure 4.37. EDM chord notched tensile samples utilized for small crack fracture mechanics experiments.
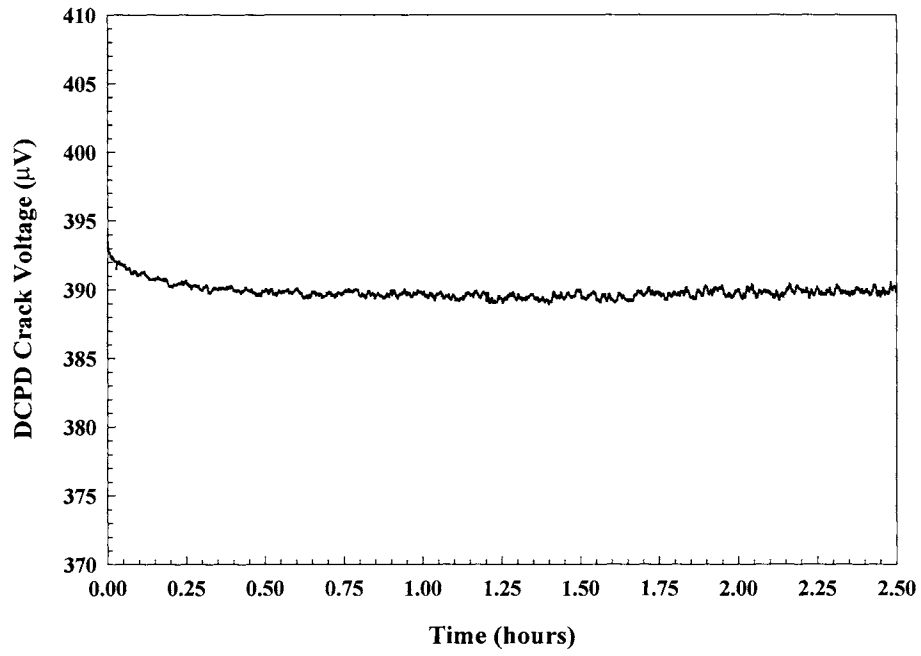
Figure 4.38.   Crack voltage as a function of time, illustrating its long-term stability
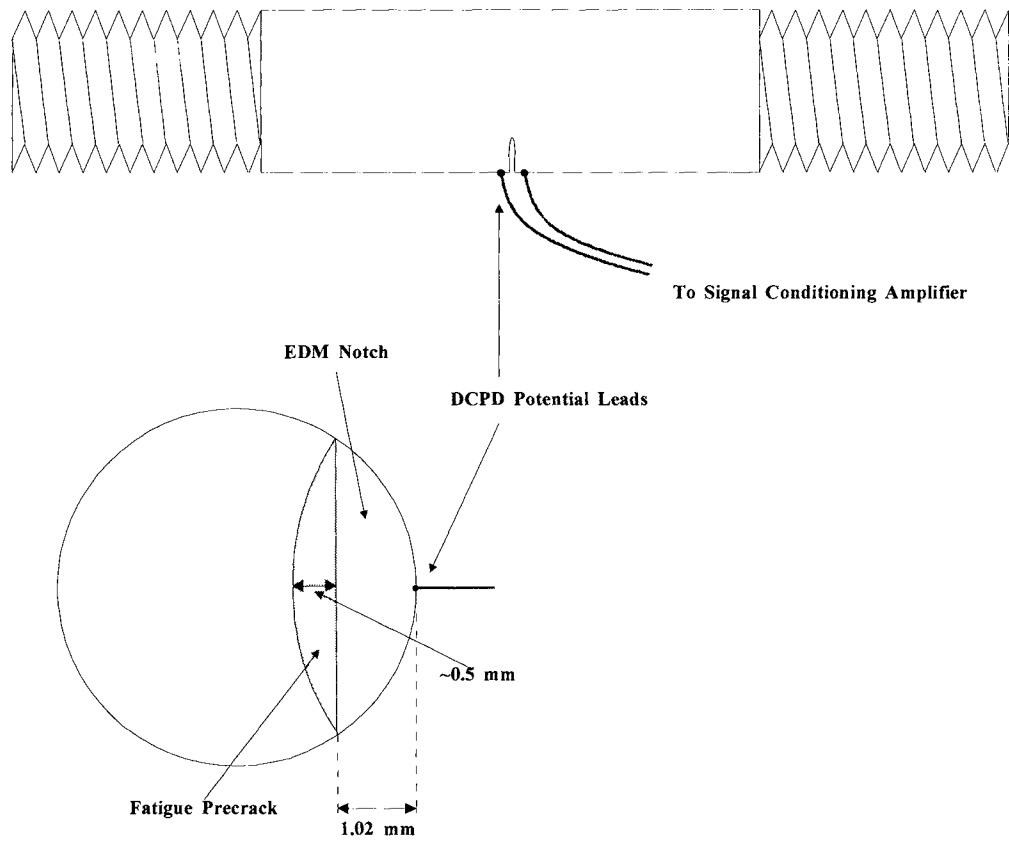
Figure 4.39.   Location of potential leads for direct current, potential drop (DCPD) monitoring of crack initiation and growth for the EDM notched tensile specimens illustrated in Figure 4.42.
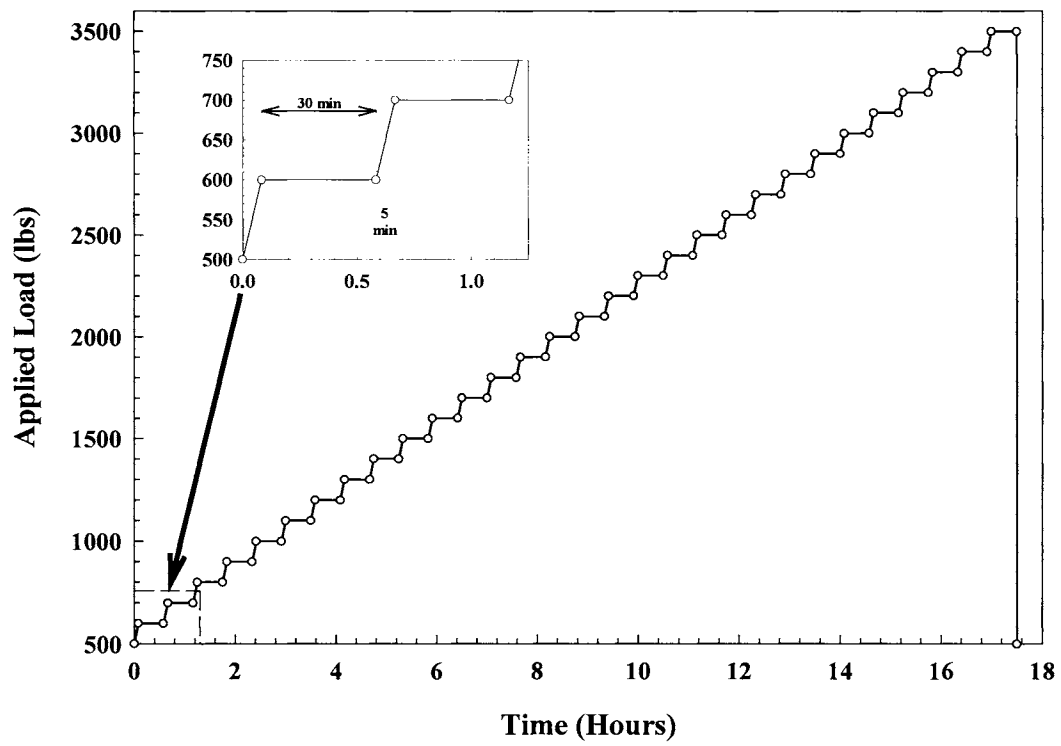
Figure 4.40. Load stepping waveform used to determine crack initiation toughness as a function of hydrogen concentration for the EDM notched and precracked specimens.
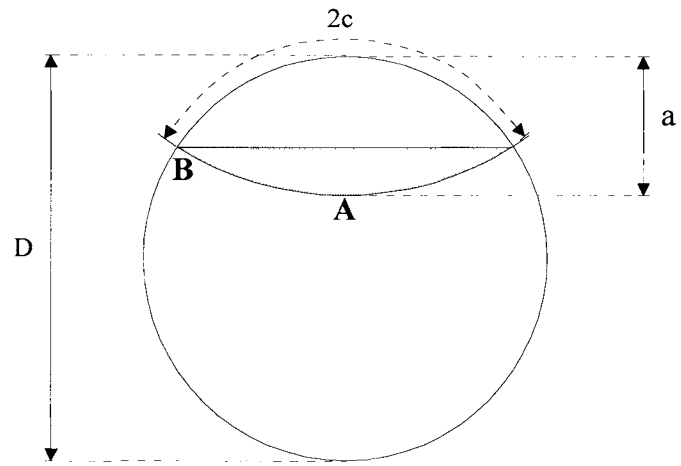
Figure 4.41. Schematic of the crack front, and significant geometrical dimensions, for the fatigue precrack.

1080 Steel Sample
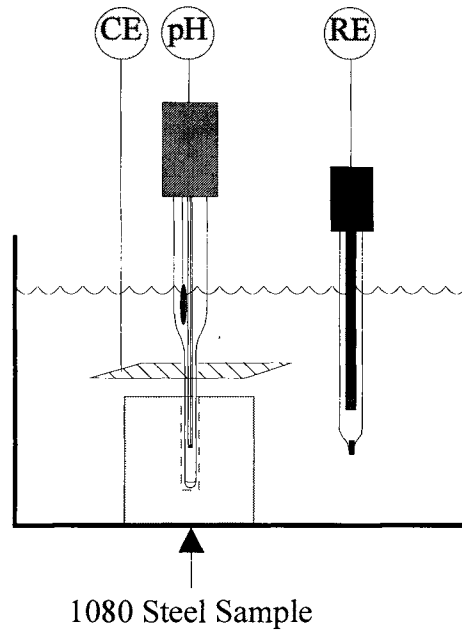
Figure 4.42. Schematic of the artificial crevice cell used to simulate a pre-stressing steel/concrete interface utilizing a glass pH electrode and a segment of undrawn, pre-stressing strand. External environment was aerated, saturated $Ca(OH)_2$ + 0.5 M NaCl at room temperature (approx. 25°C).
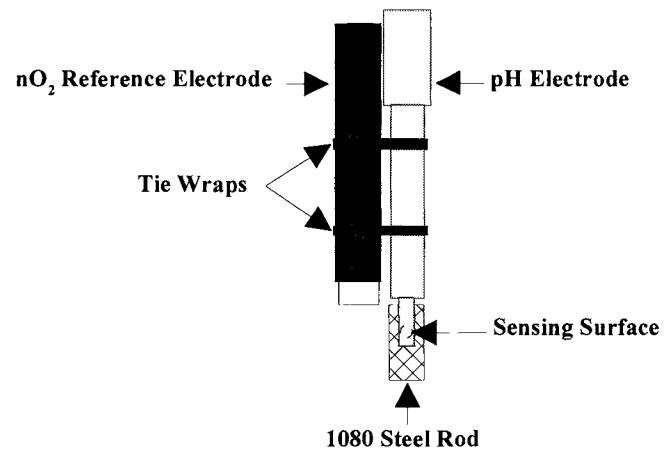
Figure 4.43.   Schematic of the embedded pH electrode assembly utilized within the laboratory scale concrete pilings. The steel crevice cell assembly is composed of a solid state FET pH electrode within an occluded cell formed by a segment of undrawn pre-stressing strand.
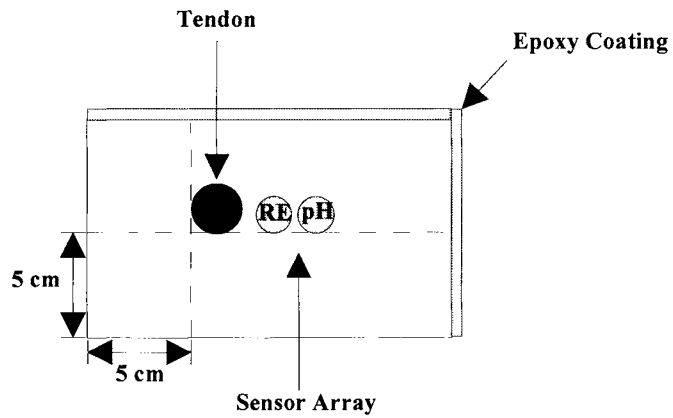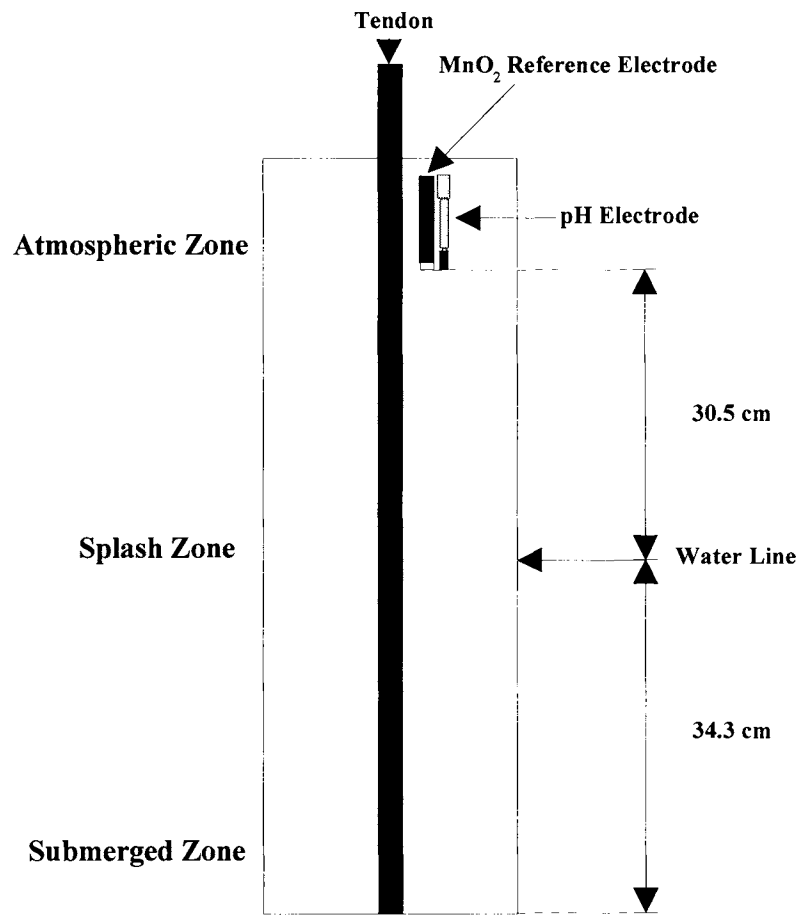
Figure 4.44. Schematic of a laboratory scale piling (piling 1) utilized to observe pH variations within the local environment as a function of time. Embedded sensor array consisted of an MnO_2 reference electrode, and an embedded pH electrode assembly (Figure 2).
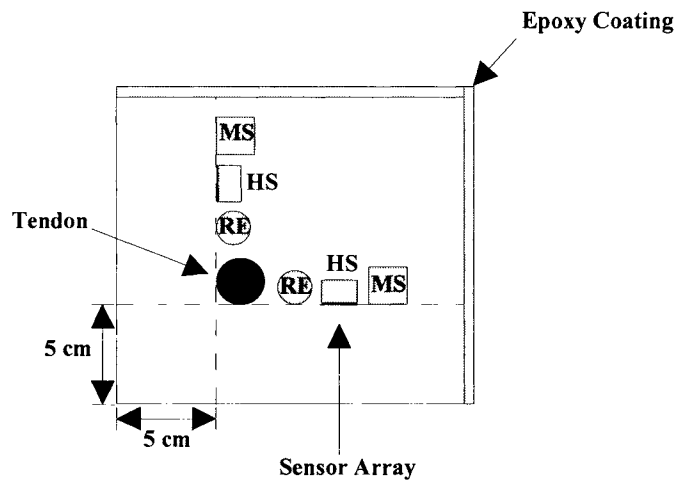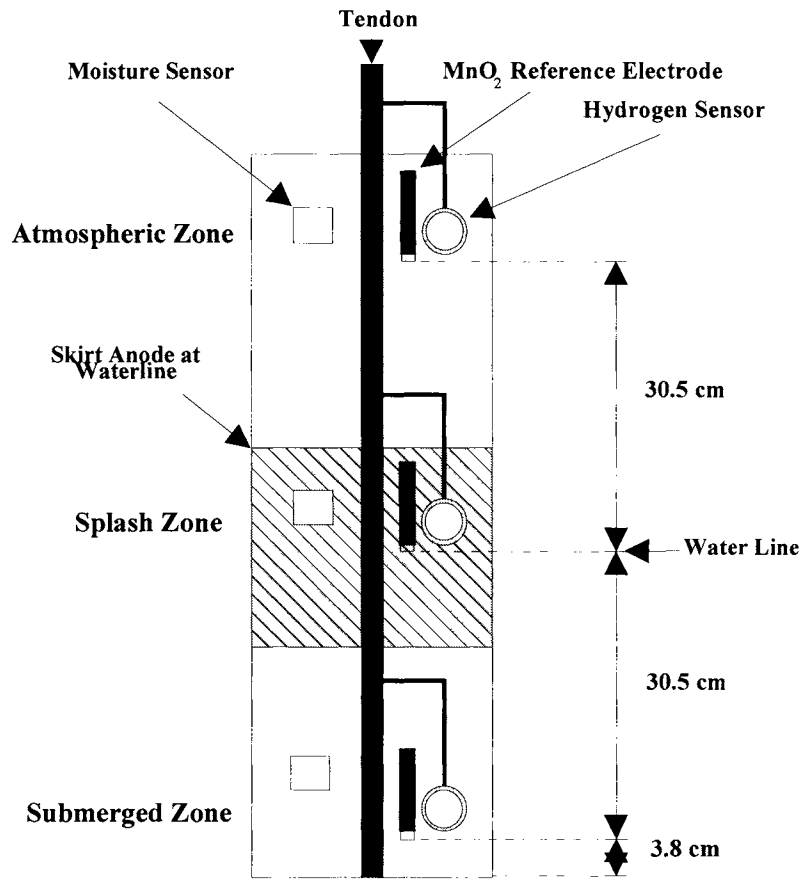
Figure 4.45. Schematic of a laboratory scale piling (piling 2) utilized for cathodic protection studies. Embedded sensor arrays consisted of an MnO_2 reference electrode, a hydrogen sensor with a mild steel window, and a moisture sensor. The permeation window of the hydrogen sensor is electrically connected to the tendon, ensuring that both received the same cathodic protection level and corresponding hydrogen surface coverage.
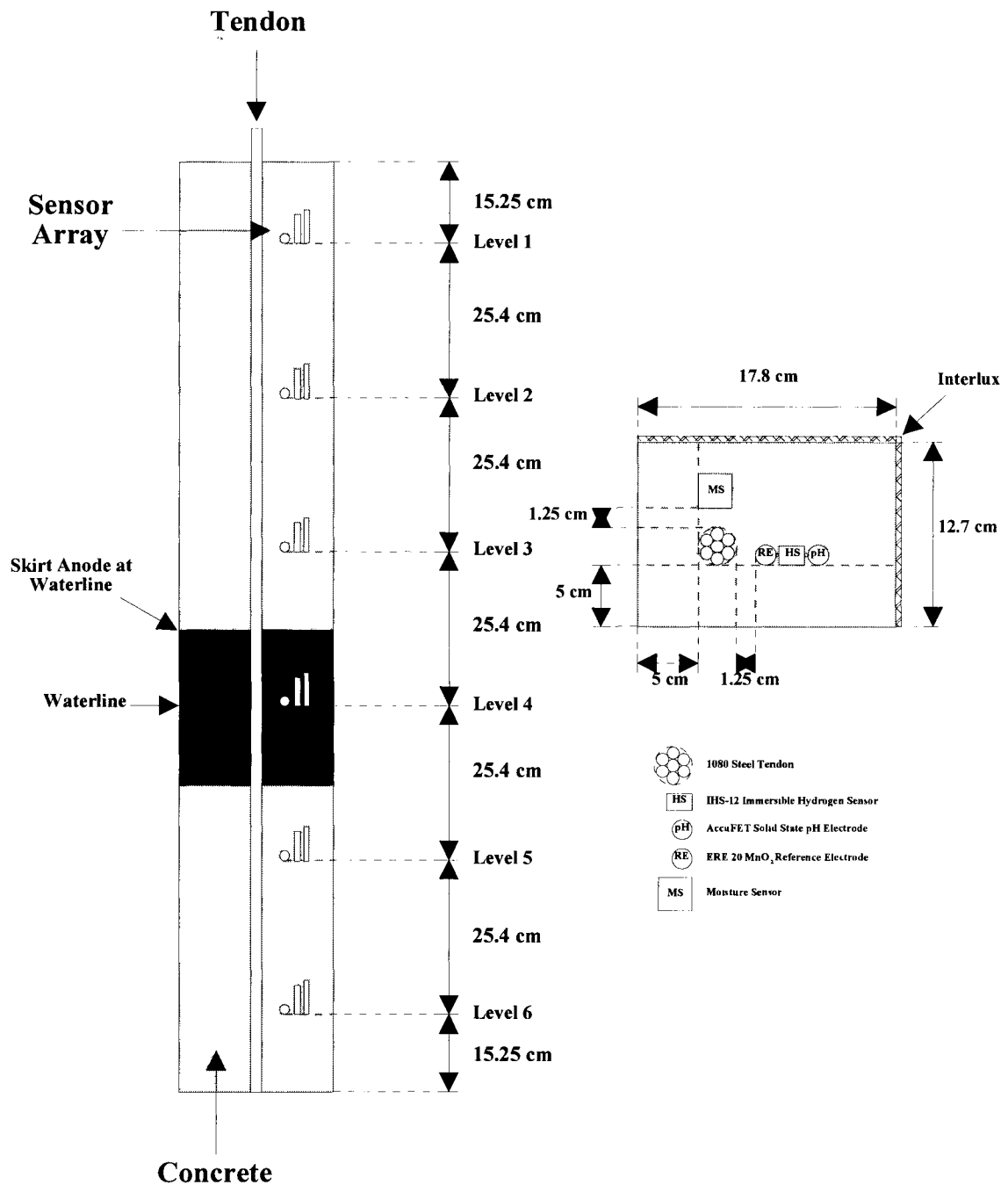
Figure 4.46. Schematic of a laboratory scale piling (piling 3) utilized for cathodic protection studies. Embedded sensor arrays consisted of an MnO_2 reference electrode, a hydrogen sensor with a mild steel window, a pH electrode assembly (Figure 2) and a moisture sensor.
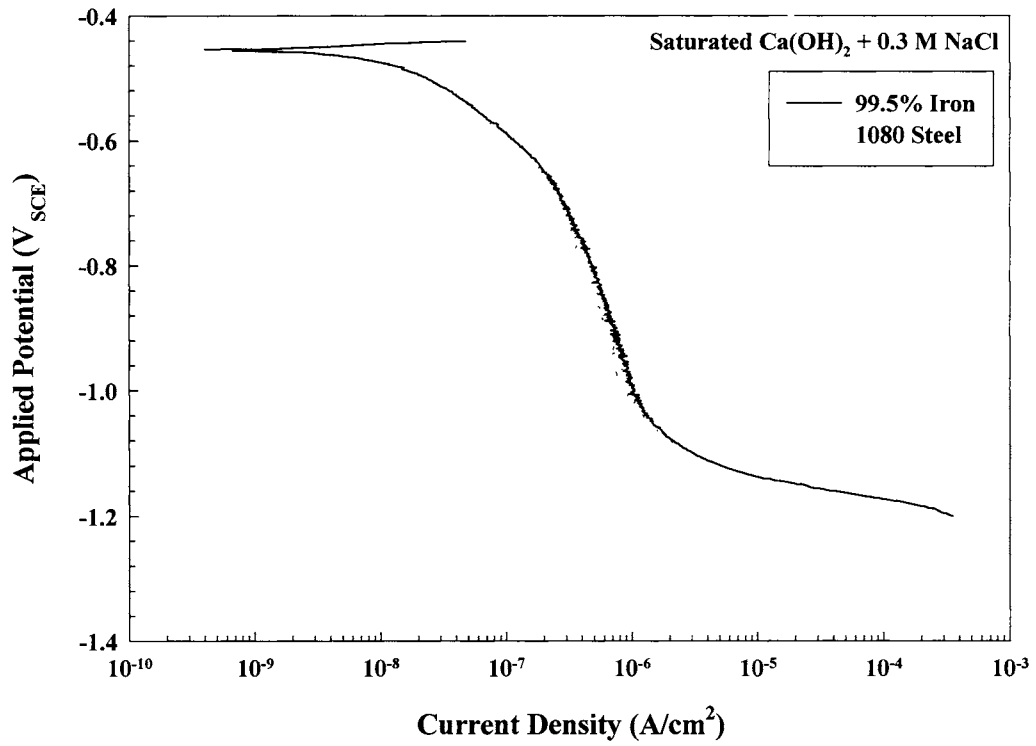
Figure 5.1. Cathodic polarization of 99.5% iron and AISI/SAE 1080 steel in saturated $Ca(OH)_2$ + 0.3 M NaCl.
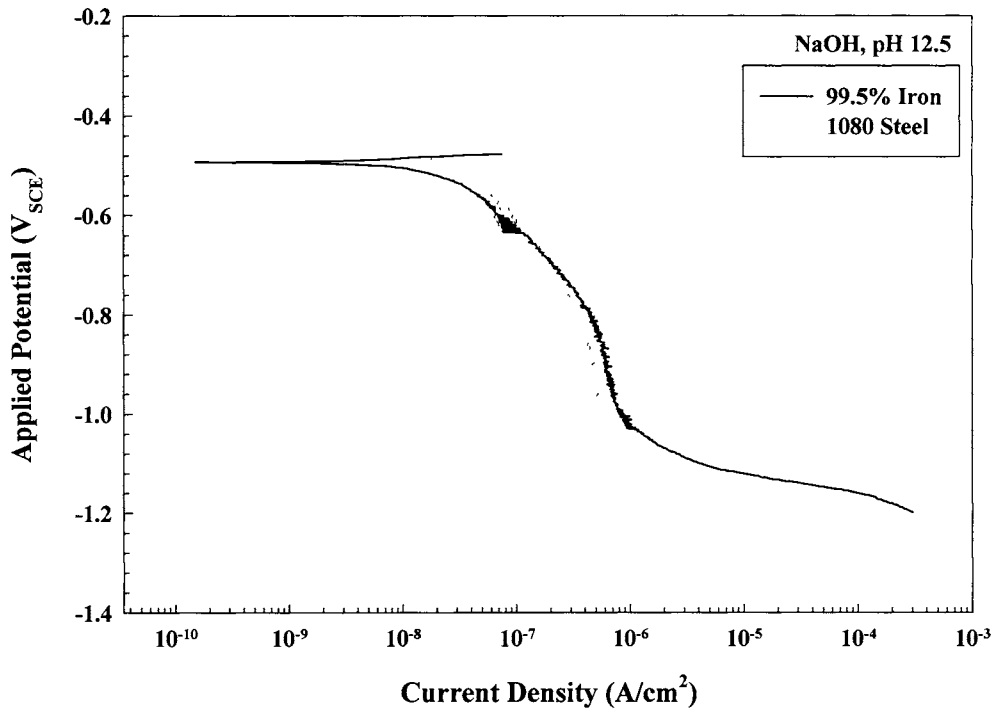
Figure 5.2. Cathodic polarization of 99.5% iron and AISI/SAE 1080 steel in pH 12.5 NaOH.
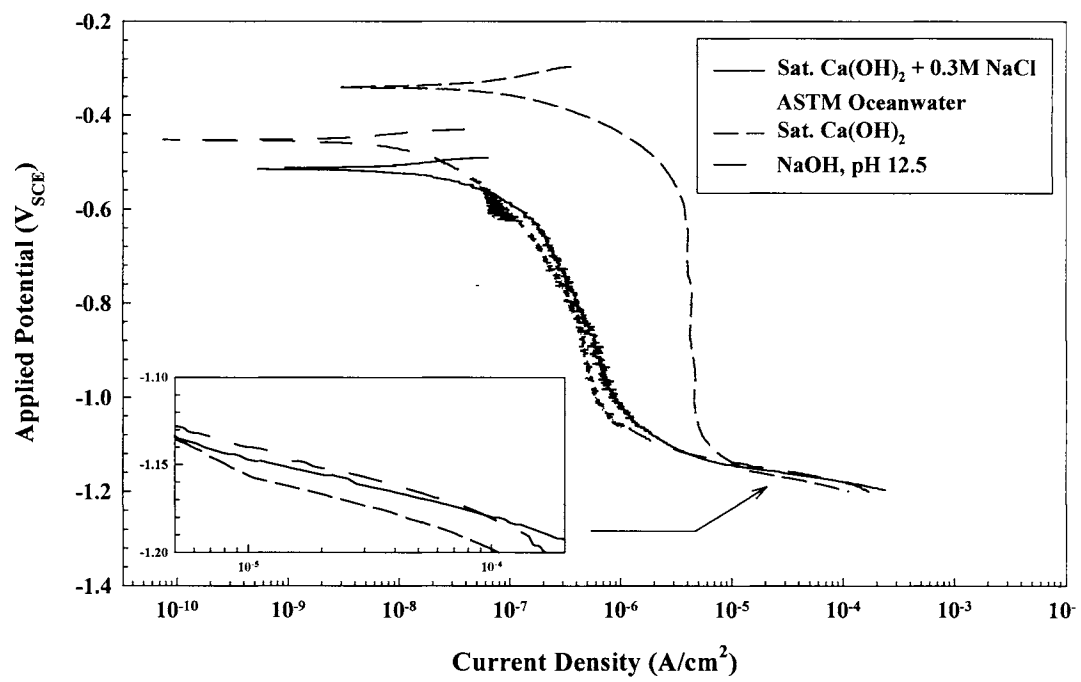
Figure 5.3. Cathodic polarization of AISI/SAE 1080 steel in saturated $Ca(OH)_2$, $Ca(OH)_2$ + 0.3 M NaCl, pH 12.5 NaOH, and ASTM artificial ocean water.

0.2

0.1

0.0

−0.1

−0.2

−0.3

Hydrogen Overpotential (V)

Applied Cathodic Current Density (A/cm²)

10⁻⁵   10⁻⁴   10⁻³

Saturated Ca(OH)₂ (pH 12.6)
Saturated Ca(OH)₂ (pH 9.2)
NaOH (pH 12.5)

pH^{surface} in Sat. Ca(OH)₂ (pH^{bulk} = 9.2)
pH^{surface} in Sat Ca(OH)₂ (pH^{bulk} = 12.6)
pH^{surface} in NaOH (pH^{bulk} = 12.5)

9 2787
12 6000
12 5000

9 3133
12 6000
12 5000

9 3453
12 6001
12 5000

9 4996
12 6002
12 5002

9 6752
12 6003
12 5004

9 7999
12 6005
12 5006

9 8967
12 6007
12 5008

10 2388
12 6017
12 5021

10 5195
12 6034
12 5043

10 6886
12 6051
12 5064

10 8100
12 6058
12 5085

RDE Results (pH and IR adjusted data)
Hydrogen Overpotential (η) = abs(E_{app})-abs(-0.241 - 0.059*pH^{surface})

Electrode: 99.9% Fe
Rotation Rate: 750 RPM
Solutions: Deaerated Saturated Ca(OH)₂ at pH 12.6 and pH 9.2 (Same [Ca²⁺])
            Deaerated NaOH at pH 12.5

Figure 5.4.   Hydrogen overpotential as a function of applied current density from rotating disk electrode experiments performed in on a 99.9% Fe disk in Ca(OH)₂ and NaOH at 750 rpm.
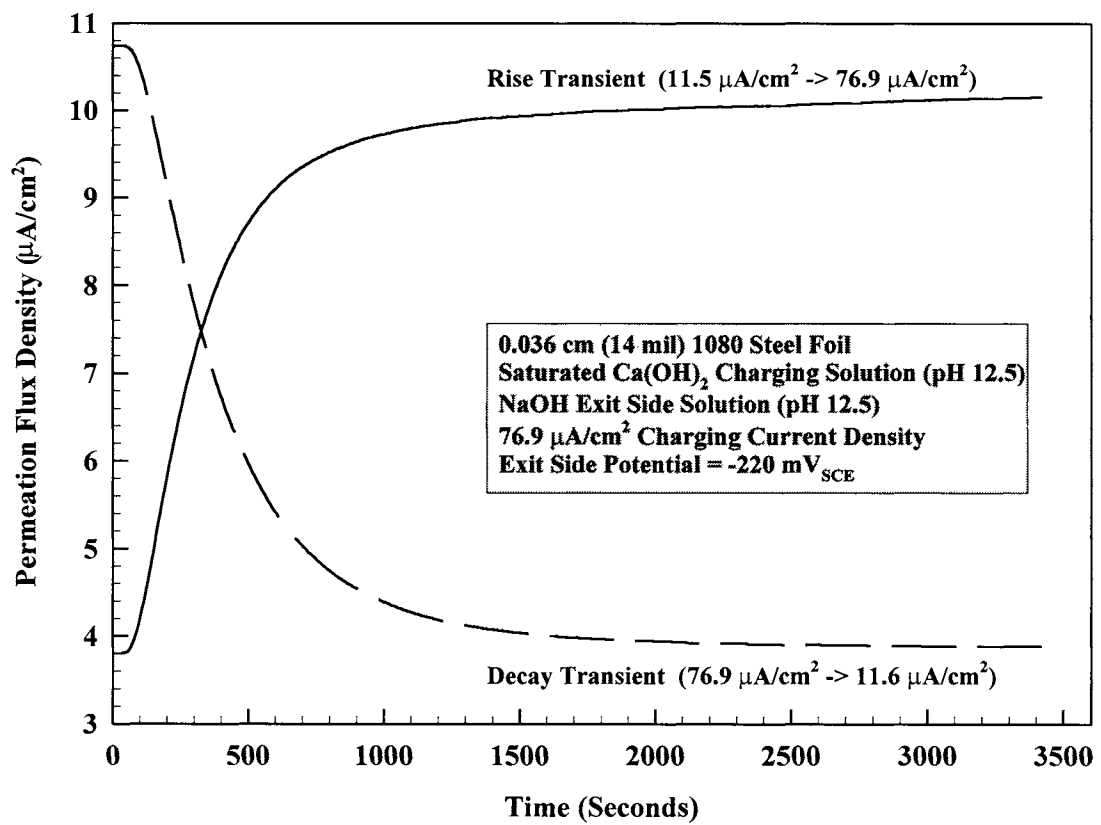
Figure 5.5. Representative rise and decay transients obtained via the Devanathan/Stachurski permeation technique for a pearlitic, 1080 steel foil.
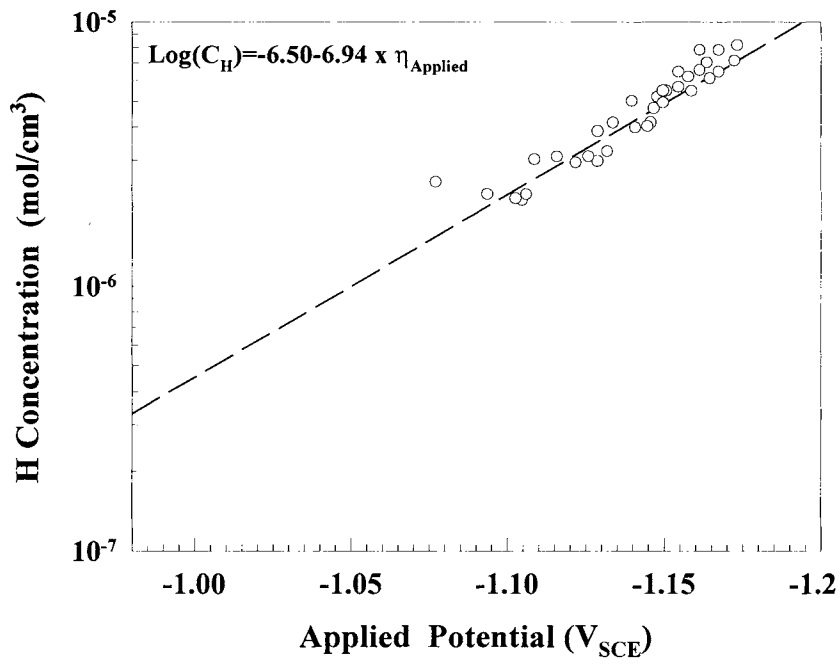
Figure 5.6: Steady state subsurface hydrogen concentration as a function of applied potential (IR corrected) from permeation experiments conducted on SAE/AISI 1080 steel foils in saturated $Ca(OH)_2$. Experiments were performed galvanostatically at a fixed temperature of 27°C. ($E_{REV}^{HER} = -0.981$ V_{SCE})
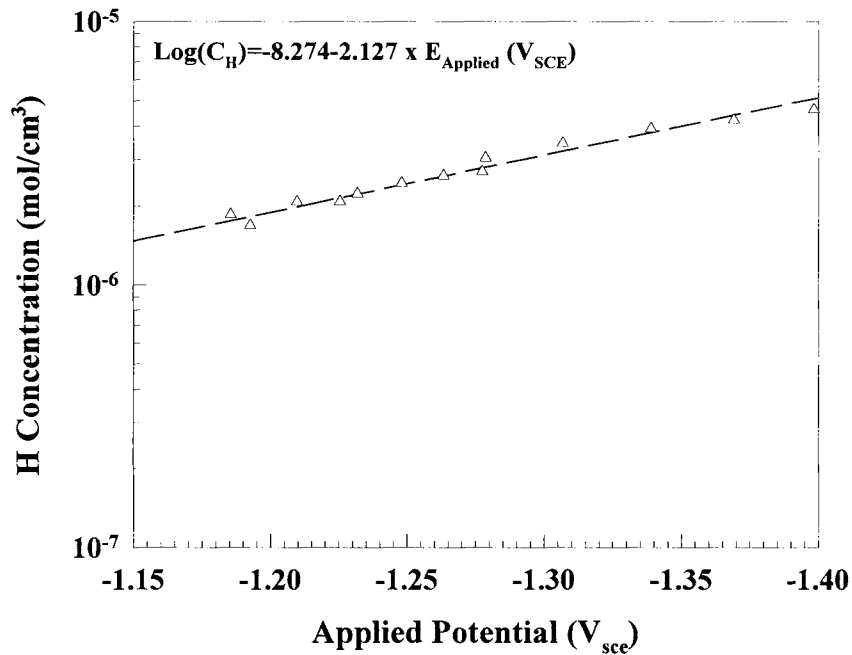
Figure 5.7: Steady state subsurface hydrogen concentration as a function of applied potential (IR corrected) from permeation experiments conducted on SAE/AISI 1080 steel foils with mortar cover in ASTM oceanwater. Experiments were performed galvanostatically at a fixed temperature of 27°C. ($E_{REV}^{HER} = -0.981$ V_{SCE}, assuming pH 12.5).
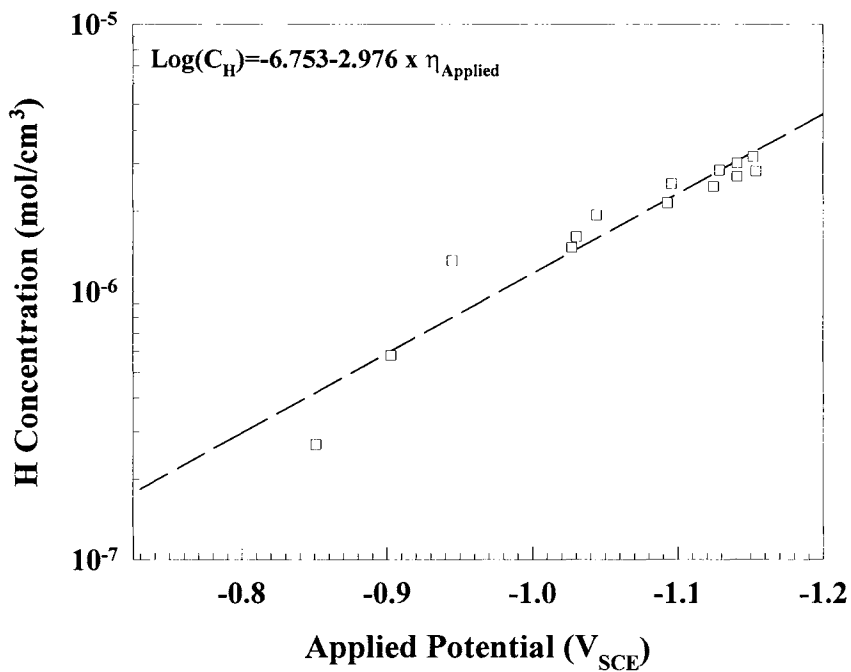
Figure 5.8: Steady state subsurface hydrogen concentration as a function of applied potential (IR corrected) from permeation experiments conducted on SAE/AISI 1080 steel foils in ASTM ocean water. Experiments were performed galvanostatically at a fixed temperature of 27°C.
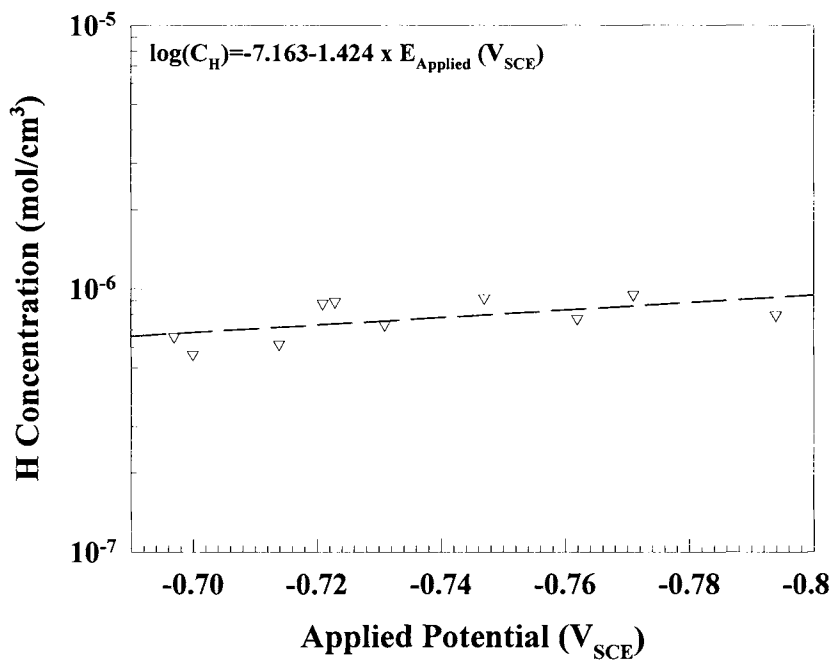
Figure 5.9: Steady state subsurface hydrogen concentration as a function of applied potential (IR corrected) from permeation experiments conducted on SAE/AISI 1080 steel foils in a pH 6 solution containing 1 N H_3BO_4 + 1 mM $Ca(OH)_2$ + 3.3 mM KCl. Experiments were performed galvanostatically at a fixed temperature of 27°C.

4.0e-6

Shaded Band - Saturated Ca(OH)₂ (pH 12.5)

3.5e-6

Mortar Cover in ASTM Oceanwater

3.0e-6

2.5e-6

ASTM Oceanwater (pH 8.2)

2.0e-6

Steel Lattice Hydrogen Concentration (mol/cm³)

1.5e-6

H₃BO₃ + Ca(OH)₂ + KCl + HCl (pH 6)

1.0e-6

-0.876 V_SCE   V_SCE   V_SCE

5.0e-7   5x10⁻⁷ mol/cm³

Ca(OH)₂   ASTM   pH 6

0.0

1   2   3   4   5   6   7   8   9   10

(Charging Current Density)¹ᐟ² (μA/cm²)¹ᐟ²
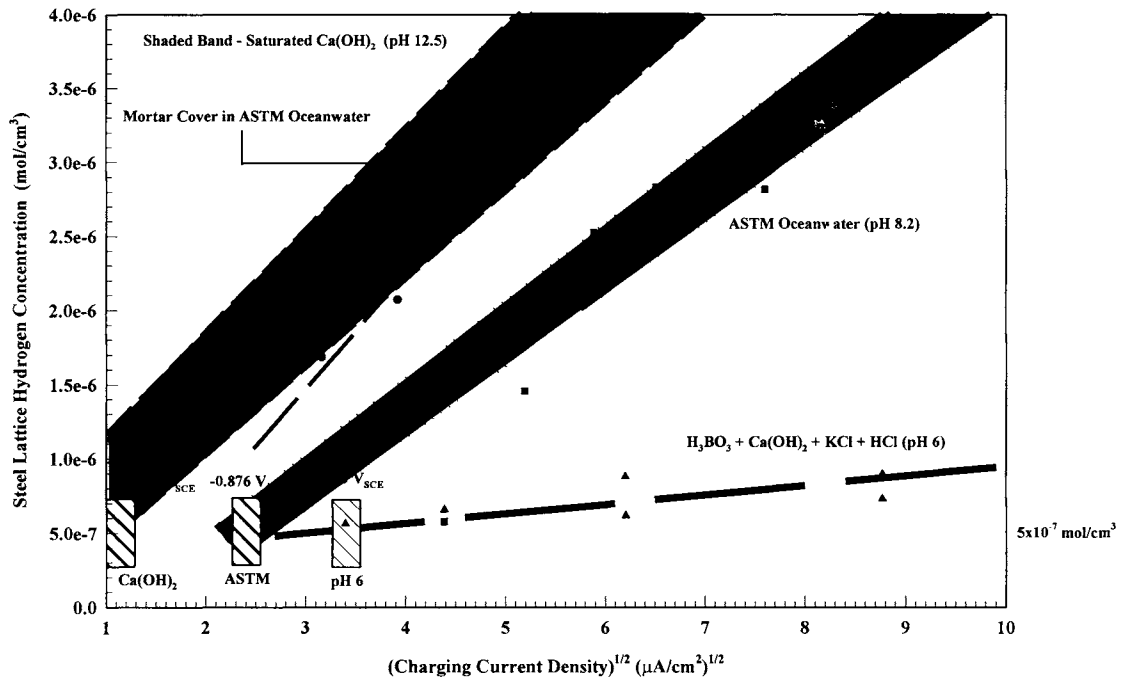
Figure 5.10: Comparison of permeation data for each of the environments investigated in this study, illustrating the potential required to achieve a given hydrogen concentration, in this case 5x10⁻⁷ mol/cm³, as a function of the environment.
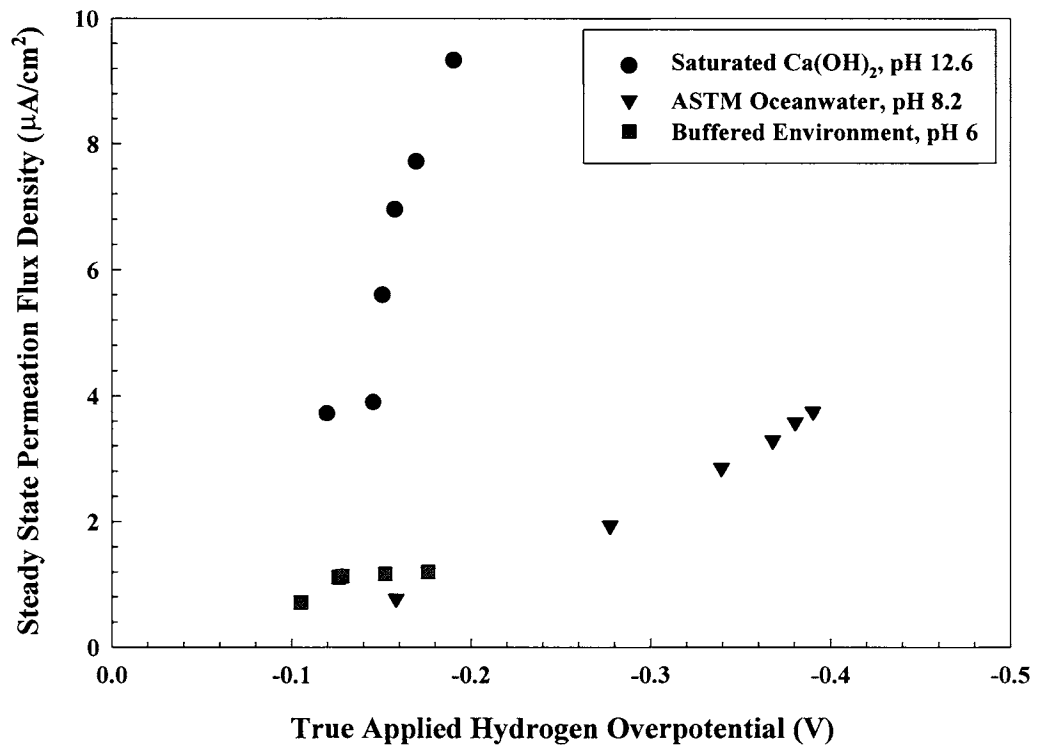
Figure 5.11: Ratio of permeation flux to charging current density for pearlitic, 1080 steel foils as a function of applied cathodic overpotential for each environment, demonstrating the effectiveness of Ca(OH)$_2$ as a recombination poison.
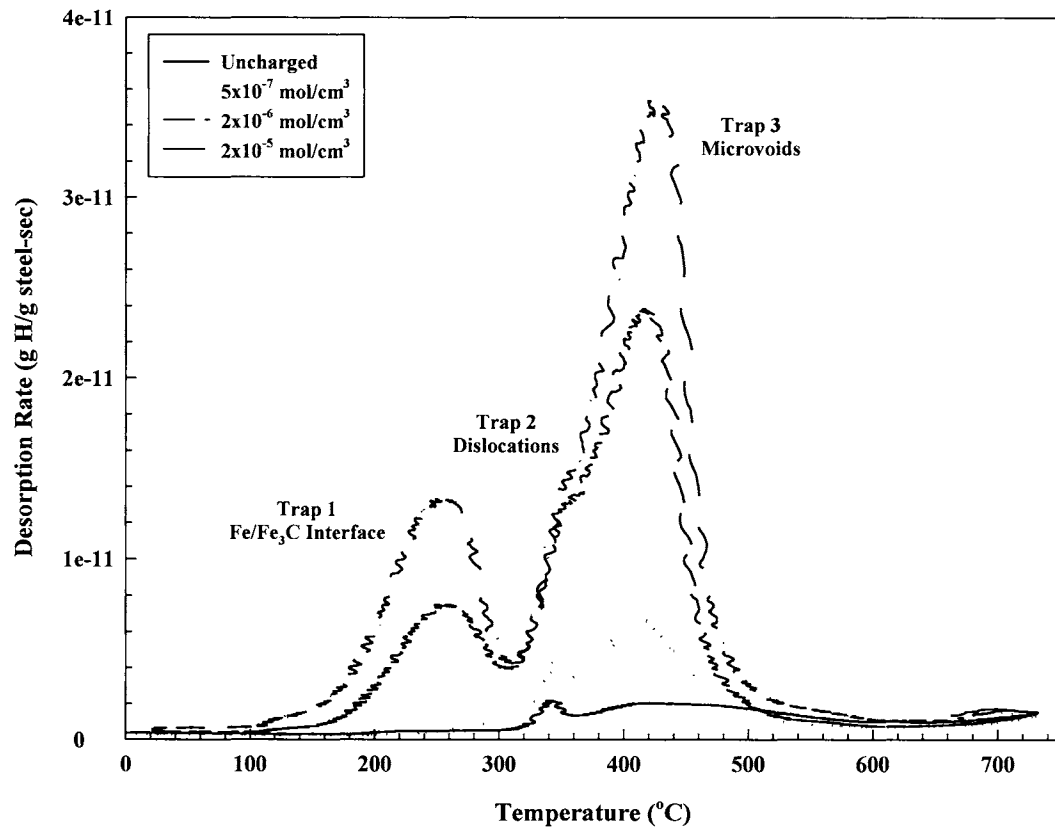
Figure 5.12: Desorption rate vs. temperature as a function of initial mobile lattice hydrogen concentration (determined through electrochemical permeation experiments), illustrating the three discrete trap states within the pre-stressing steel. Ramp rate was 4.25 degrees/minute.
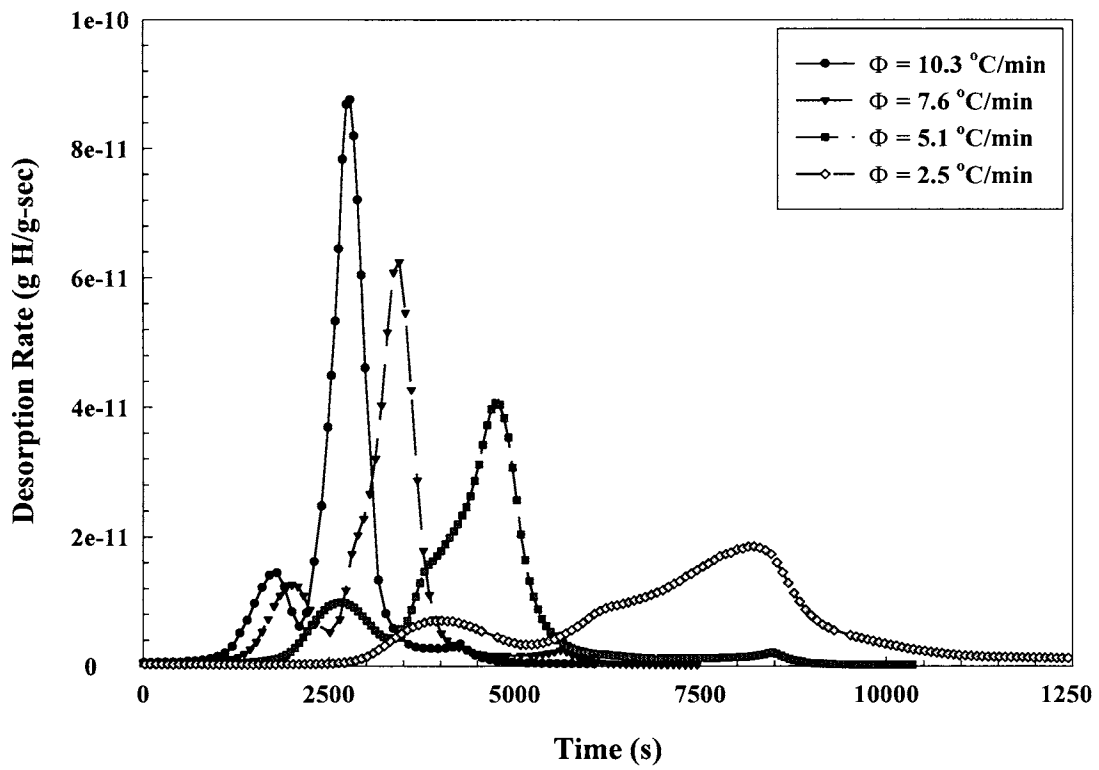
Figure 5.13: Desorption rate vs. temperature as a function of the thermal ramp rate for AISI/SAE 1080 steel pre-stressing tendon samples charged to a uniform mobile hydrogen concentration of 2×10^{-5} mol/cm^3.
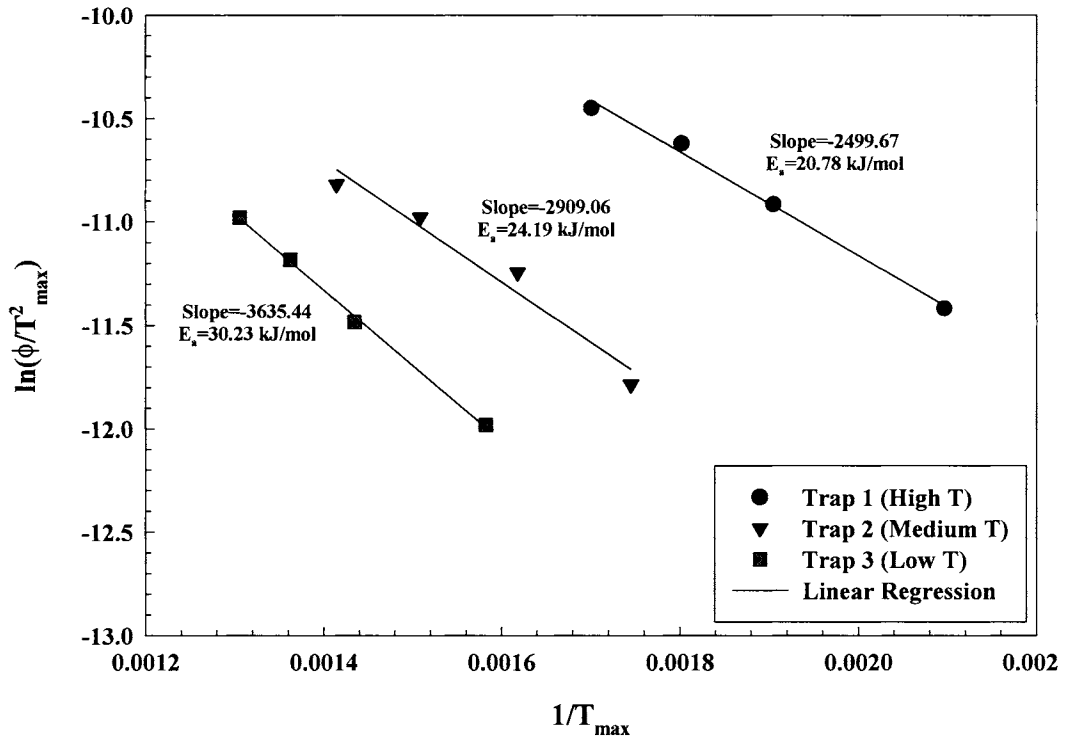
Figure 5.14: Inverse temperature of maximum desorption rate as a function of ramp rate for each trap site observed within hydrogen charged, AISI/SAE 1080 steel pre-stressing steel tendon to calculate activation energy for desorption.
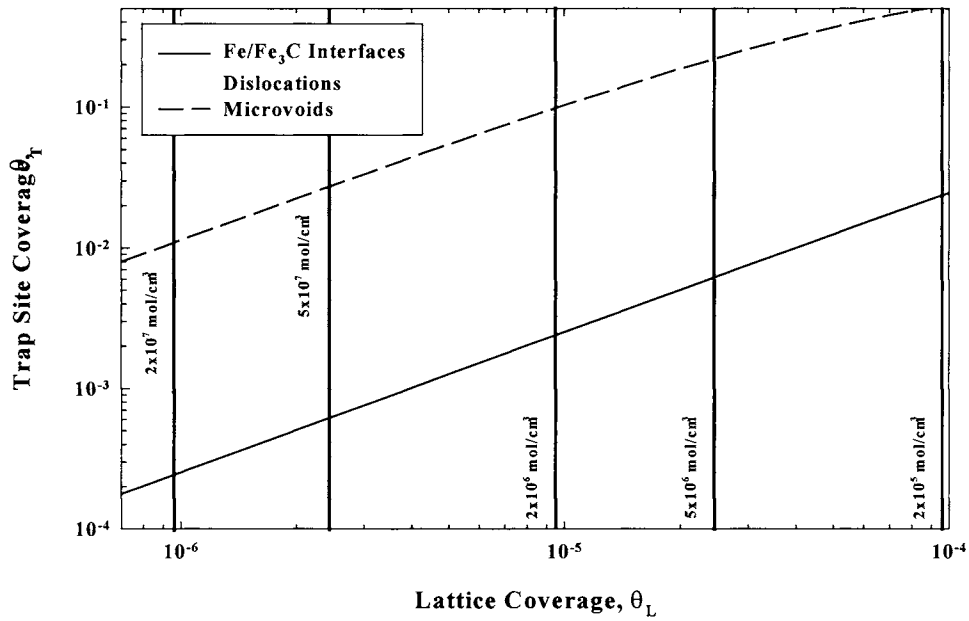
Figure 5.14b: Trap site coverage as a function of lattice coverage for fixed binding energies of 13.71 kJ/mol (Fe/Fe$_3$C interfaces), 17.12 kJ/mol (dislocations), and 23.16 kJ/mol (microvoids).
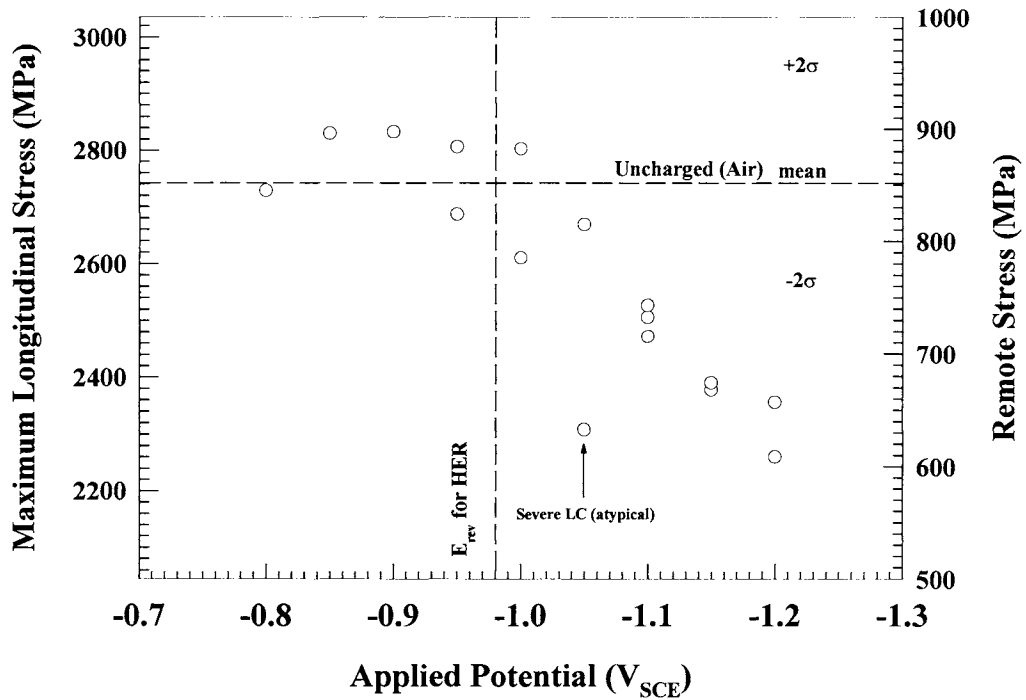
Figure 5.15: Crack initiation stress as a function of applied cathodic potential for bluntly notched 1080 steel pre-stressing steel tensile bars in saturated Ca(OH)$_2$.
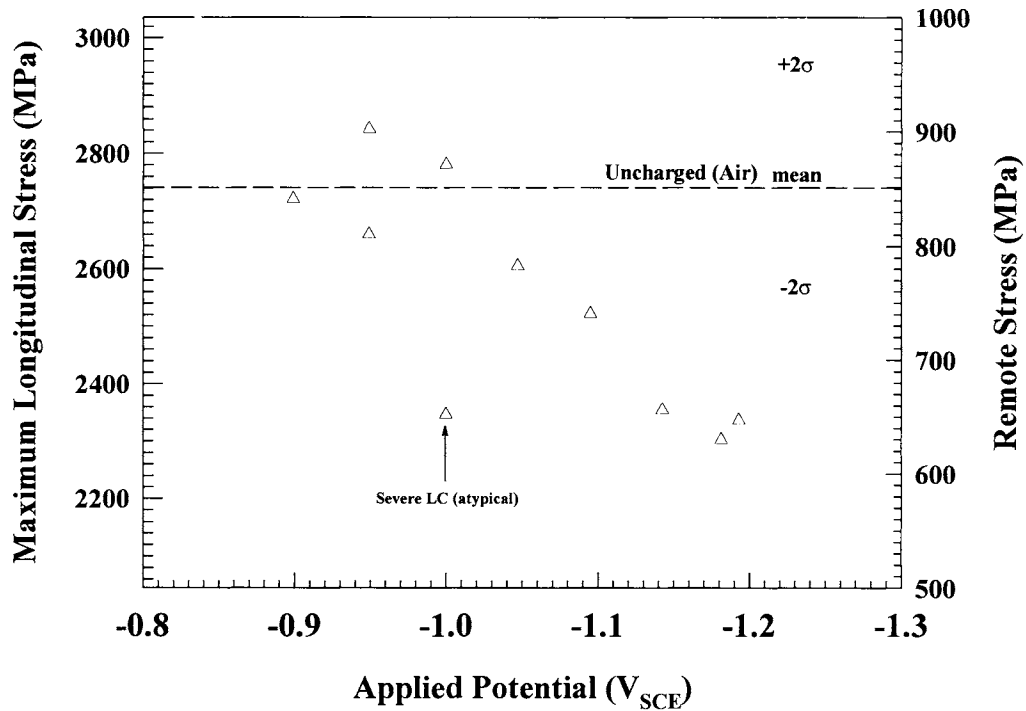
Figure 5.16: Crack initiation stress of 1080 steel pre-stressing tendon as a function of applied cathodic potential for bluntly notched tensile bars with an 0.5" mortar cover immersed in ASTM artificial ocean water.
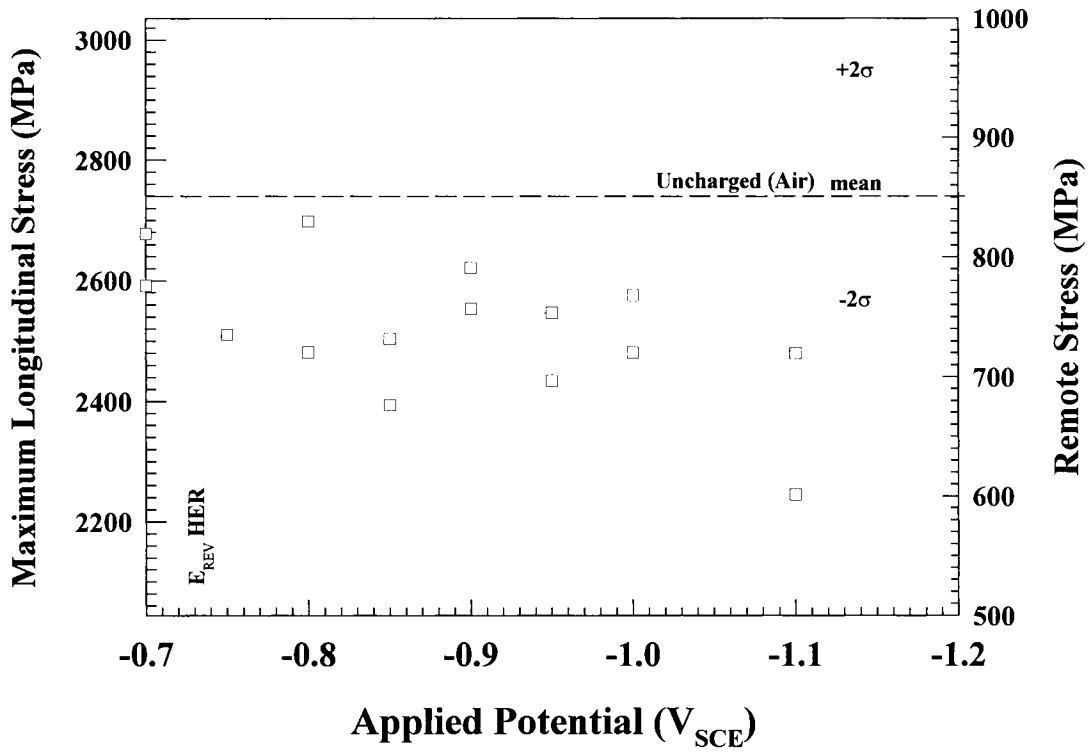
Figure 5.17:   Crack initiation stress of 1080 steel pre-stressing tendon as a function of applied cathodic potential for bluntly notched tensile bars in ASTM artificial ocean water.
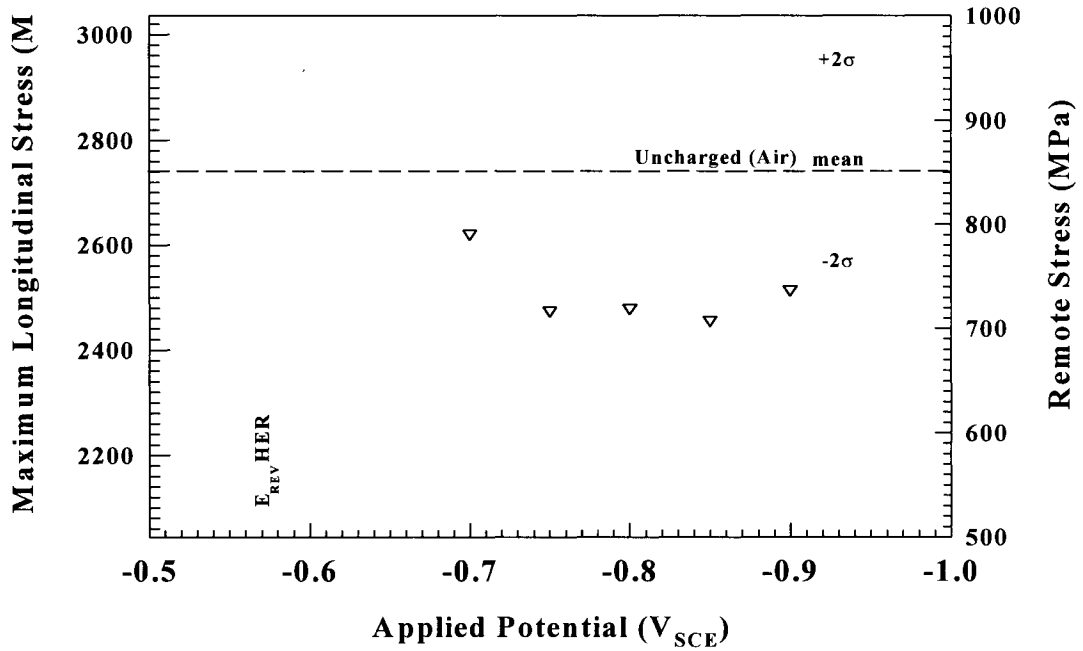
Figure 5.18:   Crack initiation stress of 1080 steel pre-stressing tendon as a function of applied cathodic potential for bluntly notched tensile bars in $1N$ H_3BO_3 + 1 mM $Ca(OH)_2$ + 3.3 mM KCl.
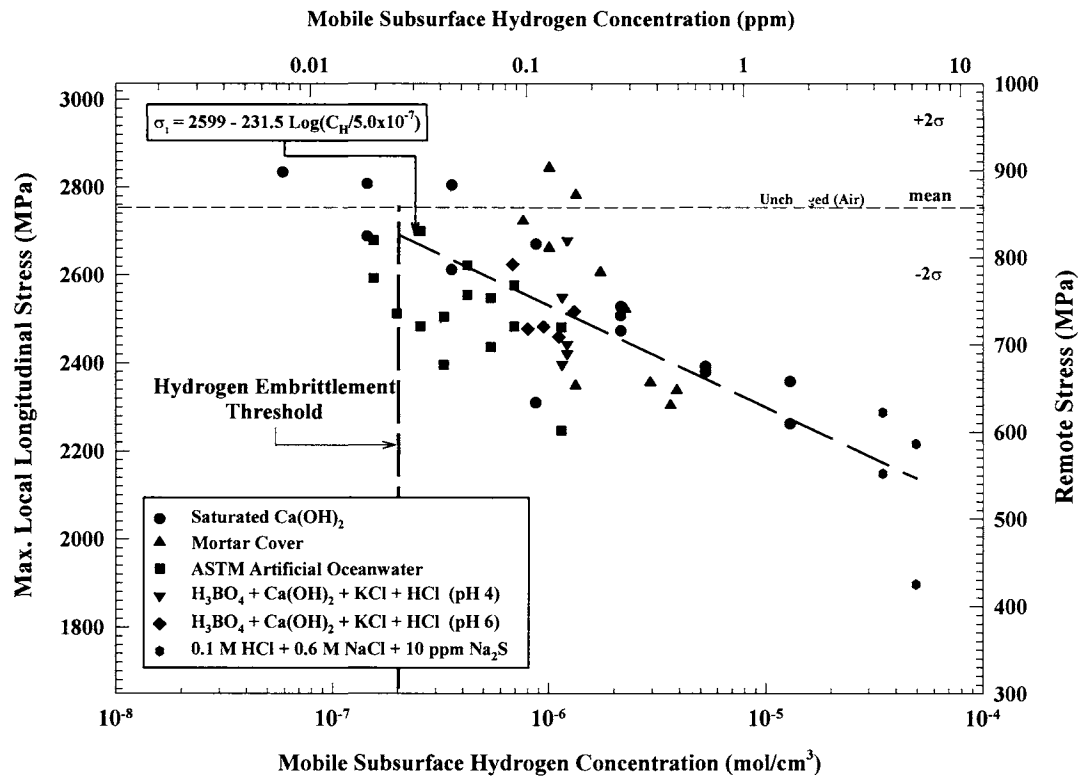
Figure 5.19:   Universal curve presenting the fracture stress of the 1080 steel pre-stressing tendon as a function of subsurface hydrogen concentration for the bluntly notched tensile bars in all environments.
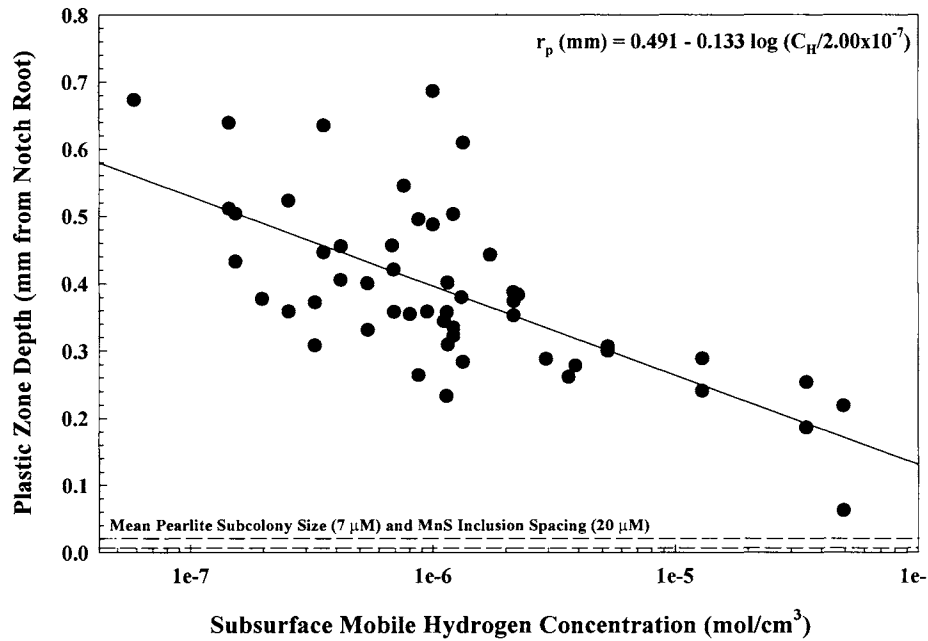
Figure 5.20a: Universal curve presenting the plastic zone size at the maximum applied stress as a function of subsurface hydrogen concentration for the bluntly notched tensile bars in all environments.
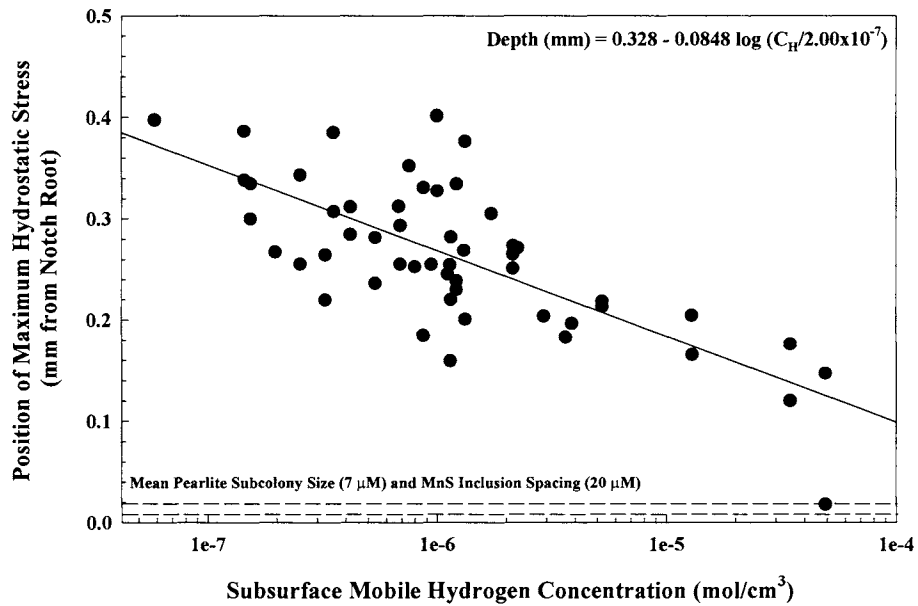
Figure 5.20b: Universal curve presenting the depth of the maximum hydrostatic tension as a function of subsurface hydrogen concentration for the bluntly notched tensile bars in all environments.
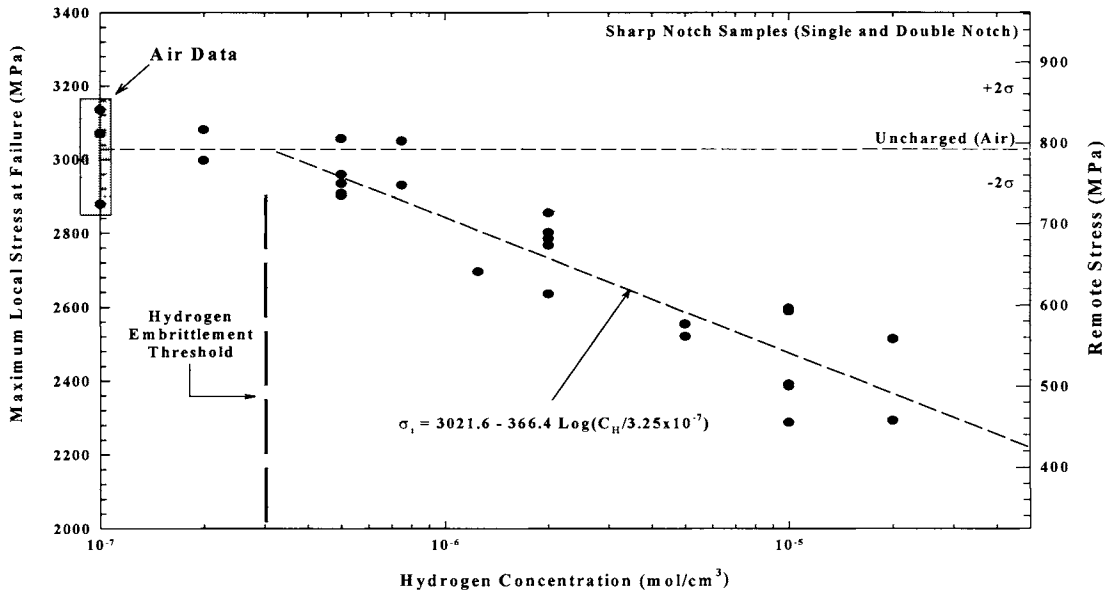
Figure 5.21a: Fracture initiation stress as a function of subsurface hydrogen concentration for sharply notched 1080 steel tensile bars. All tests were performed in saturated $Ca(OH)_2$.

Graph text includes: Sharp Notch Samples (Single and Double Notch), Air Data, $+2\sigma$, Uncharged (Air), -2σ, Hydrogen Embrittlement Threshold, $\sigma_i = 3021.6 - 366.4\ Log(C_H/3.25 \times 10^{-7})$. Axes: Maximum Local Stress at Failure (MPa), Remote Stress (MPa), Hydrogen Concentration (mol/cm^3).
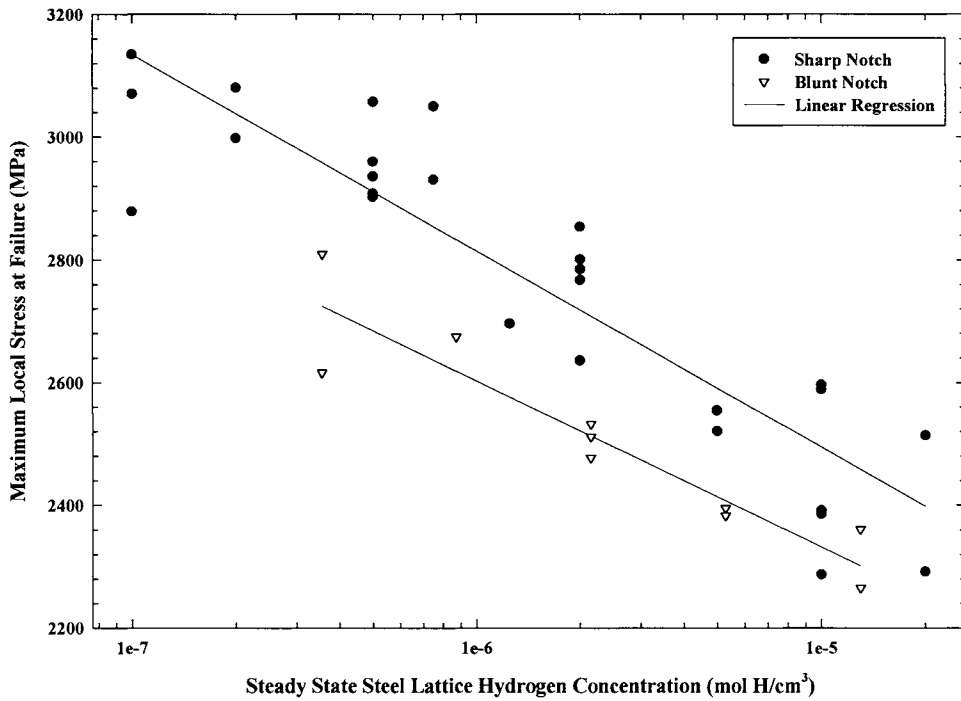
Figure 5.21b: Fracture initiation stress as a function of subsurface hydrogen concentration for bluntly and sharply notched 1080 steel tensile bars. All tests were performed in saturated $Ca(OH)_2$.

Graph legend: ● Sharp Notch, ▽ Blunt Notch, — Linear Regression. Axes: Maximum Local Stress at Failure (MPa), Steady State Steel Lattice Hydrogen Concentration ($mol\ H/cm^3$).
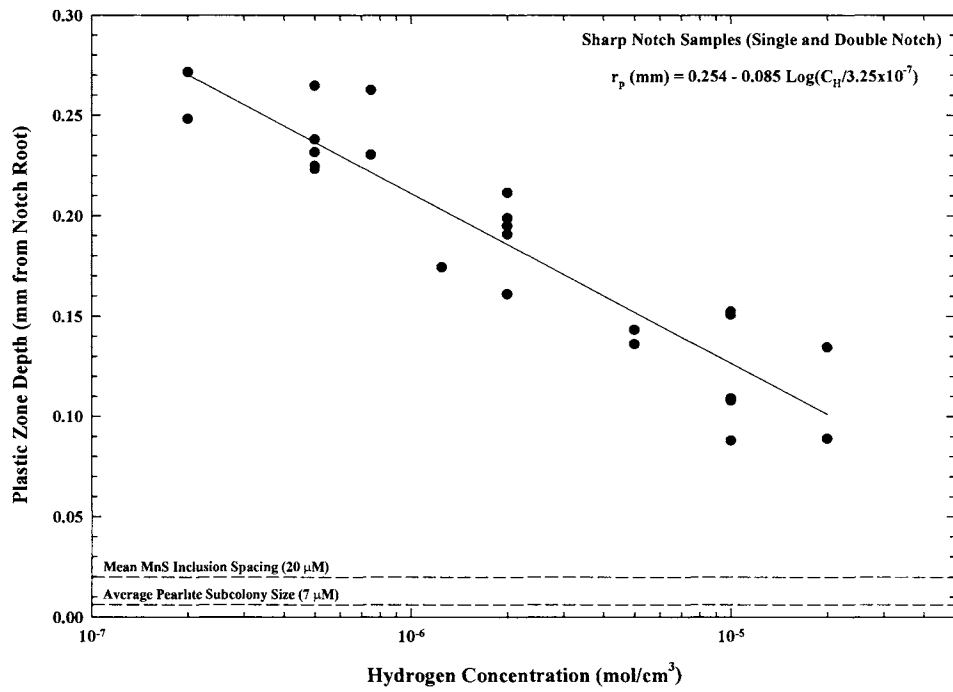
Figure 5.22a: Plastic zone size as a function of subsurface hydrogen concentration for sharply notched, 1080 steel pre-stressing steel tensile bars. All tests were performed in Saturated $Ca(OH)_2$.
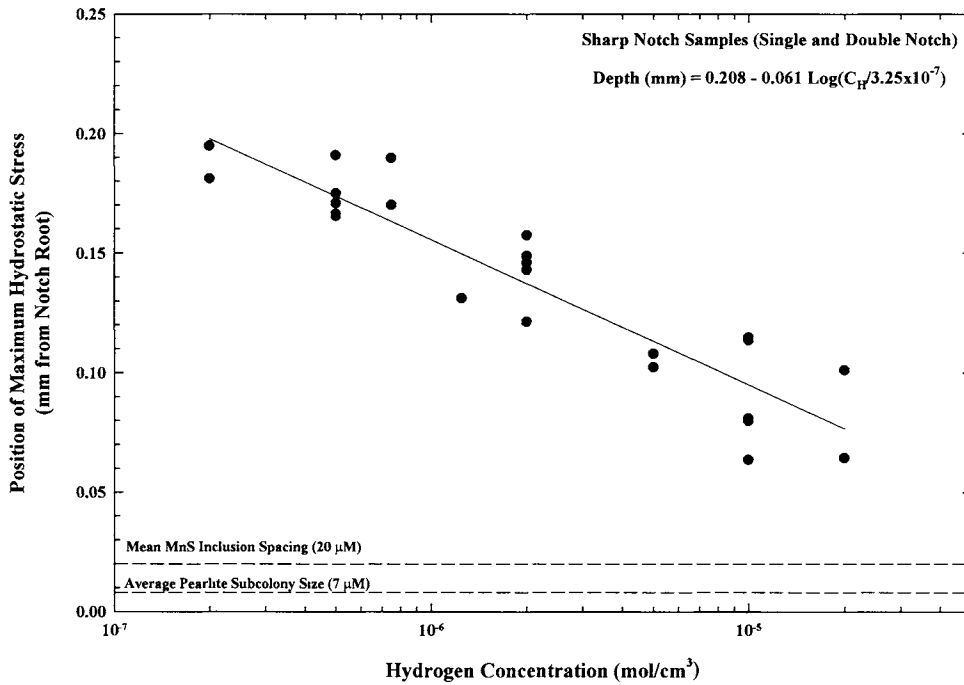
Figure 5.22b: Depth of maximum hydrostatic tension as a function of subsurface hydrogen concentration for sharply notched, 1080 steel pre-stressing steel tensile bars. All tests were performed in saturated $Ca(OH)_2$
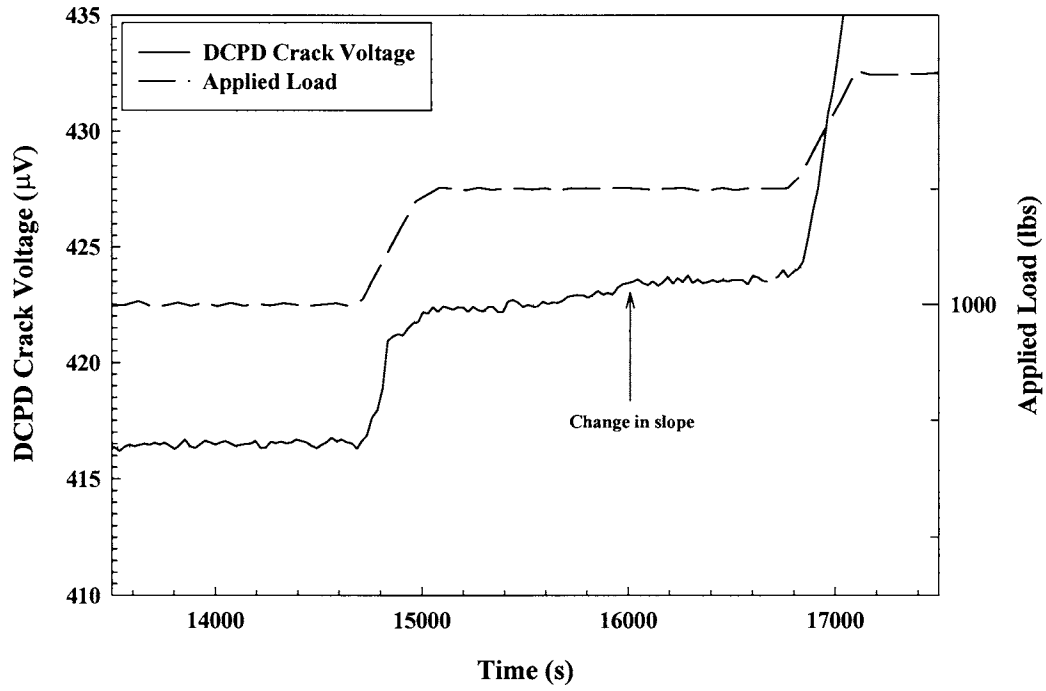
Figure 5.23:   DCPD signal and applied load as a function of time, illustrating the initiation of a hydrogen crack.
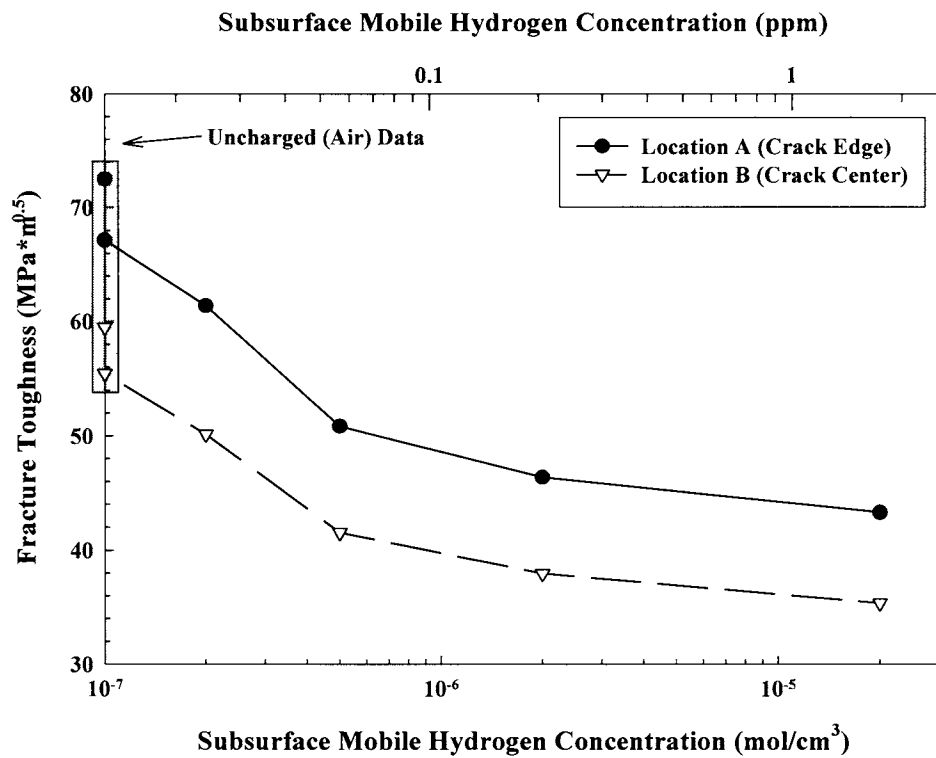
Figure 5.24: K_{IHE} as a function of subsurface hydrogen concentration at the edge (A) and center (B) of the fatigue precrack.
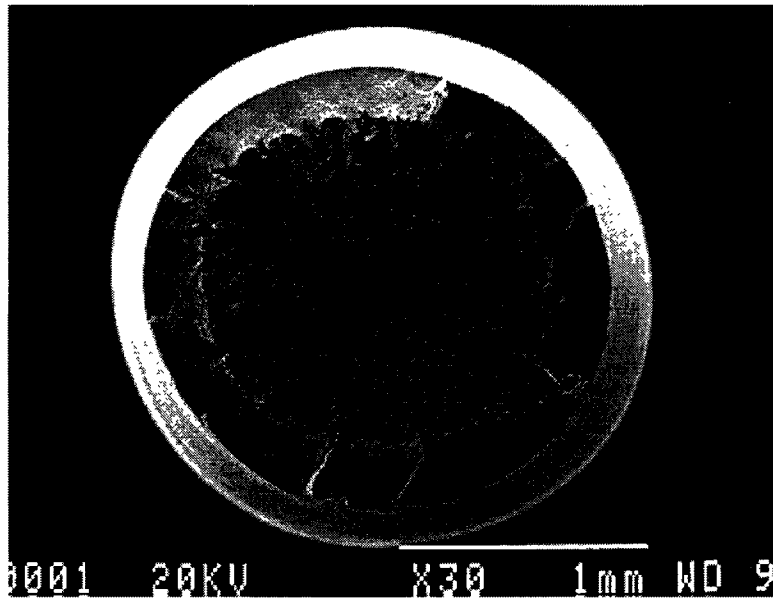
Figure 5.25:   Overview of the fracture surface for a smooth, uncharged 1080 steel pre-stressing tendon tensile specimen.
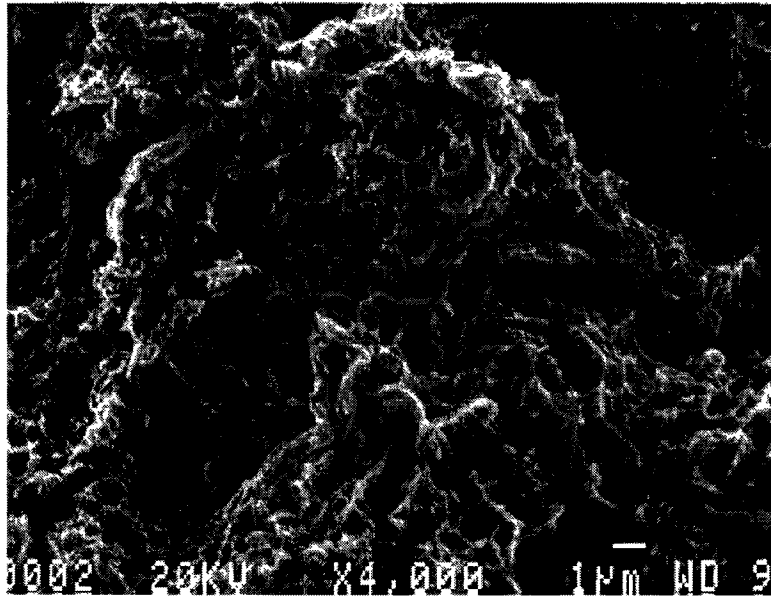
Figure 5.26:   Ductile center section of the fracture surface for a smooth, uncharged 1080 steel pre-stressing tendon tensile bar.
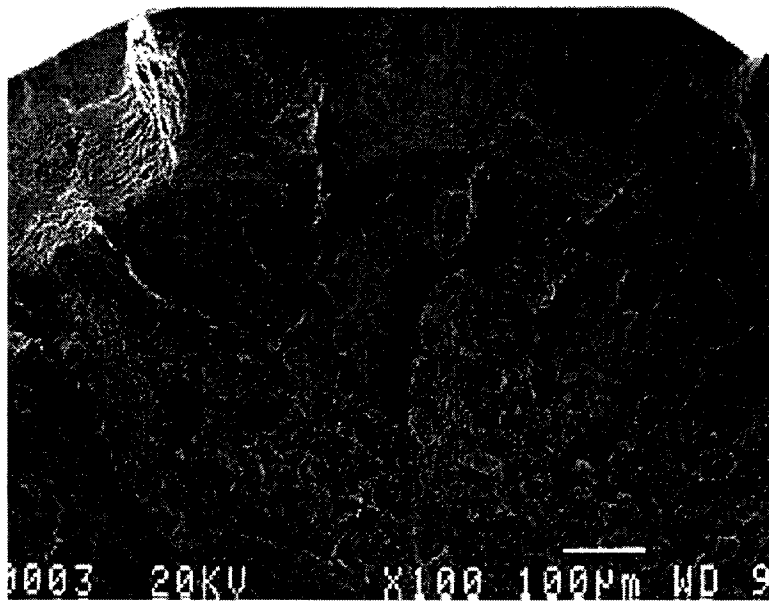
Figure 5.27:   Longitudinal splitting emanating radially outwards from the center of the unnotched tensile bar.
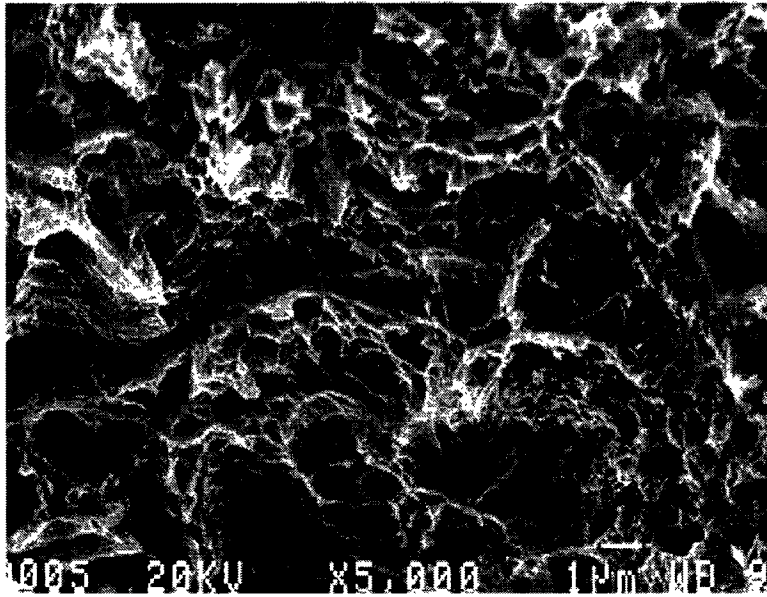
Figure 5.28:   Microscopically ductile regions with increased minor longitudinal splitting, located midway between the shear lip and the center of the uncharged, smooth bar.
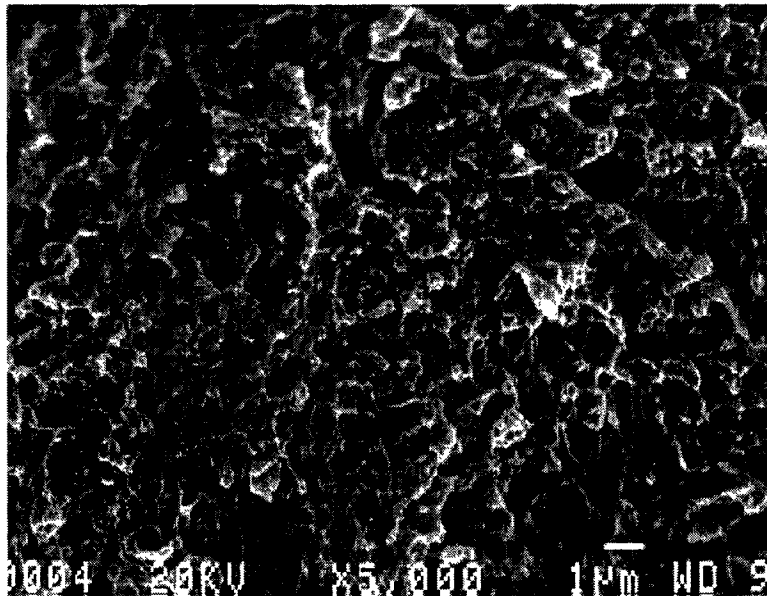
Figure 5.29:   High magnification view of the microscopically ductile, shear overload region around the periphery of the uncharged, smooth tensile bar.
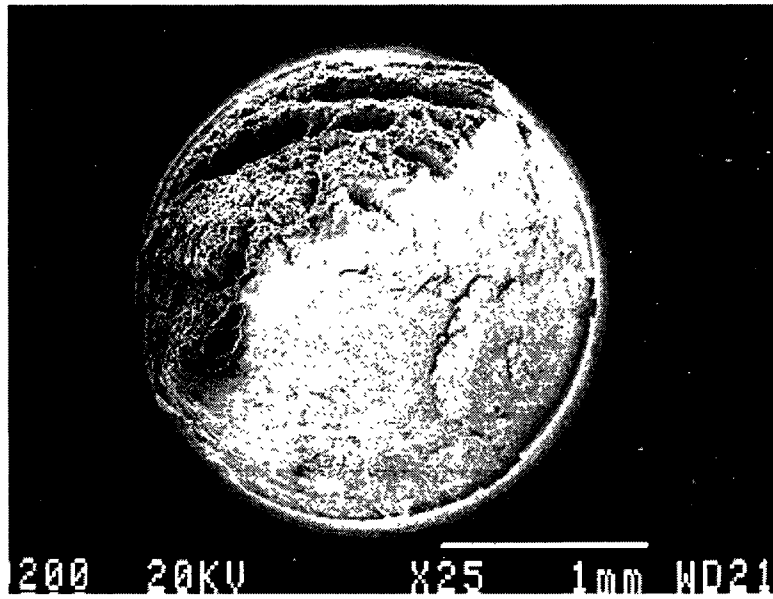
Figure 5.30: Overview of the fracture surface for an uncharged, sharply notched 1080 steel pre-stressing tendon tensile bar.
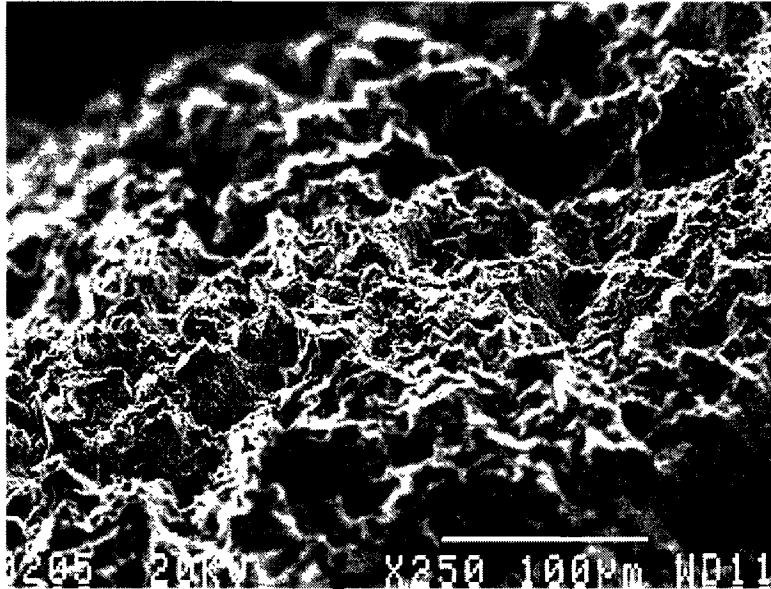
Figure 5.31a: Low magnification view looking parallel to the tensile axis at the tortuous region for an uncharged, 1080 steel pre-stressing tendon, sharply notched tensile bar.
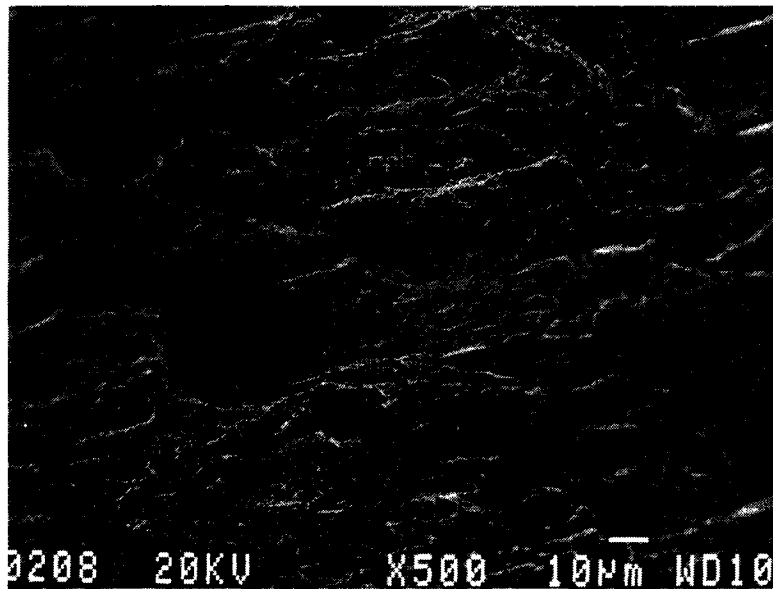
Figure 5.31b: Angle view of the tortuous region, illustrating the cleavage like appearance of the terraced regions.
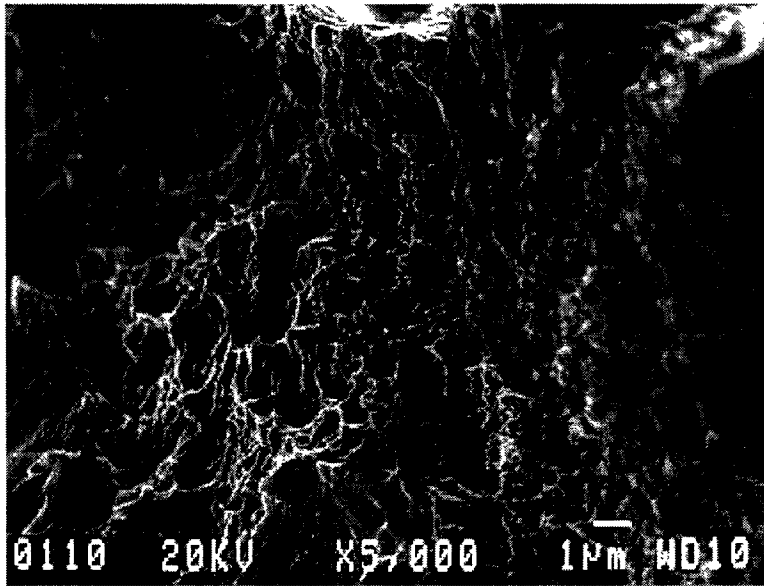
Figure 5.32a: Ductile plateau within the tortuous region for an uncharged, sharply notched 1080 steel pre-stressing tendon tensile bar.
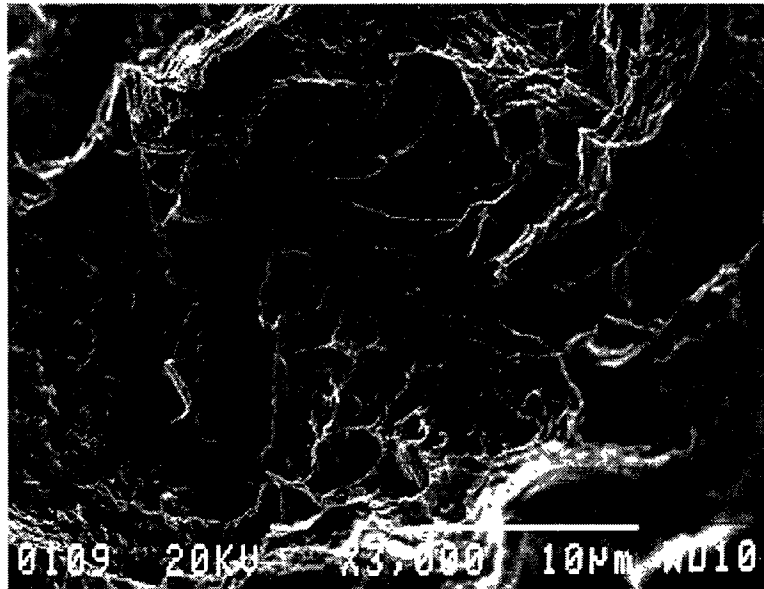
Figure 5.32b: Brittle (cleavage) plateau within the tortuous region for an uncharged, sharply notched 1080 steel pre-stressing tendon tensile bar.
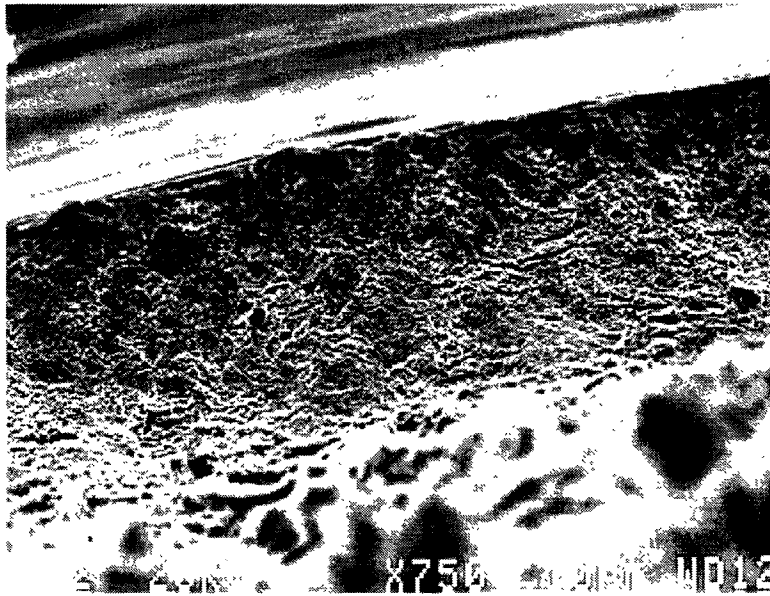
Figure 5.33a: Lip region around portions of the periphery of the fracture surface for an uncharged, 1080 steel pre-stressing tendon tensile bar.
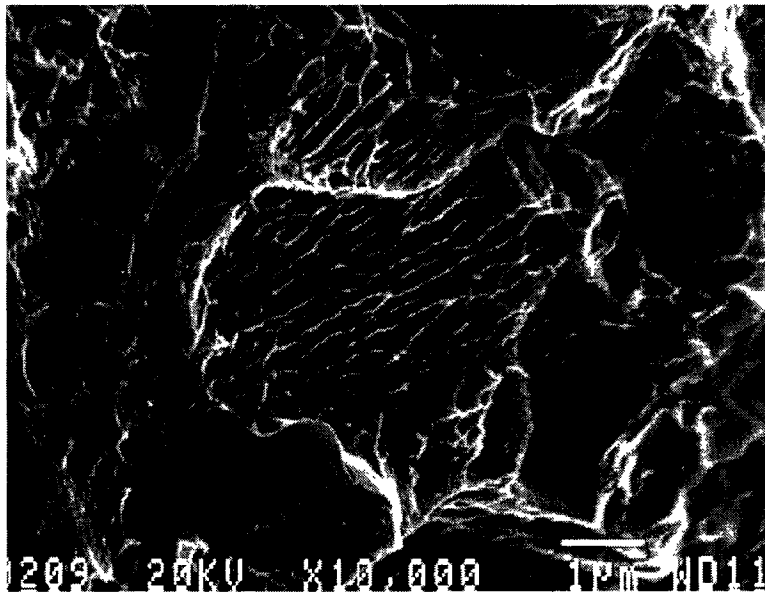
Figure 5.33b: Ductile region within the lip pictured above consisting an array of lamellar voids, likely the result of shear cracking as proposed by Miller.
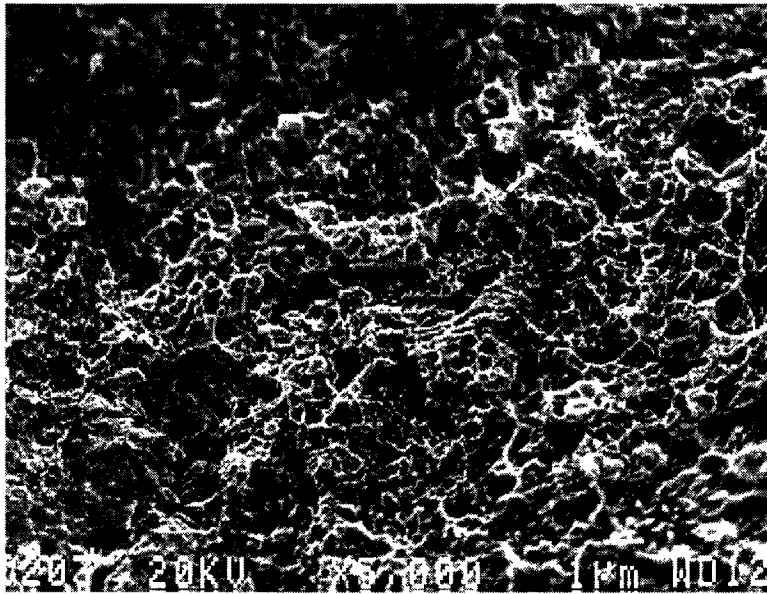
Figure 5.34:   Smooth, shear overload region within the fracture surface for an uncharged, sharply notched 1080 steel pre-stressing tendon tensile bar.
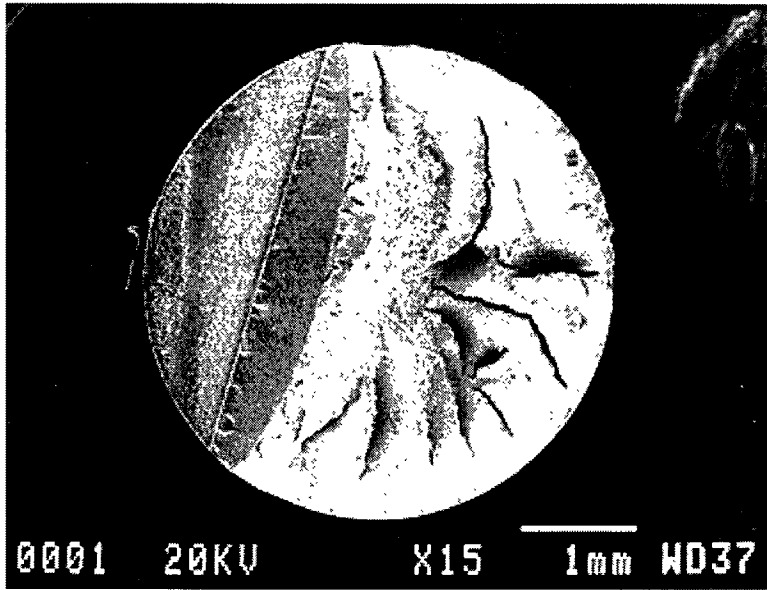
Figure 5.35a: Overview of the fracture surface for an uncharged, fatigue precracked 1080 steel pre-stressing tendon tensile bar.
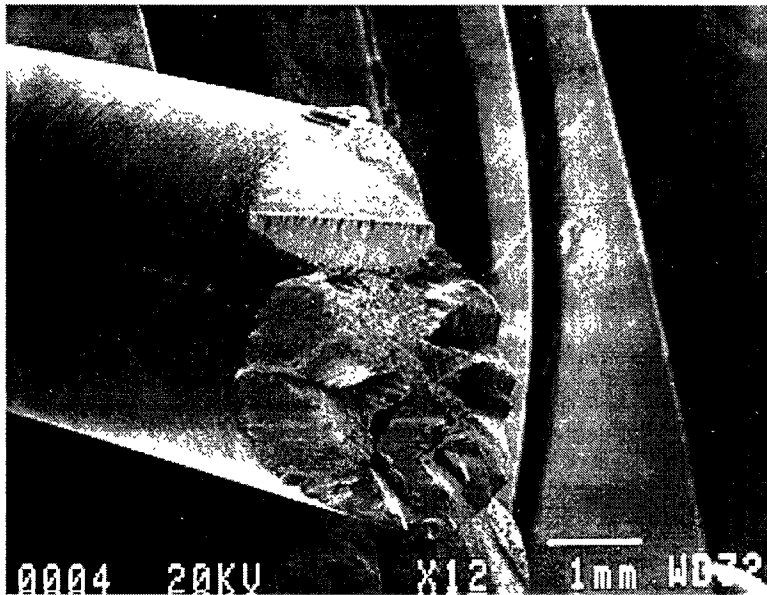
Figure 5.35b: Angle view of the fracture surface for an uncharged, fatigue precracked 1080 steel pre-stressing steel tensile bar. Note the abrupt change in direction of the advancing crack parallel to the tensile axis.
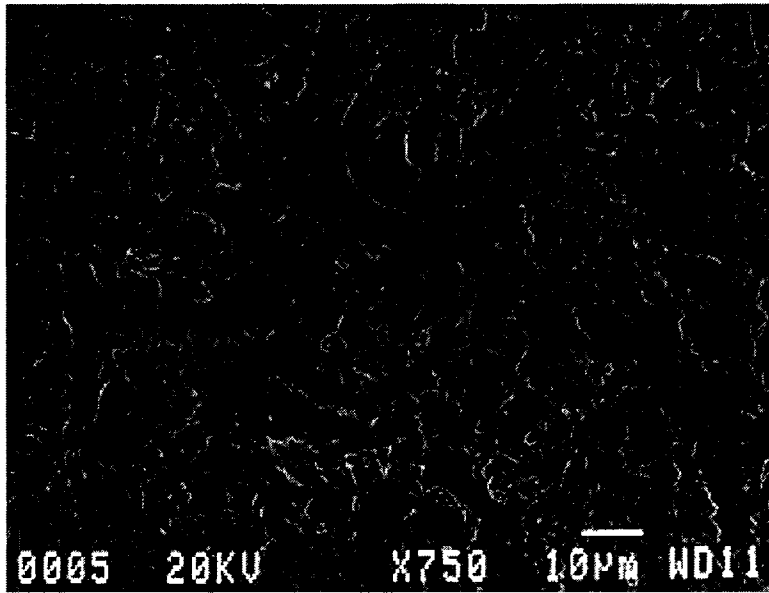
Figure 5.36:   High magnification view of the fatigue precrack advancing in from the EDM notch for an uncharged, 1080 steel pre-stressing tendon tensile sample. Direction of crack growth is downward from the top of the page.
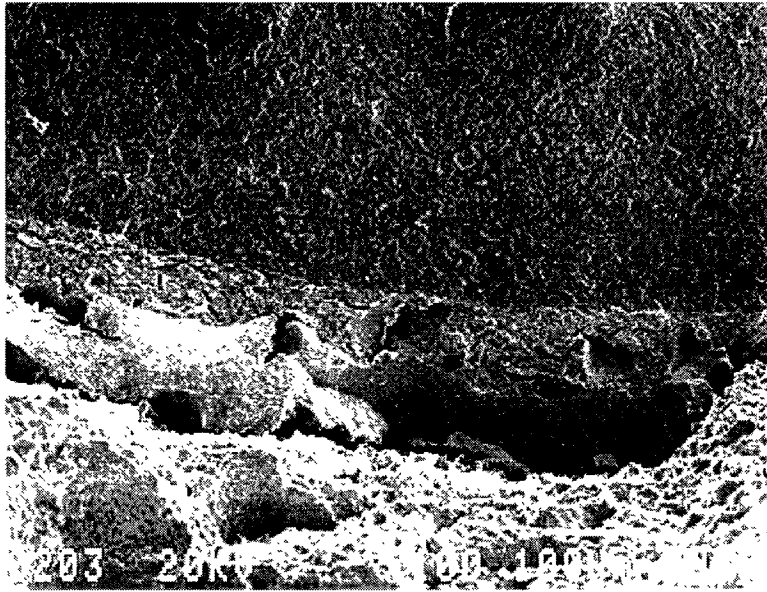
Figure 5.37a: Regions of mode I crack initiation in front of the fatigue precrack for an uncharged, fatigue pre-cracked 1080 steel tensile specimen.
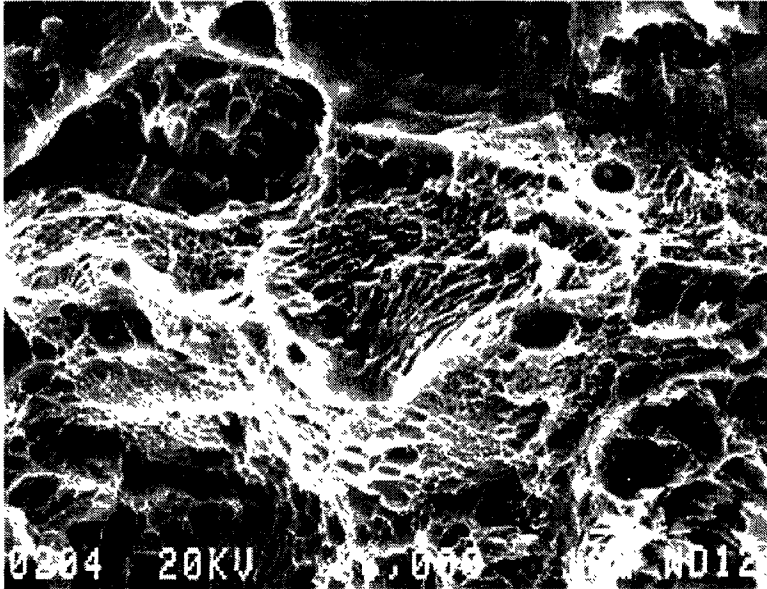
Figure 5.37b: High magnification view of the initiation regions pictured above. Note the array of lamellar voids throughout the fracture surface, indicative of shear cracking as proposed by Miller.
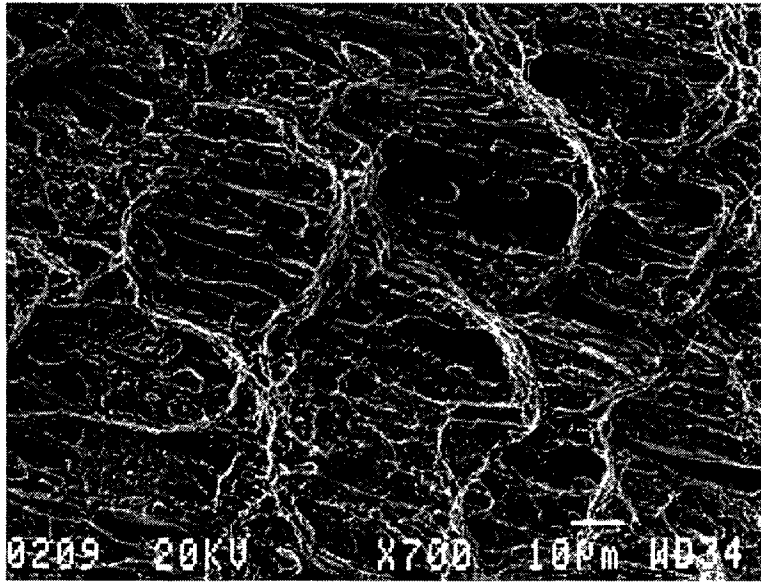
Figure 5.38a: Angle view of the crack once it has changed direction parallel to the tensile axis for an uncharged, pre-cracked 1080 steel pre-stressing tendon specimen. Note the similarity in appearance to the tortuous regions discussed for the notched tensile bars.
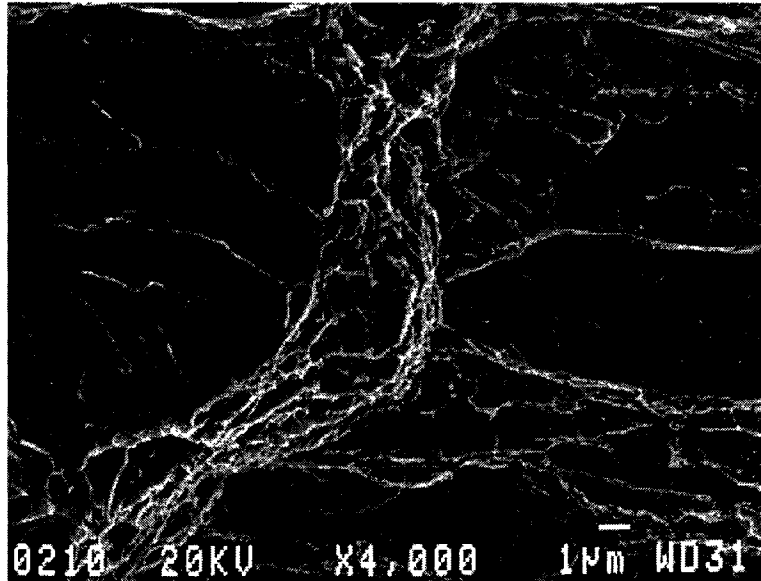
Figure 5.38b: Ductile plateau region within the above tortuous region.
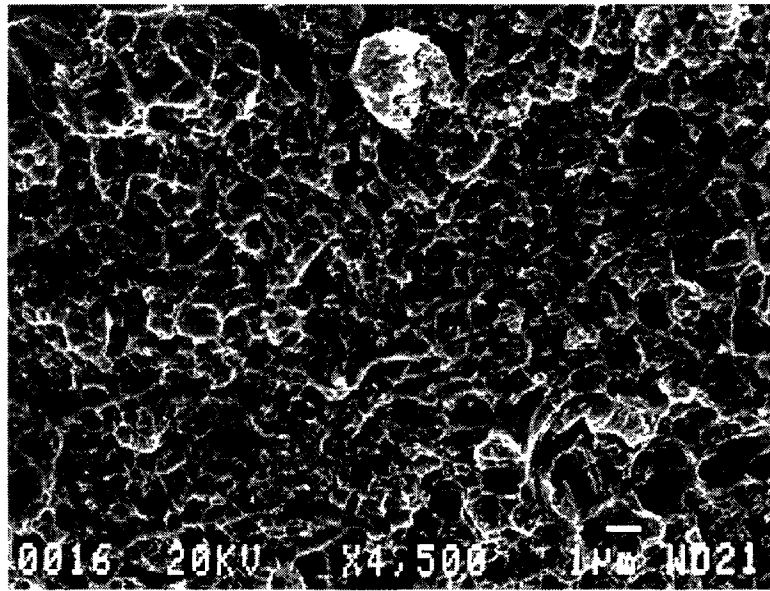
Figure 5.39: Microscopically ductile, shear overload region within the fracture surface for an uncharged, pre-cracked 1080 steel pre-stressing tendon specimen.
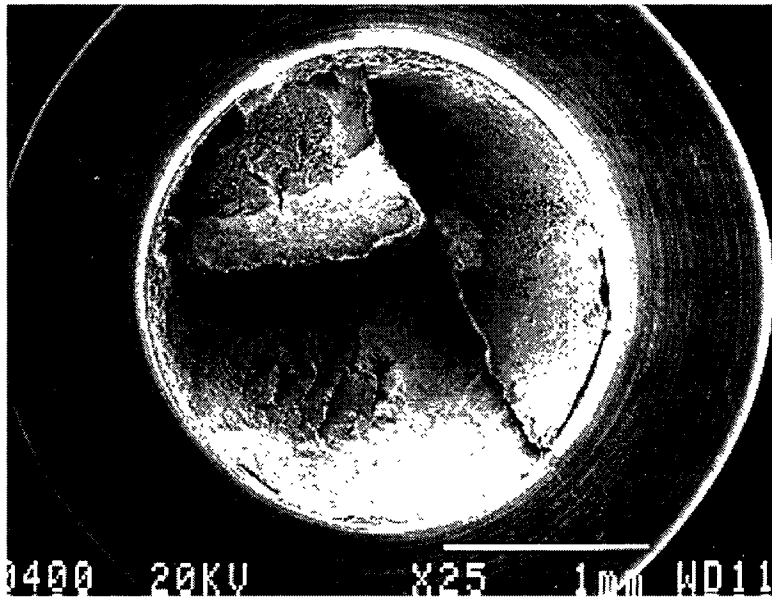
Figure 5.40:   Overview of the fracture surface for a sharply notched 1080 steel tensile bar containing 2×10^{-6} mol/cm^3 hydrogen.
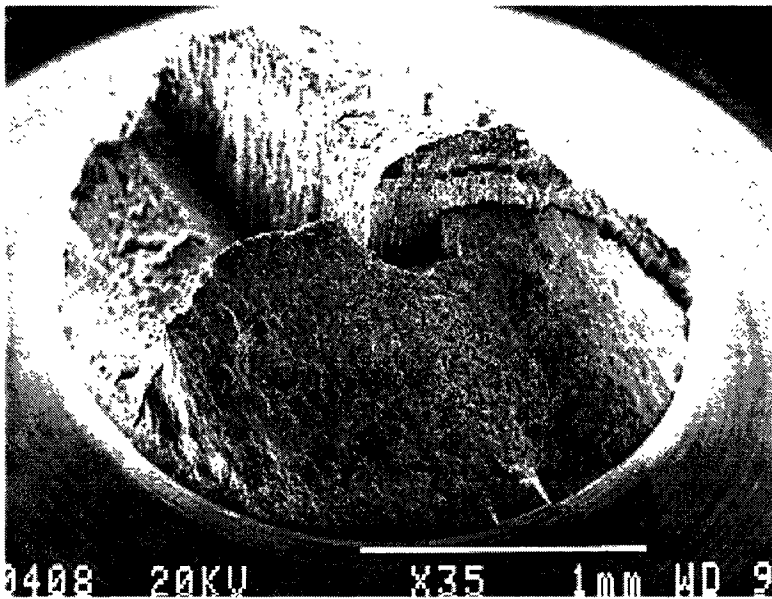
**Figure 5.41**:   Angle view of the fracture surface pictured in Figure 5.40. Note the extensive longitudinal splitting which dominates the fracture surface.
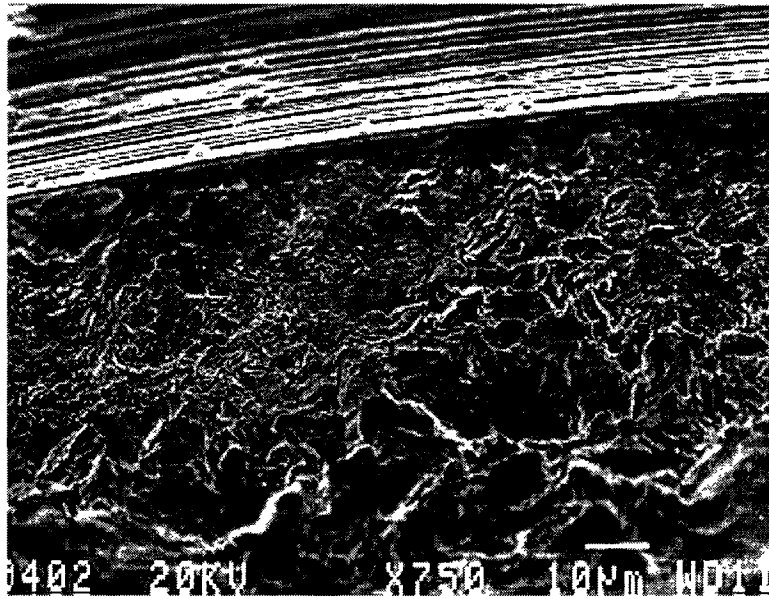
Figure 5.42a: Lip region around portions of the periphery of a hydrogen charged (2×10^{-6} mol/cm^3), sharply notched tensile bar, particularly near the tortuous region.
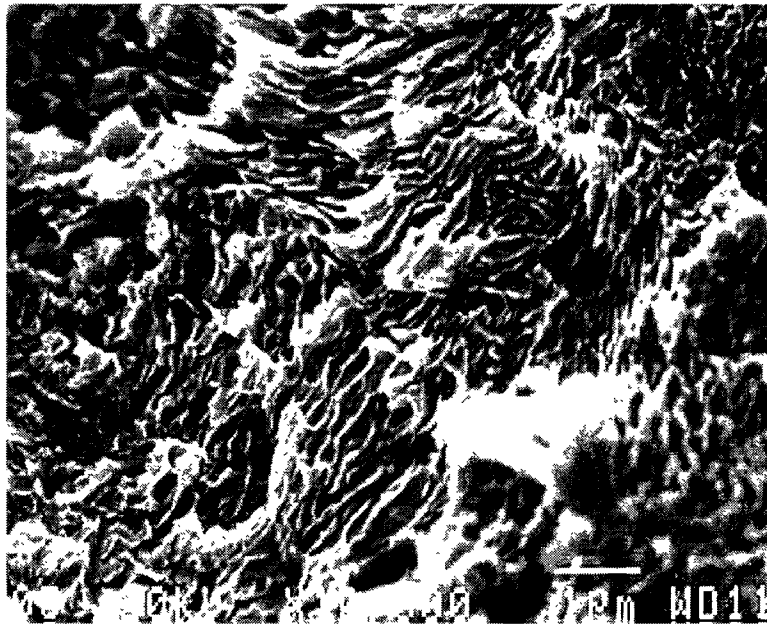
Figure 5.42b: High magnification view of the lip region picture above. Note the arrays of lamellar voids throughout the fracture surface, likely the result of the shear cracking process proposed by Miller.
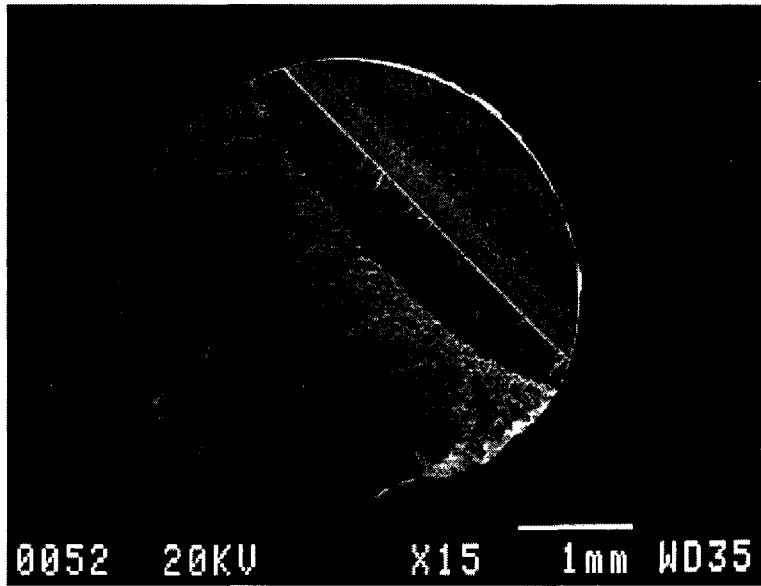
Figure 5.43a: Overview of the fracture surface for a fatigue pre-cracked, 1080 steel pre-stressing tendon tensile bar containing 2×10^{-6} mol/cm^3 hydrogen.
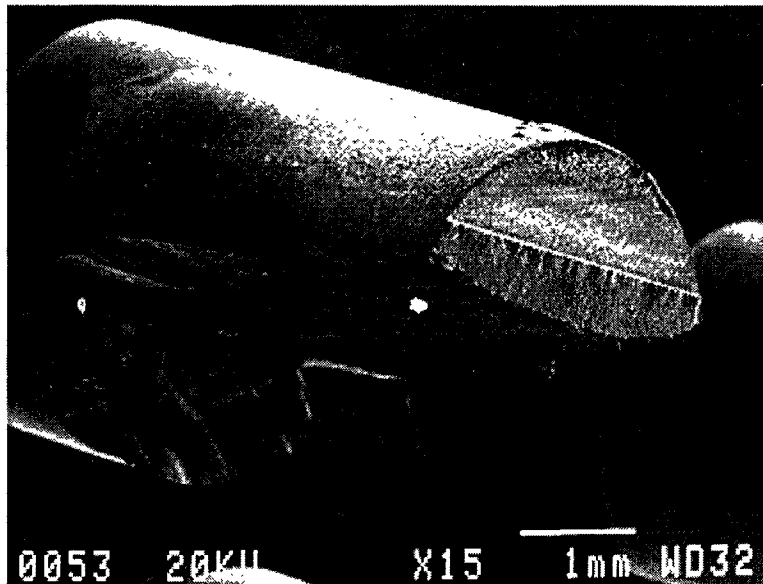

Figure 5.43b: Angle view of the above pictured fracture surface. Note the abrupt change in direction of the advancing crack, approaching a direction parallel to the tensile axis.
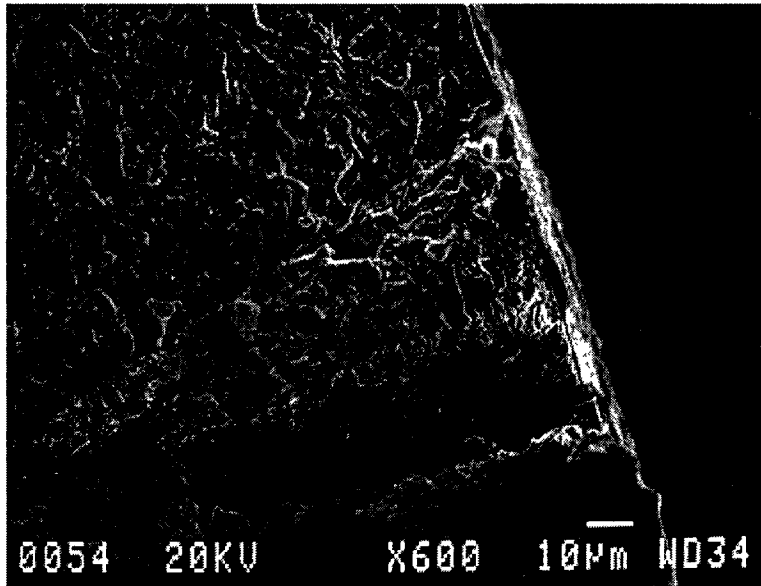
Figure 5.44: Mode I crack initiation in front of the fatigue precrack (in this case at the specimen surface) for a hydrogen charged (2×10^{-6} mol/cm^3), pre-cracked tensile specimen.
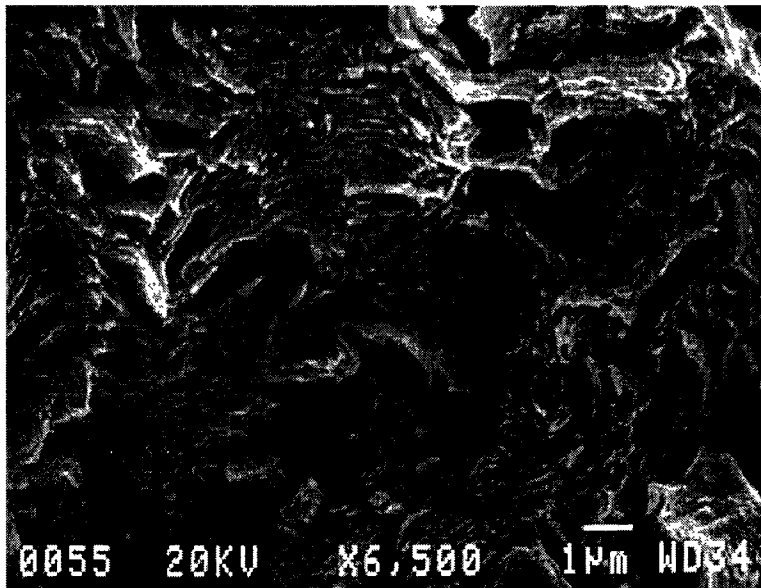
Figure 5.45: High magnification view of the above initiation region. Note the presence of numerous arrays of lamellar voids, indicative of shear cracking as proposed by Miller.
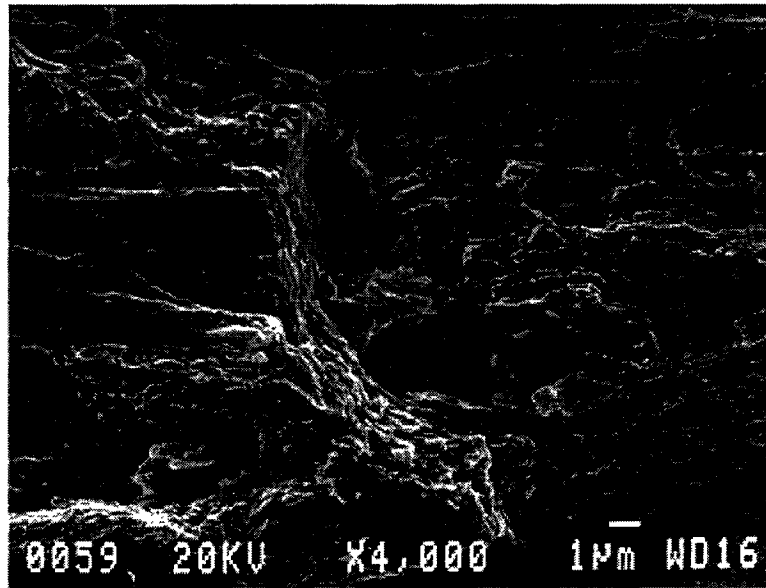
Figure 5.46: High magnification view of the advancing crack once it has changed direction roughly parallel to the tensile axis for a fatigue pre-cracked, hydrogen charged (2×10^{-6} mol/cm^3) 1080 steel pre-stressing tendon tensile bar.
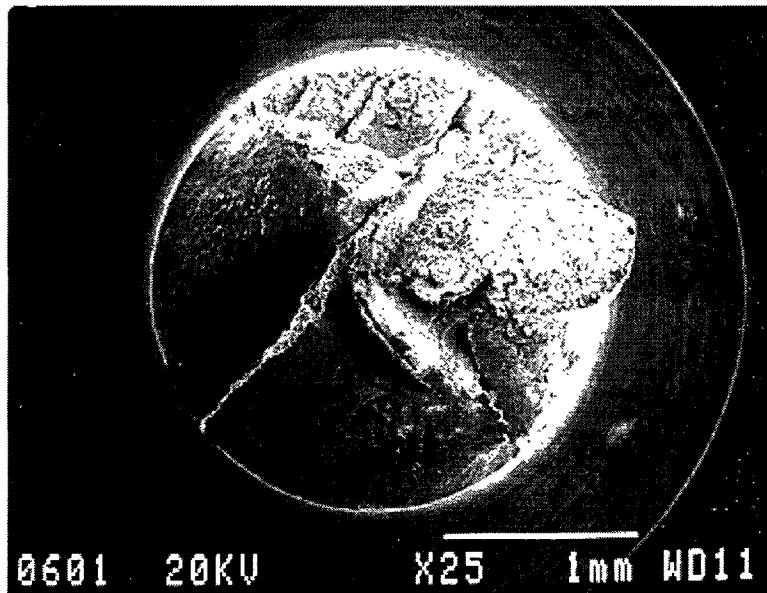
**Figure 5.47**:   Overview of a fracture surface for a sharply notched 1080 steel pre-stressing tendon tensile bar containing 2 x 10^{-5} mol/cm^3 hydrogen.
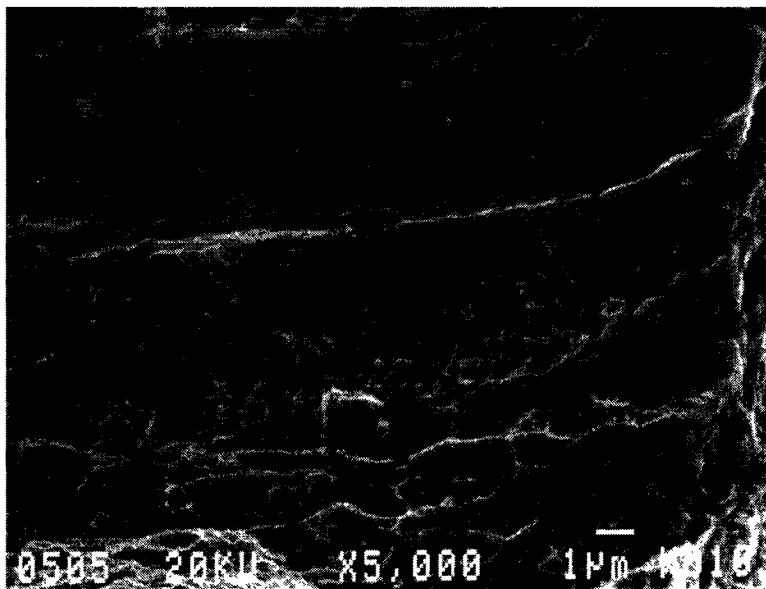
Figure 5.48:   Increased longitudinal splitting with the increased hydrogen concentration throughout the fracture surface for a sharply notched, hydrogen charges (2x 10^{-5} mol/cm^3) 1080 steel pre-stressing tendon tensile bar.
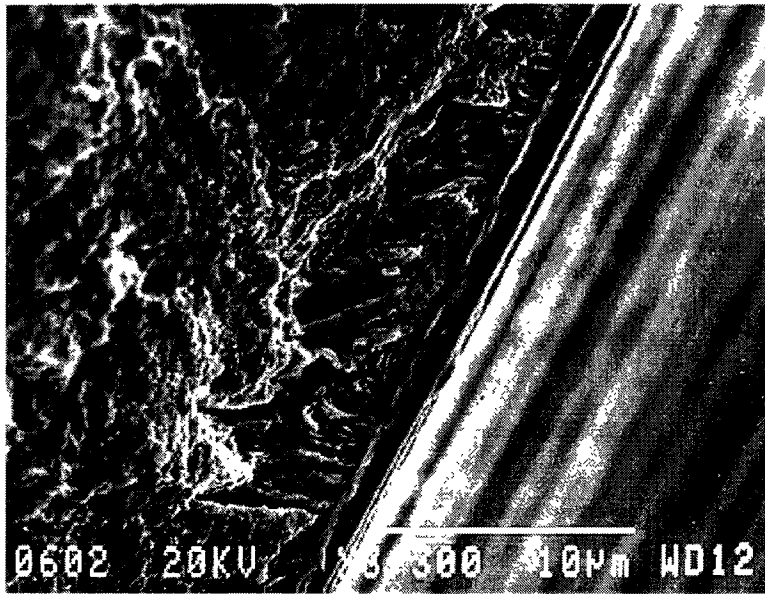
Figure 5.49a: Lip region around portions of the periphery of the fracture surface for a sharply notched, hydrogen charged (2 x 10^{-5} mol/cm^3) 1080 steel pre-stressing tendon tensile bar.

Figure 5.49b: High magnification view of the above lip region, again illustrating the arrays of elongated voids, likely the result of shear cracking.
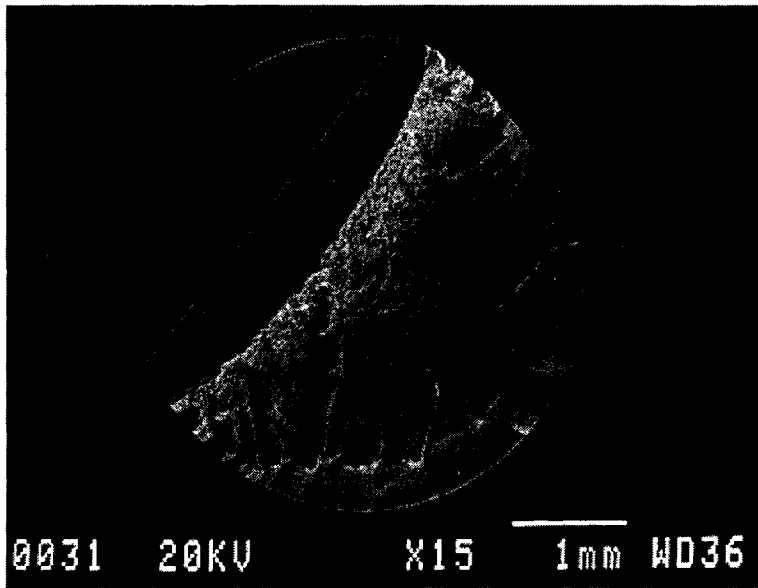
Figure 5.50a: Overview of the fracture surface for a fatigue pre-cracked, 1080 steel pre-stressing tendon tensile bar containing 2×10^{-5} mol/cm^3 hydrogen.
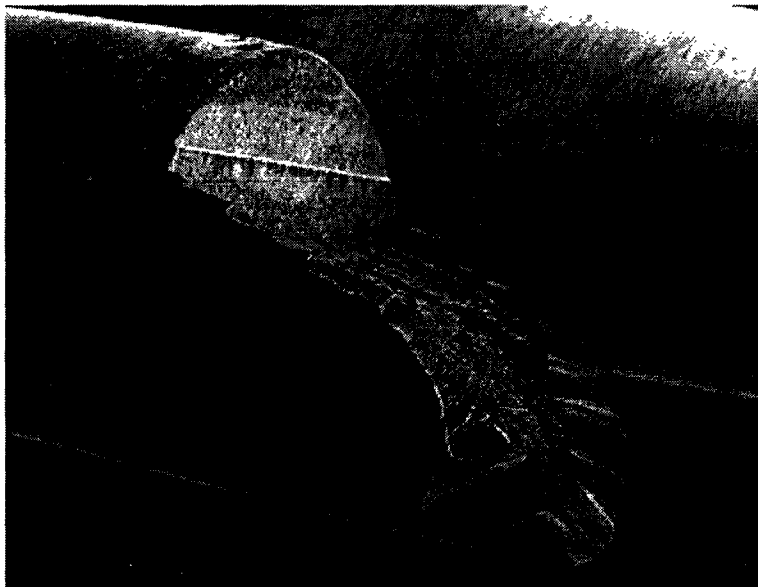
Figure 5.50b: Angle view of the above fracture surface, illustrating the change in direction of the advancing crack parallel to the tensile axis.
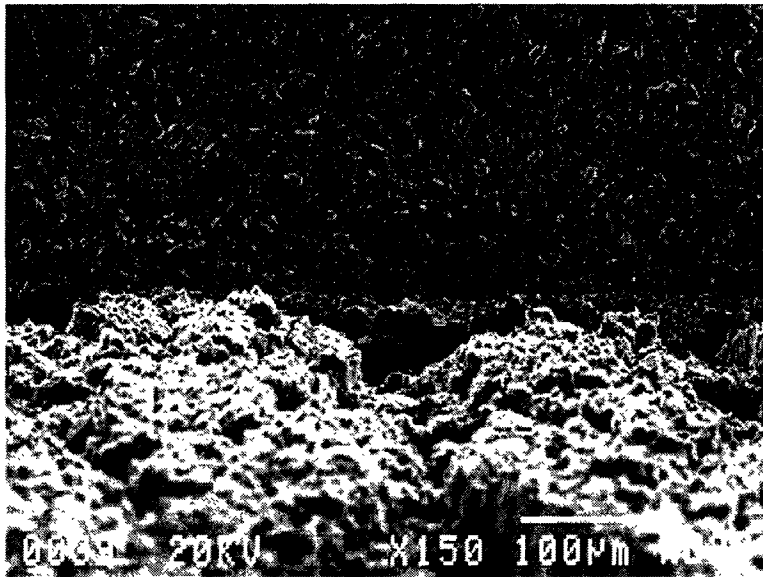
Figure 5.51a: Mode I crack initiation sites in front of the fatigue precrack for a fatigue pre-cracked, hydrogen charged (2×10^{-5} mol/cm^3) 1080 steel, pre-stressing tendon tensile bar.
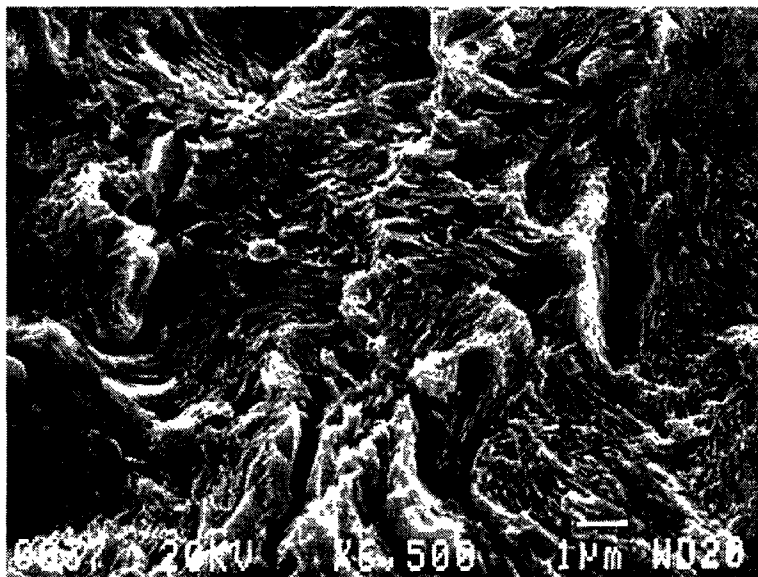
Figure 5.51b: High magnification view of the above initiation sites, illustrating numerous arrays of elongated voids, likely the result of shear cracking as proposed by Miller.
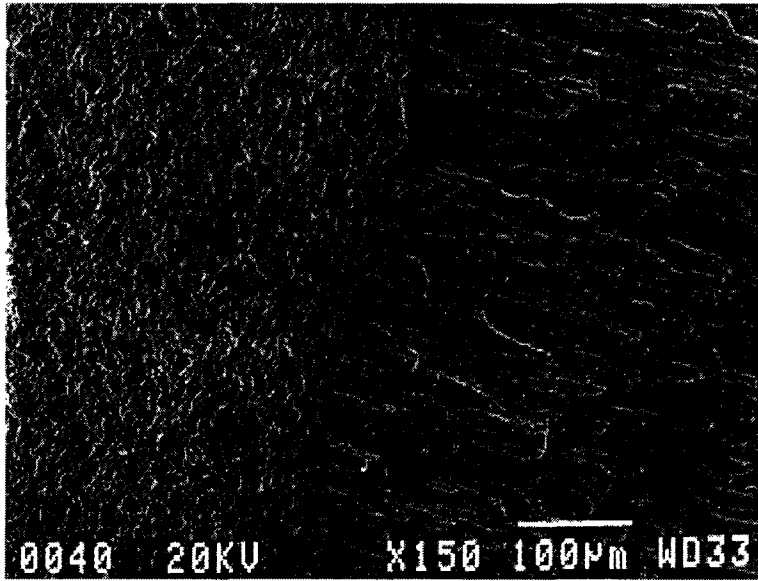
Figure 5.52a: Fracture surface for a fatigue pre-cracked, hydrogen charged (2×10^{-5} mol/cm^3) 1080 steel pre-stressing tendon tensile specimen, illustrating the abrupt change in direction of the advancing crack, approaching a direction roughly parallel to the tensile axis.
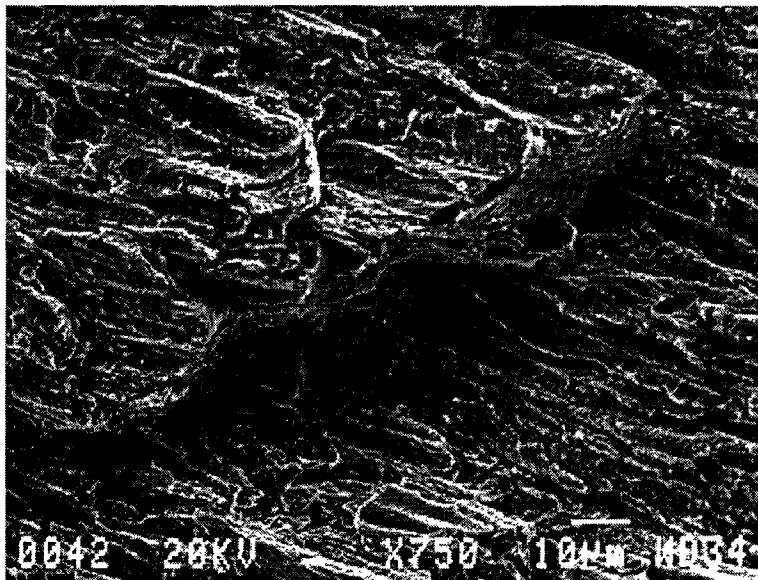
Figure 5.52b: High magnification view of the above tortuous region, illustrating its terraced nature.
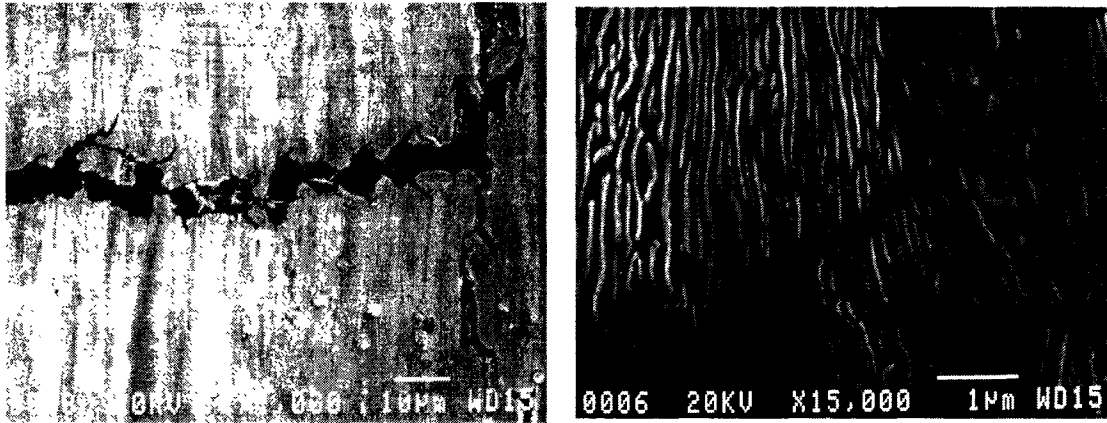
Figure 5.52c: Side view of a fatigue precracked tensile bar illustrating the shear cracking which occurs along the advancing fatigue precrack as well as the change in direction of the advancing hydrogen crack parallel to the tensile axis.
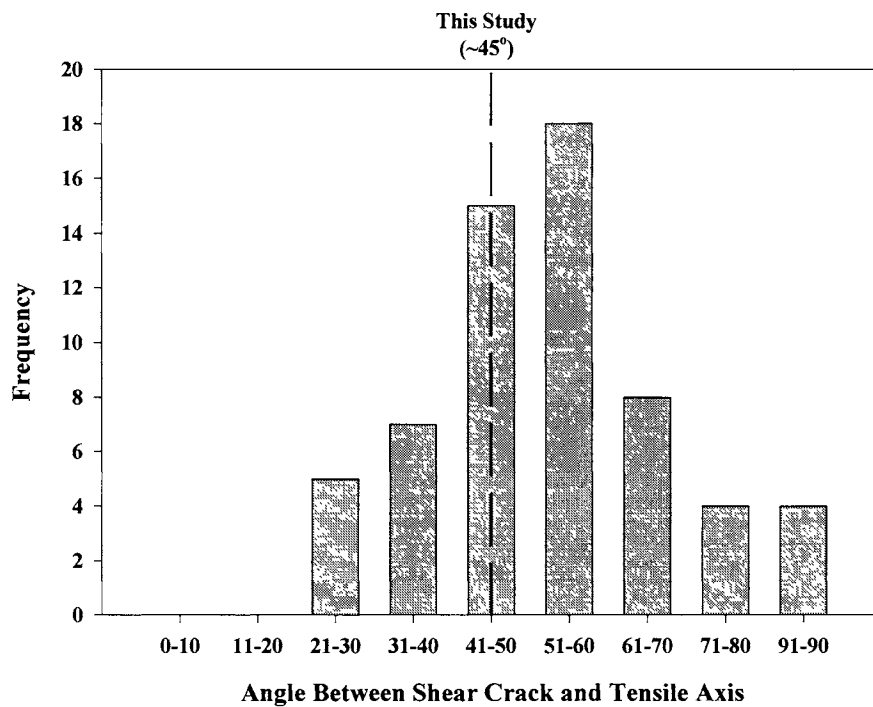
Figure 5.52d: Orientation of shear cracking determined by Miller (1970). Also noted is the average orientation of shear cracking in this study.
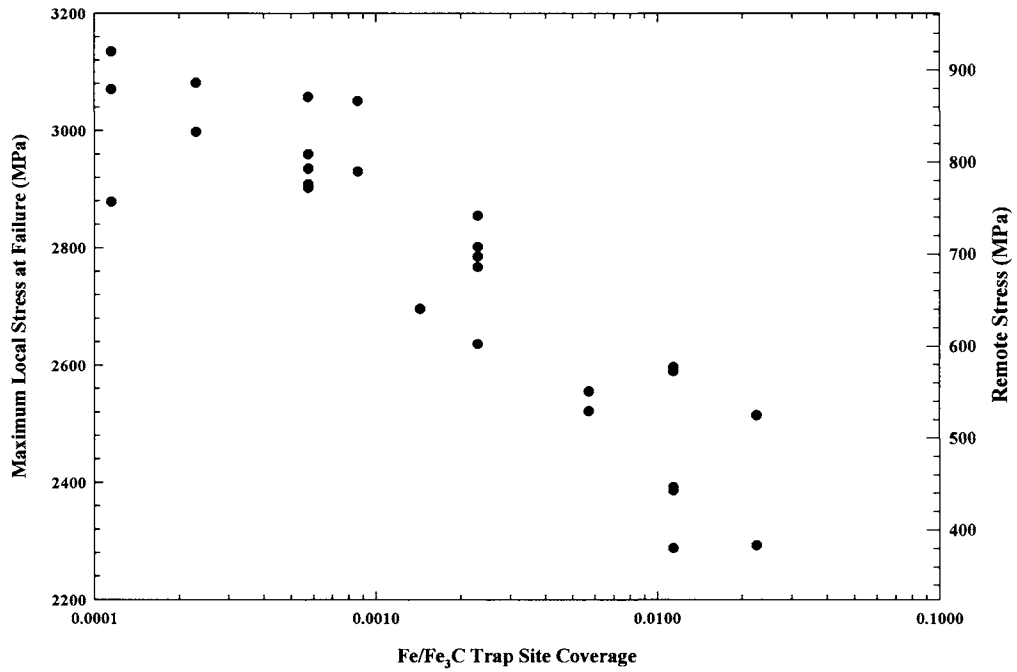
Figure 5.52e: Fracture initiation stress for sharply notched tensile bars as a function of trap site coverage for Fe/Fe$_3$C interfaces.
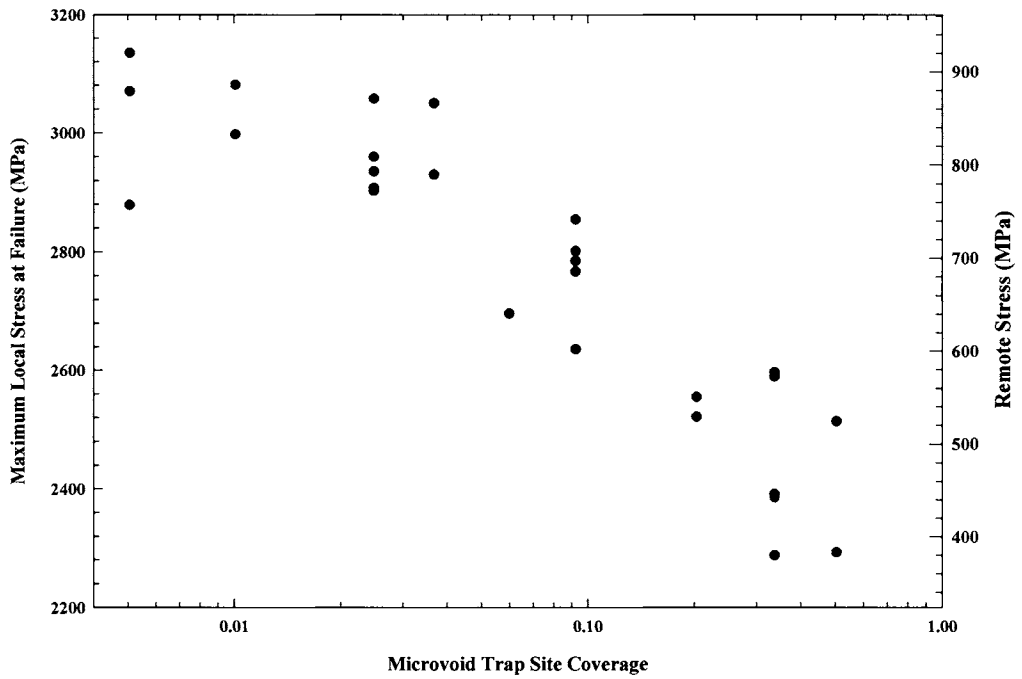
Figure 5.52f: Fracture initiation stress for sharply notched tensile bars as a function of trap site coverage for microvoids.
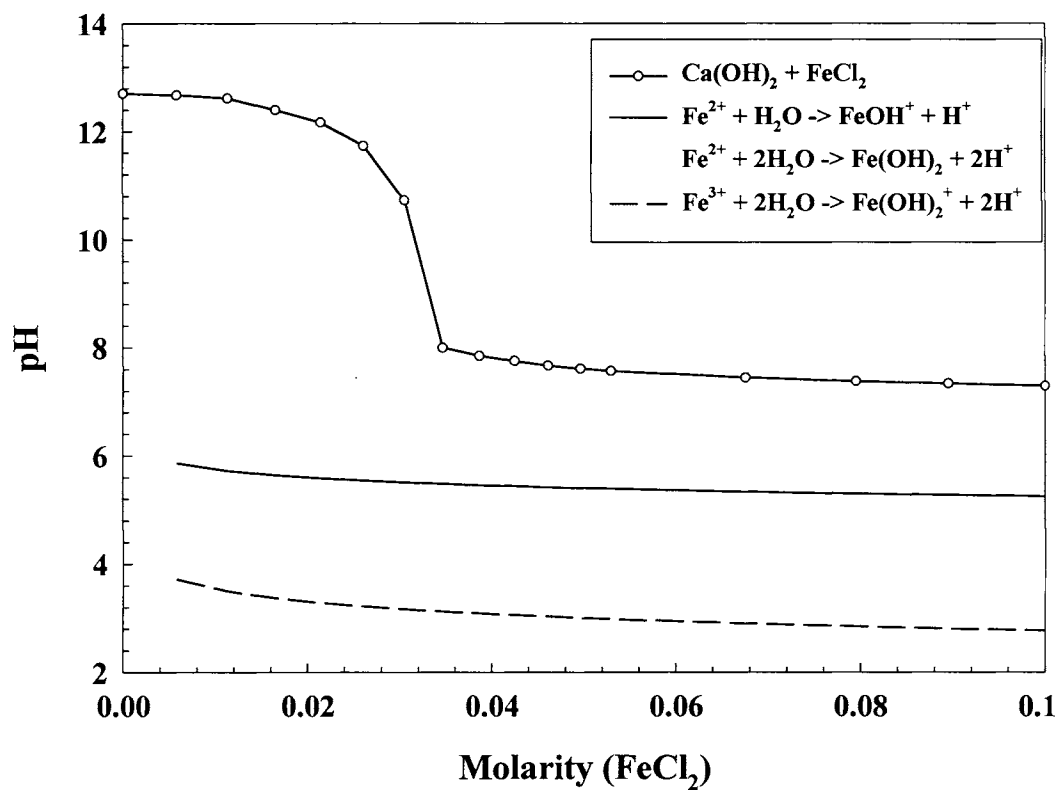
Figure 5.53: pH of an aqueous solution containing saturated $Ca(OH)_2$ and $FeCl_2$ as a function of the concentration of $FeCl_2$ present. Experiment was conducted at room temperature while continuously stirring the solution.
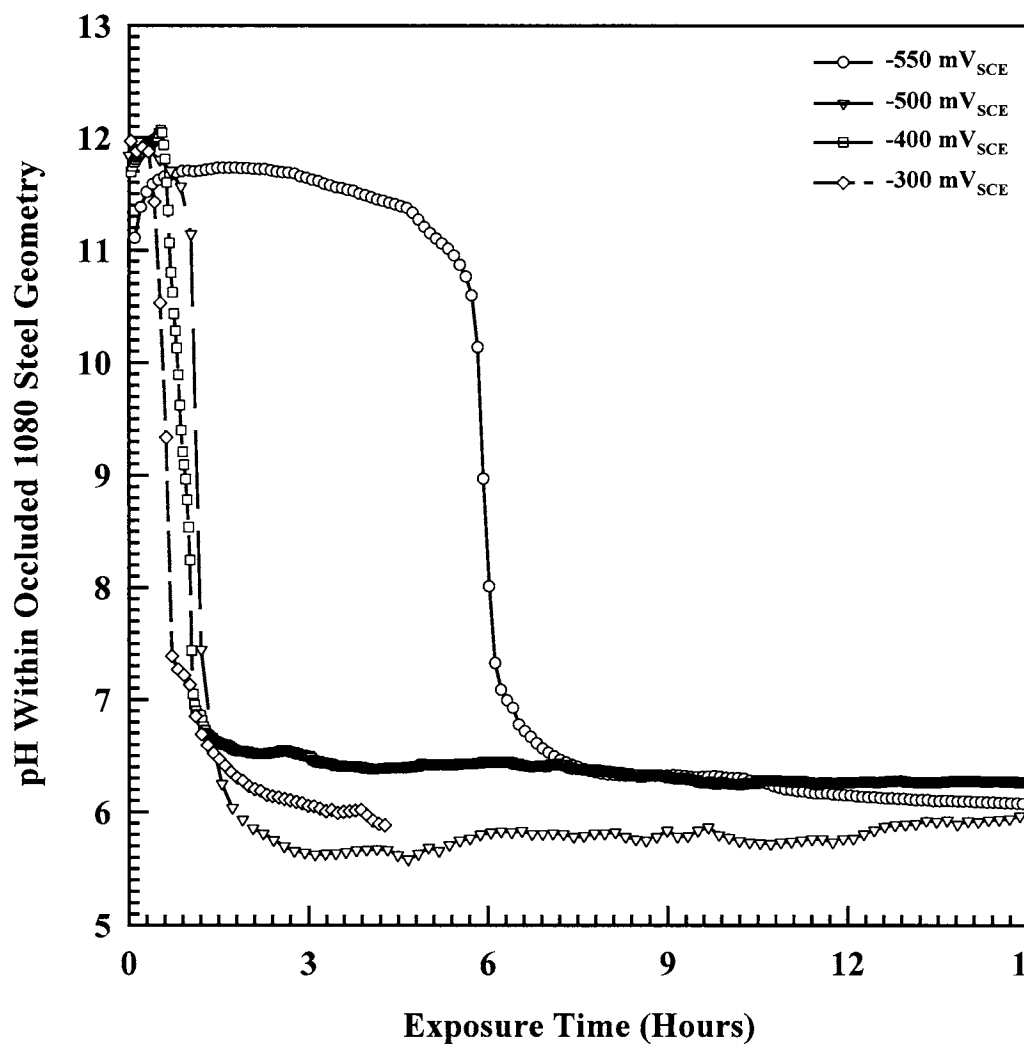
Figure 5.54: Occluded solution pH as a function of time within the pre-stressing steel crevice pictured in Figure 4.3 as a function of the applied potential. Upon the initiation of corrosion, the pH was rapidly reduced due to ferrous ion hydrolysis. External exposure environment was aerated, saturated $Ca(OH)_2$ + 0.5 M NaCl (bulk pH = 12.6).
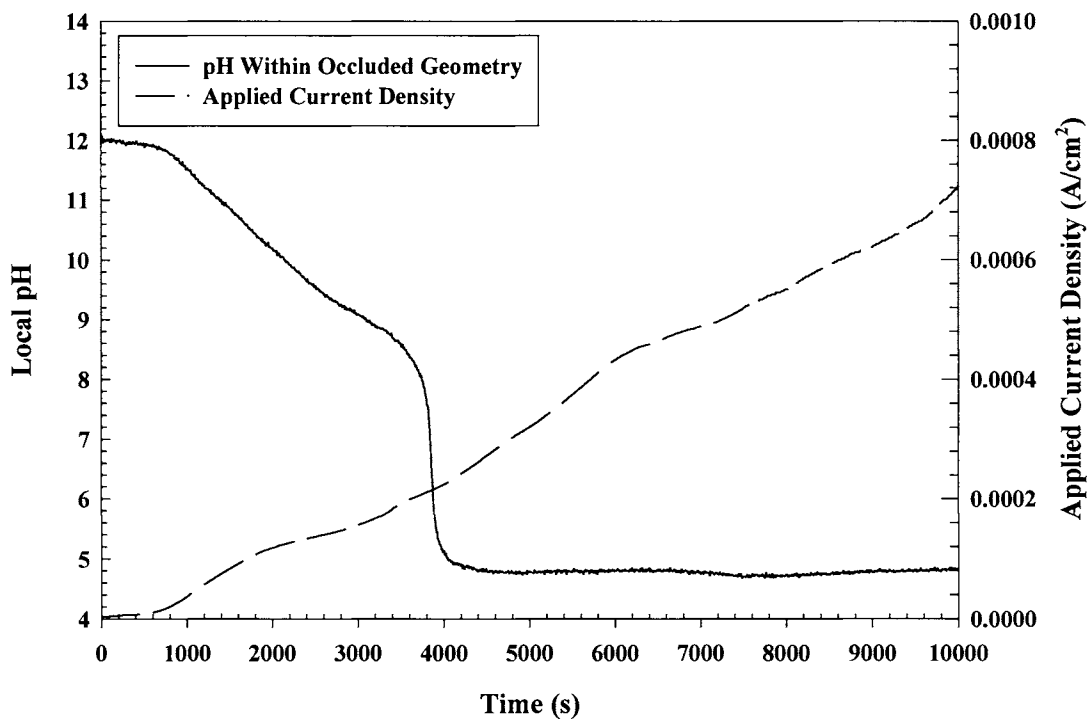
Figure 5.55: Occluded solution pH as a function of time within an occluded geometry along with the corrosion current, illustrating the increase in current commensurate with the decrease in the occluded solution pH due to the initiation of corrosion. The test was performed at an applied potential of -400 mV$_{SCE}$ within an aqueous solution of saturated Ca(OH)2 + 0.5 M NaCl.
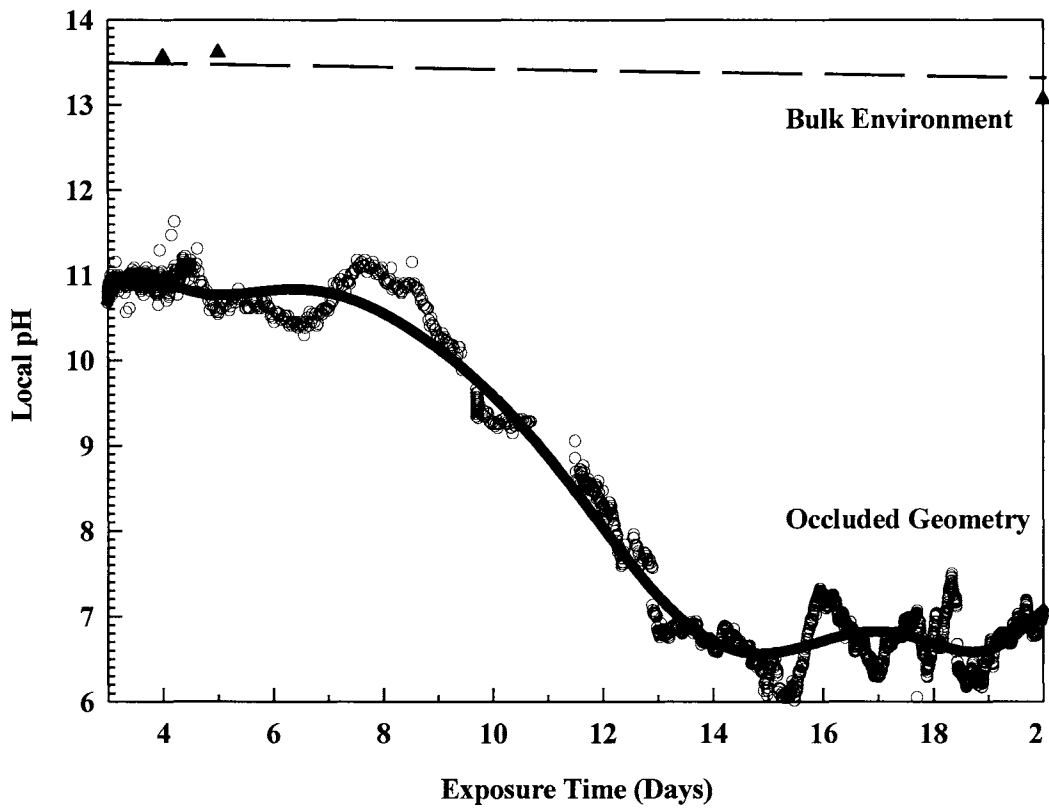
Figure 5.56: Steel occluded cell crevice solution pH as a function of time for the embedded pH sensor (Figure 4.18) in piling 1 (Figure 4.19). Sensor was located 30.5 cm above the waterline. Piling was cured for 28 days prior to immersion in ASTM artificial oceanwater. A similar reduction in the local pH to that seen during the simulated steel/concrete interface (Figure 5.51) and titration (Figure 5.50) upon the initiation of corrosion was observed.
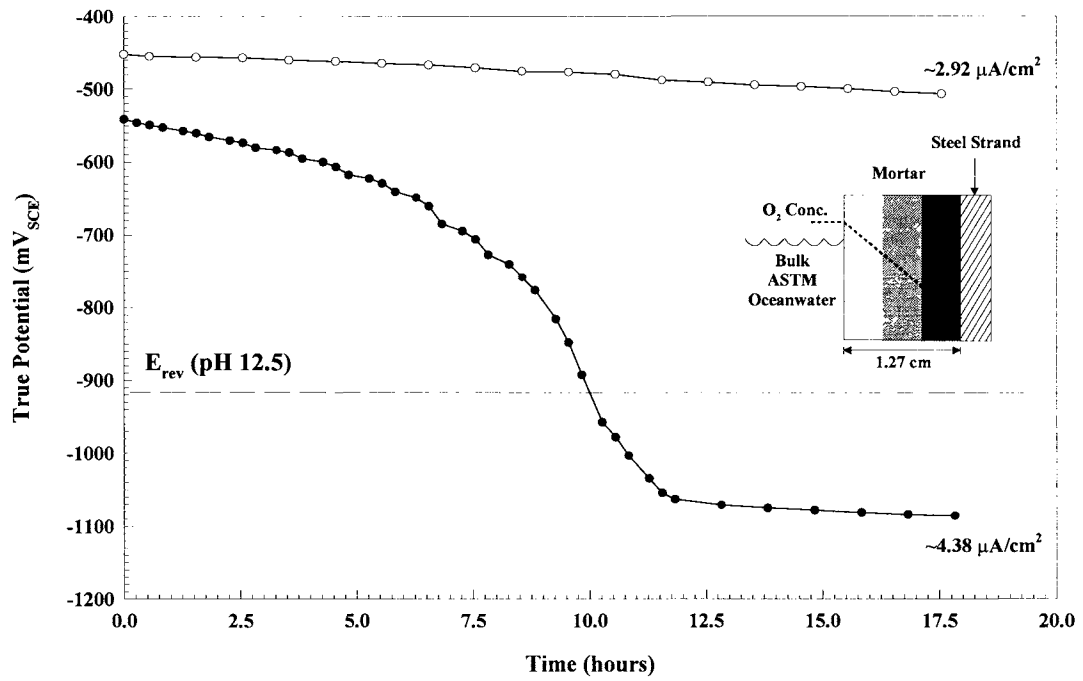
Figure 5.57: Measured internal applied potential as a function of time for a mortar covered pre-stressing strand (1.25 cm (0.5") cover) at several applied cathodic current densities. Current-on potentials decreased with time indicative of oxygen depletion at the steel/mortar interface.
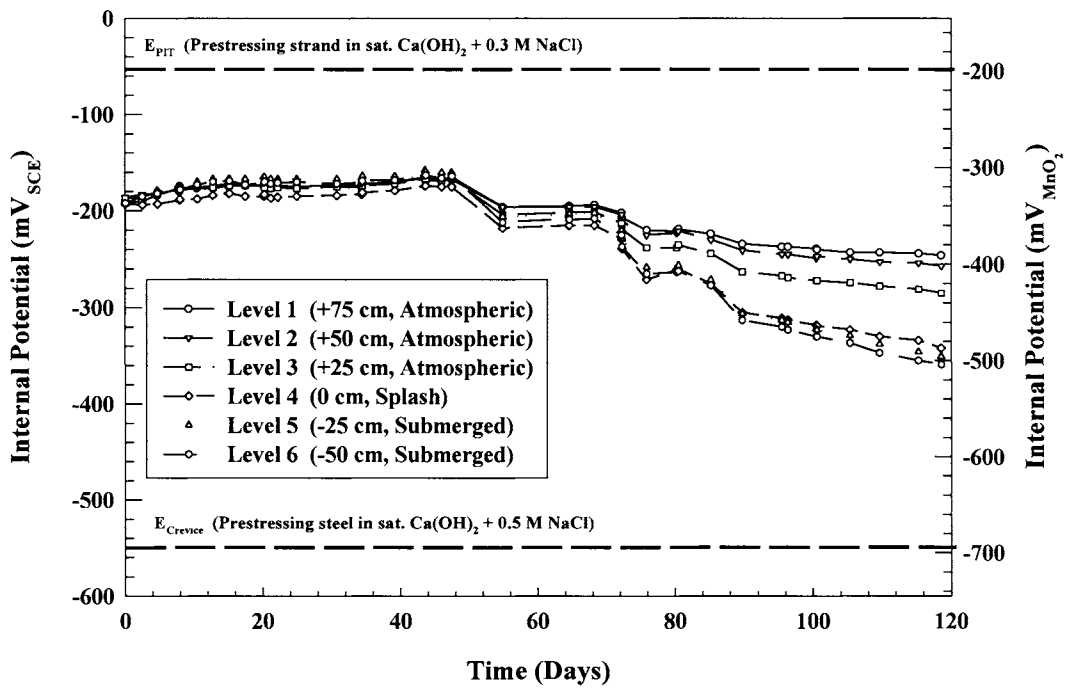
Figure 5.58: Internally measured open circuit potential data for piling 3 (Figure 4.21) as a function of time following partial immersion in ASTM artificial ocean water.
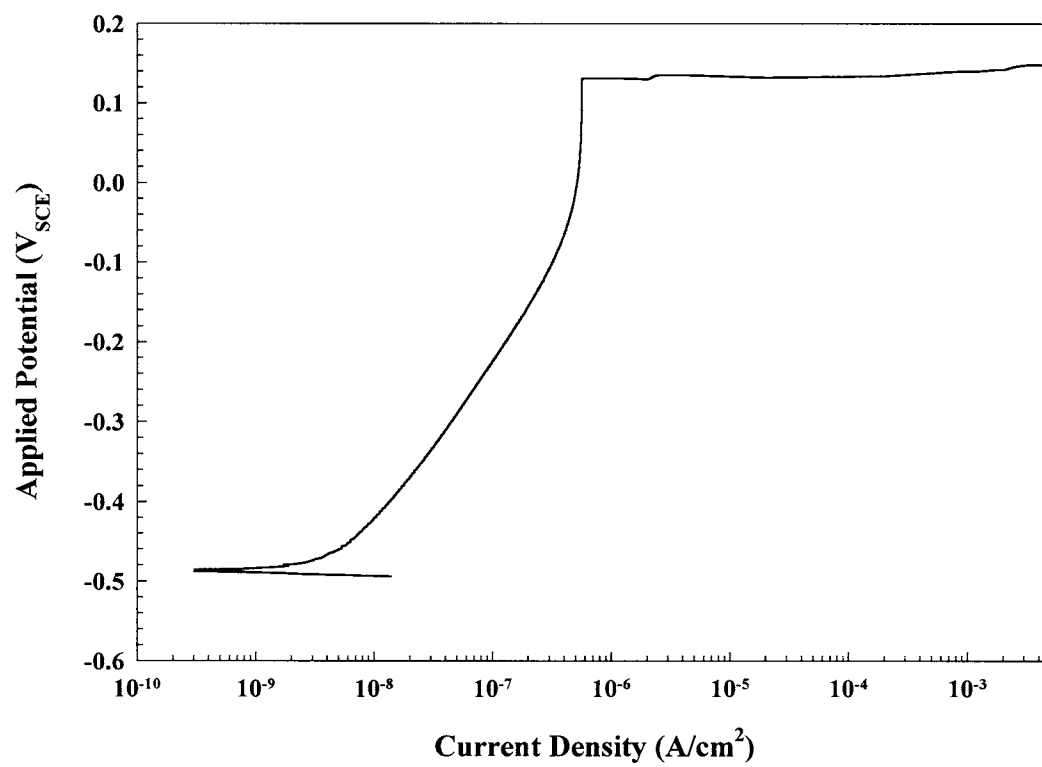
Figure 5.59: Anodic polarization of AISI/SAE 1080 steel in saturated $Ca(OH)_2$ + 0.3 M NaCl.
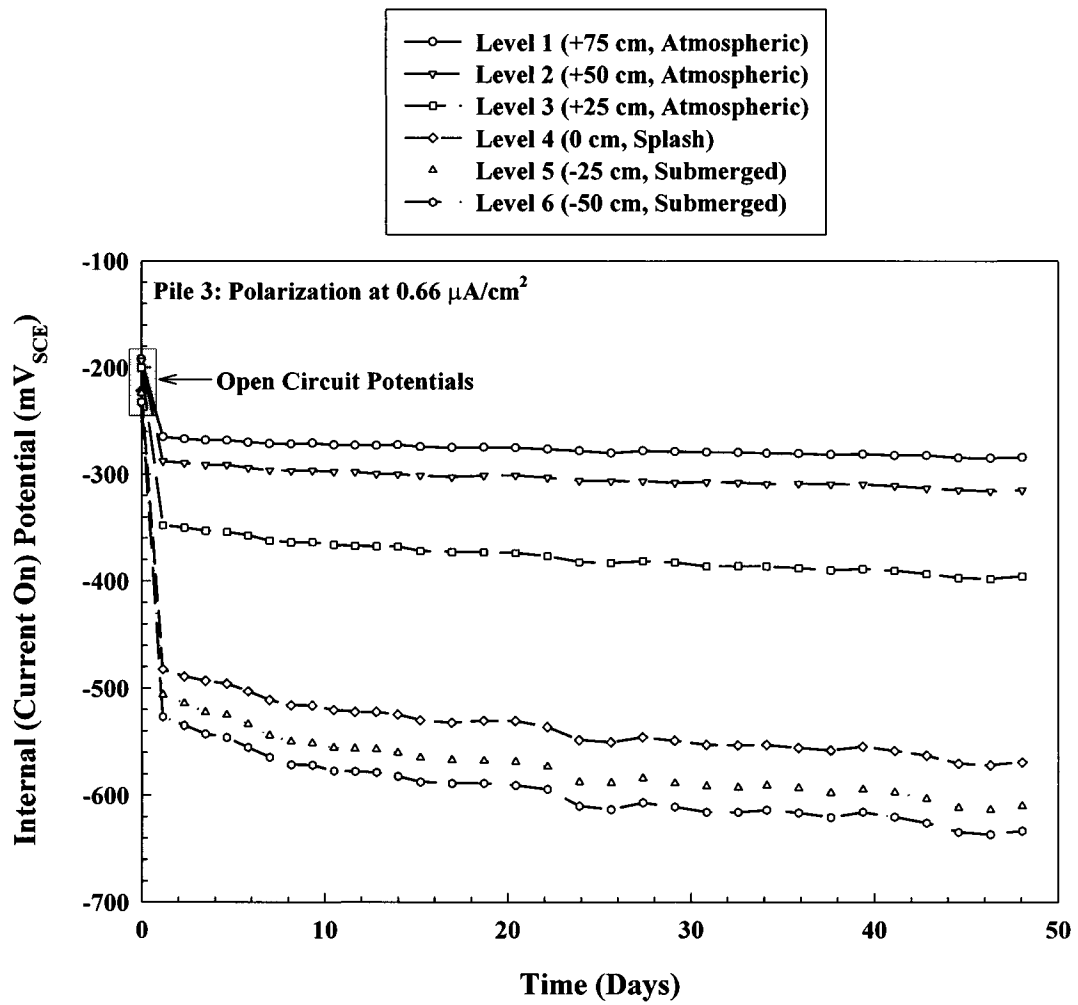
Figure 5.60: Internal current-on potentials as a function of time and position within piling 3 (Figure 4.21) for an applied current density of 0.66 μA/cm². Potentials were measured relative to embedded MnO_2 reference electrodes placed in close proximity to the steel tendon, and are essentially IR free.
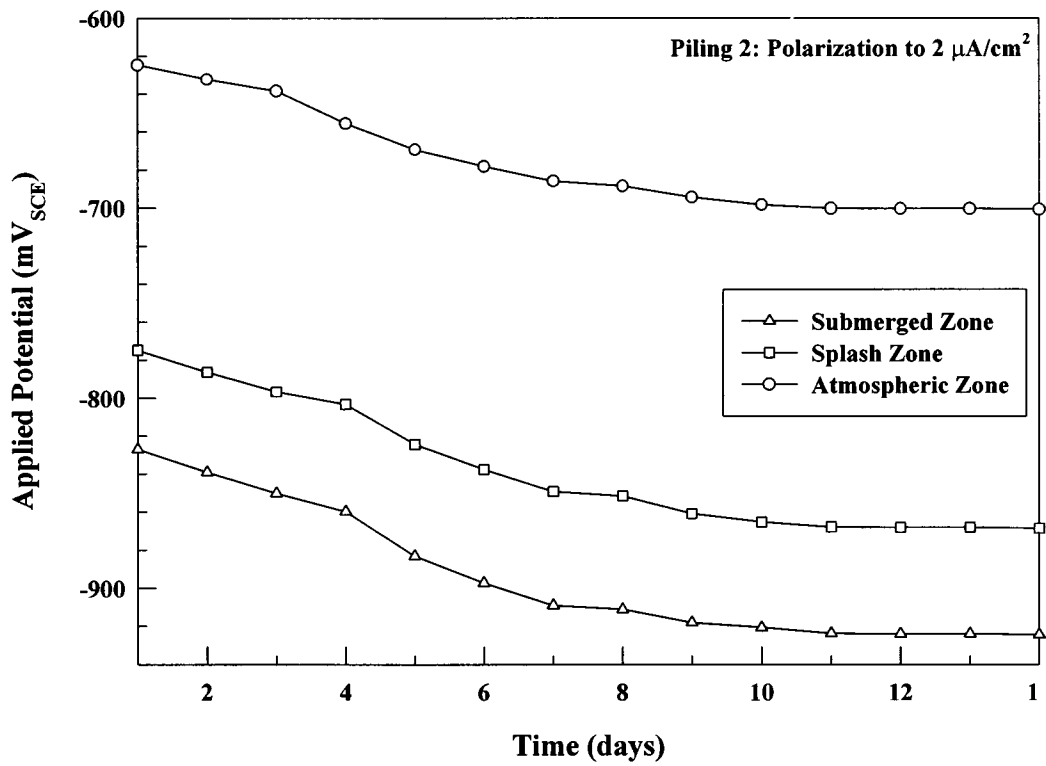
Figure 5.61: Stabilization of local potentials as a function of position within pile 2 at an applied cathodic current density of 2 $\mu A/cm^2$.
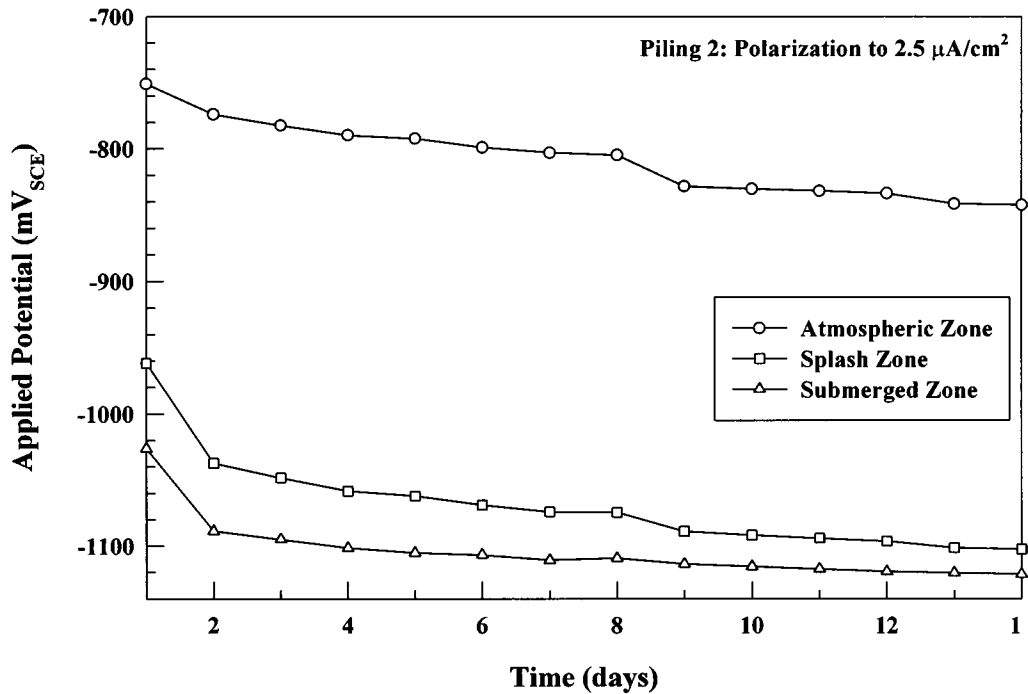

Figure 5.62: Stabilization of local potentials as a function of position within pile 2 at an applied cathodic current density of 2.5 $\mu A/cm^2$.
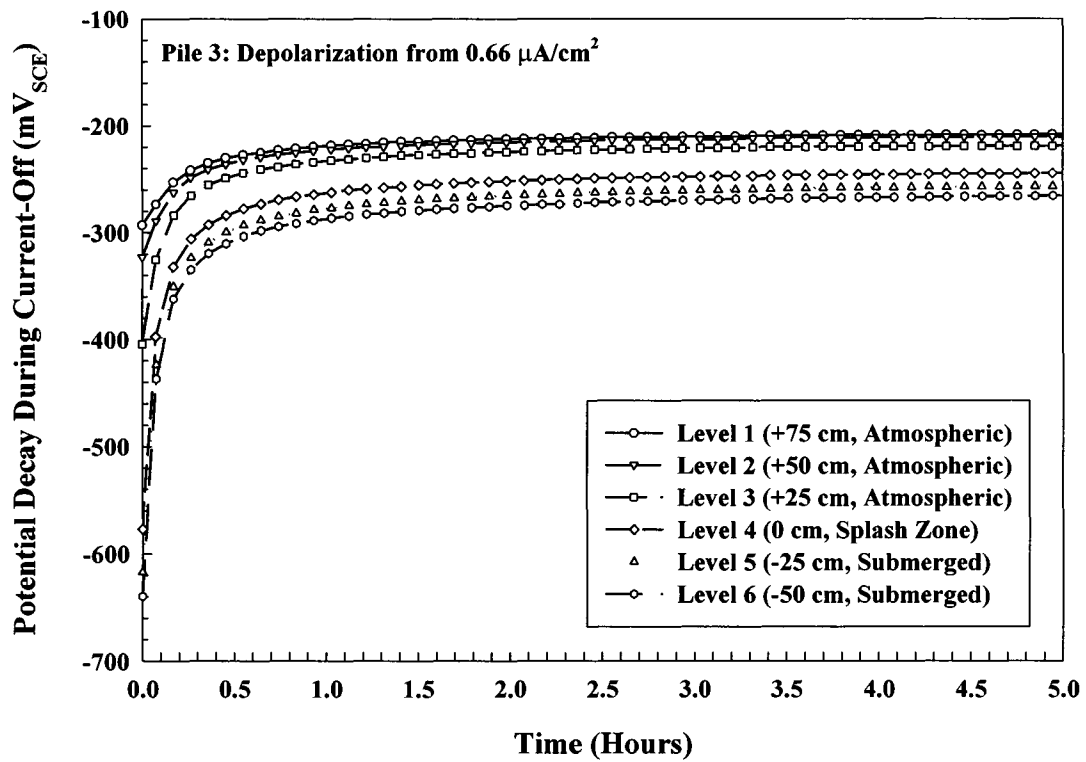
Figure 5.63: Depolarization of piling 3 (Figure 4.21) as a function of time following polarization to 0.66 μA/cm^2. Potentials were measured relative to embedded MnO$_2$ reference electrodes.
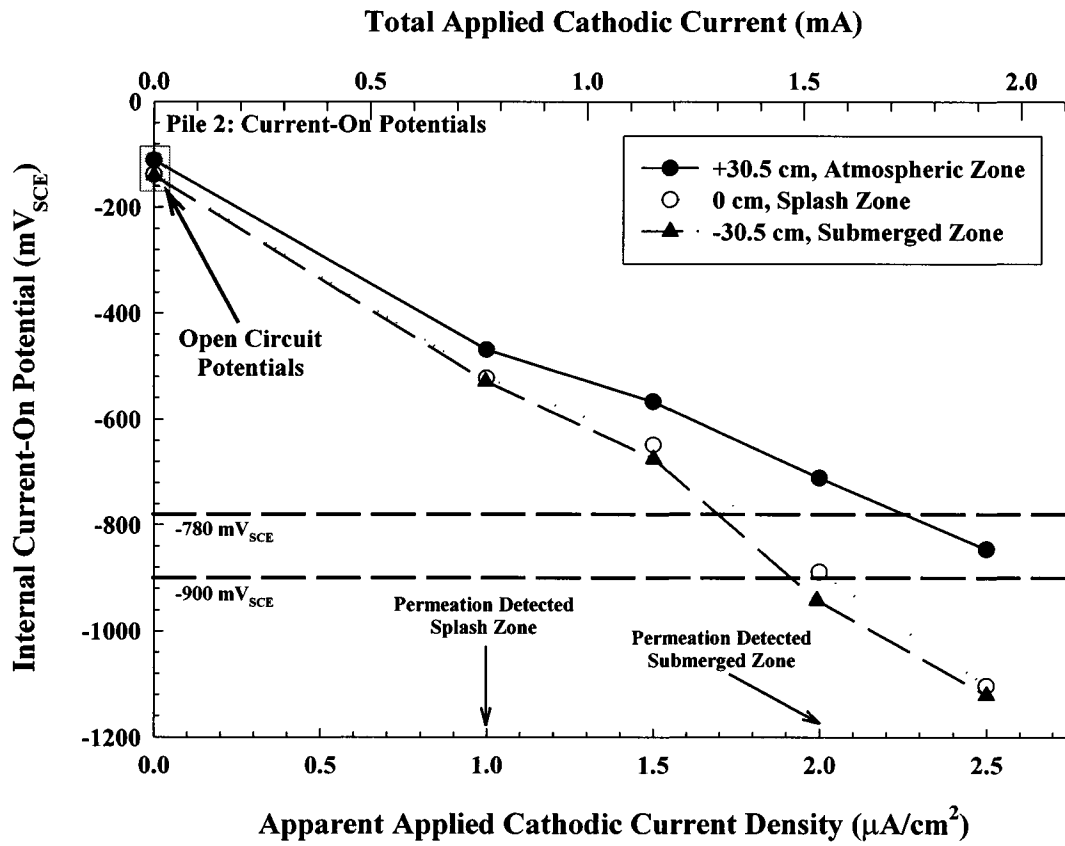
Figure 5.64:   Internal current-on potentials for piling 2 (Figure 4.20) as a function of position for each applied current density (current per unit area of reinforcement).
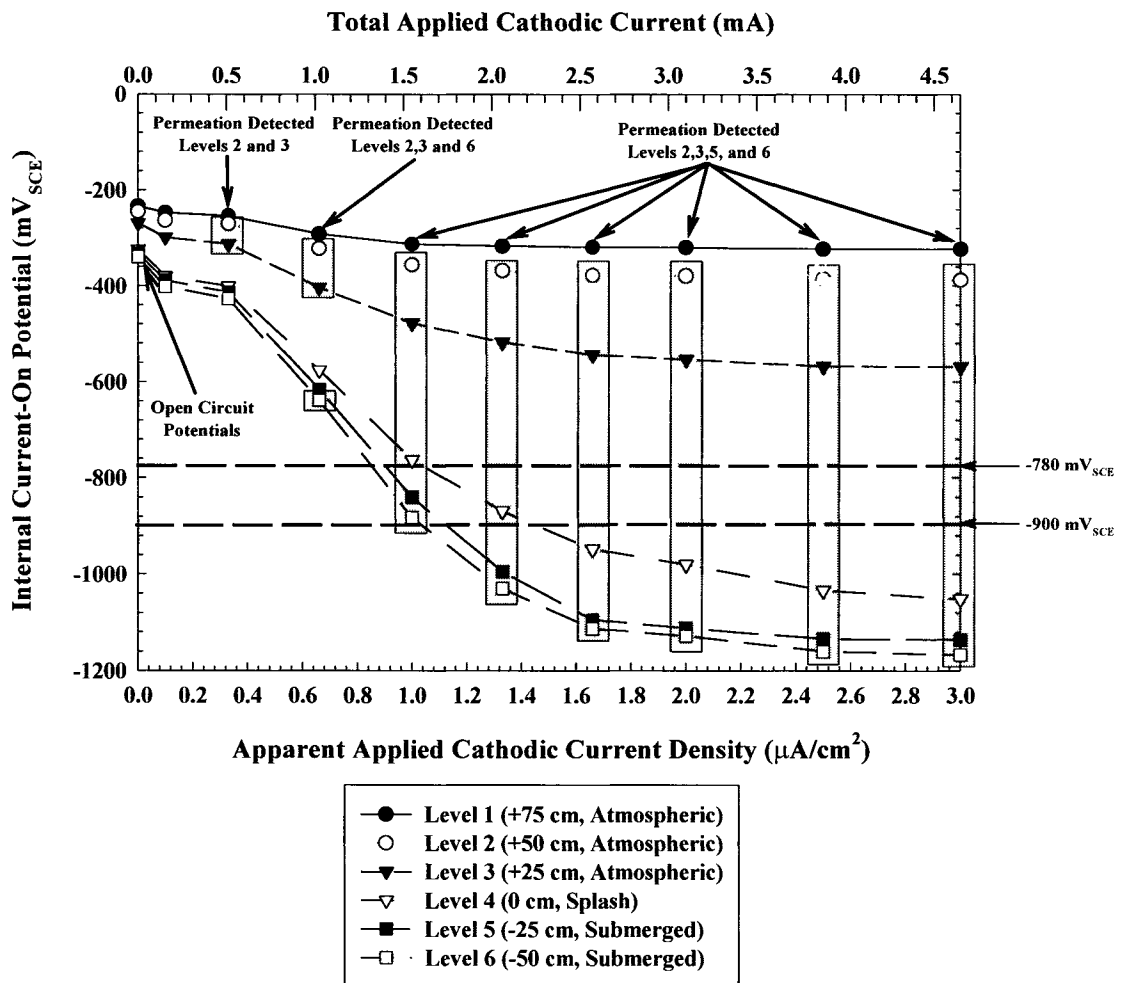
Figure 5.65: Internal current-on potentials for piling 3 (Figure 4.21) as a function of position for each applied current density (current per unit area of reinforcement).
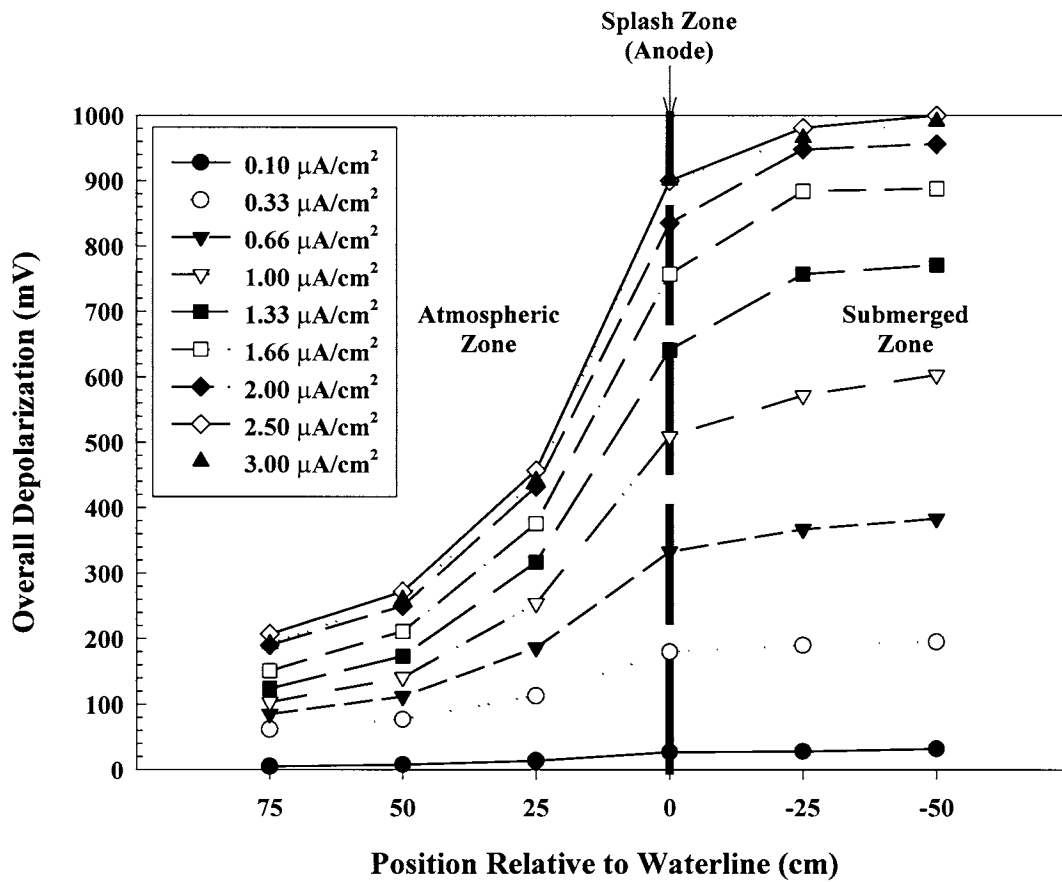
Figure 5.66: Degree of depolarization, defined as the difference between the current-on and completely depolarized potentials, as a function of vertical position in pile 3 (Figure 4.21).
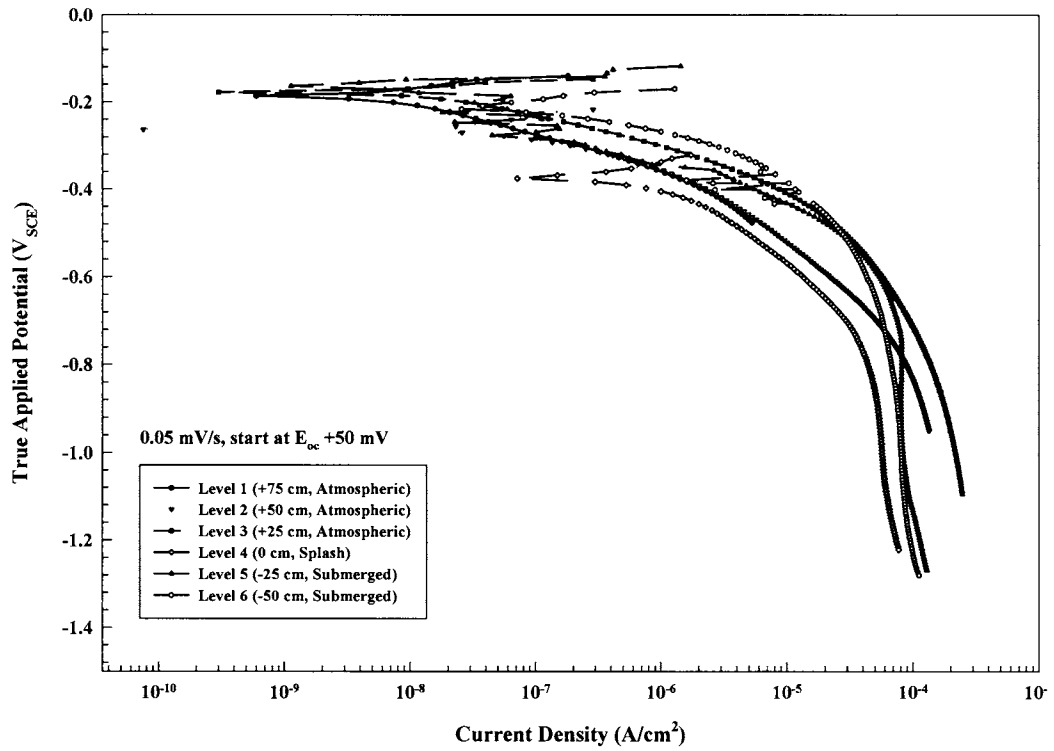
Figure 5.67: Potentiodynamic polarization scans performed on the hydrogen permeation sensor window at each sensor level upon the completion of all cathodic protection levels.
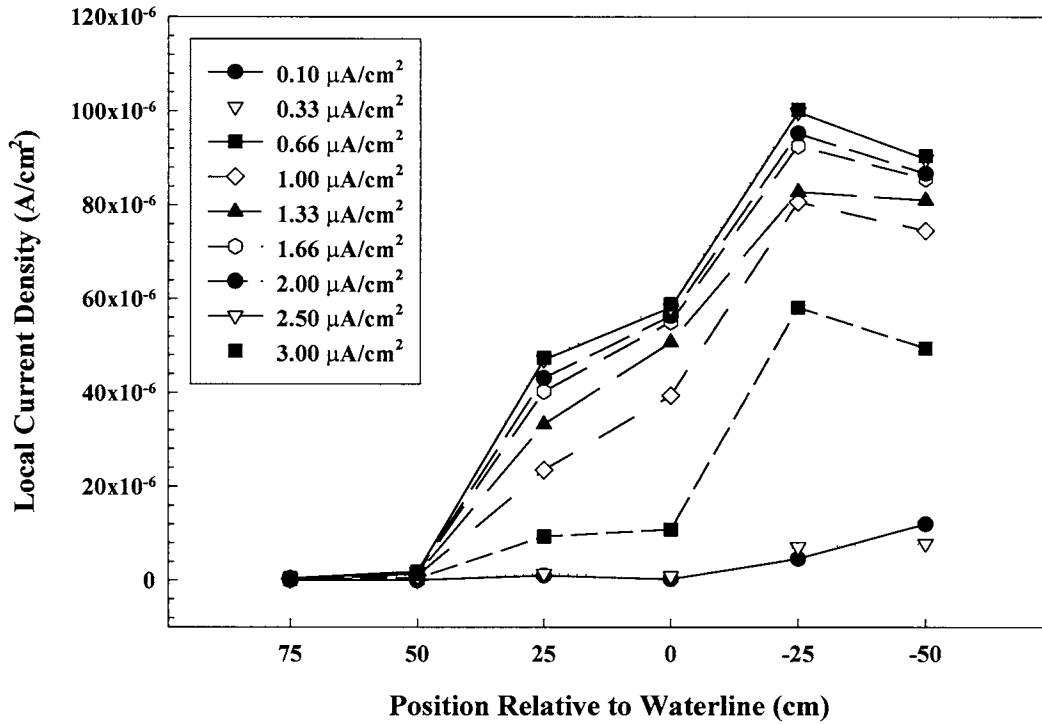
Figure 5.68: Local current density for all sensor levels within piling 3 at each applied cathodic protection level.
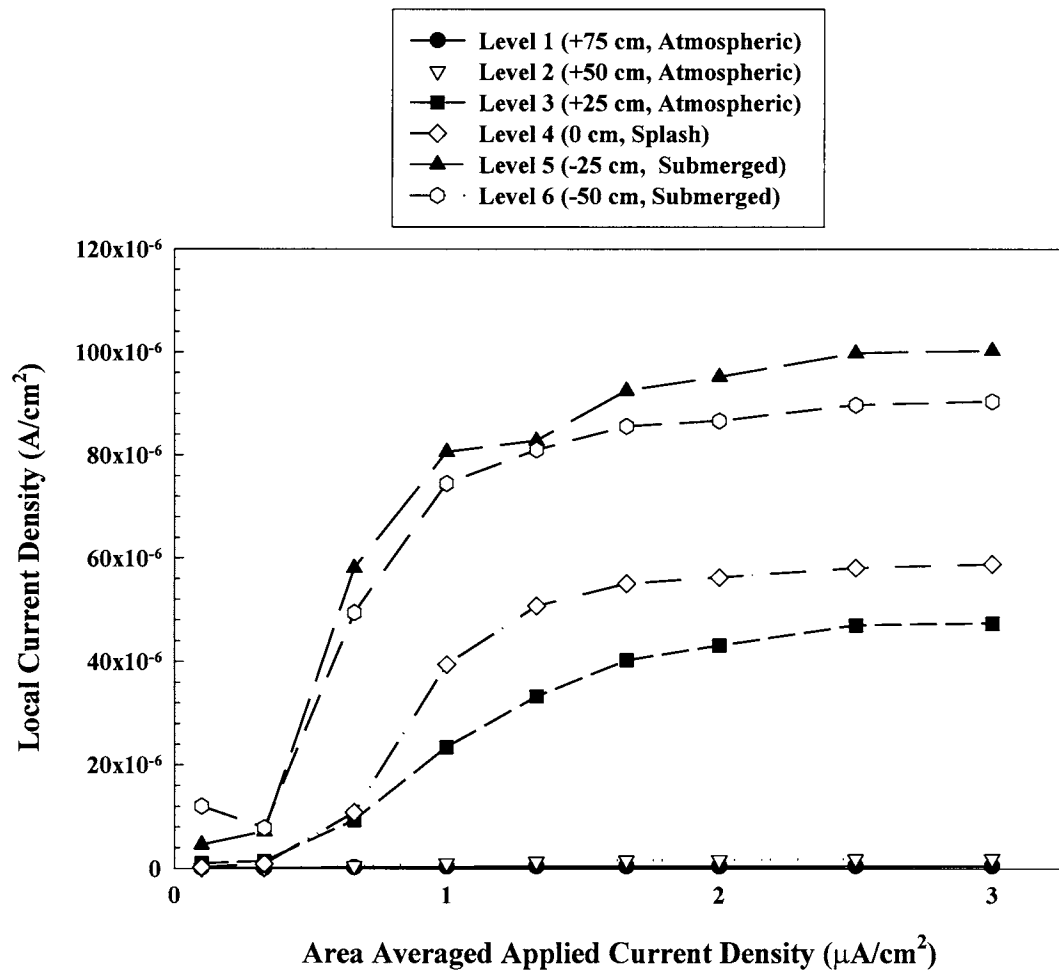
Figure 5.69: Local current density for each sensor level as a function of the applied cathodic protection level.
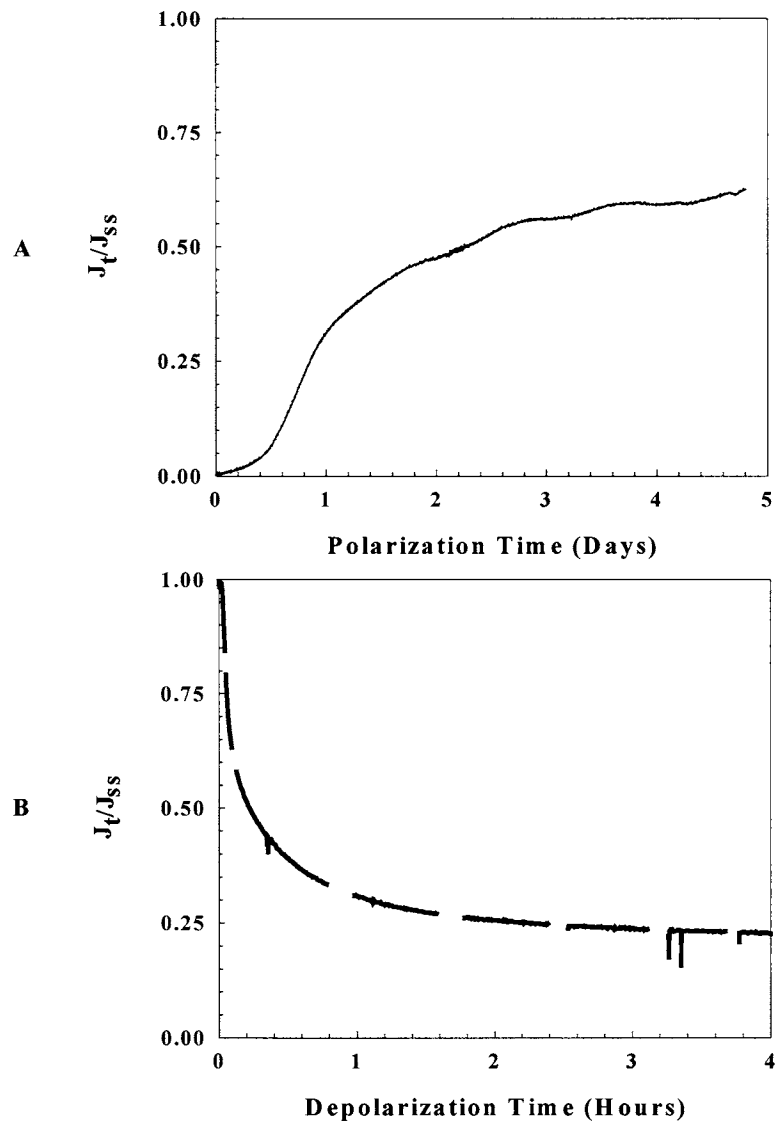
Figure 5.70: Representative rise (a) and decay (b) transients for a hydrogen permeation sensor.
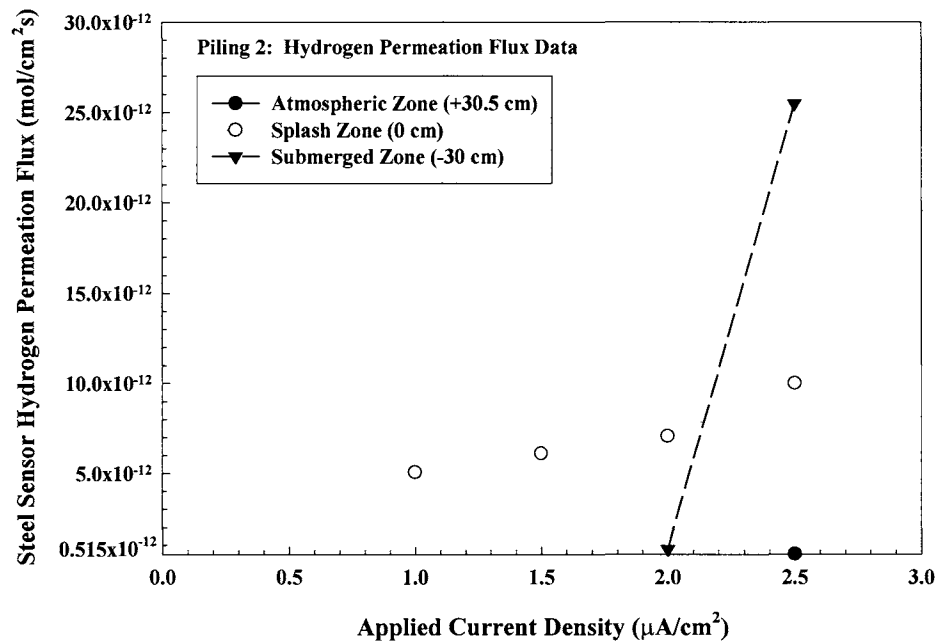
Figure 5.71: Steady state permeation flux as a function of the applied cathodic current density (current per unit area of reinforcement) from each hydrogen sensor within piling 2 (Figure 4.20). Although increasing hydrogen permeation readings were observed at the atmospheric zone, they were below the conservative detection limit of 5×10^{-13} mol/cm^{2}s used in this study.
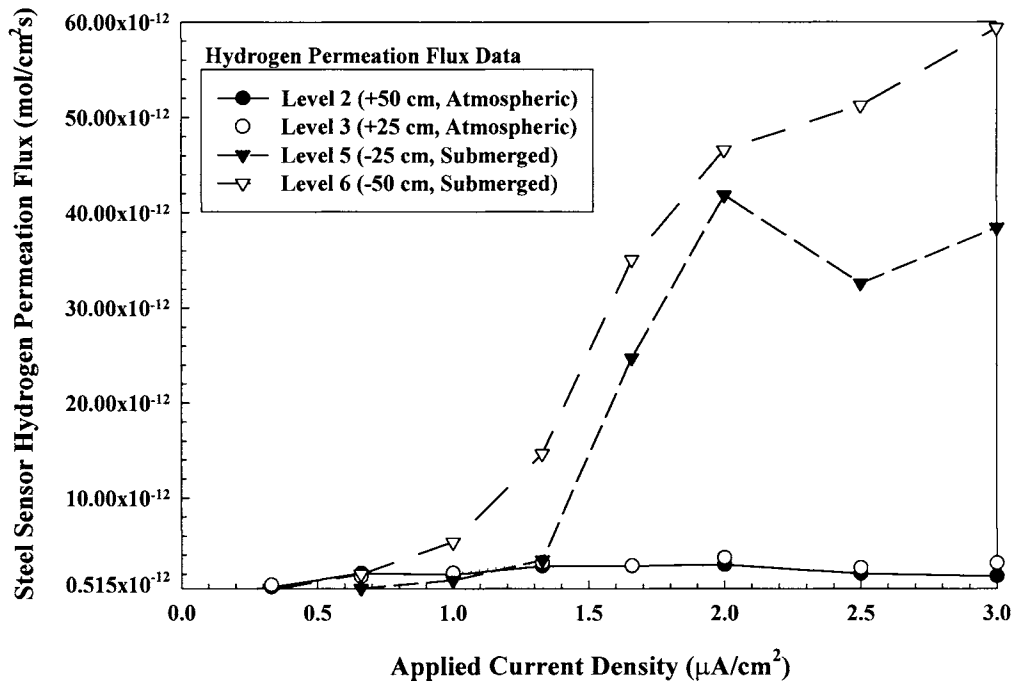
Figure 5.72: Steady state permeation flux as a function of the applied cathodic current density (current per unit area of reinforcement) from each hydrogen sensor within piling 3 (Figure 4.21). The hydrogen sensor located at the waterline (level 4) malfunctioned prior to the application of cathodic protection, and as such is not reported here.
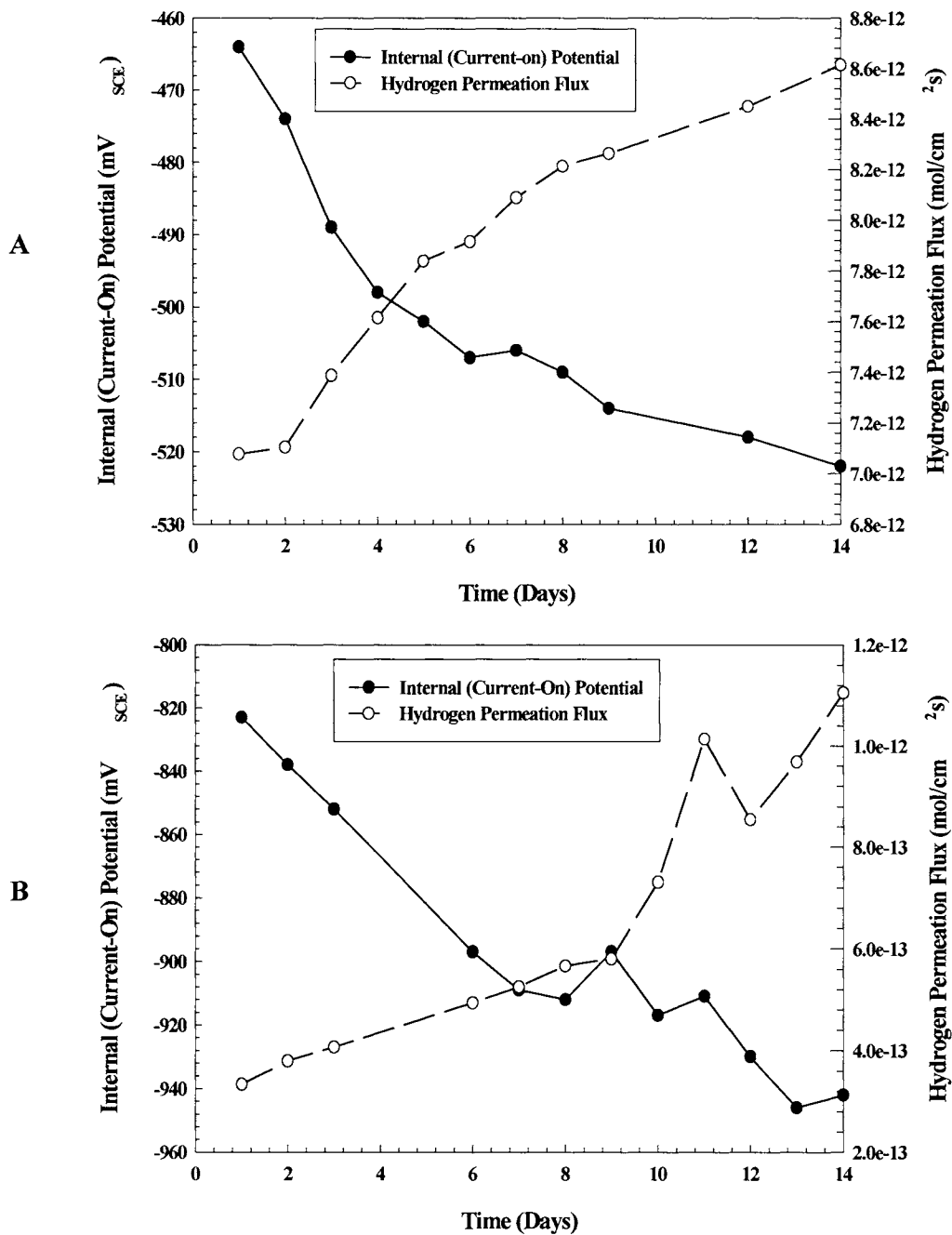
Figure 5.73: Internal potential data from a laboratory scale piling (Figure 4.20) illustrating the gradual negative shift in potential accompanied by the observance of hydrogen permeation from the sensors located within (a) the splash zone at cathodic current density of 1 $\mu A/cm^2$ (per unit area of reinforcement) and (b) the submerged zone at a cathodic current density of 2 $\mu A/cm^2$.
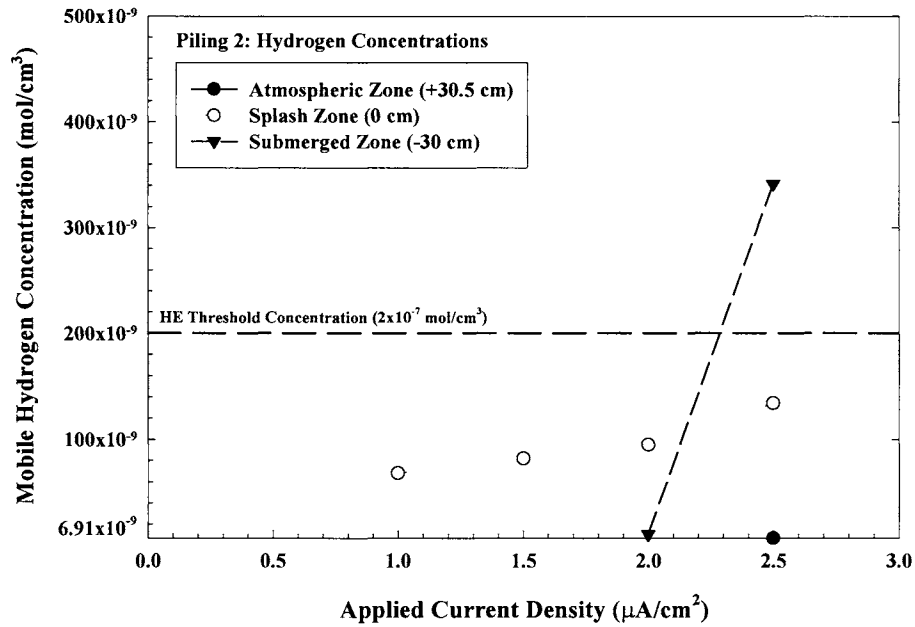
Figure 5.74: Calculated mobile hydrogen concentration within the pre-stressing steel reinforcement, calculated from Figure 4.15 and Equation 34, as a function of position and applied cathodic current density (current per unit area of reinforcement) for piling 2 (Figure 4.20). Readings for the atmospheric zone were below the previously determined detection limit of 6.9×10^{-9} mol/cm^3.
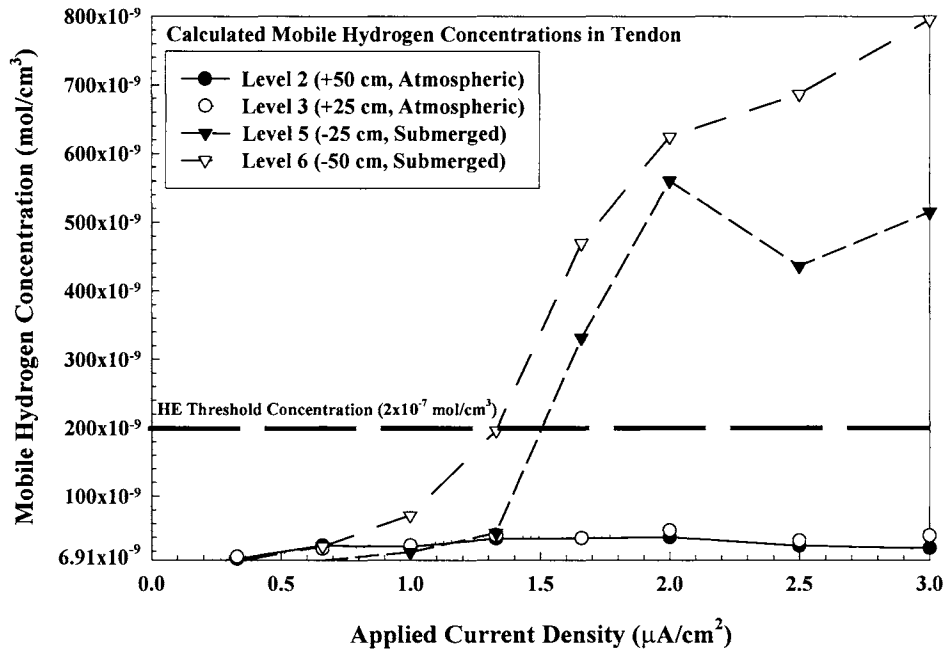
Figure 5.75: Calculated mobile hydrogen concentration within the pre-stressing steel reinforcement, calculated from Figure 4.15 and Equation 34, as a function of position and applied cathodic current density (current per unit area of reinforcement) for piling 3 (Figure 4.20). The hydrogen sensor located at the waterline (level 4) malfunctioned prior to the application of cathodic protection, and as such is not reported here.
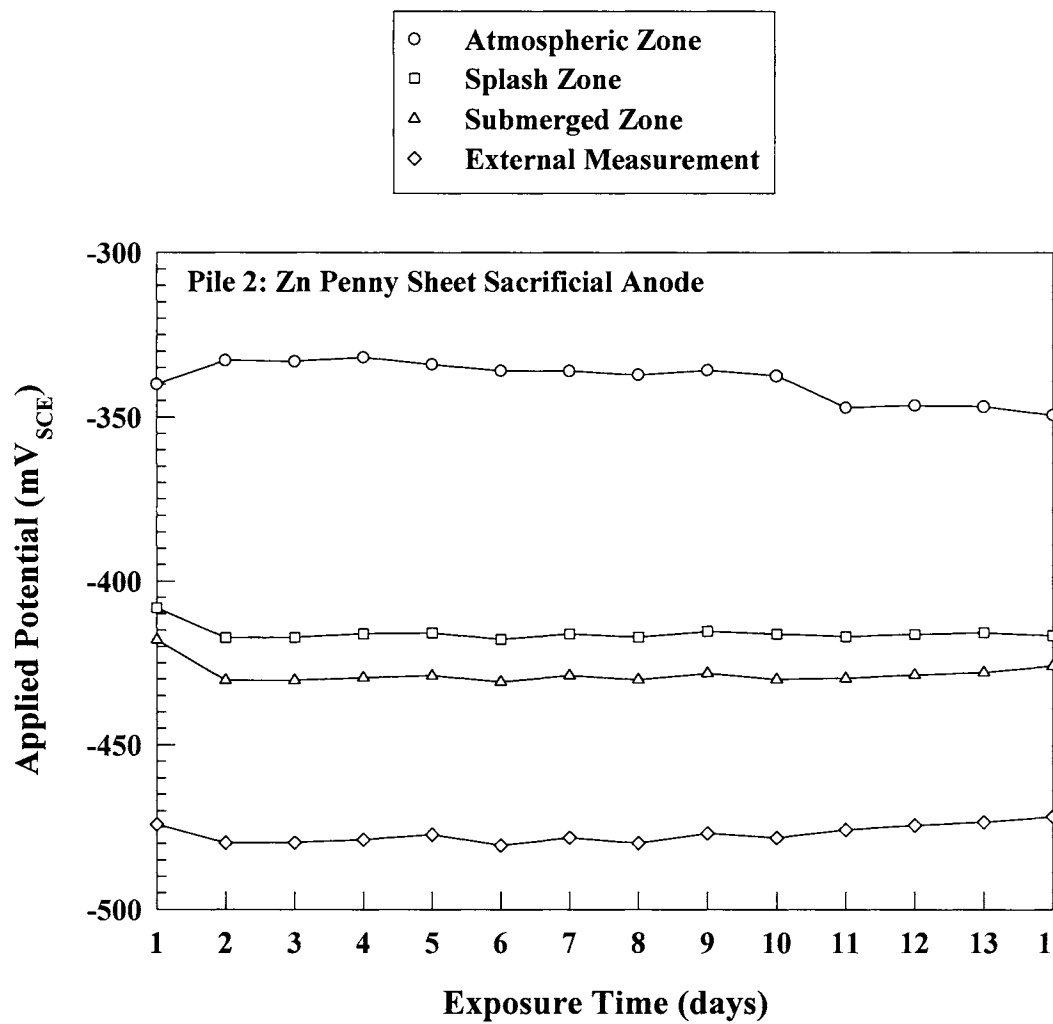
Figure 5.76: Internal potentials achieved during sacrificial anode cathodic protection of piling 2 via a Zn penny sheet.

TABLES

Table 1.1: Environmental pH resulting from metal cation hydrolysis for solutions containing various concentrations of ferrous (Fe^{2+}) and ferric (Fe^{3+}) ions.

	0.001 M Fe^{x+}	0.01 M Fe^{x+}	0.1 M Fe^{x+}	0.5 M Fe^{x+}	0.8 M Fe^{x+}
$Fe^{2+} + H_2O \rightarrow FeOH^+ + H^+$	6.25	5.75	5.25	4.90	4.80
$Fe^{2+} + 2\ H_2O \rightarrow Fe(OH)_2 + 2\ H^+$	8.14	7.64	7.14	6.79	6.69
$Fe^{3+} + 3\ H_2O \rightarrow Fe(OH)_3 + 3\ H^+$	2.61	2.28	1.94	1.71	1.64

Table 4.1. Compositional analysis of the ASTM A416 grade 270 pre-stressing strand and the hydrogen permeation sensor windows used for construction of the laboratory scale pilings.

Element	1080 Sheet	Pre-Stressing Strand	Hydrogen Sensor
Al	0.04	0.002	0.044
B	0.0004	0.0004	<0.0002
C	0.784	0.794	0.023
Cb	0.002	0.003	0.000
Co	0.003	0.003	0.005
Cr	0.184	0.101	0.020
Cu	0.007	0.039	0.020
Fe	98.000	98.022	99.60
Mn	0.624	0.667	0.190
Mo	0.006	0.008	0.014
Ni	0.048	0.048	0.020
P	0.009	0.010	0.009
Pb	0.009	0.009	0.002
S	0.007	0.009	0.012
Si	0.243	0.216	0.021
Sn	0.003	0.003	0.003
Ta	0.000	0.000	<0.003
Ti	0.002	0.002	0.002
V	0.014	0.052	0.001
W	0.004	0.002	0.010
Zr	0.0001	0.0001	0.001

Table 4.2. Mechanical properties of nominally fully pearlitic, eutectiod steels.

Material	Interlamellar spacing (nm)	Prior Austenite Grain Size (μm)	Pearlite Colony Size (μm)	Youngs Modulus (GPa)	Yield Strength (MPa)	Ultimate Tensile Strength (MPa)	DBT T (K)	K_{IC} (MPa√m)	Researchers
BS11 Grade A (0.75% C)	100	--	--	--	818	1955	--	--	Kavishe et al., 1986
~1085 (0.85% C)	300	75	--	199	600	1151	--	--	Toribio et al., 1992
Rail Stock (0.81% C)	119	40	5	--	621.2	--	406	--	Hyzak et al., 1976
Pre-Stressing Steel (0.71% C)	--	--	--	--	1490	1650	--	--	Alonso et al., 1993
Pre-Stressing Steel (0.74% C)	--	--	--	190	1500	1830	--	84	Toribio et al., 1993
Hot Rolled Bar (0.74% C)	--	--	--	195	725	1300	--	53	
Pre-Stressing Steel (0.74% C)	--	--	--	--	1443	1628	--	--	McGuinn et al., 1977
1080 Steel	110	170	6.5	--	738	1082	--	--	Lewandowski et al., 1987
Pre-Stressing Steel (1085)	--	--	--	--	1590	1800	--	--	Price et al., 1984

Pre-Stressing Steel	--	--	210	1500	--	--	80	Athanassiadis et al., 1981
Cold Drawn 1075	--	--	--	1461	1682	--	--	Townsend, 1972.
Pre-Stressing Steel	95	--	185	1696	1889	--	68.2	This Study

Table 4.3. Diffusional boundary layer thickness for a series of electrode configurations.

Type of Stirring	Boundary Layer Thickness, δ (μm)
Natural Convection	150 - 250
Magnetic Stirrer	50 - 100
RDE at 400 RPM	25
RDE at 10,000 RPM	5
Fast Impinging Jet	2 - 5

Table 4.4. Surface pH as a function of applied cathodic current density within environments relevant to this study.

Applied Current Density (μA/cm^2)	pH 6 Borate Buffer	pH 8.2 ASTM Ocean Water	pH 9.2 Ca(OH)$_2$	pH 12.5 NaOH	pH 12.6 Ca(OH)$_2$
1	7.03544	8.22618	9.20269	12.50000	12.60000
2.5	7.40868	8.26272	9.20669	12.50000	12.60000
5	7.70115	8.31752	9.21329	12.50001	12.60000
7.5	7.87435	8.36617	9.21978	12.50001	12.60000
10	7.99784	8.40992	9.22618	12.50001	12.60001
25	8.39315	8.60718	9.26272	12.50003	12.60002
50	8.69330	8.81359	9.31752	12.50007	12.60005
100	8.99389	9.05825	9.40992	12.50014	12.60010
150	9.16984	9.21379	9.48607	12.50020	12.60016

Table 4.5. Effective diffusivities for select iron and plain carbon steels.

Material	Microstructure	D_{eff} (cm^2/s)	Method	Reference
1090	Coarse pearlite (416 nm)	1.38×10^{-5}	Permeation	Jeng et al., 1990
	Medium pearlite (161 nm)	6.21×10^{-6}		
	Fine pearlite (84.4 nm)	2.70×10^{-6}		
1035	Spheroidized	3.40×10^{-5}	Permeation	Johnson et al., 1987
	Quenched and tempered	1.30×10^{-5}		
1050	Spheroidized	2.18×10^{-5}		
	Quenched and tempered	5.30×10^{-6}		
	Pearlitic (210 nm)	3.60×10^{-6}		
1090	Pearlitic (720 nm)	7.20×10^{-6}		
A-516 G60	Quenched	2.00×10^{-7}	Permeation	Luppo et al.,
(0.12 C)	Quenched and tempered (453 K)	1.70×10^{-6}		1991
	Quenched and tempered (773 K)	3.60×10^{-6}		
Armco Iron	Annealed	3.06×10^{-5}	Permeation	Nanis et al., 1972
Armco Iron	Annealed	8.40×10^{-5}	Permeation	Devanathan et. al., 1964
Armco Iron	Annealed	6×10^{-5}	Permeation	Namboodhiri et. al., 1973
99.8% Fe	Annealed	1.3×10^{-5}	Permeation	Kumnick et al., 1974
Electrolytic iron	Cold rolled	6.78×10^{-6}	Permeation	Song et al., 1990
99.5% Fe	Cold rolled	1.2×10^{-6}	Permeation	Lillard et al., 1996
1080	Cold rolled, pearlitic (95 nm)	6.72×10^{-7}	Permeation	This Study

Table 4.6.   Geometrical correction factors for the calculation of the stress intensity for an elliptical crack using the method of Raju and Newman.

a/D	a/c = 1.0		a/c = 0.8		a/c = 0.6	
	A	B	A	B	A	B
0.05	1.012	1.156	1.056	1.054	1.107	0.933
0.125	1.015	1.189	1.083	1.101	1.176	0.999
0.2	1.038	1.260	1.131	1.200	1.316	1.129
0.275	1.087	1.356	1.227	1.335	1.565	1.329
0.35	1.175	1.475	1.387	1.509	1.835	1.516

Table 4.7. Concrete mix design used for all pilings.

Water/Cement Ratio	0.49
Cement Factor	377 kg/m³ (635 lb/yd³)
Design Density	2.6
Coarse Aggregate	#7 (<1.27 cm) granite
28 Day Design Strength	>34.5 MPa (5000 psi)
Slump	0 - 10.2 cm (0 - 4 in.)
Air	4.5 ± 1.5 %
Chloride Concentration (as NaCl)	0.033% by weight of concrete (1.26 kg/m³ concrete)

Table 5.1. Summary of environments utilized and their justification for CERT and Devanathan/Stachurski permeation experiments.

Environment	pH	Justification
Mortar cover in Oceanwater	>12.6	True simulation of steel/concrete interfacial environment.
Saturated $Ca(OH)_2$	12.6	Typical pore solution analog
1.0 N H_3BO_4 + 1 mM $Ca(OH)_2$ + 3.3 mM NaCl + HCl	6 (Buffered)	Occluded environment simulant
1.0 N H_3BO_4 + 1 mM $Ca(OH)_2$ + 3.3 NaCl + HCl	4 (Buffered)	Occluded environment simulant
ASTM Artificial Oceanwater	8.2 (Buffered)	Possible result of crack in concrete
0.1 M HCl + 0.3 M NaCl + 10 ppm H_2S (via Na_2S)	1	Achievement of high hydrogen concentrations

Table 5.2.   Trap site identification and desorption peak temperatures from TDS experiments.

Trap Site	Slope	E_a (kJ/mol)	Likely Identification
1 (Low T)	-2499.67	20.78	Fe/Fe$_3$C Interface (Hong, 1983; Choo, 1982)
2 (Med. T)	-2909.06	24.19	Dislocations (Choo, 1982)
3 (High T)	-3635.44	30.23	Microvoids (Hong, 1983)

Ramp Rate (degrees/minute)	Peak Temperature (°C) for Trap Sites		
	Fe/Fe$_3$C	Dislocations	Microvoids
2.5	204	300	359
5	252	345	424
7.5	282	390	461
10	315	434	493

Note. Calculation of E_b from E_a requires subtraction of the migration energy for diffusion (7.075 kJ/mol for iron [Quick, 1978]) as $E_a = E_b + E_m$.

Table 5.3.   Literature data for trap site binding energies for carbon and alloy steels.

Trap Site	Activation Energy, E_a (kJ/mol)	Source
Grain boundaries	17.2	Choo, 1982, 1983
Fe/Fe$_3$C interfaces	18.5	Hong, 1983; Choo, 1982
Dislocations	26.9	Choo, 1982, 1983
Microvoids	35.3	Choo 1982, 1983
Iron oxide particles	47	Hong, 1983

Table 5.4. Summary of cathodic protection results for piling 2 (Figure 4). Comparison of the magnitude of the observed polarization to the 100 mV depolarization criterion, 200 mV depolarization criterion, absolute potential criterion (-780 mV$_{SCE}$), -900 mV$_{SCE}$ safe limit proposed by Hartt and coworkers. Also noted is when hydrogen permeation was detected at each sensor level (indicated by H), and whether or not the calculated hydrogen concentration exceeded the threshold concentration for the onset of embrittlement (2x10^{-7} mol/cm^3) (indicated by C$_H$>C$_H$^{crit}).

Current Density	-1 μA/cm²						-2 μA/cm²						-2.5 μA/cm²					
Criterion (mV$_{SCE}$)	100	200	-780	-900	H	C$_H$>C$_H$^{crit}	100	200	-780	-900	H	C$_H$>C$_H$^{crit}	100	200	-780	-900	H	C$_H$>C$_H$^{crit}
+30 cm (Atmosph)	yes	yes	no	no	no	no	yes	yes	no	no	no	no	yes	yes	yes	no	yes	no
0 cm (Splash)	yes	yes	no	no	yes	no	yes	yes	yes	no	yes	no	yes	yes	yes	yes	yes	no
-30 cm (Subm)	yes	yes	no	no	no	no	yes	yes	yes	yes	yes	no	yes	yes	yes	yes	yes	yes

Table 5.5. Summary of cathodic protection results for piling 3 (Figure 5). Comparison of the magnitude of the observed polarization to the 100 mV depolarization criterion, 200 mV depolarization criterion, absolute potential criterion (-780 mV$_{SCE}$), -900 mV$_{SCE}$ safe limit proposed by Hartt and coworkers. Also noted is when hydrogen permeation was detected at each sensor level (H), and whether or not the calculated hydrogen concentration exceeded the threshold concentration for the onset of embrittlement (2×10^{-7} mol/cm^3) (C$_H$>C$_H$^{crit}).

Current Density.	-0.10 µA/cm²						-0.33 µA/cm²						-0.66 µA/cm²					
Criterion (mV$_{SCE}$)	100	200	-780	-900	H	C$_H$>C$_H$^{crit}	100	200	-780	-900	H	C$_H$>C$_H$^{crit}	100	200	-780	-900	H	C$_H$>C$_H$^{crit}
+75 cm (Atmosph)	no	no	no	no	no	no	no	no	no	no	no	no	no	no	no	no	no	no
+50 cm (Atmosph)	no	no	no	no	no	no	no	no	no	no	yes	no	yes	no	no	no	yes	no
+25 cm (Atmosph)	no	no	no	no	no	no	yes	no	no	no	yes	no	yes	no	no	no	yes	no
0 cm (Splash)	no	no	no	no	---	---	yes	no	no	no	---	no	yes	yes	no	no	---	---
-25 cm (Subm)	no	no	no	no	no	no	yes	no	no	no	no	no	yes	yes	no	no	no	no
-50 cm (Subm)	no	no	no	no	no	no	yes	no	no	no	no	no	yes	yes	no	no	yes	no

Note. The hydrogen sensor located at the waterline (0 cm) malfunctioned prior to the application of cathodic protection to the piling.

Table 5.5 (Continued)

Current Density

Criterion (mV$_{SCE}$)	-1.00 µA/cm²						-1.33 µA/cm²						-1.66 µA/cm²					
	100	200	-780	-900	H	$C_H>C_H^{crit}$	100	200	-780	-900	H	$C_H>C_H^{crit}$	100	200	-780	-900	H	$C_H>C_H^{crit}$
+75 cm (Atmosph)	yes	no	no	no	no	no	yes	no	no	no	no	no	yes	no	no	no	no	no
+50 cm (Atmosph)	yes	no	no	no	yes	no	yes	no	no	no	yes	no	yes	yes	no	no	yes	no
+25 cm (Atmosph)	yes	yes	no	no	yes	no	yes	yes	no	no	yes	no	yes	yes	no	no	yes	no
0 cm (Splash)	yes	yes	no	no	--	--	yes	yes	yes	no	--	--	yes	yes	yes	yes	--	--
-25 cm (Subm)	yes	yes	yes	no	yes	no	yes	yes	yes	yes	yes	no	yes	yes	yes	yes	yes	yes
-50 cm (Subm)	yes	yes	yes	no	yes	no	yes	yes	yes	yes	yes	yes	yes	yes	yes	yes	yes	yes

Current Density

Criterion (mV$_{SCE}$)	-2.00 µA/cm²						-2.50 µA/cm²						-3.00 µA/cm²					
	100	200	-780	-900	H	$C_H>C_H^{crit}$	100	200	-780	-900	H	$C_H>C_H^{crit}$	100	200	-780	-900	H	$C_H>C_H^{crit}$
+75 cm (Atmosph)	yes	yes	no	no	no	no	yes	yes	no	no	no	no	yes	no	no	no	no	no
+50 cm (Atmosph)	yes	yes	no	no	yes	no	yes	yes	no	no	yes	no	yes	yes	no	no	yes	no
+25 cm (Atmosph)	yes	yes	no	no	yes	no	yes	yes	no	no	yes	no	yes	yes	no	no	yes	no
0 cm (Splash)	yes	yes	yes	yes	--	--	yes	yes	yes	yes	--	--	yes	yes	yes	yes	--	--
-25 cm (Subm)	yes	yes	yes	yes	yes	yes	yes	yes	yes	yes	yes	yes	yes	yes	yes	yes	yes	yes

| -50 cm (Subm) | yes | yes | yes | yes | yes | yes | yes | yes | yes | yes | yes | yes | yes | yes | yes |

APPENDIX A

RAW POLARIZATION AND DEPOLARIZATION DATA FOR PILING 3

Polarization to 0.10 μA/cm^2

Figure showing Internal, Current-On Potential (mV MnO_2) versus Polarization Time (Days) for Levels 1–6.

Legend:
- Level 1 (+75 cm, Atmospheric)
- Level 2 (+50 cm, Atmospheric)
- Level 3 (+25 cm, Atmospheric)
- Level 4 (0 cm, Splash)
- Level 5 (-25 cm, Submerged)
- Level 6 (-50 cm, Submerged)
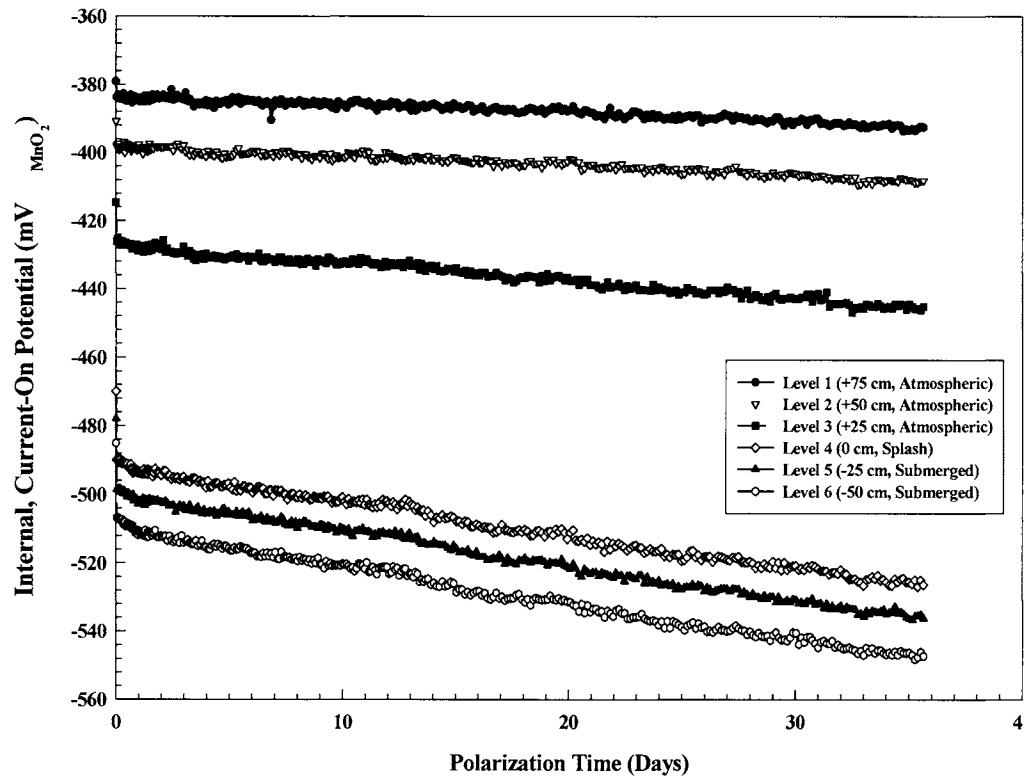
Polarization to 0.33 μA/cm^2
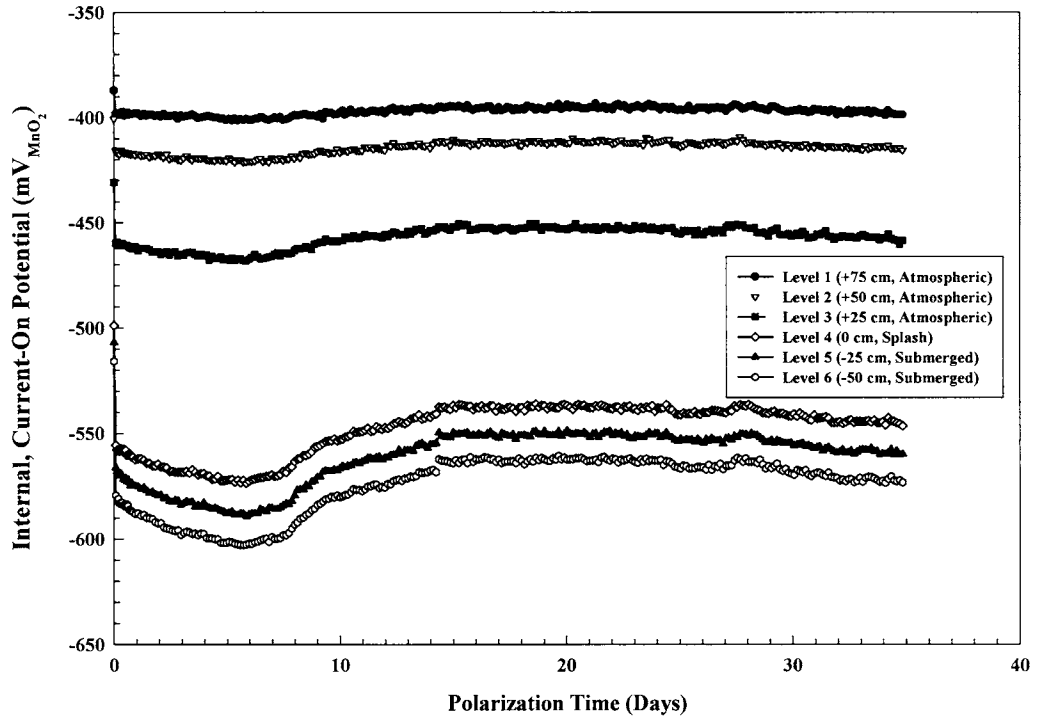
Depolarization from 0.33 μA/cm^2
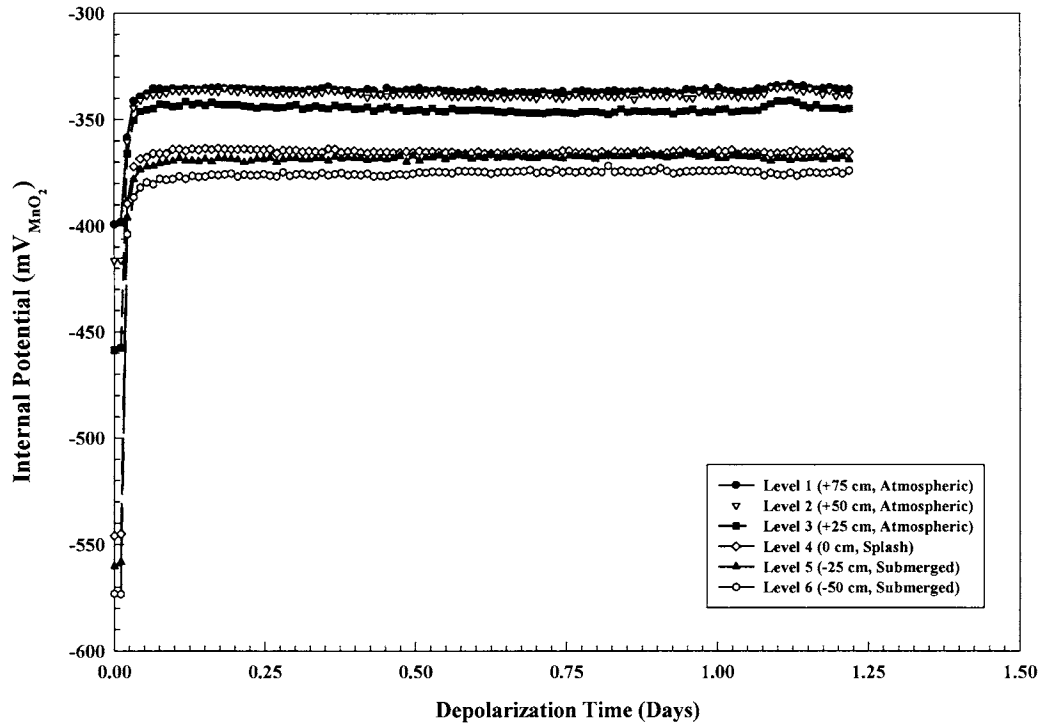
Polarization to 1.00 μA/cm^2
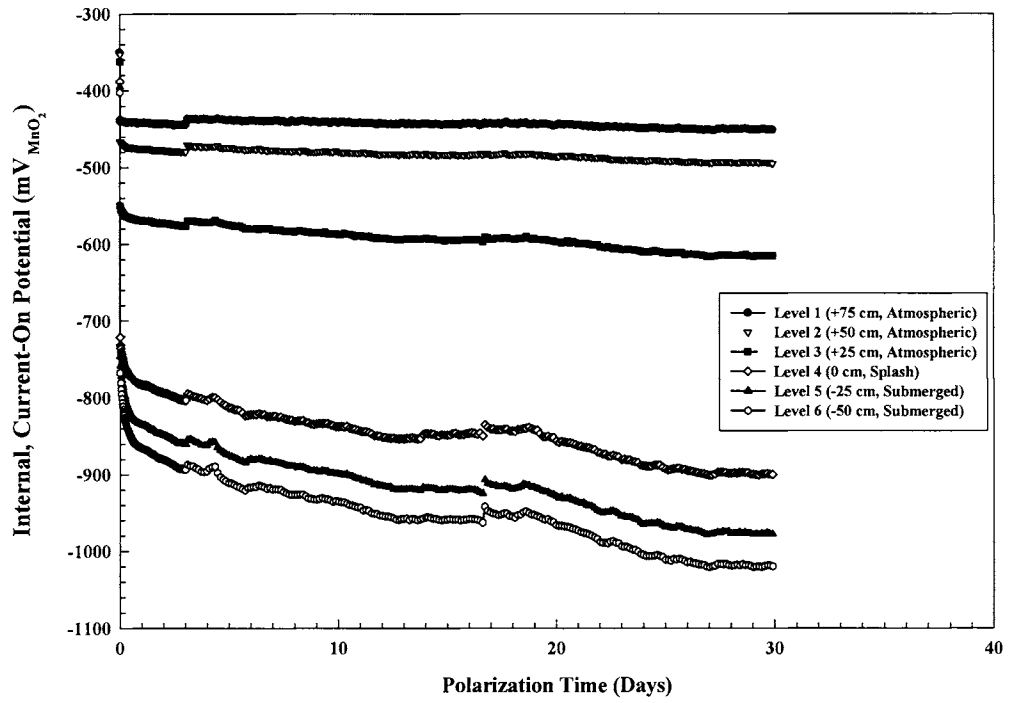
Depolarization from 1.00 μA/cm^2
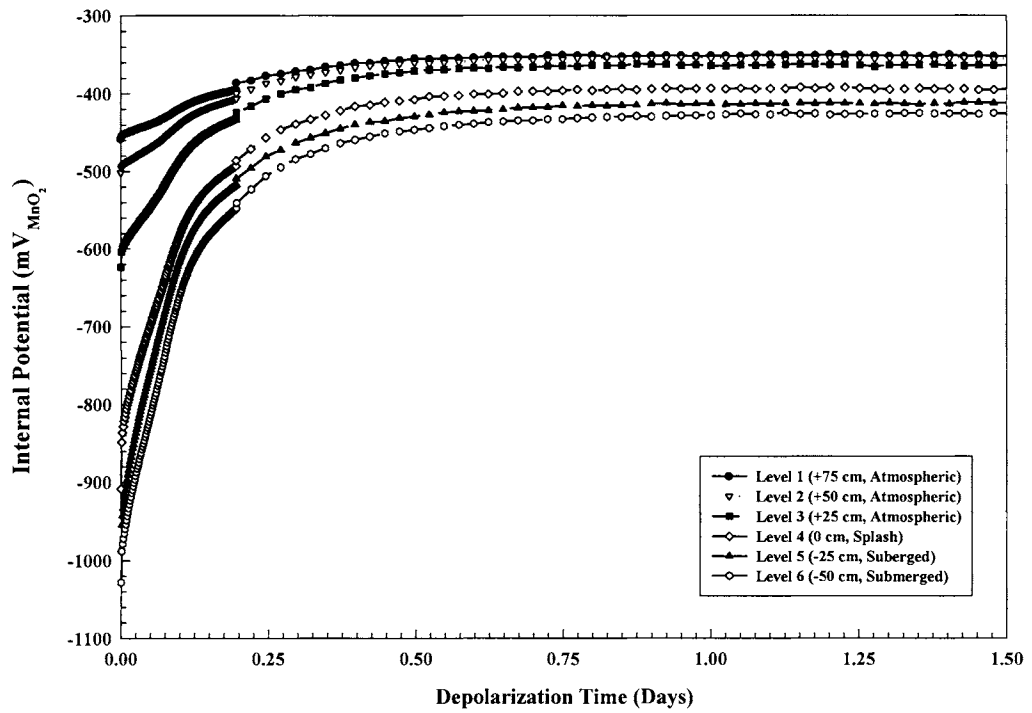
Polarization to 1.33 $\mu A/cm^2$
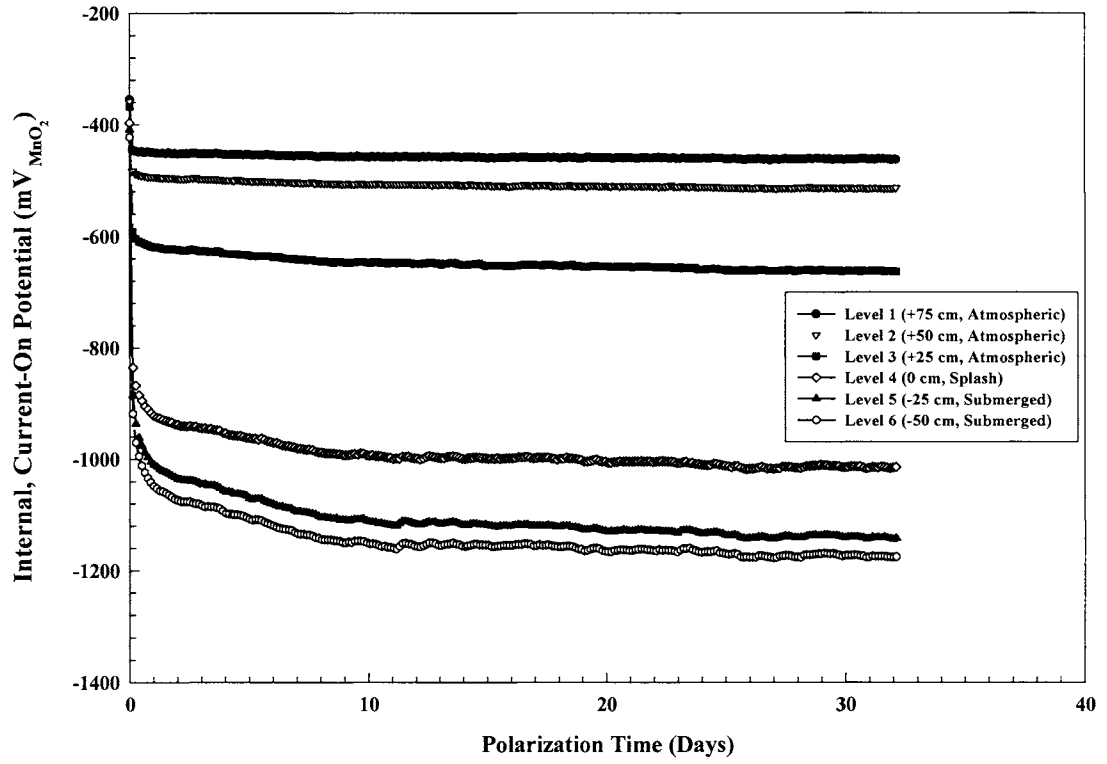
Polarization to 1.66 μA/cm^2
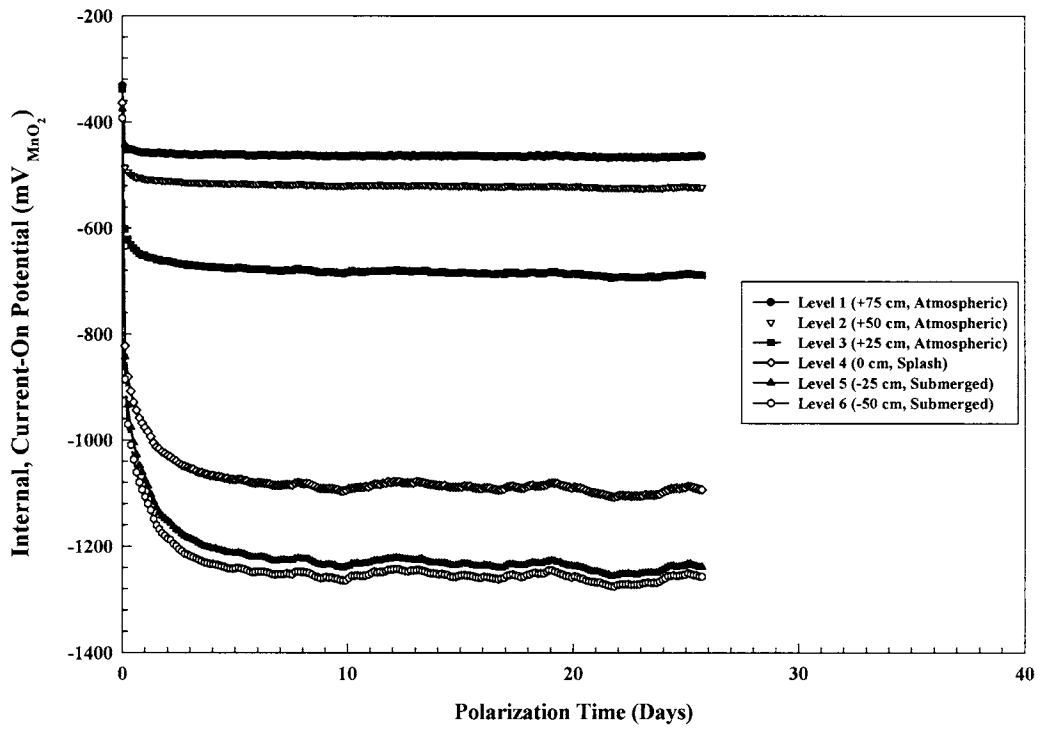
Depolarization from 1.66 μA/cm^2
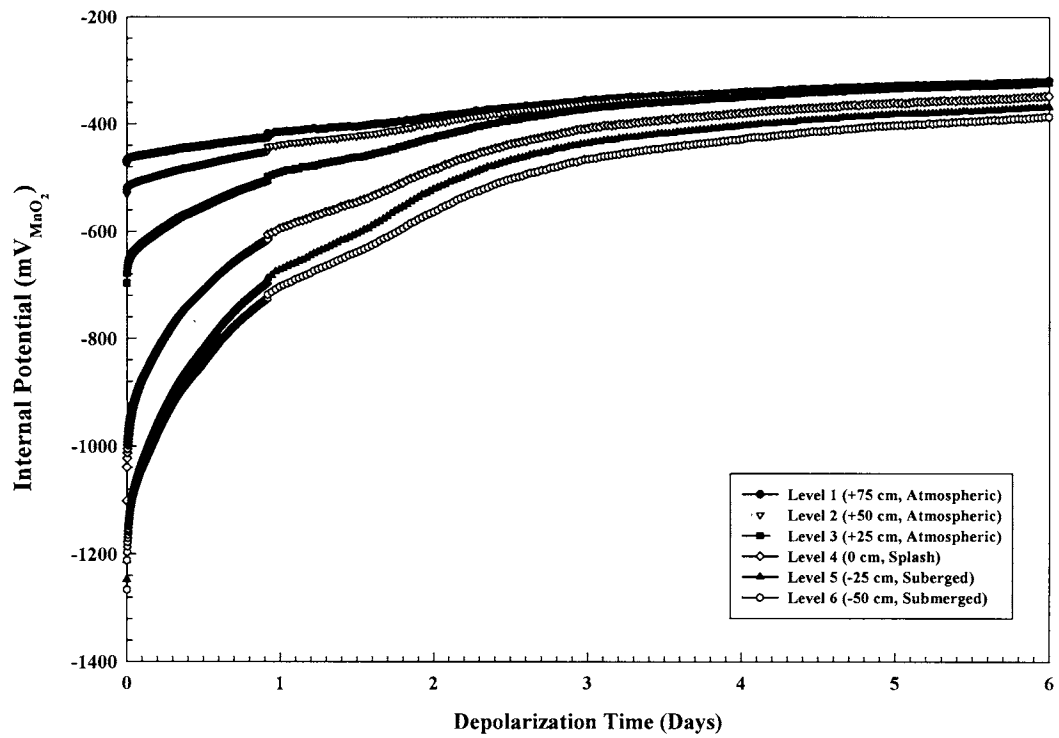
Polarization to 2.00 μA/cm^2
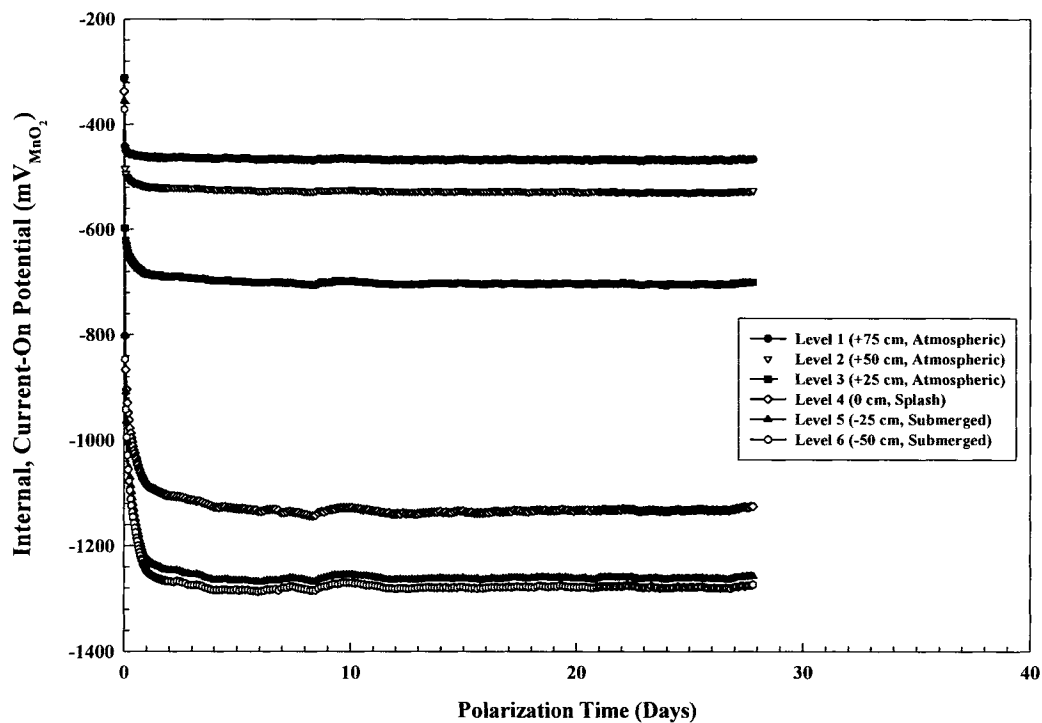
Depolarization from 2.00 μA/cm^2
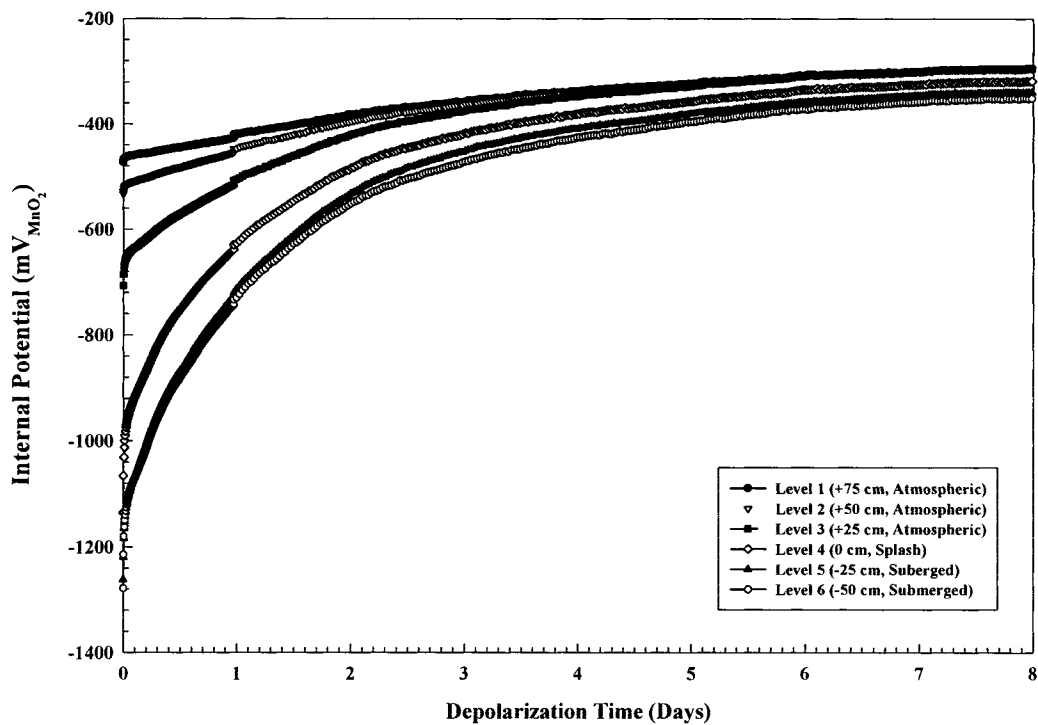
Polarization to 2.50 µA/cm²
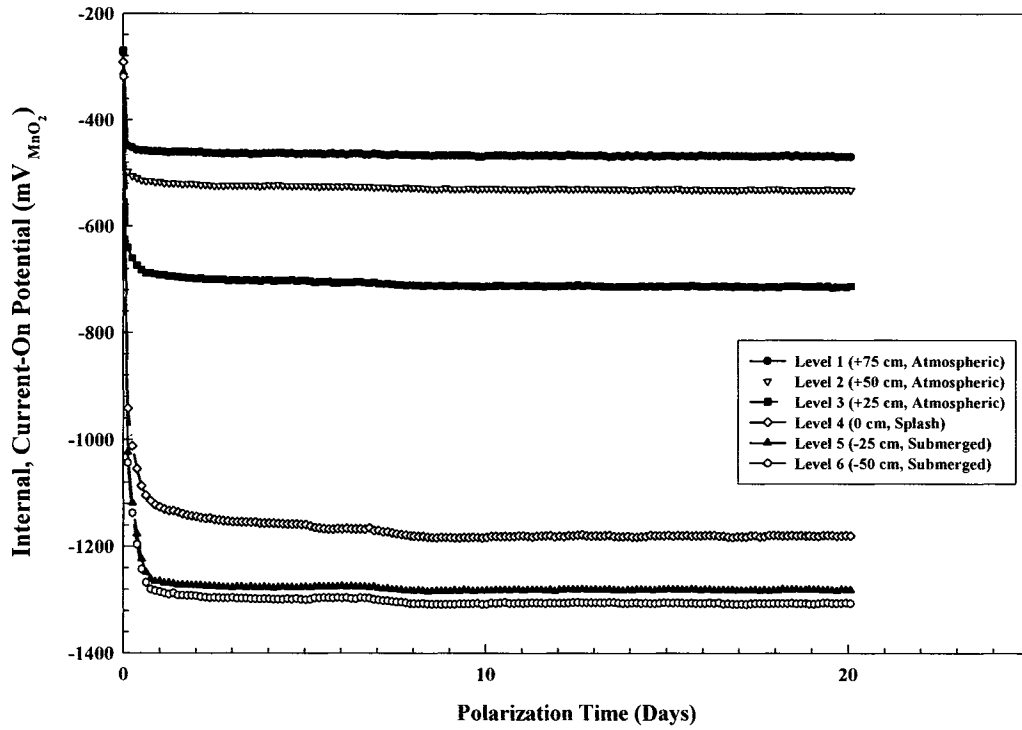
Depolarization from 2.50 µA/cm²

Polarization to 3.00 μA/cm^2

Depolarization from 3.00 μA/cm^2